Site CM2: Crust–Mantle Transition Zone and into upper mantle[1]

Kelemen, P.B., Matter, J.M., Teagle, D.A.H., Coggon, J.A., and the Oman Drilling Project Science Team[2]

Keywords: Oman Drilling Project, OmanDP, Crust–Mantle Transition Zone, CTMZ, Site CM2, Hole CM2A, Hole CM2B, Dunite Sequence, Dunite with Gabbro Sequence, Mantle Sequence, Wadi Zeeb, Samail ophiolite, rotary drilling, core cuttings

Chapter contents

Site CM2 introduction

Site CM2 (22.911°N, 58.336°E) is situated in the northern reaches of Wadi Zeeb in the middle of the Crust–Mantle Transition Zone (CMTZ) of the Samail ophiolite (see Fig. F1 in the **Introduction to Science Theme 1A** chapter). Hole CM2A (22.91097°N, 58.33574°E) is situated a few meters above the wadi (see Fig. F2 in the **Introduction to Science Theme 1B** chapter), and Hole CM2B (22.91100°N, 58.33581°E) is ~10 m to the east, due north of the diamond-cored Hole CM1A.

Based on extensive mapping of the area, described in the **Introduction to Science Theme 1B** chapter, a 300 m vertical rotary borehole (Hole CM2A) was drilled first. This wider diameter rotary well was designed to facilitate geophysical logging across the lithologic contacts using downhole tools that are not deployable in slimline wells. As predicted, Hole CM2A successfully penetrated through the dunites of the CMTZ and into the harzburgites of the uppermost mantle of the Samail ophiolite. Hole CM2B was sited adjacent to Hole CM2A and due north of the previously drilled Hole CM1A (see Fig. F2 in the **Introduction to Science Theme 1B** chapter). It had originally been planned as a 400 m deep inclined borehole, in case the dip of the CMTZ increased at depth, but based on the successful drilling across the target lithologies in Holes CM1A and CM2A, the design of Hole CM2B was modified to a 300 m vertical borehole. The data derived from these cores, cuttings, and boreholes will be used to investigate the nature of the crust–mantle transition in the Samail ophiolite.

Geological setting

Site CM2 is situated on a gravel terrace above an active wadi channel (Fig. F1). The site is located in the middle of the dunites of the Samail CMTZ. The geology is described in more detail in **Geology of Sites CM1 and CM2** in the **Introduction to Science Theme 1B** chapter.

Minor drill pad preparation was necessary at this site to clear away larger rocks and boulders. Existing access from Site CM1 to Site CM2 was via a dirt track, which was graded to facilitate access for the diamond coring drill rig and associated vehicles.

Microbiology sampling

Three rock samples were taken for microbiology analyses from the wireline diamond cored Hole CM2B. They were collected after

[1]Kelemen, P.B., Matter, J.M., Teagle, D.A.H., Coggon, J.A., and the Oman Drilling Project Science Team, 2021. Site CM2: Crust–Mantle Transition Zone and into upper mantle. *In* Kelemen, P.B., Matter, J.M., Coggon, J.A., and the Oman Drilling Project Science Team, *Proceedings of the Oman Drilling Project*: College Station, TX (International Ocean Discovery Program). https://doi.org/10.14379/OmanDP.proc.111.2020
[2]OmanDP Science Team affiliations.

MS OmanDP-111
Published 23 March 2021

normal core flow was complete, and gloves were worn during handling of these cores in an effort to minimize contamination of the samples. The microbiology samples comprise three ~30–40 cm intervals of whole-round core, sampling each of the major lithologies gabbro, dunite, and harzburgite.

Operations: Hole CM2A

An overview of all holes drilled is given in Table T2 in the **Methods** chapter.

All times are reported as local time in Oman (UTC + 4 h).

Drilling summary

- Spud-in: 23 Nov 2017, 08:21 h
- SW surface casing installed: 29 Nov 2017, 16:30 h
- MS surface casing diameter: 9-5/8 inch
- Depth of surface casing: 0.30–21.10 m below ground level (mbgl)
- Hole diameter: 8 in (22.00–218.00 mbgl); 6-1/8 in (218.0–400 mbgl)
- Total depth (TD) of borehole: 400.00 mbgl
- Completion type: open hole
- Discharge by air lift: 0.22 L/s
- Static water level: 62.60 mbgl (14 Dec 2017)

Geology summary

Serpentinized dunite and harzburgite.

Technical issues

The upper part of the borehole had to be reamed because surface casing got stuck at 13.00 mbgl during installation. Reaming was done with a 14-3/4 inch drill bit. The 8 inch hammer drill bit was switched over to a 6-1/8 inch tricone bit at 213 mbgl because the 8 inch hammer bit got stuck. Multiple mechanical failures of drill rig equipment occurred during drilling of Hole CM2A (e.g., RPM sensor installed on the rig by the Japan Agency for Marine-Earth Science and Technology [JAMSTEC] stopped working, leakage of hydraulic hoses, failure of backpressure valve on drill bit assembly).

Operations summary

- 20–21 Nov 2017: mobilize drill rig, drilling accessories, equipment, and material to site.
- 22 Nov 2017: prepare site; rig up, calibrate, and test digital drill rig sensors installed by JAMSTEC.
- 23 Nov 2017: spud and start drilling with 12-1/4 inch tricone drill bit assembly using air foam; observe a problem with drill rig compressor.
- 24 Nov 2017: mechanical maintenance on rig; continue drilling below 2.00 mbgl.
- 25 Nov 2017: drill using 12-1/4 inch tricone drill bit to 22 mbgl; observe seepage at 14 mbgl.
- 26 Nov 2017: 1.2 m of backfill in hole; wash hole to TD at 22 mbgl and complete pulling out of hole (POOH). Install run in hole (RIH) casing (9-5/8 inch); casing stuck at 3.5 mbgl. POOH RIH casing for reaming. Send truck to Muscat to collect hole stabilizers and accessories.
- 27 Nov 2017: set up 12-1/4 inch drill bit assembly with stabilizers; ream borehole to 22 mbgl. Flush hole and POOH completely. Casing struck at 13.00 mbgl. POOH casing and ream again with 14-3/4 inch bit size to 13.00 mbgl.
- 28 Nov 2017: continue reaming hole with 14-3/4 inch drill bit. Flush hole and partial POOH.
- 29 Nov 2017: continue reaming hole with 14-3/4 inch drill bit to 22 mbgl. Flush hole and complete POOH. Install MS surface casing (9-5/8 inch) to 21.10 mbgl with 0.90 m backfill to 22 mbgl. Cement grout 14-3/4 inch and 9-5/8 inch casing annulus.
- 30 Nov 2017: set up 8 inch hammer bit assembly and drill hole to 76.8 mbgl. Observe increase in seepage at 62 and 74 mbgl. Collect/describe drill cuttings every meter; collect cuttings subsamples for further analysis.
- 01 Dec 2017: drill with 8 inch hammer bit 76.8–133 mbgl. Collect/describe drill cuttings every meter; collect cuttings subsamples.
- 02 Dec 2017: drill with 8 inch hammer bit 133–175.6 mbgl. Collect/describe drill cuttings every meter; collect cuttings subsamples.
- 03 Dec 2017: drill with 8 inch hammer bit 175.6–218.00 mbgl. Collect/describe drill cuttings every meter; collect cuttings subsamples.
- 04 Dec 2017: observe drill bit blockage at 213 mbgl. Complete POOH and switch from 8 inch hammer bit to 6-1/8 inch tricone bit assembly. Wash hole 213–218 mbgl. Continue drilling to 220.2 mbgl.
- 05 Dec 2017: drill with 6-1/8 inch tricone bit 220.2–232 mbgl. Collect/describe drill cuttings every meter; collect cuttings subsamples.
- 06 Dec 2017: drill with 6-1/8 inch tricone bit 232–273 mbgl. Collect/describe drill cuttings every meter; collect cuttings subsamples.
- 07 Dec 2017: drill with 6-1/8 inch tricone bit 273–296.2 mbgl. Collect/describe drill cuttings every meter; collect cuttings subsamples; observe fast drilling and sudden drop of 0.3 m at 285 mbgl.
- 08 Dec 2017: maintenance of RPM sensor and fix broken hydraulic hose on drill rig. Observe block-

age of air foam circulation in drill bit. Complete POOH and clean bit assembly.

- 09 Dec 2017: drill with 6-1/8 inch tricone bit 285–328.00 mbgl. Collect/describe drill cuttings every meter; collect cuttings subsamples.
- 10 Dec 2017: drill with 6-1/8 inch tricone bit 328–362 mbgl. Collect/describe drill cuttings every meter; collect cuttings subsamples. Maintenance of RPM sensor on drill rig. Blockage of circulation system; partial POOH to 240 mbgl; flush borehole.
- 11 Dec 2017: drill with 6-1/8 inch tricone bit to 382 mbgl. Collect/describe drill cuttings every meter; collect cuttings subsamples.
- 12 Dec 2017: fix and test RPM sensor. Circulation blockage in drill bit; complete POOH to replace NRV assembly.
- 13 Dec 2017: drill with 6-1/8 inch tricone bit to 400.00 mbgl. Collect/describe drill cuttings every meter; collect cuttings subsamples.
- 14 Dec 2017: conduct well development test (air lift test) for 5 h, 20 min. Total yield of borehole = 0.22 L/s. Parameters monitored during air lift test: electrical conductivity = 2.81 mS/cm; pH = 10.06; resistance = 3.50 Ω·cm, T = 31.3°C (**Supplementary material** > **L_Wireline logging**.
- 15–17 Dec 2017: mobilize rig, drilling accessories, material, and equipment from Hole CM2A to Hole CM1B.
- 21 Jan 2018: observe borehole blockage at 176 mbgl. Mobilize rig from Hole CM1B to CM2A for flushing and clearing Hole CM2A from 176 mbgl.
- 22 Jan 2018: rig up and prepare site for conducting clearing/wiper run. Arrival of Schlumberger Oil Services borehole logging team.
- 23 Jan 2018: clear borehole by wiper run 175.80–350 mbgl. Static water level at 13.70 mbgl.
- 24 Jan 2018: clear borehole by wiper run 350–395 mbgl (backfill = 5 m). Complete POOH.
- 25–26 Jan 2018: geophysical borehole logging by Schlumberger Oil Services.

Petrology from drill cuttings: Hole CM2A

Rotary Hole CM2A is located 12 m from cored Hole CM2B (Figs. F2, F4 in the **Introduction to Science Theme 1B** chapter). Detailed petrological observations were made on core from Hole CM2B during summer 2018 onboard DV *Chikyu*. Here we summarize the on-site lithology log of Hole CM2A drill cuttings. The drill cuttings log is available in Table T2. A lithologic section based on the cuttings logs is shown in Figure F2.

As in Hole CM2B, the upper 143 m of Hole CM2A is dominated by dunite. The cuttings log indicates minor interlayered gabbro at 80–83 and 117 m and wehrlite at 131–133 m. It is not apparent whether these are true wehrlites. The term wehrlite has traditionally been used over decades of mapping Oman lower crustal lithologies mainly for rocks with 10%–30% plagioclase (which should be called “olivine melanogabbros” or just “gabbros”) rather than for true wehrlites (which are rare).

Harzburgite dominates the cuttings log at 144–385 m except for dunite layers at 147, 158, 180–189, 193, 195, and 228 m.

Hydrothermal alteration/veins: Hole CM2A

No alteration or vein lithologies were recorded in the cuttings log for Hole CM2A.

Geochemistry: Hole CM2A

X-ray fluorescence (XRF) analyses of cuttings were analyzed at 10 m intervals Sultan Qaboos University (SQU). These data are imprecise and inaccurate, and some values are entirely incorrect or attributed to the wrong element. Table T3 in the **Introduction to Science Theme 3** chapter compares SQU analyses of three standards (2 peridotites and 1 Mg-rich basalt) with community accepted values and illustrates working curves based on these data for elements with a systematic difference between SQU and community values that can be used to correct the SQU analyses.

Table T4 in the **Introduction to Science Theme 3** chapter presents SQU analyses of drill cuttings from Hole CM2A together with approximate CIPW norms for these data. Corrected analyses used the working curves from Table T3 in the **Introduction to Science Theme 3** chapter. In general, these data add little to our understanding of the lithologies in Hole CM2A.

Downhole measurements: Hole CM2A

Wireline logs were recorded by the University of Montpelier group using a slimline logging system and by Schlumberger Oil Services using oil-field type logging tools in January and March 2018 (Tables T56, T57 in the **Methods** chapter). Because of partial blocking or collapse of the borehole at ~200 m below surface, only logs from the upper part of the borehole are available. Resistivity from the dual laterolog log is <200 Ω·m in the upper 143 m, which is dominated by dunite, and increases to 600 Ω·m in the harzburgite deeper than 143 m. Resistivity peaks as high as 2000 Ω·m nicely indicate gabbroic interlayers. The spectral gamma log shows very low K, U, and Th concentrations, with mostly K-rich alteration zones and one prominent U-rich horizon at 160 m. Fluid column logs indicate a change of electrical fluid conductivity from 1389 μS/cm at 13.10 mbgl to 5022 μS/cm at 192.3 mbgl, whereas pH changes from 8.7 to 11.2 and redox potential changes from 308 to –564 mV (**Supplementary material** > **L_Wireline logging**).

Microbiology: Hole CM2A

Fluid, dissolved gas, and microbial samples were collected by OmanDP microbiologists/biogeochemists in January 2018 using a submersible downhole pump and subsequently analyzed. Results are discussed in the **Microbiology** chapter.

Operations: Hole CM2B

An overview of all holes drilled is given in Table **T2** in the **Methods** chapter. Drilling operations and core curation information are reported in Table **T1**.

All times are reported as local time in Oman (UTC + 4 h).

Drilling summary

- Spud-in: 19 Dec 2017, 08:15 h
- First core on deck: 19 Dec 2017, 09:00 h
- HW surface casing installed: 19 Dec 2017, 5.60 m
- Surface casing extended: 20 Dec 2017, 11.60 m and 13.10 m
- NW casing installed: 25 Dec 2017, 13.10 m
- Final core on deck: 17 Jan 2018, 16:33 h
- TD of borehole: 04 Jan 2018, 300.00 m

Geology summary

Mainly serpentinized dunite to 130 m, followed by serpentinized harzburgite with minor (centimeter thick) serpentinized dunite layers.

Technical issues

No major technical issues with this borehole!

Operations summary

- 17 Dec 2017: mobilize coring rig from Site CM1 to Site CM2. Load core boxes at Site CM1 and transport to Muscat.
- 18 Dec 2017: set up drill rig and equipment on site; install core characterization tent and infrastructure.
- 19 Dec 2017: start drilling Hole CM2B with HQ drill bit assembly. Core from ground level (GL) to 13.80 m. Ream and case hole with HW casing to 5.60 m.
- 20 Dec 2017: drill with HQ drill bit assembly to 26.60 m. Ream and case hole with HW casing to 11.60 m along with drilling.
- 21 Dec 2017: drill with HQ drill bit to 47.60 m.
- 23 Dec 2017: J. Coggon arrived and took over from J. Matter as Lead Scientist on site. Japanese film crew filmed outcrops and core flow. Drill with HQ drill bit to 64.30 m.
- 24–25 Dec 2017: drill with HQ drill bit to 98.60 m; ream and extend surface casing to 13.1 m.
- 26–27 Dec 2017: drill with HQ drill bit to 137.60 m.
- 28 Dec 2017: hole collapse with 1 m backfill. Clean hole with continuous flushing at high pressure; drill with HQ bit to 158.60 m.
- 30–31 Dec 2017: drill with HQ bit to 209.60 m.
- 1–4 Jan 2018: drill with HQ bit to 300.00 m. Hole CM2B completed; POOH.
- 6 Jan 2018: demobilize Site CM2.
- 7 Jan 2018: borehole head construction and core box transportation to Muscat.

Igneous petrology: Hole CM2B

Macroscopic core description

Summaries of all Hole CM2B units and subunits, their depths, and descriptions are provided in supplemental Table **ST1**, which contains all data recorded by the igneous petrology description team during visual inspection of the cores, and supplemental Table **ST2**, which summarizes all information related to the individual lithologic units extracted from Table **ST1**.

The main lithologic units logged in Hole CM2B are dunite, harzburgite with minor abundances of olivine gabbro, gabbro, wehrlite, anorthosite, troctolite, websterite, clinopyroxenite, and gabbronorite. Table **T3** lists the abundance of the principal rock types in unit count percentages and cumulative thickness, and Figure **F3** shows the graphical representation. Lithologic units are divided by contacts such as changes in mineral assemblage, modal abundance, and structural and other textural variations. The evolution of lithologies with depth including their mineral modes and grain sizes is shown in Figure **F4**.

Lithologic sequences

Apart from 12 m of alluvium at the top, Hole CM2B is divided into three major sequences: the Dunite Sequence, the Dunite with Gabbro Sequence, and the Mantle Sequence, directly analogous to Hole CM1A. Table **T3** lists the abundance of the rock types in each sequence, both in terms of the number of units (percentage) and cumulative thickness (percentage), and Figure **F5** presents a graphical representation.

The depths and properties of the sequences are summarized in Table T4.

Dunite Sequence

Depth: 12–74.26 m
Interval: CM2B-9Z-1 through 40Z-1
Units: 2a–6

The major lithologic unit in the Dunite Sequence is dunite (>99.9% by thickness), although some of the dunites are orthopyroxene or plagioclase bearing with <1 cm thick veins of gabbronorite, olivine gabbro, and gabbro. The contact between the Dunite Sequence and the underlying Dunite with Gabbro Sequence is marked by a prominent gabbroic layer and deformational contact at 74.26 m.

Dunite with Gabbro Sequence

Depth: 74.26–120.78 m
Interval: 40Z-1 through 60Z-2
Units: 7–11c

Major lithologic units in the Dunite with Gabbro Sequence include massive dunite (81.5% by thickness) with layers/veins of olivine gabbro, gabbro, and wehrlite. The contact between the Dunite with Gabbro Sequence and underlying Mantle Sequence is marked by a sharp modal change and the occurrence of harzburgite from 120.78 m.

Mantle Sequence

Depth: 120.78–300.14 m (bottom of hole)
Interval: 60Z-2 through 129Z-1
Units 12–67i

The ~179 m thick Mantle Sequence includes harzburgite (45.4% by thickness) and mostly orthopyroxene-bearing dunite (21.1%), both with typical characteristic porphyroclastic mantle textures. The remaining ~1.5% consists of troctolite, websterite, olivine gabbro, gabbro, anorthosite, and orthopyroxenite, mostly occurring as thin sills or veins (millimeter to centimeter thick) or as impregnations in dunite. Some of the veins and patches exhibit dunitic reaction rims. The lowermost 20 m of the hole is faulted and strongly carbonated.

Principal rock types

In this section macroscopic descriptions of the principal rock types and corresponding core images are presented in order of abundance (according to accumulated thickness; Table T3). We refer to units and subunits and their intervals, thicknesses, and other descriptors that are collated in supplemental Table ST2.

Dunites

Dunites are the most abundant lithology recovered from Hole CM2B (Fig. F3). Dunitic intervals are present in the Dunite Sequence, the Dunite with Gabbro Sequence, and the Mantle Sequence (Fig. F5; supplemental Table ST2). The Dunite and Dunite with Gabbro Sequences contain two thick dunite bodies with similar properties that are divided by gabbro and wehrlite layers at 74–79 m (Subunits 7–8e) and 80–83 m (Subunit 8i). The dunites are fine to medium grained, equigranular, and typically completely altered (e.g., Fig. F6A). Dunites have granular and (rarely) subophitic textures and sharp modal contacts with neighboring units. Subophitic textures occur only in plagioclase- or clinopyroxene-bearing intervals, where those minerals appear as poikilitic patches around olivine. Olivine grain sizes are 0.5–5 mm, and olivine comprises 98%–100% of the dunites. Olivines are equant and anhedral.

In the Dunite Sequence, many units contain equant, anhedral spinel with grain sizes of 0.5–1 mm. Toward the bottom of the sequence the spinels become euhedral. Subunits 2a–2c and 3g–3i are clinopyroxene-bearing dunites with clinopyroxene grain sizes of 2 mm; these have equant and anhedral clinopyroxenes with a mode of 1% (Fig. F6A). The plagioclase-bearing dunites with plagioclase grain sizes of 0.5–5 mm found in Units 2, 4, and 6 have interstitial anhedral plagioclase at modes of 1%–2% (Fig. F6B). A single spinel-rich dunite was observed in a broken interval of core (Subunit 3h, Fig. F6C). Trace sulfides are found in about half the dunites in the Dunite Sequence, including plagioclase-bearing and clinopyroxene-bearing lithologies (e.g., Fig. F7A). These sulfides have grain sizes of 0.1–1 mm, modes of 0.5%, and are equant and anhedral. However, taking into account the extreme alteration degree in dunites, sulfide magmatic or hydrothermal origin could not be determined on the basis of core observation alone; more investigation, notably through thin section observation, must be conducted. Some of the dunites in the Dunite Sequence are cut by gabbro, olivine gabbro, and gabbronorite veins (see sections below), and contacts with the veins are generally sharp and intrusive.

In the Dunite with Gabbro Sequence, plagioclase-bearing dunites are common (Units 8–11, 0.5–1 vol% plagioclase; Fig. F7B). Plagioclase is interstitial and anhedral with 1 mm grain sizes. Many of the dunite units contain equant, anhedral spinel with a grain size of 0.5–1 mm. Interstitial, anhedral sulfides with grain sizes of 0.1–0.5 mm are present in all units. As in the Dunite Sequence, magmatic or hydrothermal origin could not be determined for minute sulfide crystals, where noted. The dunites have equant, anhedral olivines with 0.5–3 mm grain size, in contrast to the slightly coarser olivine (1–5 mm) in the Dunite Sequence.

In the Mantle Sequence, dunites begin at Unit 13 (121.4 m) as layers within host harzburgites. Dunites in the Mantle Sequence are distinguished from dunites in the overlying sequences by their slightly larger grain sizes (typically medium–coarse grained) and porphyroclastic textures; the dunites are also frequently orthopyroxene bearing with 1–3 vol% subequant to equant anhedral orthopyroxene (Figs. F7C, F8A). Overall, the Mantle Sequence dunites have equigranular grain size distributions; olivines are equant and anhedral with grain sizes of 0.5–7 mm. Like the dunites in the overlying sequences, the Mantle Sequence dunites are spinel bearing. Spinel is interstitial or equant with anhedral or euhedral habits and grain sizes of 0.2–2 mm. The dunites in the Mantle Sequence are cut by rare gabbro, anorthosite, and troctolite veins and patches that are more abundant near the contact with the Dunite with Gabbro Sequence (see below). Contacts with adjacent harzburgite units are modal and rather sharp; contacts with crosscutting gabbro and anorthosite units are sharp and intrusive.

Harzburgite

Spinel harzburgite is the most abundant lithology in the Mantle Sequence, comprising 46% of the total recovery from Hole CM2B (Fig. F5). The harzburgites are medium to coarse grained and have equigranular grain size distributions (Fig. F8B, F8C). Grain textures are typically porphyroclastic and rarely granular (Unit 56a) but are submylonitic or cataclastic near the bottom of the hole (Fig. F9A). Harzburgites are foliated; the foliation plane is defined by shape-preferred orientation of the orthopyroxenes and Cr-spinels. The harzburgites have equant, anhedral olivines with 1–7 mm grain sizes. Orthopyroxene abundances are 7%–40%, grain sizes are 2–13 mm, and grains are subequant to equant and anhedral. Primary clinopyroxene in harzburgites was not identified visually in the cores. However, thin section inspections, bulk Ca abundances, and trace element analyses all demonstrate the presence of clinopyroxene toward the bottom of the section (see **Calculated mineral modes from XRF data**). As much as 1% spinel is present (grain size typically = 0.1–1 mm), either interstitial or anhedral. Subunit 46g contains large (5 mm) equant anhedral spinel. Trace sulfides were observed in Subunits 46e–46g, 54c, 56e, 61z, and 64; these are equant and anhedral with grain sizes of 0.1 mm. Contacts with dunite layers are typically sharp and modal, whereas contacts with intrusive websterite, anorthosite, troctolite, gabbronorite, and olivine gabbro veins are most commonly sharp and planar (see next sections).

Olivine gabbro

Olivine gabbros are the third most abundant lithology in Hole CM2B cores and make up 1.5% of the recovery. A 4.6 m thick layer is present between the Dunite and the Dunite with Gabbro Sequences (Fig. F9B). Olivine gabbros are also found as veins and patches (0.5–8.5 cm thick) in the lower half of the Mantle Sequence (e.g., Fig. F9C) and as a single 0.5 cm thick vein in the Dunite Sequence (Subunit 3f). In general, grain sizes are medium to coarse, grain size distributions are equigranular, and grains are granular.

The thick layer between the Dunite and the Dunite with Gabbro Sequences is strongly foliated with interlayered bands of dunite and gabbro (Fig. F9B). Olivine modes are 20%–40%, and olivines have grain sizes of 0.5–4 mm. Plagioclase is 30%–50% of this layer; grain sizes are 2–5 mm. Clinopyroxenes make up 20%–30% of this layer, and grain sizes are 2–3 mm. Olivine, clinopyroxene, and plagioclase grains are all elongate and anhedral. Minor (0.5 vol%) equant euhedral spinel is present with grain sizes of 0.1–0.2 mm.

Olivine gabbro veins and layers in the Mantle and Dunite Sequences contrast with the olivine gabbro layer in that they are not layered and they have coarser grain sizes (Fig. F9C). Their contacts with the host mantle are sharp and intrusive. Olivine modes are 5%–30%, generally subequant–equant and anhedral–subhedral, and grain sizes are 0.5–4 mm. Plagioclases are equant or interstitial and may be subhedral or anhedral, with grain sizes of 1–12 mm and modes of 35%–70%. Clinopyroxene modes are 10%–65%, and grain sizes are typically 1–5 mm and are equant and anhedral. Two subunits (56f, 61b) have poikilitic clinopyroxenes with grains as large as 30 mm.

Gabbro

Olivine-bearing and olivine-free gabbros are present as veins in the Dunite and Mantle Sequences (Subunits 2b, 8e, 17b, 21d, and 32l) and as a layer between the Dunite and Dunite with Gabbro Sequences (Subunit 8i; Fig. F10A). Their contacts with the host dunite or harzburgite are sharp, planar, and intrusive. The gabbro layer has 2% equant, anhedral olivine with 2 mm grain size, and the gabbro veins are olivine-free. Plagioclase constitutes 50%–90% of these gabbros. Plagioclase grain sizes are 2–4 mm, and grains are generally equant and anhedral. The clinopyroxene mode is 10%–40% with grain sizes of 0.5–3 mm. One vein (Subunit 17b) has 10 mm plagioclase and clinopyroxene, whereas another sheared subunit (8e) has microcrystalline plagioclase and clinopyroxene (both 0.5 mm). Neither orthopyroxene nor sulfides were observed in any gabbro units. Equant, anhedral spinel with a grain size of 0.1 mm is present in gabbro layer Subunit 8i, but spinel is otherwise absent from other units. A single hornblende-bearing patch is present in Subunit 22b; amphibole has a mode of 5%, grain size of 3 mm, and is interstitial and anhedral (Fig. F10B).

Wehrlite

Plagioclase-bearing wehrlite layers interspersed with gabbros are present in two subunits (8b, 8d) in the Dunite with Gabbro Sequence near the contact with the Dunite Sequence (Fig. **F10C**). Wehrlites have elongate, anhedral plagioclase with a mode of 20% and 1 mm grain size. Olivines are elongate and anhedral with modes of 49%–60% and grain sizes of 2 mm. Clinopyroxenes are elongate and anhedral with grain sizes of 5–6 mm and modes of 20%–30%. Spinels are equant and euhedral with modes of 1% and grain sizes of 0.5 mm. Orthopyroxenes and sulfides are absent.

Anorthosite

Anorthosite veins with maximum thicknesses of 2 cm and thicker patches are present in the Mantle Sequence (Fig. **F11A**). Their contact with the host mantle is sharp and intrusive. Plagioclase modes are 95%–100%, grains are subequant or equant and subhedral to anhedral, and grain sizes are 1–8 mm. In a single vein (Subunit 21b), grain sizes are up to 15 mm. Olivines are present in many units with modes of 1%–5% and grain sizes of 1–2 mm; the olivines are generally equant or anhedral. Olivine-bearing units (with 5%–7% olivine) have 1–5 mm olivines. Subunit 39b has olivines as large as 15 mm. Clinopyroxenes are absent. Subunits 42f and 42h contain trace 0.1 mm interstitial anhedral sulfides. Subunit 23d (a patch in a mantle harzburgite) contains trace abundances of 4 mm subequant, subhedral amphibole.

Troctolite

Troctolite veins and patches are present in the Mantle Sequence and have maximum thicknesses of 0.6 cm (Fig. **F11B**). They are composed of 15%–60% olivine with grain sizes of 2–5 mm. Olivine may be elongate, subequant or equant, and subhedral or anhedral. Plagioclase modes are 30%–85% with grain sizes of 2–10 mm. Plagioclase may be poikilitic, elongate, subequant, or interstitial and subhedral or anhedral. Spinel is generally absent. Subunit 61j contains 40% 12 mm poikilitic clinopyroxene, and other troctolite units are clinopyroxene-free. Troctolite veins and patches are commonly surrounded by 1–5 cm thick dunitic reaction halos, and the contact with the host mantle harzburgite is generally gradational with increases in plagioclase modal abundance to the center of the intrusion.

Websterite

Websterite veins are present in the Mantle Sequence and have maximum thicknesses of 0.6 cm (Fig. **F11C**). They have clinopyroxene modes of 15%–92% (mostly at the high end of the range), and grains are 2.5–10 mm with subequant to equant and subhedral or anhedral shapes. Orthopyroxene modes are 7%–80% (mostly at the low end of the range), grain sizes are 1.5–10 mm, and most are equant and subhedral or anhedral. Olivine is present in some units at modes of 1%–5%, grain sizes of 0.5–1.5 mm, and olivines are equant and anhedral. Subunits 61ae, 61b, and 61d contain trace abundances of equant, anhedral, 0.1 mm sized sulfides. The websterite contacts with the host harzburgite are sharp and intrusive.

Clinopyroxenite

A single, 1 cm thick clinopyroxenite vein is present in the Mantle Sequence (Unit 61y, Fig. **F12A**). It consists of 95% equant, anhedral clinopyroxene with 1 mm grain size. The remaining 5% of this vein is 1 mm equant, anhedral olivine. Neither spinel nor sulfide were observed.

Gabbronorite

Three gabbronorite veins are present in the Dunite Sequence (Subunits 2d, 3b, and 3d; Fig. **F12B**); one gabbronorite vein is present in the Mantle Sequence (Subunit 26b; Fig. **F12C**). The veins have plagioclase abundances of 60%–90% and plagioclase grain sizes of 2–10 mm; grains are generally equant and anhedral. Clinopyroxene comprises 10%–40% of the veins, with grain sizes of 2–10 mm. Clinopyroxenes are typically equant and anhedral. The gabbronorites are spinel- and sulfide-free. Their contact with the host harzburgite is sharp and intrusive.

Downhole evolution with depth

Hole CM2B is composed of 3 sequences as characterized in **Lithologic sequences**. Lithologic variations as well as modal compositions and grain size evolution are shown in Figure **F4**.

Mode

In the Dunite and Mantle Sequences, clinopyroxene and plagioclase are present only in impregnated peridotites with low modal proportion (<1%). Higher modal amounts are only present in the gabbroic and pyroxenitic veins and layers; a few gabbronorite veins exist at the top of the Dunite Sequence, and gabbro, anorthosite, gabbronorite, and pyroxenite veins are present all along the Mantle Sequence. The plagioclase modal proportion ranges 40%–100% in the gabbroic and anorthositic veins and is <1% in any other lithology. Clinopyroxene is abundant only in the websterite veins at the bottom of the hole (deeper than 250 m) and present at variable proportion in gabbroic dikes and veins.

In contrast, olivine modal proportion is >60% in dunite and harzburgite and decreases to <20% in gabbroic veins only.

Orthopyroxene is present in gabbronorite veins in the upper part of the Dunite Sequence. At lower abundance (<30%), this mineral is omnipresent throughout the Mantle Sequence where true dunite (completely devoid of orthopyroxene) is almost absent and most commonly contains >1% orthopyroxene. In contrast, dunites (without any modifier) in the Dunite and Dunite with Gabbro Sequences generally do not contain any orthopyroxene. However, this mineral appears at low proportion a few meters above the boundary to the Mantle Sequence, where it is present in thin harzburgitic layers and disseminated within dunites.

Strongly layered dunite/olivine gabbro bands are present at the top of the Dunite with Gabbro Sequence (~75–85 m). This 10 m thick interval shows the strongest modal variability in Hole CM2B, with strong fluctuations in olivine, plagioclase, and clinopyroxene proportions within and between bands (Fig. F13).

Cr-spinel is present but rare in the upper part of the Dunite Sequence. It tends to be slightly more abundant in the lower part of the Dunite with Gabbro Sequence, albeit only in ultramafic layers, and has a modal abundance of 0.1%–2% in mantle harzburgites. Cr-spinel-rich dunite is present in the Dunite and Dunite with Gabbro Sequences as Cr-spinel-rich bands in dunite associated with plagioclase and/or clinopyroxene impregnation. In these bands, lower Cr-spinel abundance is associated with the presence of interstitial plagioclase, as Cr-rich bands are devoid of plagioclase.

Grain size

Grain size evolution along the hole is related with major structural features like faults and shear zones or with specific lithologies like coarse-grained gabbroic veins and patches in the Mantle Sequence and appears to be depth independent.

Microcrystalline gabbro is present at the top of the Dunite Sequence as a very altered vein. Other than this vein, grain size ranges from fine to coarse all along the hole.

Lithologies with medium-grained textures are the most abundant. Most dunites in the Dunite with Gabbro and the Mantle Sequences, as well as harzburgites in the Mantle Sequence, are medium grained. Dunites in the Dunite Sequence exhibit intermediate grain sizes between fine and medium, ~1 mm. In the Dunite with Gabbro Sequence, dunites are fine grained in the sheared layers in contact with gabbro and medium grained in the more homogeneous suite above the Mantle Sequence.

The Mantle Sequence is composed of porphyroclastic medium-grained harzburgites. Coarse-grained intervals are gabbroic veins or patches. Fine-grained intervals include a few fine-grained veins and a submylonitic sheared sequence present above the faulted and carbonated zone at the lowermost 20 m of the hole.

Igneous layering

In Hole CM2B, igneous layering is present only in the Dunite with Gabbro Sequence. Layered gabbroic rocks occur within a limited interval at 74.26–83.89 m (interval 40Z-1, 16–52.5 cm [Unit 7], to 44Z-4, 0–32 cm [Subunit 8i]). The layering intensity varies from strong to weak with modal, sharp, and planar contacts between layers. Strong layering is clearly illustrated by the alternating bands of 1–5 cm thick dunite and olivine gabbro in interval 40Z-1, 18–41 cm (Fig. F13A). Plagioclase layers (1 cm thick) in a dominantly wehrlite unit show moderate layering in interval 42Z-1, 50–70 cm (Fig. F13B). The gabbros at 80.27–83.39 m (Sections 43Z-1 through 44Z-4) have weak layering.

Contacts

In the Dunite Sequence, thin gabbroic to anorthositic veins intrude the dunite, forming sharp and planar contacts. At 74.26 m, the Dunite Sequence has a sheared, sharp, planar contact with the Dunite with Gabbro Sequence. Modal, sharp, and planar contacts are commonly observed in the Dunite with Gabbro Sequence at 74.26–83.89 m. These are commonly demarcated by variations in the abundance of olivine and plagioclase in the gabbro. At 115.29 m, the dunite (Subunit 11a) shows modal, sharp, planar contact with the underlying spinel-rich dunite (Subunit 11b). Examples of contacts observed in the Dunite Sequence and Dunite with Gabbro Sequence are shown in Figure F14A–F14C.

The contact between the Dunite with Gabbro Sequence and the Mantle Sequence occurs at 120.78 m (Section 60Z-2, 53 cm). The lowermost subunit of dunite (Subunit 11c) shows a modal, sharp, and curved contact with the underlying harzburgite (Unit 12; Fig. F14D). The contact is clearly marked by an increase in orthopyroxene content from the dunite to the harzburgite.

Harzburgite first appears in a thin interval at Section 58Z-4, 23–26 cm. Figure F15 presents a binocular close-up of this harzburgite showing relics of augen-like deformed orthopyroxene porphyroclasts indicative of deformation resulting from the plastic flow of the upper mantle. The remainder of this section is dunite with a texture typical of dunites of the Dunite with Gabbro Sequence, characterized by a regular network of equant olivine grains with equigranular grain size distribution. Dunites and harzburgite in the Mantle Sequence are intruded by gabbroic lithologies forming sharp, planar, and anastomosing contacts (Fig. F14E, F14F).

Thin section descriptions

Principal lithologies

The following description of the principal lithologies is based on individual thin section (TS) descriptions, which are provided in **Supplementary material** > **B_Thin section descriptions**). In addition, supplemental Table **ST3** summarizes the observations made on all thin sections related to igneous petrology.

Dunite

Typical massive dunites from the Dunite Sequence or from the Dunite with Gabbro Sequence show uniform characteristics of anhedral olivines forming a dense network of equant grains with fine- to medium-grained granular texture and with equigranular grain size distribution. No relics of porphyroclastic pyroxenes are present, nor are there any textural relics of a porphyroclastic texture, as would be diagnostic of typical mantle rocks. Modal abundance of olivine ranges 99.5%–90% in those dunites that are impregnated by plagioclase and/or clinopyroxene. Modal abundance decreases to 80% in spinel-rich dunite. Average olivine grain size ranges 0.1–2 mm. Spinels are in general very small (maximum ~ 0.4 mm). Subequant, commonly subrounded spinel occurs inside the olivine grains or along olivine grain boundaries; some spinels are interstitial. Modal abundance of spinel ranges 0.5%– 3% except for a spinel-rich dunite that has 20% spinel (interval 58Z-3, 43–47 cm) (e.g., Fig. **F16**).

Massive dunites from the Mantle Sequence are also more or less totally altered to serpentine and in general show different textures and spinel features compared to the dunites from the upper two sequences. These dunites may bear textural relics of pyroxene porphyroclasts that are totally replaced by low-temperature alteration phases (commonly aggregates of chlorite, serpentine, and oxides) that obscure evaluation of the primary composition of the mineral relics. Olivine grain sizes are larger, resulting in more medium-grained textures that are granular and with equigranular grain size distribution. Spinels in mantle dunites are generally coarser grained with grain sizes >3 mm (in the spinel-rich dunite), and the modal amounts are higher (up to 5%). In general, these spinels are well preserved with alteration to Fe oxides only at the rims. Photomicrographs of this type of dunite are presented in Figure **F17**.

In the transition to the Mantle Sequence but still in the Dunite with Gabbro Sequence, some dunites bear small patches of typical mantle harzburgite with porphyroclastic texture, as shown in Figure **F15**. This patch has a size of 2 cm. Such patches, eventually in smaller scale, would imply the presence of orthopyroxene-bearing dunite.

Harzburgite

Harzburgite is the most common rock type in the Mantle Sequence. Typical harzburgites have porphyroclastic medium- to fine-grained textures with equigranular grain size distributions. Characteristic are augen-like shapes of orthopyroxene associated with crystal-plastic deformation, implying that these harzburgites represent typical mantle residues (Fig. **F18**).

Olivine is anhedral and equant, modal abundance ranges 85%–89%, and average grain size ranges 0.8–1 mm (maximum = 4 mm) in all investigated samples. Orthopyroxene is anhedral to prismatic with modal percentages ranging 5%–20% and average grain size ranging 0.5–3 mm (maximum = 5 mm). Spinel is anhedral and interstitial and can form grains as large as 2.5 mm. Spinel modal content ranges 0.2%–1%. Clinopyroxene is anhedral and mostly interstitial except for rare prismatic crystals that can have grain sizes as large as 2 mm. The modal content ranges 0%–1%.

Olivine gabbro

Olivine gabbro in Hole CM2B shows granular fine-grained textures with equigranular grain size distributions. Figure **F19** shows a representative photomicrograph of olivine gabbro.

Plagioclase is most commonly anhedral and tabular with modal contents ranging 33%–75%. In some samples, plagioclase is elongated following the overall foliation subparallel to the layering. Average grain size ranges 0.3–1 mm (maximum ~ 2 mm). Clinopyroxene occurs as subhedral prismatic crystals with average grain sizes of 1 mm (maximum = 3.5 mm) or with interstitial habit with smaller grain sizes averaging 0.4 mm (maximum = 1.2 mm). The mode varies 20%–50%. Olivine is typically anhedral and equant with modal amounts ranging 5%–33%. Average grain size ranges 0.2–0.8 mm (maximum = 2.0 mm).

Gabbro

Gabbros in Hole CM2B show a granular texture and most are fine to medium grained; grain size distribution is mostly equigranular.

Plagioclase is subhedral and tabular with mode of ~50%. Average grain size ranges 0.1–0.2 mm (maximum = 0.8 mm). Clinopyroxene is subhedral to anhedral with equant to prismatic habit and mode of ~50%. Average grain size ranges 0.1–0.7 mm (maximum = 1.2 mm). A photomicrograph of typical gabbro is presented in Figure **F20**. A cluster of clinopyroxene relics found in mylonitic gabbro probably represents a former agglomerate in TS Sample 35Z-3, 16–19 cm.

Wehrlite

In a thin section of a massive dunite from the Mantle Sequence (Sample 69Z-4, 15–19 cm; see Fig. **F21**), wehrlitic patches are observed in the vicinity of a former probably anorthositic intrusion, now totally converted to secondary phases. These patches in the dunite may represent impregnations derived from the gabbroic intrusion nearby. The wehrlite shows a granular, fine-grained texture with equigranular grain size distribution.

Clinopyroxene mode ranges 40%–55%. Clinopyroxene in TS Sample 69Z-4, 15–19 cm, forms mostly anhedral crystals with interstitial habit. Average grain size is 0.8 mm (maximum = 2 mm) for subhedral, prismatic clinopyroxene and 0.5 mm (maximum = 1.2 mm) for anhedral, interstitial clinopyroxene. Olivine modes range 40%–60%. Shape is subhedral, and habit is equant. Average grain size is 0.4 mm (maximum = 2 mm).

TS Sample 42Z-1, 6–10 cm, shows plagioclase-bearing wehrlite with up to 5% plagioclase mode. Plagioclase is subhedral with prismatic shape, and average grain size is 0.4 mm.

Troctolite

One thin section of a troctolite from the Dunite Sequence was made (TS Sample 92Z-2, 61–65 cm). The sample is totally altered, so evaluation of the primary igneous features is challenging. Olivine is completely replaced by serpentine and plagioclase by greenschist facies minerals (Fig. F22). The rock shows relict granular fine-grained texture with equigranular grain size distribution. Plagioclase is anhedral with tabular shape and a modal abundance of 75%. Olivine, which is totally altered to serpentine, is anhedral with equant shape and a mode of 25%.

Gabbronorite

One example of gabbronorite is available, but due to nearly complete alteration to low-grade metamorphic phases, evaluation of the primary igneous features is challenging (see Fig. F23). The primary texture is medium-grained granular with equigranular grain size distribution. Plagioclase, which is totally altered, is subhedral and tabular with a mode of 45%. Average grain size is 0.8 mm (maximum = 1.2 mm). Clinopyroxene is anhedral prismatic; mode is 40%. Average grain size is 0.8 mm (maximum = 1.6 mm). Orthopyroxene is anhedral and prismatic with 15% mode. Average grain size is 2 mm (maximum = 3.2 mm).

Detailed observations and special features

Gabbroic series and veins

Gabbroic rock types occur as few-meter-thick layered intervals in the Dunite with Gabbro Sequence (Subunits 7, 8a, 8c, 8i) and as relatively thin (millimeter to centimeter sized) layers and veins in the other sequences. In total, gabbroic rocks comprise ~3% of the total thickness of the lithologies in Hole CM2B.

In the Dunite Sequence, fine- to medium-grained gabbro and gabbronorite veins cut the dunite (Figs. F24–F27). Most of the veins are strongly to completely altered and deformed; relics of primary minerals are rare (intervals 12Z-1, 47–51 cm; 17Z-3, 20–24 cm, 35Z-3, 16–19 cm; Figs. F25–F27). A fine-grained gabbro at 13.97 m (interval 9Z-3, 7–11 cm; Fig. F24) is an exception and shows relatively well preserved minerals forming equigranular texture. The sample is dominantly composed of clinopyroxene and plagioclase with grain sizes <1 mm.

Olivine gabbro with associated wehrlite and dunite comprises Subunits 8a–8i (Sections 40Z-1 through 44Z-4) at 74.26–83.39 m in the Dunite with Gabbro Sequence. In particular, alternating bands of olivine gabbro and dunite-wehrlite form a “zebra-like” appearance in intervals 40Z-1, 16–52.5 cm, and 41Z-1, 0–15 cm. The gabbroic lithologies in this sequence are well preserved compared to the gabbroic veins in the other sequences (Figs. F28–F34). The olivine gabbros are mostly fine to medium grained and equigranular. Anhedral to subhedral plagioclase comprises 45%–75% of these rocks. They are elongate, subequant to equant, and exhibit prismatic to tabular habit. Clinopyroxene comprises 20%–50% of the mode, mostly forming anhedral–subhedral crystals. These grains are elongate, subequant, prismatic, and interstitial in occurrence. Olivine is the least abundant, with a mode of 5%–33%; olivines are usually elongate and subequant–equant. Wehrlite occurring with the olivine gabbro is mostly serpentinized and more altered than the olivine gabbro. Clinopyroxene (40%–55%) and olivine (40%–60%) are the main phases in the wehrlite. A gabbroic vein (interval 44Z-4, 22–26 cm; Fig. F34) in plagioclase-bearing dunite at 83.07 m is strongly altered to actinolite, prehnite, chlorite, and serpentine; very few relics of clinopyroxene are still present.

Veins in the Mantle Sequence include gabbro, olivine gabbro, troctolite, wehrlite, websterite, and anorthosite. A fine-grained troctolite vein (interval 71Z-1, 51–55 cm; Fig. F35) is completely altered to prehnite and clay minerals.

Textures of dunite

Dunite in Hole CM2B occurs in all three sequences: the Dunite, Dunite with Gabbro, and Mantle Sequences (for details see Lithologic sequences). In this section, representative dunite textures for each sequence are described, and the observed textures are shown in Figure F36A–F36E. All photomicrographs have the same magnification and are oriented in the same direction with respect to the core reference frame, which is included in Figure F36E. Most dunites are totally replaced by serpentine, but textural features such as grain size, shape, habit, and especially spinel properties, on which we focus in this section, can still be described.

- TS Sample 11Z-1, 34–38 cm (14.94 m; dunite from the Dunite Sequence): shows granular texture with equigranular grain size distribution. Anhedral, equant olivine has a mode of 98.5%, forming a fine- to medium-grained granular texture. Fine-grained, subequant spinel with grain sizes < 1 mm occur as inclusions in olivine and as interstitial phases at olivine grain boundaries, commonly in triple junctions. In general, interstitial spinels show larger average grain size than subequant types. Maximum grain size of spinel is 0.7 mm, and aspect ratio of the spinel is ~1.7 (Fig. **F36A**).

- TS Sample 37Z-1, 51–55 cm (69.11 m; dunite sampled 5 m above the contact to the Dunite with Gabbro Sequence): In one part of this section, relics of fresh olivine occur without replacement to serpentine. This is a rare example of fresh olivine preserved in dunite. Anhedral, equant olivine has a modal abundance of 99.5%. Olivine shows granular, fine- to medium-grained texture with equigranular grain size distribution. Maximum grain size of olivine is 2.2 mm, and aspect ratio of the grains is ~2.3. Subequant or interstitial spinel has a mode of 0.5%. Spinel occurs on olivine grain boundaries; inclusions in olivine are not observed. Maximum spinel grain size is ~0.2 mm, and the aspect ratio is ~1.8 (Fig. **F36B**).
- TS Sample 50Z-1, 32–35 cm (92.92 m; dunite from the Dunite with Gabbro Sequence): shows olivine and spinel grains with weak foliation following the main contacts between dunites and the major gabbroic intrusion. Olivine, now totally altered to serpentine, has a mode of 99%, with the remainder spinel. This rock shows fine- to medium-grained granular texture with subequant olivines. Shape of spinel grains ranges from euhedral isometric to anhedral interstitial with curved grain boundaries. Spinel forms inclusions in olivine and occurs on grain boundaries. Average grain size is 0.4 mm (maximum = 0.6 mm). Spinel aspect ratios are ~1.7 (Fig. **F36C**).
- TS Sample 57Z-3, 50–55 cm (112.8 m; plagioclase-bearing dunite from the Dunite with Gabbro Sequence): shows medium-grained texture and granular with equigranular grain size distribution. Olivines show primary relics and modes of 98%, the remainder being spinel. Average olivine grain size is 1.7 mm with aspect ratios of ~1.25. Most spinel grains are anhedral and interstitial. Elongated grains follow the foliation trends of the olivine. Spinel inclusions in olivine are not observed. Maximum spinel grain size is 1.2 mm with an aspect ratio of 1.5 (Fig. **F36D**).
- TS Sample 96Z-2, 68–71 cm (214.2 m; dunite from the Mantle Sequence): shows medium-grained texture and granular with equigranular grain size distribution. Olivine with 99% mode is totally altered to serpentine. Spinel is equant, roundish, and granular; some are interstitial with a vermicular shape. Maximum grain size is 1.1 mm with aspect ratio of ~1.7 (Fig. **F36E**).

Calculated mineral modes from XRF data

Peridotite mineral modes were calculated from XRF bulk rock major element analyses (see **Geochemistry: Hole CM2B**). Modes for Hole CM1A and CM2B peridotites are presented in supplementary Table **ST4**. Lithologic assignments presented in the figures and tables were made based on visual inspection of cores.

Methods

Mineral modes were calculated using a least-squares regression algorithm assuming constant mineral compositions among all peridotites. The assumed mineral compositions are presented in Table **T5**. Olivine, orthopyroxene, clinopyroxene, and spinel are from samples collected in the upper part of the mantle section of the Wadi Tayin massif, southern Oman ophiolite (OM94-115, Hanghøj et al., 2010; OM94-114, Dygert et al., 2017), whereas plagioclase is from the mantle section of the Othris ophiolite in Greece (Barth et al., 2003).

A correction for Si, Al, Fe, Mg, and Ca compositions was applied to all XRF data based on deviation of replicate analyses of US Geological Survey (USGS) dunite Standard DTS-2B from the USGS preferred composition. The uncorrected measured composition of DTS-2B (n = 29 analyses), the USGS preferred composition, and the applied correction factors are shown in Table **T6**.

Results

Mg/Si vs. Al/Si

Molar Mg/Si vs. Al/Si values are presented in Figure **F37A** for peridotites from Holes CM1A and CM2B and elsewhere in Oman (Godard et al., 2000; Monnier et al., 2006; Hanghøj et al., 2010) and compared to the terrestrial mantle array of Jagoutz et al. (1979). Many of the Hole CM1A and CM2B dunites and harzburgites plot below the mantle array, indicating Mg loss or Si addition during or after alteration, suggesting open-system behavior. Samples with decreased molar Mg/Si will have artificially high pyroxene modes compared to peridotites that experienced closed-system alteration.

Mineral modes

Calculated mineral modes are presented in supplemental Table **ST4**, and a ternary plot is presented in Figure **F37B**. Mode residuals are generally <1% (supplemental Table **ST4**). All harzburgites and dunites are clinopyroxene-poor or clinopyroxene-free. Many “dunites” have orthopyroxene modes >10%, and many “harzburgites” have orthopyroxene modes <10%. Below, we present four possible explanations for the disagreement between visual lithologic characterizations and mineral modes.

- Measured bulk compositions are not representative of the rocks. Measured subsamples are skewed toward anomalously high or low pyroxene fractions.
- Mineral compositions assumed in the mode regression are not representative of primary mineral compositions.
- Lithologic classification was inaccurate owing to the difficulty of identifying primary phases in completely altered peridotites.
- Open-system behavior (Mg loss or Si addition) increased the normative pyroxene content of the sample (see Fig. F37A).

Relative mode distributions are shown in histograms in Figure F38E. Mode distributions are similar between the two holes, but Hole CM1A has a greater abundance of high-olivine samples, consistent with core descriptions. Comparisons between individual mineral modes are shown in Figure F39. Note that many dunites have orthopyroxene modes >0.1, and some harzburgite modes are <0.1 (Fig. F39A). Clinopyroxene modes are compared with orthopyroxene modes in Figure F39D. Most peridotites are clinopyroxene-free; even pyroxene-rich peridotites have relatively low clinopyroxene modes.

Downhole variations in mineral mode are shown in Figure F40. Orthopyroxene mode increases as dunite transitions to harzburgite downhole. Clinopyroxene abundance is relatively elevated toward the bottom of both holes except where wehrlites are present at shallower depths.

Discussion

Comparison between Holes CM1A and CM2B

The Dunite, Dunite with Gabbro, and Mantle Sequences show very similar lithologic features in Holes CM1A and CM2B, whereas the uppermost Layered Gabbro Sequence is intersected only in Hole CM1A. A comparison of the corresponding lithology logs of both holes is presented in Figure F41.

The Dunite Sequence is very similar in the two holes. It is composed of massive, homogeneous dunites that are totally altered. A few centimeter-thick gabbroic or millimeter-thick Cr-spinel-rich veins disrupt the monotonous sequence, but these features are rare in both sequences.

The Gabbro with Dunite Sequence shows more lithologic variation in both holes, due to the various series of layered gabbroic rocks and wehrlites within the dunites. This sequence is ~60 m thick in Hole CM1A but slightly thinner (~45 m) in Hole CM2B. Within a few meters scale, the main lithologic units and structures fit quite well between the two holes.

The main lithologies in the Mantle Sequence—dunite and harzburgite—show identical petrographic features in both holes. However, in Hole CM1A, dunite is more abundant than harzburgite, whereas harzburgites are more abundant than dunites in Hole CM2B.

In summary, gabbros are more abundant in Hole CM1A, due to the higher stratigraphic position of this hole with respect to the paleo-Moho, resulting in higher abundances of true crustal components like layered gabbros, whereas Hole CM2B includes a greater proportion of rocks from the Crust–Mantle Transition and with distinctly higher abundances of harzburgite than dunite in the Mantle Sequence.

Potential models for formation of CMTZ based on observations from Holes CM1A and CM2B

Macroscopic and microscopic observations in Hole CM1A reveal in principle three different broader structural units: the crust, represented by the Layered Gabbro Sequence, a CMTZ, represented by the Dunite and Dunite with Gabbro Sequences, and the mantle, represented by the Mantle Sequence. Hole CM2B represents a slightly deeper horizon of the same situation, where the true crustal component, the Layered Gabbro Sequence, is missing (see Comparison between Holes CM1A and CM2B). In principle, the given situation allows us to deduce two different mechanisms for formation of the CMTZ, as illustrated in Figure F42. The CMTZ, which is basically represented by the ~150 m thick massive dunite horizon with intercalated layered gabbros, may have formed by (1) mid-ocean-ridge basalt (MORB) melt-peridotite interaction (e.g., Kelemen, et al., 1995; left side of Fig. F42) or (2) crystal accumulation in primitive MORB (right side), resulting in the formation of olivine mushes that may laterally intrude to form massive cumulate horizons, similar to magmatic processes described by Korenaga and Kelemen (1997) and Kelemen et al. (1997) (right side of the sketch in Fig. F42). Both models should be regarded as pure end-member models, and overlap of both mechanisms resulting in mixed models is indicated.

Key to unraveling the formation mechanism of the CMTZ are the dunites, and future analytical work on this lithology will probably reveal sophisticated genetic models. However, this future task is hampered because most of the dunites are totally altered to serpentine, so the focus on relict Cr-spinels is implied. For end-member Model 1, it is implied that the massive dunites of the Dunite, Dunite with Gabbro, and Mantle Sequences are all formed by a similar process (melt-peridotite interaction), so the dunites should show similar compositional and textural features, in contrast to the dunites formed in the Layered Gabbro Sequence, which formed by an accumulation process (left side of Fig. F42). On the other hand, for end-member Model 2, the dunites from the Layered

Gabbro, Dunite, and Dunite with Gabbro Sequences should show similar features (all formed by crystal accumulation at the base of the crust), whereas those of the Mantle Sequence should differ.

In order to better understand the formation of the massive dunites in the Dunite and Dunite with Gabbro Sequences of Hole CM1A, we investigated in detail the corresponding thin sections (see **Textures of massive dunite** in the **Site CM1** chapter) and studied the relict textures. In Figure **F30** in the **Site CM1** chapter, we compiled photomicrographs of representative textures from dunites from the Dunite and Dunite with Gabbro Sequences and compared these with dunites from the Mantle Sequence. With the exception of two samples, all dunites were totally serpentinized, so we could only focus on relict texture features. We included also one dunite from the Layered Gabbro Sequence (TS Sample CM1A-18Z-2, 62–67 cm) as reference texture for magmatic formation by crystal accumulation because this dunite forms a layer within a series of layered gabbro generally assumed to have formed by crystal accumulation. This comparison revealed (for details see **Textures of massive dunite** in the **Site CM1** chapter) that the relict textures of massive dunites in the Layered Gabbro, Dunite, and Dunite with Gabbro Sequences are formed by a similar magmatic process probably related to crystal accumulation at the base of the crust rather than to processes within the mantle. This assessment is also supported by the absence of any relics of crystal-plastic deformed minerals or of a typical porphyroclastic texture, as it would be diagnostic of typical mantle rocks. On the other hand, textural features of dunites from the Mantle Sequence are more compatible with the petrographic record of typical mantle peridotites (relics of porphyroclastic texture; large chromite grains), implying a mantle source for these dunites. Thus, the detailed textural analysis of dunites from Hole CM1A suggests that crystal accumulation is more probable as formation model for the CMTZ at the CM sites.

Moreover, although totally altered, bulk rock geochemical data of dunites may also help shed light on the formation of the dunites within the CMTZ of the CM sites. A reduced data set of Hole CM1A XRF analyses filtered for those dunites of Hole CM1A investigated in the detailed texture analysis from above indicates clearly different compositions for the massive dunites from the Dunite and Dunite with Gabbro Sequences compared to those from the Mantle Sequence, at least for the Mg# vs. depth plot, as shown in Figure **F43** (for details see **Geochemistry: Hole CM2B**). In general, analyses of the massive dunites of the CMTZ show slightly lower Mg# (average ~ 90) than those from the Mantle Sequence, implying a different formation mechanism for these two groups. Moreover, the dunites of the Dunite with Gabbro Sequence show specific trends: to lower Mg# in a horizon where meter-thick gabbro sills were observed and to higher values when approaching the boundary to the Mantle Sequence (see marked fields in Fig. **F43**). These trends also support a magmatic formation model for the dunites of this zone. Mg# for the most primitive rocks assumed to be formed by accumulation of primitive crystal mushes from the Oman ophiolite also support this model: Mg# = 88.7 for troctolites in gabbroic sills in the mantle (Korenaga and Kelemen, 1997); Mg# = 89 for olivines in dunites of the Tuf area assumed to be formed by crystal accumulation (Abily and Ceuleneer, 2013); and Mg# > 90 of olivines in primitive cumulate gabbros from the Ibra, Nakhl, N Oman, and Maqsad (Kelemen et al., 1997). Melts modeling for a hydrous primitive primary mantle melt of Kinzler and Grove (1993), relevant for the Oman paleoridge and slightly modified for Oman conditions also used by MacLeod et al. (2013), reveal Mg# = 89.5 for the first olivine, also in accord with magmatic formation of the massive dunites observed in Holes CM1A and CM2B (fractional crystallization model; FMQ buffer, 0.8 wt% water according to evaluations of MacLeod et al., 2013).

Alteration: Hole CM2B

Hydrothermal alteration in Hole CM2B is reflected by secondary mineral replacement of primary phases identified as (1) background alteration of the host rocks, (2) isolated alteration patches, (3) halos surrounding veins or at lithologic contacts, and (4) alteration zones related to deformation. In addition, precipitation of secondary minerals in multiple generations of veins provides records of fluid pathways and hydrothermal alteration.

In the following sections, we describe the main alteration characteristics of the variably altered and veined gabbroic and ultramafic rocks in (1) the CMTZ, consisting of dunite in an upper sequence (Sections 9Z-1 through 40Z-1) and dunite with variable amounts of clinopyroxene and plagioclase and distinct zones of layered gabbro and websterite in a lower sequence (Sections 40Z-1 through 60Z-2), and (2) the Mantle Sequence (Sections 60Z-2 through 129Z-1), consisting of harzburgite and orthopyroxene-bearing dunite (Fig. **F44A**; Table **T4**) with intercalated wehrlite, troctolite, and gabbroic layers. A distinct 10 m sequence of metasomatic talc-carbonate serpentinites occurs at the bottom of the hole. Characteristic vein generations and mineral infillings are described for the main lithologic sequences. Continuous downhole observations and compiled XRD data for Hole CM2B are given in the alteration log (supplemental Table **ST5**) and vein log (supplemental Table **ST6**). Excel spreadsheets used for calculations and downhole plots are given in supplemental Table **ST7**. Abbreviations used in the text and figures are defined in Table T5 in the **Methods** chapter. A comparison of total alteration intensity in Holes CM1A and CM2B is given in Figure F45.

During macroscopic core description, the alteration team identified and logged the alteration characteristics for each subunit identified by the igneous group and identified the proportions and mineral assemblages contributing to variations in background alteration, patch alteration, halos, and deformation-related alteration (Figs. F44, F46, F47; supplemental Table ST5). Veins were recorded in a separate log, and the general characteristics of the vein types were recorded for the intervals in which they occurred with a core section (Fig. F48, supplemental Table ST6. Overviews of the overall downhole variations in alteration intensity, alteration mineral assemblages, and vein fillings are shown in Figures F44, F46–F50.

Total alteration intensity mainly reflects the background alteration intensity and is highly variable downhole, ranging <60%–100% (Figs. F44, F46; supplemental Table ST5):

- <60% (high alteration) sections:
  - 41Z-1 (74.60–75.56 m)
  - 44Z-1 (80.60–81.36 m)
  - 111Z-2 (252.46–252.49 m)
  - 116Z-2 (267.71–267.72 m)
  - 118Z-1 (269.84–269.85 m)
- to 100% (complete alteration) sections:
  - 36Z-1 (67.60–68.27 m)
  - 83Z-3 (178.63–178.64 m)
  - 85Z-2 (183.09–183.25 m)
  - 86Z-1 (185.97–185.97 m)
  - 86Z-4 through 87Z-1 (188.60–189.17 m)
  - 89Z-2 (192.52–192.52 m)
  - 89Z-4 (194.13–194.26 m)
  - 92Z-3 (202.33–202.37 m)
  - 127Z-1 (293.60–293.64 m)
  - 127Z-2 through 129Z-1 (294.71–300.14 m)

The mean alteration intensity is ~95.05% for the Dunite Sequence, 86.44% for the Dunite with Gabbro Sequence, 91.34% for the overall CMTZ, and 85.55% for the Mantle Sequence. Alteration intensity, however, varies greatly depending on rock type and increases with increasing vein density, as discussed below. In intervals with extensive veining, alteration within vein halos can be 60%–100% of the total alteration (Fig. F50).

X-ray diffraction results

A total of 138 XRD analyses of material sampled shipboard from Hole CM2B core were performed using a PANalytical CubiX^3 X-ray diffractometer (Fig. F48; Table T7). A compilation of the spectra and sample locations within the core is given in supplemental Figures SF1–SF4. The main target of these analyses was to identify the vein fillings and their alteration halos (if present). Background compositions of the host rocks were less frequently analyzed; results of XRD on bulk rock powders collected at the rig site are given in Table T8).

XRD samples from Sections 9Z-1, 9Z-2, and 10Z-1 at the top of the Dunite Sequence showed hydrotalcite (general formula: $Mg_6Al_2CO_3[OH]_{16}\cdot 4[H_2O]$) and carbonate (dolomite and calcite) to be the main vein minerals in serpentinitized dunite (Table T7). In the lower part of the Dunite Sequence, serpentine background with diopside veins were analyzed (XRD samples from Section 35-Z; Table T7).

Veins with variable infillings are found in the Dunite with Gabbro Sequence, where many altered gabbroic intrusions were observed. These include prehnite and xonotlite veins (XRD samples from Sections 41Z-2, 41Z-4, and 44Z-2), serpentine and garnet (commonly Cr-rich uvarovite) in inclined white veins or patches in Sections 69Z-2 through 110Z-1 (Table T7; supplemental Figs. SF2, SF3, SF4). Carbonate minerals were rare in the Dunite with Gabbro Sequence; calcite was found in Section 44Z-2, and siderite + serpentine was found on the surface of a fracture in Section 53Z-4.

Serpentine was identified throughout the Mantle Sequence (XRD samples from Sections 60Z-2 through 122Z-3) and is commonly present as a background phase in the wall rocks and in veins. Altered gabbroic patches and veins in serpentinized peridotites in the Mantle Sequence are composed of garnet (hydrogrossular and possibly uvarovite), diopside, and chlorite. Less common mineral assemblages identified by XRD analyses in this sequence include amphibole + diopside + serpentine veins (Section 112Z-4), amphibole + serpentine veins (Section 116Z-2), serpentine + dolomite, and serpentine + spinel + anatase (TiO_2), although the serpentine in these veins may have been background contribution from the wall rocks. One anorthite vein was measured from Section 116Z-2. The XRD results of background wall rock and veins imply the presence of calcite in some intervals (e.g., Section 81Z-3), although its occurrence is unclear because of low and noisy peaks on XRD profiles.

In the lower part of the Mantle Sequence at the bottom of Hole CM2B (XRD samples from Cores 125Z through 128Z), talc and carbonate minerals (magnesite, calcite, and dolomite) were observed with serpentine as the main background mineral assemblages. No characteristic gabbroic or Ca-rich rodingite minerals (e.g., prehnite, grossular, and vesuvianite) were found during XRD analyses in this domain. The analyzed veins were mostly composed of dolomite and magnesite, whereas talc formed bands around coarse crystals of dolomite and surrounding sheared and banded zones (discussed in detail in **Talc-carbonate serpentinites**).

Crust–Mantle Transition

Alteration in the Dunite Sequence

Dunites (Sections 9Z-1 through 40Z-1)

The Dunite Sequence includes dunite, plagioclase-bearing dunite, clinopyroxene- or orthopyroxene-bearing dunite, plagioclase + clinopyroxene-bearing dunite, and spinel-rich layers with minor gabbroic intervals that consist of gabbro, olivine gabbro, and gabbronorite (see **Igneous petrology: Hole CM2B**; Fig. **F4**). Alteration of the ultramafic lithologies in the Dunite Sequence (12.0–74.3 m) is relatively constant and complete (>95% total alteration). As in Hole CM1A, alteration is dominated by serpentine and magnetite forming typical serpentine mesh textures after olivine (Figs. **F51**, **F52**). Serpentine makes up ~90% of the background alteration and magnetite up to 10% with relatively homogeneous distribution downhole to 54 m (Section 25Z-2), where plagioclase-bearing dunite is found (Fig. **F44**; supplemental Table **ST5**). In the serpentinized dunite, the fine-grained magnetite along the mesh rims outlines the former olivine grains, and its abundance throughout the sequence makes the core characteristically black. Brucite is difficult to determine macroscopically but was identified by XRD in bulk rock on-site samples (Table **T8**). In thin section, brucite may form brownish patches along serpentinized olivine grains or less commonly occur as patches within the grains. Plagioclase in the plagioclase-bearing intervals is altered to fine-grained aggregates that appear brownish black in thin section and are difficult to determine (Fig. **F52**). In the upper dunite-dominated intervals of Hole CM2B (Sections 9Z-1 through 40Z-1; 74.10–74.26 m), no patch alteration is recorded. Vein halos are first recognizable and become an important component of alteration at the top of the layered gabbro/dunite intervals below Section 40Z-1 (Fig. **F50**).

Total background alteration of gabbroic intervals in the Dunite Sequence above 40 m (intervals in Sections 9Z-3, 12Z-1, 15Z-3, 17Z-3, and 19Z-1) is generally lower than in the surrounding dunite but variable, ranging 75%–95%. Background alteration in these intervals is characterized by the presence of amphibole ± chlorite and plagioclase altered to fine-grained minerals that cannot clearly be identified (Fig. **F53**). XRD analyses also identified prehnite and diopside at the contacts between dunite and gabbroic rocks (Table **T7**).

Layered gabbro-dunite (Sections 40Z-1 through 58Z-3)

A layered gabbroic sequence consisting of gabbro, olivine gabbro, plagioclase-bearing wehrlite, and plagioclase-bearing dunite occurs in Section 40Z-1 (74.26 m) through interval 44Z-4, 0–32 cm (83.08 m), at the transition to the Dunite with Gabbro Sequence. Alteration in this layered interval is distinctly lower (35%–80%) than in the overlying and underlying dunite intervals (Fig. **F44**). As in Hole CM1A, alteration is dominated by alteration of clinopyroxene to chlorite ± tremolite and plagioclase altered to fine-grained aggregates giving a cloudy appearance, which cannot clearly to identified in thin section (Fig. **F54**).

Alteration of the gabbroic layers is clearly lower than in the interlayered dunite and wehrlite intervals and lower than the surrounding dunites above and below the layered sequence. Total background alteration in the gabbroic layers ranges 50%–90%; the intensity of alteration is highest (80%–90%) towards the lower part of the section (Sections 42Z-3 and 44Z-2 through 44Z-4) and is related to highly veined intervals with prehnite-chlorite vein networks. Alteration related to veining is reflected by an increase in patch alteration in the layered gabbro-dunite sequence, and that remains present but variable to the bottom of the hole (Fig. **F50**). Intensity of patch alteration in the layered intervals varies from fresh to completely altered in Sections 43Z-1 through 44Z-3 but makes up only 0%–3% of the total alteration. On the other hand, alteration occurring as vein halos increases markedly in these intervals (Fig. **F50**) and makes up to 30%–70% of the total alteration. Alteration assemblages contributing to the halo alteration in Sections 40Z-1 through 44Z-4 (74.26–83.07 m) are primarily amphibole (15%), chlorite (15%), and fine-grained grayish green to milky-white aggregates classified as secondary plagioclase (70%) (Fig. **F47**). XRD analyses suggest that these are composed of chlorite and garnet ± diopside (Fig. **F49**; Table **T7**). Interestingly and in contrast to Hole CM1A, epidote group minerals were not identified by XRD throughout the Hole CM2B drill core.

Alteration in the Dunite with Gabbro Sequence

Sections 44Z-1 through 60Z-2

Alteration in the dunite intervals at the top of the Dunite with Gabbro Sequence is similar to alteration in the overlying dunites within the Dunite Sequence. Alteration is relatively constant and very high to complete (90%–100% total alteration) from Section 44Z-1 through interval 51Z-2, 0–65.5 cm, dominated by background alteration of olivine forming typical serpentine mesh textures consisting of serpentine and magnetite. Serpentine minerals make up ~90% of the background alteration and magnetite makes up to 10%.

At ~95 m downhole (Section 51Z-1), alteration in the dunite becomes markedly lower and more variable (Figs. **F44**, **F50**). Alteration is dominated by background alteration of olivine replaced by typical serpentine mesh textures. An exception is in Sections 52Z-1 and 52Z-3, in which halo alteration contributes 80% of the total alteration (Fig. **F50**). Plagioclase-bearing dunites in Sections 53Z-2 through

58Z-3 have slightly lower total alteration and contribute to lower total alteration intensity towards the transition to the Mantle Sequence (Section 48Z-1). From an alteration point of view, a clear change in alteration intensity is seen at 95–100 m depth and occurs above the lithologic change that defines the top of the Mantle Sequence (Fig. F44).

Veins in the Crust–Mantle Transition

Veins in the Dunite Sequence

Six types of veins were recognized in the Dunite Sequence of Hole CM2B, five of which are bound to the dunitic lithologies and one related to gabbroic intrusions and metasomatic alteration fronts (Table T9).

Serpentine veins with subordinate magnetite and calcite are the most common veins in the Dunite Sequence and are present in Sections 9Z-1 through 39Z-3 (12.0–73.85 m), 42Z-2 through 42Z-3 (78.66–79.73 m), and 45Z-2 through 60Z-2 (84.56–120.24 m). They form as many as 4 generations of serpentine veins as shown in Figure F55A, F55B.

The first generation of veins (V1) is present in all core sections mentioned above and is represented by serpentine and magnetite forming micrometer-scale mesh and bastite textures that thoroughly penetrate the serpentinized dunites and surround and replace remaining primary phases, mainly olivine. V1 veins do not exceed 0.5 mm width, and they are consistently massive, uniform, and highly irregular in morphology. Widespread abundance of brucite in the V1 veins was confirmed by bulk rock XRD analyses (Table T8). Their dark green, brown, and black color, together with narrow widths, makes macroscopic identification difficult. Nevertheless, the networks are clearly visible in thin sections. No diversification in distribution of the V1 serpentine + magnetite veins was observed throughout the Dunite Sequence.

The second generation (V2) of serpentine veins cuts through the V1 mesh textures and consists mainly of serpentine (95%–100%) and magnetite (up to 5%). Magnetite-rich serpentine bands commonly constitute the centers of the veins, clearly visible on XCT scans. Their widths vary greatly (0.5–50 mm) as they form widely branched networks that spread out through the whole sections. The thicker branches are easily recognizable, whereas the thinner ones are often indistinguishable from the serpentinized background. The veins uniformly exhibit massive texture and banded structure as well as irregular morphology and black color. In some parts of the sections the V2 veins are subparallel to each other and crosscut V3 serpentine veins. From Section 22Z-1 through 39Z-3 (44.76–73.49 m), V2 veins can be locally oxidized, possibly due to migration of ascending oxidizing fluids related to the gabbroic intrusion above in which rusty orange discoloration is visible. The V2 veins commonly exhibit crosscutting connectivity parasitic veinlets forming “Frankenstein” veins, which are indistinguishable and possibly synchronous with the V3 serpentine veins (described below).

The V3 serpentine veins throughout the entire dunitic interval exhibit identical texture (massive), structure (uniform), connectivity (network), morphology (irregular), and color (yellowish white), and their width rarely varies from the average of 0.6 mm, only locally reaching 1 mm. They are composed of serpentine but can also contain subordinate calcite up to 5% (usually 1%). The network is not strongly developed, and the veins are often not clearly visible in core sections. They are variably distributed throughout, and their branches are often subparallel to each other and have a vein tip morphology.

The V4 serpentine veins are not always present in the core sections. They are represented by cross-fiber serpentine (chrysotile) veins that are steeply dipping and mostly extensively fractured along vein walls, making measurements of their true width difficult; apparent measured widths range 0.5–10 mm (average = 2.76 mm). They are banded and have irregular morphology. Similar to V3 veins, V4 veins can also contain up to 3% carbonates. Besides calcite, coalingite was also identified in V4 veins (Table T7). The color of these veins ranges from white to bright green and rusty orange-brown. Some V4 veins are subparallel, either to each other or to background foliation.

Veins in gabbroic intervals of the Dunite Sequence

Up to two generations of prehnite ± chlorite ± clinozoisite were recognized in the olivine gabbros and gabbros from Units 7 and 8 as well as surrounding the plagioclase-bearing dunites from Sections 40Z-1 through 44Z-4 (74.10–83.69 m), presented in Figure F56. The veins are mostly single with few branches, but some also form networks. Their thicknesses range <0.5–10 mm (average = 1.75 mm). They are commonly massive, but when they occur with chlorite and clinozoisite, they usually exhibit polycrystalline texture. In Section 42Z-1, prehnite is neighbored by calcite, which can make up to 50% of the vein mineralogy; these veins are anastomosing. Their morphology is always irregular and can extend throughout the entire sections; however, their width is highly variable and locally they may not be recognizable macroscopically. Chlorite occurs together with prehnite in Sections 40Z-1 through 41Z-4 as well as 44Z-2 through 44Z-4, where clinozoisite is also present, and together they form an extensive vein network with a wide alteration halo that extends almost throughout the whole core at the boundary between gabbros and dunites. Thorough XRD investigations show the abundance of xonotlite, diopside, and grossular in the gabbroic intervals, which suggest Ca metasomatic processes related to the alteration of the gabbroic body.

Mantle Sequence

Alteration of dunite in the Mantle Sequence

Dunites are present in the following Mantle Sequence sections:

- 60Z-3
- 61Z-1
- 62Z-1
- 65Z-2
- 66Z-1
- 67Z-1
- 69Z-3 and 69Z-4
- 83Z-4
- 89Z-1
- 93Z-4
- 94Z-1
- 95Z-3 and 95Z-4
- 96Z-1 through 96Z-3
- 103Z-1 and 103Z-4
- 106Z-2
- 111Z-2
- 113Z-1 through 113Z-4
- 114Z-1 and 114Z-4
- 116Z-3

Their alteration and vein characteristics are summarized in Figures F56, F57, and F58. A comparison of alteration within vein halos in the Dunite Sequence in the Crust–Mantle Transition and the Mantle Sequence are shown in Figure F59.

The dunites in the Mantle Sequence are completely altered and have a total average alteration intensity of 91.1%, which essentially reflects the proportion of background alteration (Fig. F44). Background alteration in the Mantle Sequence averages 88.7% of the total alteration, whereas halo alteration accounts for the remaining 11.3%. Background alteration is uniformly pervasive and remains high to complete (average intensity = 90%). The distribution of alteration is inhomogeneous and ranges 80%–95%. Serpentine always occurs with magnetite (average = 6.7%) and is the most abundant secondary mineral contributing to the background alteration, accounting for 93% of all secondary minerals in the dunites within the Mantle Sequence (Fig. F47). In Core 113Z, 5% secondary plagioclase was recorded in plagioclase-bearing intervals. In strongly veined intervals of dunites in Sections 94Z-1, 95Z-3, 95Z-4, and 116Z-3, total alteration was related to halos around veins. In these sections and in most sections where halo alteration was observed, the secondary mineral assemblage was identical and composed of serpentine (90%) and magnetite (10%) (supplemental Table ST7).

Alteration of harzburgite in the Mantle Sequence

Cores 129Z–128Z

Compared to the dunites from the Mantle Sequence, the harzburgites are less altered (average total intensity = 82.7%) (Fig. F44). Alteration only becomes complete (95%–100%) in highly veined zones, as follows (Figs. F60, F61):

- High intensity of halo alteration:
  - 69Z-2 (138.46–139.09 m)
  - 103Z-3 (232.19–232.65 m)
- High vein intensity:
  - 89Z-4 (193.83–194.13)
  - 91Z-2 (198.23–198.31)
  - 97Z-2 (216.59–217.59)
  - 107Z-4 through 108Z-3 (244.64–248.23 m)
- Carbonate serpentines (bottom of hole):
  - 125Z-1 through 129Z-1 (288.07–300.14 m)

The total length of harzburgite intervals is 140.98 m, and the most common alteration type is background alteration, which accounts for 88.3% of the total alteration, whereas halo alteration is responsible for the remaining 11.7% (supplemental Tables ST5, ST7). No patch or deformation-related alteration was observed in the harzburgites. Total average intensity of background alteration is 79.9% and is always pervasive. The most abundant mineral occurring in the background alteration is serpentine (average = 94% of all secondary minerals present; range = 73%–100%); the average percentage of magnetite is 5.2% (range = 0%–10%). In Sections 60Z-3 through 81Z-3 (120.78–177.34 m), amphibole is also present (average = 3.2%; range = 1%–20%). Secondary plagioclase is identified as a background alteration phase in Sections 110Z-3 (250.20–250.95 m) and 112Z-4 (256.21–257.41 m) and makes up 5% of the average total alteration. As in other plagioclase occurrences, alteration produces fine-grained aggregates with undistinguishable compositions that are simply classified as secondary plagioclase. Total intensity of alteration in the halos is 59.5%. The mineral assemblage within the halos is homogeneous throughout the entire Mantle Sequence and consists of serpentine (90%) and magnetite (10%).

Alteration in other orthopyroxene-bearing lithologies

Other orthopyroxene-bearing lithologies observed in the Mantle Sequence include orthopyroxene-bearing dunites and pyroxenites with total lengths of 27.35 m (27.19 and 0.16 m for orthopyroxene-bearing dunites and pyroxenites, respectively). Average total alteration intensity in orthopyroxene-bearing dunites is 93.6%, which is higher than in pyroxenites (total average intensity = 80.5%), and the proportions of types distribution between those two lithologies vary greatly.

Orthopyroxene-bearing dunites occur in the following Mantle Sequence sections:

- 62Z-4 through 73Z-3 (125.54–151.51 m)
- 78Z-2 through 78Z-3 (165.47–167.02 m)
- 79Z1 through 79Z-2 (166.90–167.69 m)
- 80Z-3 through 82Z-1 (168.86–174.24 m)

- 83Z-4 through 84Z-1 (179.55–179.64 m)
- 86Z-3 (187.46–188.00 m)
- 87Z-2 (189.50–190.04 m)
- 93Z-4 (206.10–206.30 m)
- 100Z-2 (222.68–222.95 m)
- 103Z-3 through 103Z-4 (232.67–233.28 m)
- 105Z-1 through 105Z-2 (236.87–237.33 m)
- 106Z-3 through 106Z-4 (241.90–242.24 m)
- 113Z-4 through 114Z-1 (260.34–260.82 m)
- 127Z-1 through 127Z-2 (293.64–294.53 m; related to the talc-carbonate serpentinites)

Pervasive background alteration is the most common type of alteration observed in orthopyroxene-bearing dunites and amounts for 86.5% of total alteration (see supplemental Table ST7). Halo alteration constitutes the remaining 13.5%. Patch alteration is rare in the Mantle Sequence and occurs only in orthopyroxene-bearing dunites (0.03% of total average alteration).

The most abundant secondary mineral contributing to background alteration is serpentine (average = 93%; range = 89%–100%). Subordinate minerals include magnetite (total average proportion = 6.7%; range = 0%–10%) and amphibole (present in Sections 68Z-1 though 81Z-4; average = 1%; range = 0%–2%). Alteration related to vein halos was observed at multiple random intervals throughout the Mantle Sequence and consistently consists of serpentine (90%) and magnetite (10%). Alteration halos are commonly seen as rusty-orange oxidation fronts around veins. Irregular-shaped alteration patches with a size of <3 cm were observed in Section 65Z-2 (130.66–30.83 m). These patches contains secondary plagioclase (80%) and amphibole (20%).

Olivine-bearing clinopyroxenites were only observed in Section 120Z-2 (276.26–276.27 m). In the pyroxenites the proportions of background to halo alteration are nearly equal, with pervasive background alteration constituting 54.6% of the total alteration and halo alteration 45.5%. Amphibole accounts for 100% of the secondary mineralogy in the background alteration.

Magmatic intrusions in the Mantle Sequence

Magmatic veins and layers of troctolites, olivine gabbros, gabbros, and rodingitized anorthosite (diopsidites) occur throughout the Mantle Sequence. Total alteration in the gabbroic intervals ranges 65%–100% (Fig. F44) and lies within the range of total alteration percentages recorded in the surrounding harzburgites. The least altered (65% total alteration) intervals occur in websterite and olivine gabbro in the lowermost 50 m of the hole. Serpentine ± magnetite are the dominant alteration phases in the troctolites, replacing olivine in the olivine gabbros (Figs. F60, F61). The gabbros and olivine gabbros are predominantly altered to amphibole (20%–75% total alteration) and chlorite (20%–50% total alteration) after clinopyroxene and plagioclase, with fine-grained aggregates (classified as secondary plagioclase) in the centers of the plagioclase (see supplementary Table ST7).

Troctolites are present in the following sections:

- 71Z-1 (144.12–144.24 m)
- 91Z-2 (198.31–198.32 m)
- 92Z-2 (201.90–201.95 m)
- 92Z-3 (202.33–202.37 m)
- 100Z-3 (224.04–224.05 m)
- 115Z-3 through 115Z-4 (265.93–266.16 m)
- 116Z-2 (267.45–267.59 m)

The total length of troctolite intervals is 0.60 m. The overall alteration intensity is 83.5%, whereby background alteration accounts for 98.4% and vein-related halo alteration is responsible for 1.6% of the total alteration. Secondary mineral assemblages in the troctolites include varying proportions of the following (Fig. F60A, F60B):

- Serpentine (average = 63%; range = 35%–95%)
- Chlorite (average = 27%; range = 20%–30%, present only in 91Z-2 and 92Z-3)
- Secondary plagioclase (average = 25%; range = 5%–60%, present only in 71Z-1, 91Z-2, and 115Z-3)
- Amphibole (average = 20%, present only in 92Z-2 and 97Z-3)
- Prehnite (average = 5%, present only in 91Z-2)
- Magnetite (average = 5%)

Alteration intensity in halos within the troctolites is 1.6% and is only present in Section 100Z-3. The halos in this section contain serpentine (90%) and magnetite (10%).

Veins of olivine gabbros and gabbro were recognized in the following sections:

- 94Z-2 (207.88–207.88 m)
- 94Z-3 (208.22–208.22 m)
- 104Z-2 through 104Z-3 (235.25–235.31 m)
- 111Z-2 (252.46–252.49 m)
- 113Z-4 (260.30–260.34 m)
- 115Z-1 (264.48–264.49 m)
- 115Z-4 (266.55–266.56 m)
- 116Z-1 (266.98–266.99 m)
- 116Z-2 (267.78–267.85 m)
- 116Z-3 (267.94–267.95 m)
- 119Z-3 (274.76–274.85 m)
- 120Z-4 (278.03–278.04 m)

The overall length of all gabbroic intervals is 0.47 m. Total alteration intensity in the olivine gabbros and gabbros is 81.3% and is made up entirely of background alteration (Fig. F60C). The secondary mineral assemblages consist of the following:

- Secondary plagioclase (average = 44.4%; range = 20%–70%)
- Amphibole (average = 39%; range = 20%–75%)
- Chlorite (average = 28.6%; range = 20%–50%)

- Prehnite (average = 15%, present only in 91Z-2)
- Serpentine (average = 7.3%; range = 5%–10%)
- Magnetite (average = 2%, present only in 94Z-2 and 94Z-4)

Magmatic veins and layers of rodingitized anorthosite occur throughout the Mantle Sequence (Figs. **F44**, **F46**, **F60**, **F61**). Anorthosites are commonly coarse grained to pegmatitic and are present in the following sections:

- 69Z-4 (140.22–140.34 m)
- 71Z-4 (146.43–146.53 m)
- 77Z-2 (162.56–162.56 m)
- 83Z-3 through 83Z-4 (178.63–179.37 m)
- 84Z-1 (179.64–179.68 m)
- 89Z-2 (192.52–192.52 m)
- 92Z-4 (203.32–203.40 m)
- 93Z-4 (206.09–206.10 m)
- 94Z-3 (208.72–208.74 m)
- 94Z-4 (209.30–209.55 m)
- 95Z-3 (211.77–211.79 m)
- 103Z-4 (233.07–233.09 m)
- 106Z-3 through 1106Z-4 (242.06–242.42 m)
- 107Z-2 (243.67–243.68 m)
- 110Z-1 (248.70–249.16 m)
- 112Z-4 (257.41–257.42 m)

With the exception of Section 77Z-2 (90% altered), the anorthosites are completely altered (95%–100% of total alteration; average intensity = 85.8%). Background alteration accounts for an average of 94.4% of the total alteration (average intensity = 90.6%). Halo alteration amounts for the remaining 5.6% of the total alteration (5.28% of the total alteration intensity) (supplemental Table **ST7**).

The alteration assemblages in the altered anorthosites are similar to the rodingites recovered in Hole CM1A and consist of 60%–100% diopside ± garnet, 10%–30% chlorite, and 0%–20% (tremolitic) amphibole. Garnet also occurs in veins within the altered anorthosites, and olivine-bearing intervals are altered to serpentine. Other Ca-rich minerals in the altered anorthosites include diopside, locally up to 100%, (tremolitic) amphiboles, calcite, dolomite, and xonotlite, all of which occur in various proportions that were difficult to assess macroscopically (Fig. **F61**; supplemental Table **ST5**).

Talc-carbonate serpentinites

Sections 125Z-4 through 129Z-1

The lowermost 10 m of Hole CM2B (Sections 125Z-4 through 129Z-1) is marked by spectacular progressive carbonation features and a transition from serpentinized harzburgite to talc-serpentine-calcite-dolomite harzburgite to talc-magnesite-dolomite serpentinite (Figs. **F62**, **F63**). The transition from serpentinization-dominated alteration to carbonate-rich alteration is seen in Cores 126Z and 127Z and is characterized by highly heterogeneous intervals of variably veined and deformed serpentinized and carbonated harzburgite (99.7% total average alteration) intermittent with white intervals altered to serpentine + talc and pink to red patches of serpentine + chlorite + dolomite, in which the serpentinite fabrics have been obliterated (Figs. **F62**, **F63**).

XRD analyses revealed the first occurrence of calcite and dolomite together with serpentine in interval 125Z-4, 65–69 cm (290.5 m), and the presence of magnesite and dolomite together with talc and serpentine from Section 127Z-2, 26–27 cm, to the bottom of the hole (see Figs. **F62**, **F63**; Table **T7**; supplemental Fig. **SF4**). The magnesite and dolomite domains occur as coarse to very coarse grained, well-crystallized veins, lenses, and irregular patches as long as 30 that are as thick as the diameter of the core. Chaotic distribution of alteration phases and irregular veining patterns suggest high fluid pressures and hydrofracturing associated with CO_2-rich fluid infiltration (see **Alteration history/comparison with Hole CM1A**).

A steep metasomatic front within the serpentinized harzburgite is observed at the bottom of interval 127Z-2, 51–71 cm, and is characterized by the occurrence of magnesite in the serpentinized harzburgite and relative bleaching (lighter gray color of the harzburgite host rock) (Figs. **F62A**, **F63A**). In addition, Cores 126Z and 127Z have domains that are highly deformed, showing variable cataclastic, mylonitic, and sheared features around less deformed serpentinized and carbonated harzburgite. Banded zonation is observed in a deformed interval in the bottom of interval 127Z-3 (23–65 cm) which continues to the top of Section 127Z-4, 2–26 cm (Fig. **F62B**). XRD analyses indicate that the bands in these sections are made up of varying proportions of talc, serpentine, calcite, and dolomite (Table **T7**; supplemental Fig. **SF4**). The light gray appearance of the altered wall rock in Cores 126Z and 127Z suggests that magnesite ± dolomite carbonation is common throughout the wall rock. On the whole, the structures, textures, and mode of occurrence of the talc-carbonate alteration domains in this sequence are reminiscent of ophicarbonate sequences in Alpine ophiolites, such as in the Northern Apennine ophiolite in Liguria, Italy (Treves and Harper, 1994; Schwarzenbach et al., 2013).

Veins in the Mantle Sequence

Veins in the Mantle Sequence can be grouped into 7 types in the harzburgite lithologies, 1 type of Ca-rich assemblage in gabbros and dunites, and veins related to the talc-carbonate serpentine domain at the bottom of the Hole CM2B (Table **T9**). Often, the relationships between the vein generations cannot be distinguished with macroscopic observations because of a high degree of overprinting, widespread fracturing, and reopening of fractures. In addition, categorization is hampered by irregular distribution of the vein types throughout the sequence.

Examples of typical veins within the harzburgites are shown in Figure F64. The first type of veins in the harzburgites is the serpentine mesh vein network. The mesh-textured veins are described above for the dunite sequence (see **Veins in the Dunite Sequence**), and their appearance and distribution are identical in the Mantle Sequence.

The second type of vein in the harzburgites are the minute-scale serpentine veins, which range from <0.5–3 mm in width and lead to maximum 50% alteration in the primary minerals they cut. They are commonly homogeneously massive in texture and either uniform or banded in the upper part of the sequence (down to Section 73Z-3; 120.30–151.93 m); vein halos are better developed below Core 74Z. Alteration halos associated with the serpentine V2 veins have variable widths from 0.5 to even 20 mm and are brownish in color resulting from iron oxyhydroxides that point to oxidation within the wall rock during vein formation. The V2 serpentine veins are often poorly developed and almost completely obliterated by later overprinting and further alteration processes, which together with their dark green and black color makes them unrecognizable macroscopically.

Magnetite-rich serpentine veins constitute the third type of veins (V3). These veins form networks that can be traced throughout entire cores and are very prominent and distinguishable in the core sections. Thickness of the magnetite-rich serpentine V3 veins ranges 1–100 mm; they are uniformly black in color, massive in texture, and either haloed or uniform in structure. The magnetite-serpentine V3 veins are chiefly branched with vein tip morphology and are commonly crosscut by later calcite veinlets. The magnetite content in the centers of the veins varies (0%–5%) and can be clearly seen on X-ray computed tomography (XCT) scans, which also provide a good tool for recognizing V3 veins that are often extensively overprinted by later veins and alteration processes (Fig. F64). The alteration halo associated with V3 magnetite-serpentine veins can be zoned, with an inner domain consisting of serpentine with disseminated crystals of magnetite and an outer zone diffusively extending into the background. The outer zone is likely a remnant after penetration of highly oxidizing fluids, which explains the typical rusty-orange color and abundance of iron oxyhydroxides. The alteration halos invoke alteration of the primary minerals, with relict pyroxene crystals commonly recognizable and wall rock alteration <50%.

The black serpentine ± magnetite V3 veins are commonly cut by green or orange-green serpentine veins (V4) in their centers or at the margins (Fig. F65B). Down to Section 70Z-1, the V3 serpentine-magnetite veins exhibit cross-fiber texture, but from Section 80Z-2 downhole, they are slip-fiber and consist of either chrysotile or lizardite or both. In addition to the characteristic slip-fiber texture, the V3 veins are banded and heavily fractured. The surfaces of the fractures are often slickensides and record the steeply dipping character of the veins. Most of the V3 veins are single and planar, but locally they can also form irregular networks, especially where a fault or a fracture zone is involved. Their width is highly variable, ranging 0.5–10 mm, but is difficult to properly assess because of their susceptibility to fracturing. In some intervals the serpentine-magnetite V3 veins are not present (e.g., Sections 115Z-4 through 121Z-3; 266.05–280.62 m), but they are always present in zones of higher fracture intensity. This relationship between V3 veining and fractures could explain why fractures are concentrated in intervals with high V3 intensities.

In zones of higher fracturing density, a fifth type of serpentine veins (V5, likely lizardite) is locally present. The V5 serpentine veins are green with bluish hue and appear only on the surfaces of and partially infill fractures (Fig. F64A). Locally, they can be dislocated by later vein generations as seen in Figure F65A. They are massive and uniform and irregularly follow the shapes of the fractures. The width of the V5 veins is variable, ranging 1–6 mm, and depends highly on the spacing created by fractures.

Chrysotile veins are the sixth type of veins in the harzburgites (V6). Their sizes vary 0.5–3 mm; they are massive, uniform, and either curved or irregular. The chrysotile V6 veins stand out among other types of veins because of their bright white color as well as their distinct wavy appearance, which is similar to ribbons. On the cut core surfaces, the white chrysotile veins are easily recognized by touch, as they extend above the cut surface due to their swelling nature. They can completely follow the pathways of earlier veins (e.g., Fig. F65B) where they overprint margins of magnetite-rich serpentine veins and slip-fiber serpentine veins. The V6 chrysotile veins commonly form 0.5 mm wide veinlets that crosscut margins of the magnetite-rich serpentine V3 veins and their distinct alteration halos (Fig. F65C). The chrysotile veins commonly occur in the centers of earlier V3 magnetite-rich veins as well as at the margins of V3 halo zones, leading to a pronounced appearance in these overprinted zones. Often, the white chrysotile veins form "swarms" of parallel, isolated, or connected and curved veinlets that closely follow the pathways of the earlier vein generations described above and form wide, extensively veined zones (Fig. F66) and overprinting earlier vein generations. The chrysotile veins can contain up to 10% calcite (Sections 61Z-1 through 69Z-1; 121.80–138.45 m; 95Z-3 through 97Z-3; 211.52–217.91 m; and 107Z-1 through 126Z-5; 243.17–294 m).

The serpentine veins are commonly followed by a later generation of calcite veins (V6), which closely follow the earlier fluid pathways (Fig. F64A). The late V6 veins usually contain up to 100% carbonates (calcite locally with coalingite; Table T9); they can be almost completely dissolved, with the only remnant of their presence being rusty-orange discoloration of the surrounding wall rock. The width of the calcite veins does not exceed 0.5 mm. Their first appearance is recorded in Section 93Z-4 (206.42 m), and they continue to be present in almost all sections until the bottom of the hole (Section 126Z-1; 291.48 m). The calcite veins have massive textures, uniform structure, and irregular morphology and are either orange-white or yellow. Where present, they can form polygonal or subpolygonal networks extending from the cross-fiber fractured veins into the background (Fig. F64A). In Sections 107Z-4 through 124Z-3 (245.35–287.88 m) some branches of the calcite veins can extend vertically throughout the cores.

The distribution and the crosscutting relationships of veins in the harzburgitic lithologies are complicated, and the sequence of formation can be ambiguous. In many core sections, not all of the vein types described above are present or visible because of later overprinting and alteration. In some sections with the lowest vein density, the only vein types present are the mesh serpentine ± magnetite-rich veins and the single V2 serpentine veins. These can also occur in intervals with the wide banded V3 serpentine ± magnetite veins with distinct vein halos. The green steeply dipping and slip-fiber V4 veins follow the centers of the magnetite-rich serpentine veins in sections with higher density of vein-related alteration and brittle deformation, which may be enhanced by the fibrous habit of the serpentine crystals. Although in some cases slip-fiber V4 veins are the sole generation visible in a section and cannot be put in the categories discussed above.

The fracture-infilling V5 serpentine veins can crosscut the other serpentine vein types, but in some cases they can also be distinguished as the latest generation because they dislocate the chrysotile and calcite veins. It is often unclear whether the carbonate veins (chiefly calcite ± coalingite confirmed by XRD analyses in Table T7) are the latest stage of mineralization or whether they formed simultaneously with the white chrysotile veins. These two types often crosscut each other, following the paths of earlier vein generations. In some cases, the chrysotile veins overprint all other types, and in other cases the calcite veins are the last overprinting generation. The calcite veins locally extend outwards into the background from the fractured zones. Other types of veins in the Mantle Sequence are shown on Figure F67.

The talc-carbonate serpentinites at the bottom of the Hole CM2B (Sections 127Z-1 through 129Z-1; 293.61–300.14 m) contain a vein network related to a carbonate metasomatic zone of undefined thickness. The veins contain a wide variety of vein-filling minerals including talc, serpentine, dolomite, magnesite, and calcite (Fig. F67B). They are polycrystalline and intravenous, but understanding their primary characteristics requires further investigations due extensive overprinting and alteration.

A further vein type in the Mantle Sequence occurs in the Ca-rich metasomatic assemblages related to the gabbroic and dunitic intrusions and intercalations in harzburgites. They are distinctly developed in only three intervals throughout the whole sequence, but they are likely present in a number of micrometer-scale igneous/metasomatized domains. The Ca-rich assemblages are seen in Sections 83Z-2 through 83Z-3 (177.34–178.72 m), 106Z-4 (242.28–242.41 m), and 120Z-3 (277.60–277.82 m). They form polycrystalline, often branched, intravenous intervals with single vein width ranging 0.5–4 mm. They are extensively haloed, and their greenish and purplish colors stand out in the black serpentinized rocks. XRD analyses confirm the presence of diopside, serpentine, amphiboles, chlorite, hydrogrossular (indistinguishable from garnets), and xonotlite as vein filling phases in the gabbroic intervals. An example of vein connectivity in those domains can be seen in Figure F67A.

In summary, abundant veins are found in the serpentinized harzburgites throughout the whole Mantle Sequence and include numerous generations, which can be divided into mesh serpentine veins; single serpentine veins; banded serpentine ± magnetite veins; fractured green-orange, commonly subhorizontal serpentine veins that also occur on fracture surfaces; white swelling chrysotile ± calcite veins; and calcite veins. Veins within the gabbroic intervals are filled with Ca-Al–bearing minerals ± serpentine.

Discussion

CO_2 metasomatism of ultramafic lithologies

The most unique mineral assemblages observed in Hole CM2B occur in the carbonatized and serpentinized peridotites and talc-carbonate serpentinites in Cores 126Z–129Z. The mineral assemblage in the talc-carbonate serpentine includes varying proportions of talc, magnesite, dolomite, calcite, and serpentine. XCT analyses and microscopic observation of the on-site sample from this domain (129Z-1, 5–10 cm) revealed no relict minerals (olivine, pyroxene) and no Ca amphibole such as tremolite. The presence of carbonate in the serpentinites suggests that external CO_2-bearing fluids reacted with the variably serpentinized ultramafic rocks, although the origin of CO_2 is unclear in the studied hole. In a number of previous studies in the literature, talc-carbonate zones are observed around contacts between ultramafic rocks and quartzo-feldspathic country rocks (Koons, 1981; Bach et al., 2013).

Temperature conditions of CO_2 metasomatism in Hole CM2B can roughly be constrained in the *P-T* diagram shown in Figure F68A, which was calculated using PerpleX version 6.7.9. (Connolly, 2009) with the hp11ver.dat data set (Holland and Powell, 2011) and assuming X_{CO2} = 0.2. Assuming a constant pressure of 1.0 kbar, which is typical pressure of oceanic lithosphere, the temperature of CO_2 metasomatism is estimated to be <380°C, based on the microscopic observation that no tremolite is formed in the carbonated serpentinite, as would be predicted from thermodynamic phase equilibria. Calcite, dolomite, magnesite, and talc are stable over a range of X_{CO2} (Fig. F68B).

Previous studies of carbonate-bearing serpentinites exposed on land indicate a wide range of carbonation temperatures that vary from ambient to 340°C (Halls and Zhao, 1995; Boschi et al., 2009; Wilson et al., 2009; Klein and Garrido, 2011; Schwarzenbach et al., 2013), which is largely consistent with our estimation. Further detailed studies of oxygen isotope compositions and radiogenic isotope studies of the carbonate minerals are necessary to more precisely constrain the temperatures of carbonate precipitation and origin of CO_2.

The simplest carbonation reaction after olivine is expressed in the following (Reaction 1):

$$Mg_2SiO_4 \text{ (olivine)} + 2CO_{2(aq)} \\ = 2MgCO_3 \text{ (magnesite)} + SiO_{2(aq)}$$

Reaction (1) releases aqueous silica, which may cause an increase in silica activity in the fluids and lead to talc precipitation. It is known that the maximum reaction rates for this reaction occur at temperatures of 185°C (Kelemen and Matter, 2008), whereas maximum reaction rates for serpentinization occur at temperatures of 250°–300°C (Malvoisin et al., 2012). This carbonation reaction could generate maximum crystallization pressures of ~2.5 GPa, which could cause formation of fractures and maintain or increase permeability (Kelemen and Hirth, 2012). When carbonation occurs after serpentinization is completed, the overall reaction can be expressed as follows (Reaction 2):

$$2Mg_3Si_2O_5(OH)_4 \text{ (serpentine)} + 3CO_{2(aq)} = \\ 3MgCO_3 \text{ (magnesite)} + Mg_3Si_4O_{10}(OH)_2 \text{ (talc)} + \\ 3H_2O$$

CO_2-metasomatism of serpentine via Reaction (2) is a dehydration reaction, which potentially could cause an increase in pore fluid pressure and hydrofracturing, as suggested in silica-metasomatic rocks from the Mid-Atlantic Ridge (Escartín et al., 2003; Boschi et al., 2006).

Alteration history/comparison with Hole CM1A

Hydrothermal alteration occurs throughout Holes CM1A and CM2B. The rocks have undergone multiple phases of fluid infiltration and water-rock reactions under a range of temperature conditions and fluid compositions throughout its tectonic evolution to present-day exposure in the mountains of Oman. Based on the sequence of mineral assemblages determined by macroscopic and microscopic observations and XRD analyses, temperatures of alteration and fluid-rock interaction in Hole CM2B are similar those in recorded Hole CM1A. In both holes, the dominant temperatures of alteration are estimated to be within greenschist facies conditions, based on the fact that high-temperature amphiboles are not abundant. In addition, the presence of brucite suggests a maximum temperature of ~350°–380°C (Früh-Green et al., 2004). Multiple phases of fluid infiltration and alteration with cooling are recorded by prehnite-pumpellyite facies assemblages in the rodingitized domains and zeolites that are predominant in the gabbroic sequences in Hole CM1A.

Within the CMTZ in both holes, the background alteration intensity is consistently high throughout the entire sequence and generally exceeds 95%. It is dominated by serpentine and magnetite vein network-forming mesh textures, which is identical in both holes. Similarly, the remaining three serpentine vein generations described in Hole CM1A also appear in Hole CM2B. The V3 magnetite-rich serpentine veins can reach up to 300 mm in width in Hole CM2B, whereas the maximum width observed in CM1A is 50 mm. Moreover, in Hole CM2B no late-stage calcite vein network was observed in the Crust–Mantle Transition sequences, and the overall proportion of vein-related alteration is lower relative to Hole CM1A. Chromite-rich layers with alteration intensity ~70% were only observed in Hole CM1A. A greater number of rodingitized intervals are found in Hole CM1A, and the mineral assemblages identified in these intervals are also more diverse, with the occurrence of vesuvianite, hibschite, and andradite, which are not present in Hole CM2B.

The total alteration intensity is slightly lower in Hole CM2B than in Hole CM1A, which can be also deduced by a lower density of veining and vein-related alteration. Fewer intrusion-related metasomatic alteration intervals were also observed in Hole CM2B, although a distinctive zone of talc carbonatization is present in the lowermost 10 m of the hole. A greater diversity and number of vein generations were identified in the Mantle Sequence from Hole CM2B compared to Hole CM1A, and, although less abundant, they form more complicated crosscutting succession relationships.

The presence of talc-carbonate serpentinites at the bottom of Hole CM2B points to the presence of an external source of CO_2 and fluid-rock interaction within the serpentinites and dunite intervals. Based on calculations of *P-T* constraints of formation of the talc-carbonate domain, the estimated temperature of the metasomatic alteration is <380°C, which is in accordance with petrological observations and estimations based on the composition of secondary mineral assemblages. Such fluid-rock reactions could also lead to hydrofracturing that might have been responsible for severe deformation features observed in multiple intervals throughout Hole CM2B as well as Hole CM1A.

In summary, the pressure and temperature conditions of formation of secondary mineral assemblages in Holes CM1A and CM2B were probably similar, although some differences could be observed between the two holes. The presence of talc-carbonate serpentines calls for further investigations and may be evidence for a more complicated system of fluid-rock interactions below the base of the hole.

Magnetite-rich veins are macroscopically and microscopically observed in serpentinized harzburgite and dunite. The vein-related alteration causes highly altered zones in dunite and harzburgite, such as alteration halos (Fig. F59). The background magnetic susceptibility (MS) in the Dunite Sequence and upper Dunite with Gabbro Sequence are clearly higher than that of MS in the Mantle Sequence (Fig. F69). This is consistent with total alteration intensity in downhole variation because MS primarily reflects the alteration degree of dunite and harzburgite. The magnetite-rich veins are present in alteration halos in dunite and harzburgite below 94.5 m within the lowermost Dunite with Gabbro Sequence and Mantle Sequence, but not above. Total alteration intensity of dunite is relatively weak at these levels (although still highly altered). This indicates that the formation of halos related to magnetite-rich veins depends on the primary serpentinization of dunite, although the background MS in the lowermost Dunite with Gabbro Sequence is similar to that in the Dunite Sequence. In the Mantle Sequence, high-MS pulses in the downhole profile are mainly located at magnetite-rich veined harzburgite based on observations of halos (Fig. F69). Although its relationship with total alteration intensity in harzburgite is unclear, the variation of total alteration intensity in the Mantle Sequence probably reflects the highly alteration zone of halos rather than the primary serpentinization degree of harzburgite.

Structural geology: Hole CM2B

Hole CM2B yielded 293.60 m of core that records the transition from the Dunite Sequence to the Mantle Sequence. The core started within the Dunite Sequence, traversed the Dunite with Gabbro Sequence, and recovered 179.36 m of core from the Mantle Sequence. Here are reported macro- and microstructural observations and measurements of magmatic and ductile and brittle deformation observed on core and in thin section. All dips are measured relative to the core reference frame (CRF). Consequently, the measurements are reported in a reference frame that is rotated 30° compared to the CRF for Hole CM1A and to the mantle reference frame because the Moho dips 30° south-southeast at this locality (see Fig. F4 in the **Introduction to Science Theme 1B** chapter). All dips of magmatic layers, contacts, foliation, veins (magmatic and alteration), fractures, and faults have been measured and plotted when possible. A summary of key structural observations is presented at the end of this section as well as a summary of the inferred structural history of cores from both Holes CM1A and CM2B.

Lithologic contacts

Harzburgite/dunite contact

The top of the Mantle Sequence is a 26.37 m interval (120.78–148.15 m) of interlayered dunite and harzburgite (Figs. F70, F71). The contacts between the dunite and the harzburgite layers are mostly irregular and gradational, with the gradation occurring over ~1–2 cm (Fig. F70A). These irregular and gradational contacts are difficult to measure. At the top of the Mantle Sequence, the dip of the contacts ranges 30°–52° except for one extremely low value of 3°. Excluding this low value, mean dip is 35° ± 8° (Fig. F72A). Deeper in the Mantle Sequence, measurable dunite/harzburgite contacts steepen at 151 m (dip = 59°) and 233 m (dip = 65°) (Fig. F72A). Additional dunite/harzburgite contacts are present elsewhere in the Mantle Sequence but have irregular and gradational boundaries that are difficult to measure.

Dunite/gabbro contact

The Hole CM2B core contains a ~9 m long sequence of gabbro interlayered with dunite located at 74.1–83.39 m (Figs. F70B, F71, F72). This gabbro-dunite sequence lies within a later brittle fault zone (see Fig. F86G) and is itself cut by small offset faults; one at 78.90 m creates a visible change in dip between two adjacent gabbroic layers (red dashed lines on Fig. F72B). The contacts between the gabbro and dunite layers are sharp and planar (Figs. F70B, F71), and the dip of the contacts ranges ~22°–54°. The first contact between dunite and gabbro at 74.25 m dips 35°, and the next one at 74.31 m dips 44°. From this second contact, the dip progressively decreases to 26° at 76.81 m, forming gradual fanning over 2.5 m (Fig. F72). From this depth, dip increases from 26° to 52° over the next 2 m until the fault at 78.88 m.

In the lower part of the gabbroic sequence below the fault at 78.88 m, the dip of the layering gradually decreases once again, from 45° to 39° at 79.75 m. Below this, several faults disrupt the layering (Figs. F71, F72) and the dip of the layering is 60° (80.15 m) within this small fault zone. Below this small fault zone in a thin, coherent faulted interval at 80.35–80.47 m, dip of the layering increases from 11° to 30°. At 80.65 m, a small disrupted olivine-rich layer dips 11°. Below 80.65 m, the gabbro shows a consistent mineral foliation dip, but there is no strong layering until 82.67 m, where an olivine gabbro layer that is discordant to foliation dips at 48° at the upper boundary and 36° at the lower boundary. Below this is one final thin gabbro layer at 83.12–83.39 m that dips 18° (Fig. F72).

The same type of cycling of the dip and gradual fanning of the magmatic layering was observed in the Layered Gabbro Sequence in Hole CM1A (see the Site CM1 chapter). The gabbro layers at 74.26–83.39 m in Hole CM2B (9 m thick) likely correlate with a similar sequence of four thinner gabbro layers that occurs at 258.03–292.76 m in Hole CM1A (34.73 m thick) (Fig. F76).

Veins and gabbroic patches

Gabbroic veins are found in the upper part of the Dunite Sequence at 12.79–35.72 m and in the lower part of the Dunite with Gabbro Sequence at 107.02–112.38 m (Fig. F72). They are also distributed in the Mantle Sequence below the dunite-harzburgite interlayered sequence from 126.8 m until the bottom of the hole (Fig. F72). However, in the Mantle Sequence gabbroic veins do not occur in two intervals: 221.76–233.19 m (11.4 m) and 243.67–260.33 m (16.7 m). Throughout the entire Hole CM2B core, the gabbro veins have mostly sharp and irregular contacts with dunite and harzburgite (Fig. F73A–F73E).

In the Dunite Sequence, vein dips cluster at 26°–51° (average = 36° ± 7°) (Fig. F72). In the rest of the core (107.02–300.1 m), the dip of the gabbroic veins is highly variable, 1°–88° (average = 51° ± 18°) (Fig. F72). The dip vs. depth diagram highlights several clusters of gabbroic veins with steep dips. For instance, at ~200 m a cluster of veins dips 51°–65°, and below 260.33 m, vein dip ranges 58°–81°. The frequency distribution for all the gabbro veins indicates a slight predominance of dips in the 50°–80° range (Fig. F72C).

Discrete gabbro intrusions are also found as irregular gabbroic patches occurring only in the Mantle Sequence from 130.83 m to the bottom of the hole. They show irregular and sharp contacts with the host dunite and harzburgite (Fig. F73C, F73E). Crosscutting relationships between gabbroic veins and patches at 242.1 m indicate that the gabbroic veins were crosscut by the gabbroic patches.

Two anorthosite veins documented at 77.66 and 78.92 m occur in the layered gabbro in the Dunite with Gabbro Sequence (Fig. F72). They both have sharp and irregular contacts with the host peridotite.

Deeper in the hole, at 187.03–267.73 m in the Mantle Sequence, seven centimeter-scale pyroxenitic veins were measured. Their contacts with the harzburgite are sharp and irregular, and they all have a steep dips varying 57°–78°.

Rare centimeter-scale veins of chromite are observed in the Dunite Sequence at 32.85–41.12 m. Their contacts with the dunite are either sharp and planar or sharp and irregular (Fig. F73F, F73G). Four of them record dips ranging 57°–63° in the CRF. The strongly chromite-rich (20 vol% modal chromite) layer (Subunit 11b) at 115.29 m towards the base of the Dunite with Gabbro Sequence has a dip of 39° (Figs. F71A, F75A).

Layering

Dunite and harzburgite layering

The top of the Dunite Sequence was not sampled during coring of Hole CM2B, so only 62.26 m of the Dunite Sequence was recovered. The dunite layers in the Dunite with Gabbro and Mantle Sequences range in thickness from a few centimeters to 6 m, except for one 37.4 m layer at 83.39–120.78 m (Fig. F74A). This layer forms the lower part of the Dunite with Gabbro Sequence, whereas the upper part is formed by interlayered gabbro and dunite discussed in **Harzburgite** in Macroscopic core descriptions in **Igneous petrology: Hole CM2B**. In the latter, most of dunitic layers are 1–10 cm thick (Fig. F74). For comparison, in Hole CM1A individual dunite layers in the Mantle Sequence are no thicker than 16.67 m (Fig. F62 in the **Site CM1** chapter). The thickness of the dunite layers in the Mantle Sequence in Hole CM2B define an approximate ln-normal distribution (mean thickness = 0.89 ± 1.2 m). This thickness is similar to the mean thickness of 1.24 m for the corresponding dunite layers in Hole CM1A.

The top of the Mantle Sequence is composed of a ~27 m thick interval of interlayered dunite and harzburgite (121.45–148.15 m), which even after correction for the dip of the hole, is thicker (23.4 m) than the corresponding interval (~13 m thick; 311.7–324.69 m) of interlayered dunite and harzburgite in Hole CM1A (Fig. F62 in the **Site CM1** chapter; Fig. F74A). In this part of Hole CM2B, the thickness of the dunite layers decreases from 1 m to few centimeters over the first 4.8 m (120.8–125.56 m) and then below a 6 m thick dunite layer, the thickness of layers increases from 0.13 to 4.5 m over 16.5 m (131.64–148.15 m; Fig. F74). At 148.15–265.90 m, the maximum layer thickness of dunite is 2.5 m. Below this depth, no dunite layers occur because the core consists only of harzburgite.

A spinel-rich layer occurs at 115.31–116.11 m (Figs. F72A; F75A, F75B). The spinel distribution in this layer is heterogeneous, with an enriched (30 vol%) area with large grains (up to 0.5 cm in diameter) within a less enriched (20 vol%) area containing a more scattered distribution of smaller grains (<1 mm diameter). Moreover, in the harzburgite, a few meters above this enriched layer, the presence of spinel is more obvious than elsewhere in the core, with a slightly higher modal proportion (1.5 vol%) and slightly larger grains (1 mm) than usually observed.

Gabbro

The gabbro layering at 74.25–83.39 m (~9 m) in igneous Unit 8 is defined by variations in the modal composition of plagioclase, clinopyroxene, and olivine and is most easily seen when olivine is altered, showing a dark brownish color (Figs. F70B, F75B–F75D). Boundaries between layers within this unit were measured when sharp and planar, corresponding to abrupt modal variation. Many other layers are defined by gradational modal variations (Fig. F75B), and grain-size defined layering is not present (Fig. F75D). This gabbro unit likely correlates with the package of 4 thinner gabbro layers that occur at 258.03–292.76 m (34.73 m) in Hole CM1A. Two 1.3 m and 2.01 m thick gabbro layers are found at 75.4 m and 80.65 m, respectively (see more details in Igneous petrology: Hole CM2B). With the exception of these olivine/pyroxene-poor intervals, all gabbro layers are thinner than 0.5 m, with the most common thickness <5 cm (Fig. F76).

Gabbro veins and others

Most gabbroic veins are <5 cm thick (average = 0.66 ± 0.7 cm; the high standard deviation indicates a large variation in vein thickness) (Fig. F76). Only two larger veins with thicknesses of 12 and 15 cm were documented. There are no clear relationships between the frequency and thickness of the gabbroic veins. For instance, the cluster of veins occurring at 201.03–211.77 m has similar vein thicknesses to veins scattered throughout the hole (mostly 0.2–1 cm) (Figs. F72, F77).

Foliation and plastic deformation

Harzburgite and dunite

In the Mantle Sequence, harzburgites are undeformed to weakly foliated, and moderate to strong crystal-plastic fabrics are very rare (Fig. F78B). Foliation was measured using the alignment and elongation of orthopyroxene grains and/or spinel grains. Measurements indicate a relatively constant steep dip ranging 39°–60° (average = 57° ± 7°) (Fig. F78A). A relationship between the orientation of the harzburgite foliation and dunite/harzburgite contacts is difficult to assess because only 2 dunite/harzburgite contacts were measured in the Mantle Sequence (Figs. F72A, F78A). However, both of these contacts have a high dip angle (>47°).

Deformation recorded in the harzburgites is easier to characterize than in the dunites using the elongation of orthopyroxene and the preferred orientation of spinel grains. However, in some samples the orthopyroxene forms round aggregates and lineations are hard to discern (Fig. F80A). In weakly deformed harzburgite, large orthopyroxene grains are elongated (up to an aspect ratio of ~5:1), contain numerous thin exsolution lamellae, and can be folded and kinked (Fig. F80B, F80D, F80E). Many of the orthopyroxenes form aggregates, and in these aggregates the smaller grains are without exsolution lamellae and show 120° triple junctions, suggesting equilibration (Fig. F80E). These equilibrated grains are only rarely present below 181.33 m and are more common below 251.16 m. In the weakly deformed harzburgite, the olivine grains show undulose extinction and few subgrain boundaries (Fig. F79D), and orthopyroxene is more deformed than olivine.

Estimating crystal-plastic deformation recorded by olivine in dunite is difficult because of high degrees of serpentinization (up to 95%, see Alteration: Hole CM2B). However, the shape of the olivine crystals can be preserved during isotropic serpentinization, and in some thin sections, a relict weak olivine shape-preferred orientation defining foliation is observed (Fig. F79A, F79B). In all samples, including less deformed dunite, the relict olivine grain boundaries show 120° triple junctions (Fig. F79A, F79B). Some fresh grains of olivine remain in a few dunites after serpentinization, such as in TS Samples 37Z-1, 51–55 cm, and 89Z-1, 6–10 cm, in which olivine shows millimeter-size crystals with subgrains and undulose extinction (Fig. F79C). However, in these samples the subgrain boundaries are random and do not record lineation. Some spinels can record lineation in the dunites (Fig. F79A).

The harzburgites and especially the dunites of the ultramafic sequences have been impregnated by gabbroic melt, forming plagioclase trails or lenses that are easy to measure (Figs. F73E; F75E, F78F). These measurements are reported in Figure F78A as plagioclase segregations. The first occurrence of plagioclase segregations in the Dunite Sequence is observed at 55 m (297.5 m in the Dunite with Gabbro Sequence in Hole CM1A; Fig. F68 in the **Site CM1** chapter). The measured dips range 20°–64°, with most of the dips >39° (average = 46° ± 11°; Fig. F78A). The average dip in the CRF calculated for impregnated ultramafic rocks in Hole CM1A is 16° ± 4°, the same as the 46° ± 11° average dip for Hole CM2B (Fig. F68 in the **Site CM1** chapter) after correcting for the 60° inclination of Hole CM1A.

Only one protomylonite is recorded at the bottom of the hole at 283.89–284.09 m (20 cm thick) (Figs.

F78B; F80A–F80C). The protomylonite is altered and so the deformation is revealed by the shape of the metamorphic plagioclase lenses and the elongation of a few olivine grains (Fig. F80C). However, most olivine grains show 120° triple junctions, suggesting annealing, possibly similar to that seen by the orthopyroxene in the harzburgites.

The chromite-rich layer (115.31–116.11 m) in the Dunite with Gabbro Sequence contains large chromite grains up to 0.5 cm in diameter with pressure shadows filled with altered plagioclase (Fig. F80F). The shape of these pressure shadows suggests a component of pure shear deformation.

Gabbro

The gabbro layers are almost undeformed, but weak magmatic foliation is observed in few layers, defined by the shape-preferred orientation of olivine, plagioclase, and clinopyroxene and a weak plagioclase crystallographic preferred orientation (Fig. F75D). No deformation twins are observed in the plagioclase grains, and some plagioclase aggregates are texturally equilibrated, showing 120° triple grain junctions.

Brittle deformation

Brittle structures

Brittle deformation structures are ubiquitous throughout Hole CM2B. The styles and intensity of brittle deformation vary with depth and also correlate with rock type, with quantifiable differences in the intensity of brittle deformation in the dunitic sequences and the Mantle Sequence. Similar to Hole CM1A, the highest temperature brittle deformation features are diopside/chlorite/tremolite veins in gabbro that are synchronously deformed with serpentine veins in ultramafic units—demonstrating a paucity of deformation between magmatic conditions and greenschist-grade conditions. Similar crosscutting relationships are observed among the sequence of carbonate/talc veins, serpentinites, and faulting at the base of Hole CM2B. Significant brittle deformation only commenced after development of the serpentinite mesh texture, with the most intense brittle deformation occurring synchronously with the last stages of serpentine veining.

The orientations, deformation intensity, and downhole distribution of brittle deformation features were recorded in all drilled sections (see Tables T10–T13). The intensity of discrete brittle structures was recorded at the centimeter scale using a scale that ranges from 1 (minor fracturing) to 5 (ultracataclasite); a rank of 6 was reserved for pseudotachylite, which was not observed (see the **Structural geology** in the **Methods** chapter). In total, 817 brittle features were logged. In addition, semiquantitative logs of fracture and vein densities were recorded. These data are summarized in Figure F81, which shows how fracture density, deformation intensity, and vein density vary with depth in Hole CM2B. These data were smoothed by averaging the value of each 10 cm interval in the core with the values in the 10 cm intervals immediately above and below it (repeating the averaging calculation three times). The location of fault zones identified in the core are also shown in Figure F81.

In the following sections we present an overview of the styles of faulting and brittle deformation features observed in the core, an analysis to identify the most significant fault zones in Hole CM2B, and data on the orientations of these features in the CRF. These data are then included in the overview of the structural history, integrating results from Hole CM1A and CM2B, in **Summary**.

Fault zones

Overview of brittle deformation features

Fault zones are observed in all sequences of Hole CM2B (Fig. F81); 3 styles of faulting are observed: cohesive cataclastic zones, vein/fracture networks, and incohesive cataclastic zones. Table T12 summarizes the depth intervals of the damage zones for these fault zones.

Cohesive cataclastic zones form in discrete intervals marked by narrow deformation zones exhibiting semibrittle deformation microstructures in serpentine, chlorite, and talc, as well as cemented brecciation with a wide range of clast sizes (Figs. F82, F83). Although not prevalent enough to be significant in terms of deformation intensity, these zones are structurally significant because they represent the earliest (and highest temperature) style of faulting in Hole CM2B. The cohesive cataclastic zones are often overprinted by localized brittle slip surfaces. For example, the ~4 cm wide semibrittle shear zone shown in Figure F66A and F66B—involving distributed deformation of diopside, serpentine, and likely chlorite—is overprinted by an extremely narrow (~10 µm) slip surface localized along the boundary between serpentinite and diopsidite layers. The minor fault zone shown in Figure F82C–F82E illustrates synchronous deformation of an amphibole/chlorite vein (in a gabbroic layer) and a serpentine vein (in the ultramafic layer); semibrittle deformation microstructures involving chlorite and serpentine are then overprinted by a localized slip surface along the vein, and then by late carbonate veins.

Similar textural relationships are observed for the carbonate-rich fault zone observed at the base of Hole CM2B. Here, carbonate- and talc-rich veins show microstructures indicative of ductile/semibrittle mechanisms; the carbonate exhibits grain flattening, development of subgrains, and dynamic recrystallization (Fig. F83B) with foliations in talc-rich regions that wrap around the deformed carbonate-rich regions. These features are overprinted by localized brittle slip surfaces (Fig. F83C, F83D).

Vein-related faulting is the culmination of high-strain deformation on fault zone networks defined by crosscutting and parallel shear veins and extensional fractures and is associated with areas of greater wall rock alteration (e.g., Fig. F84). In the core, many of these fault zones are marked by intervals of rubble comprising phacoids (cobble-sized fragments bounded on all sides by slickensides).

Incohesive cataclasite is defined by significant grain size reduction that in some occurrences produces clay-like gouge (e.g., Fig. F85). Fault zones with incohesive cataclasite overprint preexisting vein-related deformation (e.g., Fig. F86C, F86D) and form within zones with a high intensity of vein-related deformation. These observations indicate that the incohesive cataclasite forms at lower temperatures by strain localization within preexisting fault zones.

Assessment of brittle deformation intensity and distribution of fault zones

Based on core description alone, it is difficult to assess displacement on fault zones that intersect the core. To provide a basis for identification of the most significant faults in Hole CM2B, we applied a Fault Zone Intensity Index (FZII), a semiquantitative formula that combines the logging data for fracture density, cataclastic deformation intensity, and damage zone thickness (see description in Fault zones in the **Site CM1** chapter). The FZII is calculated using the formula

$$\mathrm{FZII} = (F/3 + D/5) \times (T/T_{\mathrm{max}}), \quad (1)$$

where

F = smoothed fracture density (0–3; see Structural geology in the **Methods** chapter),
D = smoothed deformation intensity (0–5),
T = fault damage zone thickness, and
T_{max} = maximum damage zone thickness.

The locations of all faults with FZII > 0.5 are summarized in Table T12.

The downhole variation in FZII is illustrated in Figure F87, together with the locations of core discontinuities and the distribution of different styles of faulting. This summary demonstrates that the most intense brittle deformation is associated with vein-related faulting and that brittle deformation intensity is greatest and most pervasive in the Dunite Sequence. The decrease in the pervasiveness of brittle deformation correlates with a general decrease in the level of background alteration with depth in Hole CM2B (see Alteration: Hole CM2B).

The decrease in brittle deformation intensity also correlates with a decrease in abundance of dunite with depth in Hole CM2B. In the transition from the Dunite with Gabbro sequence to the Mantle Sequence, the numerous layers of dunite and harzburgite provide an opportunity to test if deformation intensity correlates with lithology (Fig. F87). In the depth interval between the top of the Mantle Sequence to ~200 m, visual inspection of Figure F87 suggests a strong correlation between the location of dunite and high FZII; this correlation is quantified in the table included in the figure. Deeper than ~200 m, the correlation breaks down; high-intensity faults cut through harzburgite, whereas intervals of dunite remain relatively undeformed. At face value, these observations suggest changes in the relationships among alteration, faulting, and lithology with depth in Hole CM2B.

Orientations of alteration veins

The orientations of 1501 alteration veins were measured. For Hole CM2B, we logged vein orientations using the same approach used for logging veins in ultramafic units in Hole CM1A. Specifically, a representative orientation was measured for each set of parallel veins in a given vein generation within each core section. To facilitate comparisons of similar structural features between Holes CM1A and CM2B, we maintained consistency in the classification of vein generations. In detail, there are subtle differences in how veins were classified by the alteration team and the structure team in Holes CM1A and CM2B; these differences are outlined in Table T13. The differences arise from the observation of a distinct new generation of veins (between V2 and V3) that we classified as “V2.5.” In addition, the alteration team developed a more qualitative classification for veins in the harzburgite sequence, with many crosscutting relationships described as variable. For example, what are identifiable as thick V3 veins and V4 veins have mutually crosscutting relationships. However, through our measurements of these features, we found some systematic relationships in this variability that are summarized in Table T13. Thus, we maintain the same classification for consistency with the observations from Hole CM1A. Finally, structural relationships demonstrate that very thin (<0.2 mm) chrysotile ± calcite veins initially classified as V3 by the alteration team during logging (listed as variable in Table T13) always crosscut V4 veins; we classify these as V5a. Figure F88 illustrates examples of crosscutting relationships.

The dips of veins in Hole CM2B are illustrated in Figure F89. This figure shows that the average dip of V1 and V2 veins does not vary significantly between intervals defined by the location of the most significant faults (with FZII > 0.5) in Hole CM2B. This observation suggests that the rocks cored in Hole CM2B represent a relatively coherent structural unit despite the relatively pervasive brittle deformation observed throughout the core. For this reason, in the plots that follow we do not split out structural intervals on the basis of the brittle deformation intensity.

Histograms of vein dips, sorted by vein generation, are illustrated in Figure F90. In detail, the histograms for V2, V2.5, V3, and V4 veins are all very similar, showing a broad distribution of dips with a mode of ~60°–70°. The V1 veins show a more random distribution with a mode near 45°–50°. These observations suggest that the later stage serpentine veins (up to V4) form by reactivation of preexisting vein sets, consistent with crosscutting relationships observed in the core. The latest generation veins (V5a and V5) show flat distributions with significantly more oriented veins in vertical and horizontal orientations; this observation supports the classification of V5a veins (i.e., the population of very thin chrysotile ± carbonate) as late-stage veins rather than V3 veins.

Orientations of extensional fractures, slickensides, and faults

Extensional fractures with and without mineral vein fill are abundant throughout Hole CM2B; where no clear offset (or slickenlines) was observed, these were classified as extensional fractures. Where slickenside planes with clear slickenline lineations were observed, the sense of shear was recorded. Irregular and/or hemispheric-shaped cracks oriented approximately normal to the core, similar to those observed in Hole CM1A, were also observed in Hole CM2B. As described for Hole CM1A, the shape of these cracks indicates that they grew in a stress field with a symmetric gradient around the hole, suggesting they formed during drilling. These features were noted in the log/brittle spreadsheet, but we do not include them in the analysis of fracture orientations.

The downhole distributions of dips for faults, extensional fractures, and slickensides are shown in Figure F91; there are no systematic variations with depth in the dips of these features. Histograms for the dips of these same features (separated by vein generation for extensional fractures and veins) are shown in Figure F92. The distributions of dips on slickenside planes are similar among V2, V3, and V4 veins, with a mode for each at ~60°. Thus, the mode in the distribution of slickenside dips is similar to that for the veins (Fig. F89), indicating that the apparent bias in slickenside dips within the Layered Gabbro Sequence presented in Hole CM1A (see the **Site CM1** chapter) does not appear in the Hole CM2B ultramafic rocks. In contrast, the histograms for the dips of extensional fractures on these veins (i.e., those for which no slickenlines are observed) all exhibit more random distributions (with a mode near 45°). This observation indicates that the extensional fractures form under a different stress state than the slickensides. Finally, we show that the distribution of dips on faults is also similar to that of the veins and slickensides (Fig. F92), consistent with the observations that vein-related faulting dominates in Hole CM2B.

A total of 226 shear sense indicators on slickensides were recorded (Table T10), 205 with measurable plunge (Fig. F93). As observed for Hole CM1A (see **Structural geology** in the **Site CM1** chapter), there is no systematic variation in dip with depth or in the distribution of reverse, normal, and strike-slip displacement features. This suggests that deformation on the networks of faults and veins in Hole CM2B is not particularly coherent. However, the high fraction of low-angle slickenline plunges indicates that strike-slip displacements are significant.

The relatively long intervals of continuous cores recovered in Hole CM2B (Fig. F86) provide an opportunity to analyze structural relationships in more detail. Lower hemisphere stereonets of structural features in the longest continuous interval (173–212 m) are shown in Figure F94. While acknowledging that the data remain rather scattered, two trends are apparent. First, similar concentrations of poles to slickensides, faults, and harzburgite foliations plunge ~30°–50° to the southwest (indicating planes dipping to the northeast) in the CRF. Second, a broad distribution of poles to mafic magmatic veins, faults, and slickensides are all orientated on a relatively steeply dipping plane striking northwest–southeast, indicating that these features all dip relatively steeply from the southeast, through the southwest, to the northwest. These relationships indicate that the brittle deformation features (veins and faults) form on material heterogeneities (magmatic veins and high-temperature foliations). The data set was further split into slickensides showing either reverse or normal sense of shear (Fig. F94B); no clear trends emerge beyond those described above.

In Figure F94, we also illustrate the orientations for the entire data set of V4 veins and slickensides on V4 veins (Fig. F94C, F94D). If the relative orientation of cores across discontinuities is random, a small-circle girdle of poles to these features should emerge. However, maxima are apparent for the orientations of these features in the CRF in the same orientations as those determined for the longest section of continuous core (with some smearing along the small-circle girdle). This observation suggests the following:

- The basis for core cutting in the field was a consistent measure of the orientation of the core in the geographic reference frame (indicating structural continuity in the hole). This likely reflects the importance of initial heterogeneities in controlling the orientation of veins.
- By application of paleomagnetic data, the cores can be reoriented and preferred orientations of structural features will emerge—allowing further investigation of structural history.

Summary

Here we provide an overview of the key observations from the high-temperature history recorded in Hole CM2B, the lower temperature history of Hole CM2B, and an integrated summary of the main structural conclusions bases on correlations between structures observed in both Holes CM1A and CM2B (with speculative interpretations in italics and uncertain temporal relationships denoted with "?"). A schematic cross-section illustrating structural relationships between Holes CM2B and CM1A is presented in Figure F95.

Key observations from high-temperature structures

- Gabbro layers in the Dunite with Gabbro Sequence show both increasing and decreasing dip as a function of depth.
- The average dips of impregnated dunite in Holes CM1A and CM2B are consistent (46°) with each other—showing a difference of ~30°—due to the different drill orientations.
- The dip angle of harzburgite/dunite lithologic contacts is relatively constant throughout Hole CM2B (average = 57° ± 7°) and is consistent with the dip measured for Hole CM1A core (21° + 30° to account for the different plunge of Hole CM1A).
- The average thickness of dunite layers in the Mantle Sequence is ~1 m in both Holes CM1A and CM2B.
- The dunite appears annealed, with few subgrain boundaries, little undulose extinction, and abundant 120° triple grain junctions.
- Harzburgite texture varies between apparently annealed and weakly deformed; evidence for crystal-plastic deformation includes alignment of pyroxenes (which commonly show annealed recrystallized grains), spinel lineations, and optical evidence for an olivine crystal-preferred orientation (though olivine also appears annealed).
- Only 20 cm of protomylonite was observed near the bottom of the core a few meters above the major carbonated fault. Therefore fault-related crystal-plastic deformation is largely absent from both Holes CM2B and CM1A.

Key observations from low-temperature structures

- Deformation features during cooling between magmatic and greenschist-grade conditions are essentially negligible.
- Greenschist-grade veins and associated semibrittle deformation are the highest temperature brittle deformation features observed in Hole CM2B.
- Significant brittle deformation is associated with the development of veins and postdates the formation of mesh-textured serpentinite.
- The similar dips of veins, slickensides, and faults further support the role of vein formation as a key step in the evolution of brittle deformation.
- Structural relationships indicate that brittle deformation is focused at lithologic contacts (e.g., between gabbro and ultramafic rock), and within the ultramafic sequences, there is a tendency for brittle deformation to be more intense in dunites than in harzburgites.
- Veins have a broad distribution of orientations, but (where oriented in continuous core) show concentrations parallel to gabbroic veins and harzburgite foliations.
- The generally consistent orientation of these features throughout Hole CM2B suggests that the cored intervals are a relatively coherent structural body.
- Whereas fault zones are observed throughout both Holes CM1A and CM2B, the consistent lithologic stratigraphy and structural relationships observed by correlation between the holes suggests the faults only accommodated modest displacements.

Summary of inferred structural history (combining Holes CM1A and CM2B)

1. Formation of dunite layers in the mantle and development of high-temperature mantle fabric during corner flow.

2a. Formation of the Dunite Sequence and development of chromitite veins.

2b. Formation of the Layered Gabbro Sequence.

3a. Annealing of mantle deformation fabrics.

3b. Intrusion of thin (few meters thick) foliated gabbro into the Dunite with Gabbro Sequence.

3c. Intrusion of wehrlites/dunites into bottom of the Layered Gabbro Series.

3d. Boudinage and ductile (folding) and brittle deformation of the gabbro sequence during plate spreading to form cycles of fanning foliation/layering in the gabbros and the rare extensional faulted horizon in the gabbro in the Dunite with Gabbro Sequence.

4. Small intrusive gabbros/gabbro veins crosscut layered gabbros.
5. Sparse high-temperature amphibole veins in uppermost section indicate some but limited high-temperature metamorphism and water input.

6a. Very limited formation of sparse, small-displacement crystal-plastic/semibrittle fault zones (300°–350°C?).

6b. Serpentinization and formation of mesh texture in the ultramafic rocks—*Oceanic deformation re-*

lated to crustal cracking during flexure at the initiation of obduction?

6c. Formation of V1 and V2 fractures/veins.

7a. Brittle and semibrittle high-angle faulting, including cutting the crust/mantle boundary. Associated greenschist (e.g., chlorite/tremolite alteration of gabbroic bodies and serpentine veins in ultramafic sequences)—*Oceanic deformation related to obduction?*

7b. Formation of talc-carbonate veins and associated semibrittle deformation at the base of Hole CM2B—*during obduction? Are Si and C derived from underlying carbonate platform (Hawasina)?*

8. Formation and brittle deformation associated with V3 and V4 veins.

9. Late fault motion focused on networks of V4 fractures and slickensides, cutting V1, V2, and V3 veins, and overprinting greenschist-grade deformation fabrics (including semibrittle deformation textures in talc-rich carbonated peridotite)—*Post-obduction deformation?*

10. Formation of latest calcite veins and 9 m thick weathering profile at the top of Hole CM2B—*at the weathering surface?*

Geochemistry: Hole CM2B

We performed chemical analyses on 67 samples collected from Hole CM2B, including 2 alluvium samples, 2 gabbros, 1 anorthosite, 2 wehrlite, 28 dunites, 31 harzburgites, and 1 carbonate vein. A total of 38 samples were selected by the shipboard science party as representative of the different lithologies recovered from the Hole CM2B. A thin section was taken systematically at the top of each geochemistry sample (see **Thin section descriptions**). A total of 29 samples were collected on site every 10 m during operations; they were powdered and analyzed at the University of Southampton (see **Geochemistry** in the **Methods** chapter). A thin section was taken for each on-site sample, and XRD analyses were performed on each on-site geochemistry sample for detailed mineral characterization.

Shipboard and on-site ignited powders were analyzed using XRF for determination of major and trace element concentrations, and gas chromatography was performed on non-ignited powders for volatile element contents determination (H_2O, CO_2, and inorganic carbon). Analytical procedures and precision and accuracy of the methods are described in detail in **Geochemistry** in the **Methods** chapter. Additional trace element concentrations in whole rock and pyroxenes were determined by laser ablation–inductively coupled plasma–mass spectrometry (LA-ICP-MS) (see **Geochemistry** in the **Methods** chapter). Whole-rock major, trace, and volatile element contents are all reported in Table **T14**. Whole-rock, clinopyroxene, and orthopyroxene LA-ICP-MS trace element compositions are reported in Tables **T15**, **T16**, and **T17**, respectively.

Loss on ignition, CO_2, and H_2O contents

The geochemistry samples from Hole CM2B have loss on ignition (LOI) values ranging 1.66–23.0 wt% (Figs. **F96**, **F97**). These variations are related to the lithology of the samples, resulting in the addition of variable amounts of volatile contents to the original assemblage. Dunites are characterized by an average LOI of 14.2 wt%. The rocks interspersed within the dunites (wehrlites, gabbro, olivine gabbro, and anorthosite) have LOIs ranging 1.66–11.42 wt%, with the lower values recorded in the gabbro and the olivine-gabbro and the highest in the two wehrlites and the anorthosite. Mantle harzburgites have average LOI of 11.5 wt%, excluding the deepest of these samples (127Z-3, 61.0–65.0 cm; 295.69 m), which is carbonate vein bearing and has LOI = 23 wt%; this is similar to the two alluvium samples from the top of Hole CM2B (4Z-1, 17.5–24.0 cm, and 6Z-1, 39.0–45.0 cm; 5.80 and 8.81 m depth; LOI = 12 and 22 wt%, respectively).

Concentrations of H_2O measured in Hole CM2B samples correlate with the measured LOI values. However, as in Hole CM1A, H_2O values appear systematically higher compared to LOI values. Dunites have the highest H_2O concentrations (<31.3 wt%). The average H_2O concentration in dunite is 28.3 wt%, excluding one sample with a lower value (37Z-3, 31.0–36.0 cm; 70.42 m depth; LOI = 11 wt%). The average H_2O concentration in harzburgite is 23.5 wt%, excluding two samples with lower H_2O content (<10.7 wt%). Water content in wehrlite is similar to harzburgites. Water concentrations in dunites and harzburgites decrease slightly towards the bottom of the core.

Concentrations of CO_2 measured in Hole CM2B samples range 0.1–19.5 wt%. The highest CO_2 concentrations are recorded in one of the two alluvium samples from the top of the core (6Z-1, 39.0–45.0 cm; 8.81 m; CO_2 = 13.1 wt%), the carbonate vein (127Z-3, 61.0–65.0 cm; 295.69 m; CO_2 = 18 wt%), and the carbonate-rich harzburgite (129Z-1, 5.0–10.0 cm; 299–674 m; CO_2 = 19.5 wt%) from the bottom of the core. The high CO_2 value is consistent with the high carbonate contents in the samples.

Whole-rock major and minor elements

Two gabbros from the Dunite with Gabbro Sequence in Hole CM2B (74.26–83.89 m) were selected for chemical analysis; the olivine gabbro (41Z-1, 15.0–20.0 cm; 74.78 m) and the gabbro (44Z-2, 40.0–45.0 cm; 78.95 m). The olivine gabbro is characterized by Mg# = 85 and TiO_2, CaO, Al_2O_3, Cr, and Ni contents of 0.12 wt% TiO_2, 18.8 wt% CaO, 16.0 wt% Al_2O_3, 869 ppm Cr, and 288 ppm Ni. The gabbro is characterized by Mg# = 80, lower than the olivine gabbro sample. This gabbro displays TiO_2, Al_2O_3, CaO, Cr, and Ni contents of 0.12 wt% TiO_2, 17.5 wt% Al_2O_3, 16.6 wt% CaO, 800 ppm Cr, and 252 ppm Ni (Figs. **F97**, **F98**).

Peridotites from Hole CM2B are characterized by bulk-rock compositions reflecting significant hydrothermal alteration and an abundance of alteration phases. A total of 2 wehrlites, 28 dunites, and 31 harzburgites from the CMTZ (Dunite and Dunite with Gabbro Sequences) and Mantle Sequence were selected for chemical analysis. Dunites represent the second most abundant lithology in Hole CM2B (27.51%; see **Igneous petrology: Hole CM2B**).

Dunite intervals occur throughout all lithologic sequences of Hole CM2B. The contact between the Dunite Sequence and the Dunite with Gabbro Sequence, located at 74.26 m depth, is marked by a deformation contact. Dunites from the Dunite Sequence have lower Mg# (mean = 88.4) compared to the dunites from the Dunite with Gabbro Sequence (mean = 89.2). Dunites from the Mantle Sequence display the highest Mg# values (mean = 89.9). CaO, Al_2O_3, and TiO_2 compositions of dunite from the three sequences are similar (with the exception of Sample 35Z-3, 16.0–23.0 cm), ranging 0.02–0.57 wt% CaO, 0.22–5.60 wt% Al_2O_3, and 0.02–0.06 wt% TiO_2. The Cr and Ni contents in dunite are different from the other chemical elements; the successive increasing and decreasing trends show a well-defined zigzag pattern for Ni and less defined zigzag for Cr and Zn (i.e., Ni decreases from 2554 to 1691 ppm at 4.99–70.42 m, increases from 1691 to 2607 ppm at 70.42–115.6 m, and then decreases again from 2607 to 2304 ppm at 115.6–139.98 m) (Fig. **F97**).

Wehrlite occurs as a minor lithology in dunitic units. Two samples (42Z-1, 6.0–12.0 cm, and 42Z-2, 47.0–51.0 cm; 77.71 and 78.96 m) were analyzed. Mg# = 86.3 and 86.7, CaO = 4.6 and 1.8 wt%, Al_2O_3 = 5.3 and 2.1 wt%, and TiO_2 = 0.03 and 0.04 wt%, respectively. The two wehrlites show similar Cr and Ni contents, with Cr = 2672 and 1954 ppm and Ni = 1491 and 1522 ppm, respectively.

The anorthosite Sample 69Z-4, 22.0–29.0 cm (140.24 m) has Mg# = 88.2 and CaO = 16.0 wt%, as well as Al_2O_3 = 11.7 wt%, TiO_2 = 0.38 wt%, Cr = 1386 ppm, and low Ni = 765 ppm.

The carbonate vein 127Z-3, 61.0–65.0 cm (295.75 m) has Mg# = 92.3, CaO = 17.9 wt%, Al_2O_3 = 0.47 wt%, and TiO_2 = 0.08 wt%, as well as high Ni (2473 ppm) and low Cr (1109 ppm) contents.

Harzburgite is the most abundant lithology in the Mantle Sequence of Hole CM2B (38.43%, see **Igneous petrology: Hole CM2B**). The Mg# in Hole CM2B harzburgites ranges 89.8–92.0. CaO, Al_2O_3, TiO_2, Cr, and Ni contents range 0.61–5.3 wt% CaO, 0.51–0.87 wt% Al_2O_3, 0.002–0.072 wt% TiO_2, 2204–2978 ppm Cr, and 1832–2434 ppm Ni (Fig. **F97**).

Along the Mantle Sequence, TiO_2 and Al_2O_3 contents do not show any systematic change with depth. CaO concentration also varies very little with depth in the Mantle Sequence, with the exception of Samples 104Z-3, 5.0–10.0 cm (gabbro from 234.3 m; CaO = 22.5 wt%), 69Z-4, 22.0–29.0 cm (anorthosite from 140.24 m; CaO = 16.0 wt%), 129Z-1, 5.0–10.0 cm (carbonate vein-bearing harzburgite from 299.67 m; CaO = 5.30 wt%), and 121Z-2, 0.0–5.0 cm (carbonate vein from 295.69 m; CaO = 17.9 wt%).

Hole CM2B dunites and harzburgites have similar major and minor chemical compositions to the same lithologies sampled in Hole CM1A and other Oman ophiolite samples. FeO and MgO variations are consistent with Hole CM1A samples and published data from Oman ophiolitic peridotites (Fig. **F99**). The Hole CM2B dunites plot above the mantle fractionation array in the MgO/SiO_2 vs. Al_2O_3/SiO_2 diagram, whereas the Hole CM2B harzburgites and some impregnated dunites plot below the mantle fractionation array.

Whole-rock trace elements

Dunites

Dunites from Hole CM2B exhibit variable trace element contents, with Ni, Co, and Cr concentrations ranging 866–3852 ppm Ni, 15.6–177 ppm Co, and 1442–5978 ppm Cr (Fig. **F100**). Yb_{CN} is generally restricted to values ranging 0.13–0.20, with the exception of one sample that has a value of 0.33. Three of the six dunites (11Z-1, 34.0–39.0 cm; 18Z-2, 77.0–83.0 cm; 35Z-2, 1.0–5.0 cm; 14.99, 34.27, and 66.29 m) show spoon-shaped rare-earth element (REE) patterns with depletion from heavy REE (HREE) to mid-REE (MREE) (Gd_{CN}/Yb_{CN} = 0.15–0.53) and a near-flat LREE–MREE segment (La_{CN}/Sm_{CN} = 0.73–1.0). A fourth dunite sample (15Z-4, 38.0–43.0 cm; 26.26 m) shows the same MREE depletion (Gd_{CN}/Yb_{CN} = 0.47), as well as LREE enrichment relative to MREE (La_{CN}/Sm_{CN} = 1.7). Multielement patterns for these 4 dunites show strong positive anomalies in U (U_{PMN}/La_{PMN} = 2.7–10.1), Pb (Pb_{PMN}/Ce_{PMN} = 2.2–22.8), and Ti (Ti_{PMN}/Gd_{PMN} = 1.8–8.6). The dunite Sample 35Z-3, 16.0–23.0 cm (6.72 m), is characterized by enrichment in MREE relative to HREE (Gd_{CN}/Yb_{CN} = 1.2) and LREE (La_{CN}/Sm_{CN} = 0.67), with a strong positive Eu anomaly (Eu/Eu* = 3.6), and by strong depletion in high–field strength elements (HFSE) relative to REE (Nb_{PMN}/La_{PMN} = 0.19; Zr_{PMN}/Sm_{PMN} = 0.09). The dunite sample with the higher Yb content (27Z-1, 13.0–18.0 cm; 56.56 m) displays a REE pattern showing a flat HREE–MREE segment (Gd_{CN}/Yb_{CN} = 0.97) followed by depletion from MREE to LREE (La_{CN}/Sm_{CN} = 0.17). Both negative and positive Eu anomalies (ranging 0.74–3.6) are observed with no systematic relationship with the shape of the REE pattern.

Pyroxene minor and trace elements

Clinopyroxene

A clinopyroxene in one olivine gabbro from Hole CM2B (Sample 41Z-1, 15.0–20.0 cm; 74.79 m) shows Ti = 1357 ppm and Yb_{CN} = 3.7 (Fig. **F101**). Its REE pattern is characterized by a slight enrichment in MREE relative to HREE (Gd_{CN}/Yb_{CN} = 1.2), a strong depletion in LREE relative to MREE (La_{CN}/Sm_{CN} = 0.05; La_{CN}/Yb_{CN} = 0.04), and a slight negative Eu anomaly (Eu/Eu* = 0.72). The multielement pattern shows a clear depletion in HSFE relative to MREE, with Zr_{PMN}/Sm_{PMN} = 0.18.

A clinopyroxene in one anorthosite (Sample 69Z-4, 22.0–29.0 cm; 14.39 m) was analyzed for trace element composition. Ti and Yb_{CN} contents are higher than in the olivine gabbro, with values of 2805 ppm Ti and 1.0 Yb_{CN}, respectively. The shape of its REE pattern is similar to that of the olivine gabbro regarding the HREE segment that displays a slightly negative slope (Gd_{CN}/Yb_{CN} = 1.1). However, this sample presents a less important depletion in MREE (La_{CN}/Sm_{CN} = 0.18; La_{CN}/Yb_{CN} = 0.16) and a slightly more important negative anomaly in Eu (Eu/Eu* = 0.63). The anorthosite multielement pattern shows moderate depletion in HFSE relative to MREE in comparison to the olivine gabbro (Nb_{PMN}/La_{PMN} = 0.16; Zr_{PMN}/Sm_{PMN} = 0.54) as well as a negative Sr anomaly (Sr_{PMN}/Nd_{PMN} = 0.20).

Orthopyroxene

Orthopyroxenes in 2 dunites from Hole CM2B (Samples 57Z-3, 50.0–55.0 cm [115.67 m], and 89Z-1, 6.0–11.0 cm [191.70 m]) contain Co, Ti, Mn, and Yb_{CN} contents ranging 47.5–54.9 ppm Co, 86.9–502 ppm Ti, 936–1322 ppm Mn, and 1.0–3.2 Yb_{CN} (Fig. **F101**). In few samples, MREE and LREE contents were determined despite their very low concentrations. REE patterns show continuous depletion from HREE to MREE (Er_{CN}/Yb_{CN} = 0.33–0.92) to LREE (La_{CN}/Sm_{CN} = 0.07 in 1 sample; La_{CN}/Yb_{CN} ~ 0.1 in 2 samples).

Orthopyroxenes in harzburgites contain more variable to higher Co (0.77–117 ppm) and Mn (839–1610 ppm) concentrations and lower Ti (4.5–302 ppm) and Yb_{CN} (0.16–1.8) contents than in dunites. REE patterns show a strong depletion from HREE to MREE, similar to higher than in dunites, with a Er_{CN}/Yb_{CN} ratio varying 0.12–0.68. Multielement patterns show low Zr content (Zr_{PMN} = 0.001–0.039) and quite high large-ion lithophile elements (LILE), Th, and U contents (e.g., Zr_{PMN} = 0.03–0.08) relative to MREE (Ce_{PMN} = 0.001–0.01; Yb_{PMN} = 0.05–0.61).

Paleomagnetism: Hole CM2B

Remanent magnetization

Magnetic remanence measurements were made at the University of Iceland in 2019 on discrete sample cubes taken from the working half cores from Hole CM2B. A total of 113 discrete samples were measured, of which approximately one-third (29 samples) were thermally demagnetized while all others were subjected to stepwise alternating field (AF) demagnetization in tumbling mode to isolate the characteristic remanent magnetization (ChRM) direction. Some irregularly shaped and broken samples were omitted from measurements.

Natural remanent magnetization (NRM) intensity ranges 4.2 × 10^{-5} to 39 A/m (geometric mean = 2.2 A/m) (Fig. **F102**). NRM magnitudes in the upper half of the hole vary greatly but are generally greater than the site mean value and decrease progressively with depth to ~150 m. Remanence intensities are more consistent and relatively low in the lower half of the core. NRM orientations are nearly all negatively inclined (Fig. **F103**). Principal component analysis of the demagnetization data was used to identify distinct remanence components.

A stable ChRM that trends to the origin at the highest field and temperature steps was identified in all but 2 samples measured. The ChRM inclinations are consistently negative and very similar to those of the NRM, with inclinations generally scattered between 0° and –60° (Fig. **F103**). The ChRM inclinations resulting from thermal demagnetization and AF demagnetization are very similar, indicating that both demagnetization methods isolated the same remanence component. Mean inclinations calculated using the Arason and Levi (2010) maximum likelihood method give a mean inclination for the highest temperature/coercivity component of –26.1° (k = 21.1, $\alpha95$ = 3.0°, n = 111). In comparison, the inclination-only statistics for NRM orientations yield a very similar mean inclination of –22.6° (k = 12.1, $\alpha95$ = 4.0°, n = 113).

A secondary component with lower coercivity or unblocking temperatures and a distinct orientation from the ChRM was isolated in 58 samples, here termed the "soft" component. Approximately half of the samples contained only a single remanence component (Figs. **F104A**, **F105A**). The orientation of the soft component varies greatly, but negative inclinations are slightly more abundant in the upper 150 m, whereas the lower 150 m contains predominantly positive inclinations of variable steepness (Fig. **F103**). This soft secondary remanence component was identified more frequently in thermally demagnetized samples than in AF-demagnetized samples.

All samples subjected to AF demagnetization were effectively demagnetized to <90% of their NRM intensity by 100 mT (Fig. **F104**). Median destructive field (MDF) values range 4.0–37 mT (mean = 21 mT) (Table **T18**). MDF values are notably lower in the uppermost 100 m of the hole (mean MDF = 16 mT) than in the lower portion of the hole (mean MDF = 23 mT) (Fig. **F106**). Many samples exhibited either a single vector component or a very small secondary remanence that was removed after the first few demagnetization steps.

Thermal demagnetization was complete in the majority of Hole CM2B samples by 580°C (Fig. **F105**). A distinct decrease in remanence intensity was observed of ~580°C in most samples (Fig. **F105B**), which was interpreted as the ChRM. This unblocking temperature is close to the magnetite Curie temperature of 580°C, which indicates highly stoichiometric magnetite as the magnetic mineral phase carrying a stable remanence in Hole CM2B. Median destructive temperatures (MDT) range 373°–543°C (mean = 500°C), with lower MDT values occurring slightly more frequently in the uppermost 100 m of Hole CM2B (Fig. **F106**). Nearly all thermally demagnetized samples exhibit conspicuous deviations in the remanence directions at temperature steps of 400°, 450°, and 475°C, which appear as jogs in the otherwise linear demagnetization paths on orthogonal vector diagrams (Fig. **F105B**). The reason for these anomalous orientations is not clear, but since the deviations do not occur in a consistent direction, they are unlikely to be due to instrument errors in either the furnace or the magnetometer. As several samples display a drop in remanence intensity around this temperature interval, it is possible that mineralogical changes induced by thermal alteration of the samples influenced the remanence directions at these steps. This portion of the data was not used to identify the remanence component vectors during analysis. Changes in magnetic susceptibility measured after each heating step were complex and varied across samples and across temperatures steps.

Magnetic susceptibility

Bulk magnetic susceptibility

Volume susceptibility values range 0.19–250 × 10^{-3} SI (Fig. **F102**; Table **T19**) (geometric mean = 20 × 10^{-3} SI). The downhole profile of bulk magnetic susceptibility is similar to that of NRM intensity, suggesting that the variation in both properties with depth is controlled by the concentration of magnetic minerals rather than differences in magnetic grain size and mineralogy. As with NRM intensity, bulk susceptibilities in the upper 100 m are significantly higher than the average values for the hole, with two narrow intervals of exceptionally high susceptibility between 50 and 100 m depth.

The Koenigsberger ratio, *Q*, in Hole CM2B ranges 0.10–34 (geometric mean = 3.8). The majority of samples exhibit $Q > 1$ (Fig. **F102**; Table **T19**), indicating that the total in situ magnetization of the rocks is controlled by remanent magnetization for much of Hole CM2B. The relatively high mean Q values indicate the presence of strong, stable remanence-carrying magnetic minerals.

Anisotropy of magnetic susceptibility

Anisotropy of magnetic susceptibility (AMS) determinations were performed on all discrete samples prior to stepwise demagnetization to characterize the shape-preferred orientations of magnetic minerals in the core samples. Magnetic fabrics are dominantly characterized by magnetic foliation with an average shape parameter (*T*) of 0.35, indicating oblate anisotropy ellipsoids (Fig. **F107A**). Samples with a relatively high degree of anisotropy ($P' > 1.2$) are almost exclusively oblate (Fig. **F107C**). The degree of anisotropy (P') is generally high throughout the hole (average is nearly 1.18) and is not significantly correlated with bulk susceptibility (K_{mean}) (Fig. **F107B**).

Both K_{max} and K_{int} axis orientations tend to be moderately dipping with mean inclinations of ~27° (Figs. **F107A**, **F108**). K_{min} axes are consistently steeper, with an average inclination of 42. Furthermore, a distinct subvertical maximum in K_{min} orientations is seen in the contoured stereoplot in Figure **F108** in addition to a weak girdle along the ± *Y*-direction in the CRF. Magnetic fabric orientations do not vary systematically with depth.

Physical properties: Hole CM2B

Physical properties of ultramafic and gabbroic rocks from Hole CM2B were characterized through a series of measurements on whole-round sections, section halves, section-half pieces, and discrete samples (see **Physical properties** in the **Methods** chapter). All whole-round sections were run through the XCT scanner and measured for gamma ray attenuation (GRA) density, magnetic susceptibility (MS), noncontact electrical resistivity (NCR), and natural gamma ray radiation (NGR) on the Whole-Round Multisensor Core Logger (MSCL-W). Whole-round *P*-wave velocity was not measured because of a mechanical issue of the transmitter. We also measured point magnetic susceptibility (MSP) and reflectance spectroscopy and colorimetry (RSC) with the Split Half Multisensor Core Logger (MSCL-C) and linescan color image with the Multisensor Core Logger (MSCL-I) on the split surface of archive halves. Thermal conductivity was measured on section-half pieces. Compressional wave (*P*-wave) velocity (V_P), electrical resistivity (IMP), and density and porosity (MAD) were measured on discrete minicube samples

(20 mm × 20 mm × 20 mm). MAD measurements were also conducted on some irregular shaped discrete samples. The rock names reported in data tables correspond to the primary lithologies described in **Igneous petrology: Hole CM2B** (Fig. F3; Table T3).

Whole-round and section-half measurements

A total of 408 whole-round and archive-half sections from Hole CM2B were measured from Core 1Z to 129Z. The downhole data plot is shown in Figure F109 for whole-round measurements and Figure F112 for half-round measurements. Data are summarized in Table T20, and all data are shown in Supplemental Tables ST8 and ST9.

X-ray computed tomography

XCT was continuously logged for all 408 whole-round core sections recovered from Hole CM2B. The XCT number of minerals is essentially a function of the density and chemical composition of the sample. Hence, XCT numbers in the core sections result from a combination of their mineral composition and pore structure in a voxel (0.625 mm × 0.175 mm × 0.175 mm). Figure F110 shows examples of XCT images from Sections 40Z-1, 58Z-3, 102Z-3, and 127Z-4. An XCT image of the archive-half split surface with XCT number represented on a color scale was generated for every section. The average and the mode of XCT numbers for every scan slice (0.625 mm thick) were also computed and plotted downhole (Fig. F109F). Average XCT number is susceptible to the effect of cracks in the core section because the XCT number of air is significantly lower than that of minerals (XCT number of air ~ –1000; see **Physical properties** in the **Methods** chapter). On the other hand, the mode of XCT number tends to reflect a representative lithology in a scan slice (e.g., "zebra stripe" gabbro/dunite layer in Section 40Z-1: Fig. F110A), although it overlooks some minor but dense minerals such as Cr spinel (e.g., Section 58Z-3: Fig. F110B).

Intact gabbro, dunite, and harzburgite have average XCT numbers of ~3500, ~3000, and ~3200, respectively. Cr spinel ($[Fe,Mg]Cr_2O_4$)-rich layers yield high XCT numbers > 4000. Lower CT numbers for dunite and harzburgite than gabbroic rocks reflects the high degree of serpentinization of peridotites and/or the porous nature of serpentinite intervals in Hole CM2B. Harzburgite shows higher XCT numbers than dunite. This could suggest that the degree of serpentinization in harzburgite is slightly less than that of dunite or reflect the higher abundance of orthopyroxene in harzburgite layer.

Because XCT number of a core section depends on mineral composition and porosity in core sections, the trends of the average and the mode of XCT number in the downhole plot clearly follow that of GRA density (Fig. F109B–F109F). Figure F111A shows the correlations between XCT number > 2000 and GRA density > 2.0 from Hole CM2B. All lithologies in the figure show a relation between XCT number and GRA density. These correlations can be controlled by several factors, such as modal abundances of low-density minerals (e.g., serpentine), high atomic number elements in minerals (e.g., calcium in diopside, iron in magnetite, and chromium in Cr spinel), and pore structure. Overall, variability in the downhole trend of XCT numbers reflects lithologic and structural variations observed in Hole CM2B.

Colorimetry

RSC data were obtained for 408 sections of archive halves (Cores 1Z–129Z). The specular component included (SCI) setting was used in measurement of the Hole CM2B cores; this setting provides data that are closer to the actual color than those of the specular component excluded (SCE) setting (see **Physical properties** in the **Methods** chapter). Color data acquired from reflectance spectroscopy and high-resolution images can provide insights into the variability of different lithologic units recovered from Hole CM2B. Lightness (L*) and chromaticity (a* and b*) variables were generated from the reflected light collected through the spectrophotometer every 2 cm. High L* value indicates lighter colors, with 0 representing black and 100 representing white. Directions toward more +a* denote a shift toward red from green, whereas those toward +b* depict a shift toward yellow from blue. High-resolution (100 pixels/cm) half-section images produced by the MSCL-I provide an alternative source of 2-D color data.

A downhole plot of color parameters is shown in Figure F112. The values of reflectance and chromaticity parameters a*, b*, and L* range –5.53–10.62, –5.48–24.52, and 6.28–83.71, respectively. The CMTZ tends to show positive a*, negative b*, and L* ~ 25; the Mantle Sequence shows negative a*, positive b*, and L* ~ 40. These values mean that the colors of cores in the CMTZ are more brownish (reddish), bluish, and darker, whereas those of the Mantle Sequence are more greenish, yellowish, and brighter compared with each other. This feature changes gradually from ~100 m depth in the Dunite with Gabbro Sequence to the Mantle Sequence. Difference of color spectrum between dunite and harzburgite could indicate that harzburgite is less serpentinized and contains more pyroxene than dunite. Gabbroic layers in the Dunite with Gabbro Sequence show more or less similar a*, b*, and L* values: a* ~ –3, b* ~ 3, and L* ~ 60.

Gamma ray attenuation density

GRA measurement was conducted on 408 sections at a spacing of 4 cm. Data are summarized in Figure

F109B and Table T20. GRA density and the standard deviation (1σ) of gabbroic and intact ultramafic rocks are 2.86 ± 0.42 g/cm³ and 2.55 ± 0.44 g/cm³, respectively (Table T20). These low densities for ultramafic rocks (~2.55 g/cm³) suggest that olivine (density ~ 3.3 g/cm³) in these rocks is nearly 100% serpentinized (density of lizardite serpentine: ~2.58 g/cm³; Mellini and Zanazzi, 1987) and there is some extent of porosity in the intact cores throughout Hole CM2B. GRA densities of major lithologies in Hole CM2B are 2.91 ± 0.39 g/cm³ for gabbro, 2.82 ± 0.84 g/cm³ for olivine gabbro, 2.44 ± 0.46 g/cm³ for dunite, 2.66 ± 0.39 g/cm³ for harzburgite, and 2.69 ± 0.50 g/cm³ for wehrlite. The GRA density of talc and carbonated harzburgite occurring deeper than ~294 m is 2.87 ± 0.11 g/cm³. The depth profile of bulk density obtained by discrete sample measurements (edged symbols in Fig. F109B) seems to follow nearly the upper bound of the GRA depth profile.

Electrical resistivity

NCR data indicate that the cores from Hole CM2B are resistive (Fig. F109D), especially gabbros in the Dunite with Gabbro Sequence and harzburgites in the Mantle Sequence. Most readings in these sequence are saturated and equal to the maximum measurable value (~85 Ω·m); therefore, actual averages of NCR for these sections should be higher than those shown in Table T20. In contrast, dunites and wehrlites in the CMTZ are less resistive, ~5 Ω·m on average. These low-resistivity intervals are probably due to the high abundance of conductive phases such as magnetite in the strongly to completely serpentinized dunites. There are negative peaks of low resistivity in the Mantle Sequence, which are also recognized in magnetic susceptibility as positive peaks (in detail, see **Whole-round and half-round magnetic susceptibility**, below). NCR in the Dunite Sequence (average = 4.69 Ω·m; Table T20) is lower than that in the Mantle Sequence (average = 9.60 Ω·m; Table T20). This could be explained by differences in the modal abundances of the conductive phase (i.e., magnetite) and nonconductive phase (e.g., fresh olivine and orthopyroxene) in each sequence. We note that NCR is systematically ~20× lower than electrical resistivity measured in discrete samples (Figs. F109D, F113F). This can be due to the low accuracy of the NCR measurements for high-resistivity samples because the instrument is designed for measuring resistivity in porous and conductive ocean wet sediments. However, the overall characteristics of the NCR depth profile are similar to those of the discrete sample data.

Whole-round and half-round magnetic susceptibility

MS of whole-round core sections before splitting was measured using the MSCL-W with a 125 mm loop sensor. MSP of archive-half sections was measured using the MSCL-C with a contact sensor probe. Because of instrument problems, MSP measurements were only carried out to Section 37Z-1 (68.7 m depth) in Hole CM2B (supplemental Table ST9). Whole-round MS (WRMS) values are shown in downhole plots (Fig. F111), and MSP and colorimetry are shown in Figure F112. MS of the gabbroic layer averages ~900 × 10^{-5} SI, whereas averages of ultramafic layers are 6270 × 10^{-5} SI for dunite and 2265 × 10^{-5} SI for harzburgite. There is a very large change in the average MS between the CMTZ and the Mantle Sequence, from 6270 × 10^{-5} SI to 2265 × 10^{-5} SI. Although the background MS value in the Mantle Sequence is nominally low (~1000 × 10^{-5} SI), zones yielding high-MS spikes are irregularly present throughout the Mantle Sequence, with peak MS values mostly higher than 10,000 × 10^{-5} SI. Similarly, negative peaks in NCR are observed at the same depths where positive peaks of MS are observed. Figure F111C–F111E shows the correlation between MS and the inverse of NCR (i.e., electrical conductivity) measured at the same depths. MS and inverse NCR show a somewhat linear correlation regardless of lithology. This suggests the presence of high-MS and conductive minerals, such as magnetite, in the peaks in ultramafic layers. Interestingly, these high-MS and low-resistivity spikes also appear to coincide with high intensities of fault zones (Fig. F86), veins (Fig. F81, and alteration (Fig. F44). There could be two explanations for magnetite concentrations along the fault zone. First is that only magnetite-rich veins ("serpentine-magnetite vein" as described in **Alteration: Hole CM2B**) contribute to the high-MS and low-resistivity spikes and these veins do not contribute significantly to the total vein intensity, and that magnetite-rich veins typically exist along the fault zones. The second hypothesis is that the fault zones are the location of very intense alteration that is enough to lead to overgrowth on preexisting magnetite grains or even alter Cr-spinel. The total alteration intensity is nominally high throughout Hole CM2B (>65%; see **Alteration: Hole CM2B**), and very strong alteration is common in many sections of the core.

Natural gamma ray radiation

NGR in the Mantle Sequence is higher than that in the CMTZ, but NGR in Hole CM2B is generally low (average = 3.7 count/s; Fig. F109E). There seems to little relationship with other physical property data and structural observations.

Discrete sample measurements

P-wave velocity

P-wave velocity was measured on 111 cube samples from Hole CM2B along the 3 principal directions *x*, *y*, and *z* in the CRF (see Table T22; Fig. F113A). *P*-wave velocity ranges 3.56–7.18 km/s (average = 5.44 ± 0.59 km/s). Gabbro samples exhibit higher velocities (maximum = 7.00 km/s). In contrast, dunite samples have significantly lower velocity (as low as 3.91 km/s; average = 5.19 ± 0.37 km/s). Harzburgite also has relatively low and widely variable velocity (range = 3.56–6.83 km/s; average = 5.53 ± 0.58 km/s). The lowest velocity among the cube samples is in a harzburgite with cracks (3.56 km/s). Wehrlite and rodingitized gabbro samples have high velocities (6.12 and 6.19 km/s, respectively). *P*-wave velocity of dunite samples at the bottom of the Dunite Sequence (I) decrease from ~56 m depth to the bottom of the sequence (I) and increase within the Dunite with Gabbro Sequence (II) with depth and sandwiching the gabbro intrusion that has the highest velocity (Fig. F113A). The Mantle Sequence (III) shows higher *P*-wave velocity (average = 5.48 ± 0.57, up to 7.18 km/s), although it is low enough to be consistent with high extents of serpentinization.

Density and porosity

Bulk density, grain density, and porosity were calculated from measurements on 112 cubic (20 mm × 20 mm × 20 mm) and 2 irregularly shaped samples taken from the working half sections from Hole CM2B, ~1 sample per core, and where possible reflecting lithologic and alteration variations (Table T21; Fig. F113B–F113E). Average bulk and grain densities of cube samples from Hole CM2B are 2.66 ± 0.11 and 2.70 ± 0.10 g/cm^3, respectively. As was also the case for Hole CM1A, the cube samples were mostly taken from relatively homogeneous intervals with fewer or no visible cracks or veins, although some were taken from large veins and vein halos. Non-cube irregular-shape samples and broken cubes in highly altered or deformed intervals were measured only for density and porosity (Table T21). The highly altered or deformed samples have high porosities (up to 9.47%) and lower bulk densities (down to 2.47 g/cm^3) and grain densities (2.53 g/cm^3). One gabbro sample and olivine gabbro samples show high bulk (2.96 g/cm^3; average = 2.93 ± 0.12 g/cm^3, respectively) and grain (2.97 g/cm^3; average = 2.94 ± 0.12 g/cm^3, respectively) densities than samples of dunite (bulk/grain density averages = 2.60 ± 0.06 g/cm^3 and 2.64 ± 0.06 g/cm^3), harzburgite (averages = 2.70 ± 0.08 g/cm^3 and 2.72 ± 0.07 g/cm^3), and wehrlite (averages = 2.84 g/cm^3 and 2.98 g/cm^3). As in Hole CM1A, rodingitized rocks have the highest densities (average bulk density = 2.98 ± 0.05 g/cm^3, grain density = 3.06 ± 0.00 g/cm^3) of all the rock types measured in Hole CM2B.

As shown in Figure F113B, F113C, the discrete samples have lower bulk and grain densities (averages = 2.59 ± 0.08 and 2.64 ± 0.09 g/cm^3, respectively; Table T21) in the Dunite Sequence (I) and show the lowest and nearly constant densities among Hole CM2B. In the intervening Dunite with Gabbro Sequence (II), gabbroic rocks including a rodingitized rock in the Dunite with Gabbro Sequence have the highest densities (bulk density > 2.84 g/cm^3 and grain density > 2.94 g/cm^3) measured in Hole CM2B. Bulk density of harzburgite in the Mantle Sequence (III) widely varies at 2.47–2.87 g/cm^3, and the grain density of harzburgite in the sequence (III) ranges widely (2.53–2.87 g/cm^3), but variation is smaller than that of the harzburgite. Dunite in the Mantle sequence has similar and lower densities in this section.

The porosity of discrete cube samples ranges 0.09%–10.88% (mean = 1.65%). Except for an alluvium sample (porosity = 10.88%), which is weathered former peridotite, the porosity is highest in dunite (average = 2.41% ± 1.56%). A gabbro sample has the lowest porosity (0.09%). The Dunite Sequence (I) shows the highest porosity in Hole CM2B (average = 2.78% ± 2.02%), whereas the Dunite with Gabbro Sequence and the Mantle Sequence show relatively low porosities on average (1.63% ± 1.37% and 1.68% ± 1.98%), but also show large variation (0.09%–4.70% and 0.19% ± 9.47%; Fig. F113D, F113E).

The relationships between densities, *P*-wave velocity, and porosity are shown in Figures F114, F115, and F116. Data from Hole CM1A are also shown in the diagrams for comparison. Densities and *P*-wave velocity are inversely proportional to porosity, but gabbros and wehrlite show trends different from ultramafic rocks. Such relationships are also seen in the same lithologies (gabbros and ultramafics) from other OmanDP holes (Holes GT1A, GT2A, and BT2B; see **Physical Properties** in the **Site CM1A** chapter). *P*-wave velocity is a function of both bulk and grain densities (Fig. F115A, F115B). *P*-wave velocity has linear correlation with bulk density, also seen in samples from other OmanDP holes (GT1A, GT2A, and BT1B; Fig. F115A). In contrast, the correlation between *P*-wave velocity and grain density is less clear (Fig. F115B). Downhole plots of *P*-wave velocity with color scale of porosity reveals certain differences between the sequences and also lithologies (Fig. F117).

Electrical resistivity

Electrical resistivity was measured in 148 cube samples from Hole CM2B (Table T21; Fig. F113F). Resistivities range from <1.4 Ω·m to 115,500 Ω·m. Correlation with *P*-wave velocity is shown in Figure F117. Electrical resistivity in Hole CM2B is slightly higher than that of Hole CM1A. It has some correlation with the bulk magnetic susceptibility of the same cube samples following Equation 2 (Fig. F118;

also see **Anisotropy of magnetic susceptibility** and **Paleomagnetism: Hole CM2B**),

$$R = 0.014 \times B^{-3.4} \qquad (R^2 = 0.61), \qquad (2)$$

where R is electrical resistivity of the cube sample and B is bulk magnetic susceptibility of the cube sample. This suggests that the electrical resistivity is a power function of the bulk magnetic susceptibility in the minicube samples from Hole CM2B (Fig. **F118**).

Thermal conductivity

A total of 78 measurements were taken on core pieces from the working halves of Hole CM2B (Table **T23**; Fig. **F113G**). Thermal conductivity ranges 2.15–4.10 W/m·K, and the standard deviation of the average 6 or 3 measurements for each piece ranges 0.00–0.22 W/m·K. Harzburgite has the lowest thermal conductivity (2.15 W/m·K), whereas carbonated harzburgite has the highest value (4.10 W/m·K). Thermal conductivity in the Dunite Sequence is uniform and relatively high (average = 3.20 ± 0.06 W/m·K). Thermal conductivities have greater variation in the Dunite with Gabbro Sequence (2.47–3.39 W/m·K) because of the variety of rock types, such as gabbro and wehrlite, in this sequence. In addition, thermal conductivities of dunite slightly decrease with increasing depth. This could reflect that the degree of serpentinization and the abundance of magnetite, as a by-product of serpentinization, are also decreasing with increasing depth (Table **T5**). In the Mantle Sequence, thermal conductivities of harzburgite, dunite, and orthopyroxene-bearing dunite are uniform and relatively low (average = 2.49 ± 0.16 W/m·K). These values are similar to those of harzburgite from Hole 1274A, ODP Leg 209, Mid-Atlantic Ridge 15°20´N Fracture Zone (Kelemen et al., 2004). In contrast, the carbonated harzburgite in the lowest part of the Mantle Sequence shows high thermal conductivity (3.59 and 4.10 W/m·K); these values are similar to thermal conductivity of listvenite near the basal thrust in Oman DP Hole BT1B.

Downhole measurements/ hydrogeological testing: Hole CM2B

Downhole logging and hydrogeological testing operations and acquisition parameters for each borehole are available in Table **T56** and **T57** in the **Methods** chapter. Raw and processed data from all downhole logs are available in **Supplementary materials** > **L_Wireline logging** and in the ICDP Oman Drilling Project online data repository (**http://oman.icdp-online.org**).

Core scratch test: Hole CM2B

A total length of 44.6 m (117.14–144.24 m) of core was tested from Hole CM2B. Only a few sections were poor quality.

The cores were ~3 inches in diameter, slabbed into halves, and labeled as working and archive. They were unpreserved before and after testing. A major constraint requirement from project scientists was to limit the scratch groove depth to 5 mm. This objective was met except for a few sections where the groove was 6 mm deep. The cumulate length of these sections is <1 m.

Three independent sets of data were acquired: strength, ultrasonic velocity V_P and V_S logs, and groove panoramic pictures (Perneder, 2018). The testing campaign was successful in the sense that the scratch and ultrasonic data could be measured on all selected samples while causing little damage to the cores and keeping the groove <5 mm, except for very few sections.

Continuous profiles of strength (unconfined compressive [UCS]-equivalent) at centimeter resolution scale (Fig. **F119A**), ultrasonic P-wave and S-wave velocity measurements along the core axial direction at centimeter resolution (Fig. **F119B**), and high-definition photographs of the core under visible light taken before the scratch test, focusing on the clean fresh rock surface at the bottom of the scratch groove were acquired.

Imaging spectroscopy: Hole CM2B

All sections of Hole CM2B were imaged onboard the *Chikyu* during Leg 3. The ~300 m of Hole CM2B was imaged in 5.5 twelve-hour shifts in 3 days. A total of 409 sets of images (very near infrared [VNIR] and short-wave infrared [SWIR]) were acquired on core sections. A select number of images from the SWIR were processed to reflectance to check data quality and assist the alteration core description team, particularly at the bottom of the borehole. The remainder of the images, including all from the VNIR sensor, will be processed at Caltech, and mineral maps of each core section will be generated.

An example of preliminary mapping is shown in Figure **F120**. Here, interval 127Z-3, 39–64 cm, is classified by main mineral composition. Figure **F120B** shows a false-color infrared view of the core that demonstrates the mineralogic diversity of alteration in this section. The mineral classification in Figure **F120C** is preliminary; additional work with samples is needed to improve the accuracy of the mineral mapping and move toward quantitative assessments of mineral abundance when multiple phases are present in a single pixel. Nevertheless, the textures and relationships between minerals in this complex zone of alteration are apparent.

References

Abily, B., and Ceuleneer, G., 2013. The dunitic mantle-crust transition zone in the Oman ophiolite: residue of melt-rock interaction, cumulates from high-MgO melts, or both? Geology, 41:67–70.

Arason, P., and Levi, S., 2010. Maximum likelihood solution for inclination-only data in paleomagnetism. Geophysical Journal International, 182:753-771. https://doi.org/10.1111/j.1365-246X.2010.04671.x

Bach, W., Jöns, N., and Klein, F., 2013. Metasomatism within the Ocean Crust. In Harlov, D.E., and Austrheim, H. (Eds.), Metasomatism and the Chemical Transformation of Rock. (Springer):253–288.

Barrat, J.A., Zanda, B., Moynier, F., Bollinger, C., Liorzou, C., and Bayon, G., 2012. Geochemistry of CI chondrites: Major and trace elements, and Cu and Zn isotopes. Geochimica et Cosmochimica Acta, 83:79-92. https://doi.org/10.1016/j.gca.2011.12.011

Barth, M.G., Mason, P.R., Davies, G.R., Dijkstra, A.H., Drury, M.R., 2003. Geochemistry of the Othris ophiolite, Greece: Evidence for refertilisation? J. Pet., 44(10):1759-1785. https://doi.org/10.1093/petrology/egg058

Boschi, C., Dini, A., Dallai, L., Ruggieri, G., and Gianelli, G., 2009. Enhanced CO_2-mineral sequestration by cyclic hydraulic fracturing and Si-rich fluid infiltration into serpentinites at Malentrata (Tuscany, Italy). Chem. Geol., 265:209–226.

Boschi, C., Früh-Green, G.L., and Escartín, J., 2006. Occurrence and significance of serpentine-hosted, talc- and amphibole-rich fault rock in modern oceanic setting and ophiolite complexes: an overview. Ofioliti, 31:129–140.

Clark, R.N., and Roush, T.L., 1984. Reflectance Spectroscopy: Quantitative Analysis Techniques for Remote Sensing Applications. J. Geophys. Res., 89(B7):6329-6340. https://doi.org/198410.1029/JB089iB07p06329

Connolly, J.A.D., 2009. The geodynamic equation of state: what and how. Geochem., Geophys., Geosyst., 10:Q10014.

Dygert, N., Kelemen, P.B., Liang, Y., 2017. Spatial variations in cooling rate in the mantle section of the Samail ophiolite in Oman: Implications for formation of lithosphere at mid-ocean ridges. Earth Planet. Sci. Lett., 465:134-144. https://doi.org/10.1016/j.epsl.2017.02.038

Escartín, J., Mével, C., MacLeod, C.J., McCaig, A.M., 2003. Constraints on deformation conditions and the origin of oceanic detachments: The Mid-Atlantic Ridge core complex at 15°45′N. Geochem., Geophys., Geosys., 4.

Gerbert-Gaillard, L., 2002. Caracterisation Geochimique des Peridotites de l'ophiolite d'Oman: Processus Magmatiques aux Limites Lithosphere/Asthenosphere. Ph.D. Thesis (Université Montpellier II).

Godard, M., Jousselin, D., Bodinier, J.-L., 2000. Relationships between geochemistry and structure beneath a palaeo-spreading centre: a study of the mantle section in the Oman ophiolite. Earth Planet. Sci. Lett., 180:133-148.

Halls, C., and Zhao, R., 1995. Listvenite and related rocks: perspectives on terminology and mineralogy with reference to an occurrence at Cregganbaun, Co. Mayo, Republic of Ireland. Miner. Depos., 30:303–313.

Hanghøj, K., Kelemen, P.B., Hassler, D., Godard, M., 2010. Composition and genesis of depleted mantle peridotites from the Wadi Tayin massif, Oman ophiolite: Major and trace element geochemistry, and Os isotope and PGE systematics. J. Petrol., 51(1-2):201-227. https://doi.org/10.1093/petrology/egp077

Holland, T.J.B., and Powell, R., 2011. An improved and extended internally consistent thermodynamic dataset for phases of petrological interest, involving a new equation of state for solids. J. Metamorphic Geology, 29:333–383.

Jagoutz, E., Palme, H., Baddenhausen, H., Blum, K., Cendales, M., Dreibus, G., Spettel, B., Lorenz, V., Wänke, H., 1979. The abundances of major, minor and trace elements in the Earth's mantle as derived from primitive ultramafic nodules. Proc. Lunar Planet. Sci. Conf. 10th, 2031-2050.

Kelemen, P.B., and Hirth, G., 2012. Reaction-driven cracking during retrograde metamorphism: Olivine hydration and carbonation. Earth Planet. Sci. Lett., 345–348:81–89.

Kelemen, P.B., Kikawa, E., Miller, D.J., et al., 2004. Proc. ODP, Init. Repts., 209: College Station, TX (Ocean Drilling Program). https://doi.org/10.2973/odp.proc.ir.209.2004

Kelemen, P.B., Koga, K., Shimizu, N., 1997. Geochemistry of gabbro sills in the crust-mantle transition zone of the Oman ophiolite: Implications for the origin of the oceanic lower crust. Earth Planet. Sci. Lett., 146:475-488.

Kelemen, P.B., and Matter, J., 2008. In situ carbonation of peridotite for CO_2 storage. Proc. Natl. Acad. Sci., 105:17295–17300.

Kelemen, P.B., Shimizu, N., Salters, V.J.M., 1995. Extraction of Mid-Ocean-Ridge Basalt from the Upwelling Mantle by Focused Flow of Melt in Dunite Channels. Nature, 375:747-753.

Khedr, M.Z., Arai, S., Python, M., Tamura, A., 2014. Chemical variations of abyssal peridotites in the central Oman ophiolite: evidence of oceanic mantle heterogeneity. Gondwana Research, 25(3):1242-1262. https://doi.org/10.1016/j.gr.2013.05.010

Kinzler, R.J., and Grove, T.L., 1993. Corrections and further discussion of the primary magmas of mid-ocean ridge basalts, 1 and 2. J. Geophys. Res., 98(B12):22339–22347. https://doi.org/10.1029/93JB02164

Klein, F., and Garrido, C.J., 2011, Thermodynamic constraints on mineral carbonation of serpentinized peridotite. Lithos, 126:147–160.

Kokaly, R.F., Clark, R.N., Swayze, G.A., Livo, K.E., Hoefen, T.M., Pearson, N.C., Wise, R.A., Benzel, W.M., Lowers, H.A., Driscoll, R.L., and Klein, A.J., 2017. USGS Spectral Library Version 7. US Geological Survey Data Series 1035. https://doi.org/10.3133/ds1035

Koons, P.O., 1981. A study of natural and experimental metasomatic assemblages in an ultramafic-quartzofeldspathic metasomatic system from the Haast Schist, South Island, New Zealand. Contrib. to Mineral. Petrol., 78:189–195.

Korenaga, J., and Kelemen, P.B., 1997. Origin of gabbro sills in the Moho transition zone of the Oman ophiolite: Implications for magma transport in the oceanic lower crust. J. Geophys. Res., Solid Earth, 102:27729-27749.

MacLeod, C.J., Lissenberg, C.J., Bibby, L.E., 2013. Moist MORB axial magmatism in the Oman ophiolite: The evidence against a mid-ocean ridge origin. Geology, 41:459-462.

Malvoisin, B., Brunet, F., Carlut, J., Rouméjon, S., and Cannat, M., 2012. Serpentinization of oceanic peridotites: 2. Kinetics and processes of San Carlos olivine hydrothermal alteration. J. Geophys. Res., Solid Earth, 117:1–13.

McDonough, W.F., and Sun, S.S., 1995. The composition of the Earth. Chemical Geology, 120(3-4):223-253. https://doi.org/10.1016/0009-2541(94)00140-4

Mellini, M., and Zanazzi, P.F., 1987. Crystal structures of lizardite-1T and lizardite-2H1 from Coli, Italy, American Mineralogist, 72:943-948.

Monnier, C., Girardeau, J., Le Mée, L., Polvé, M., 2006. Along-ridge petrological segmentation of the mantle in the Oman ophiolite. Geochem. Geophys. Geosyst., 7(11). https://doi.org/10.1029/2006GC001320

Nicolle, M., Jousselin, D., Reisberg, L., Bosch, D., and Stephant, A., 2016. Major and trace element and Sr and Nd isotopic results from mantle diapirs in the Oman ophiolite: implications for off-axis magmatic processes. Earth Planet. Sci. Lett., 437:138–149

Perneder, L., 2018. Scratch test report strength and ultrasonic logging. JAMSTEC - P004W. EPSLOG S.A.

Rospabé, M., Benoit, M., Ceuleneer, G., Hodel, F., and Kaczmarek, M.-A., 2018. Extreme geochemical variability through the dunitic transition zone of the Oman ophiolite: Implications for melt/fluid-rock reactions at Moho level beneath oceanic spreading centers. Geochim. Cosmochim. Acta, 134:1-23.

Schwarzenbach, E.M., Früh-Green, G.L., Bernasconi, S.M., Alt, J.C., and Plas, A., 2013. Serpentinization and carbon sequestration: A study of two ancient peridotite-hosted hydrothermal systems. Chem. Geol., 351:115–133.

Sun, S.-S., and McDonough, W.F., 1989. Chemical and isotopic systematics for mantle composition and processes. Geo. Soc. London, Spec. Publ., 42:313-345. https://doi.org/10.1144/GSL.SP.1989.042.01.19

Takazawa, E., Okayasu, T., and Satoh, K., 2003. Geochemistry and origin of the basal lherzolites from the northern Oman ophiolite (northern Fizh block). Geochem., Geophys., Geosyst., 4.

Treves, B., and Harper, G.D., 1994. Exposure of serpentinites on the ocean floor: sequence of faulting and hydrofracturing in the northern Apennine ophicalcite. Ofioliti, 20(2):111-122.

Wilson, S.A., Dipple, G.M., Power, I.M., Thom, J.M., Anderson, R.G., Raudsepp, M., Gabites, J.E., and Southam, G., 2009. Carbon dioxide fixation within mine wastes of ultramafic-hosted ore deposits: Examples from the Clinton Creek and Cassiar Chrysotile deposits, Canada. Econ. Geol., 104:95–112.

Figure F1. A. Photograph showing the CM2 drill site during rotary drilling operations at Hole CM2A, looking east along the wadi. **B.** The CM2B borehole was drilled a few weeks later, and is viewed here, during diamond coring, from a peak to the northwest of Site CM2.

Figure F2. Lithologic column for cuttings, Hole CM2A.

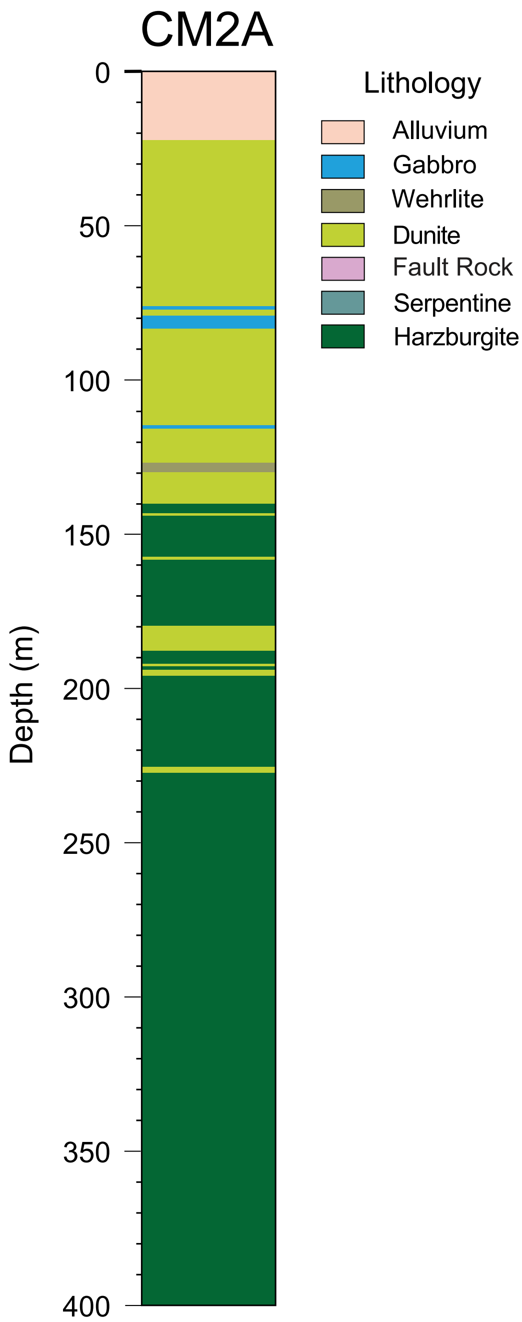

Figure F3. Pie charts showing unit (**A**) thickness and (**B**) counts, Hole CM2B.

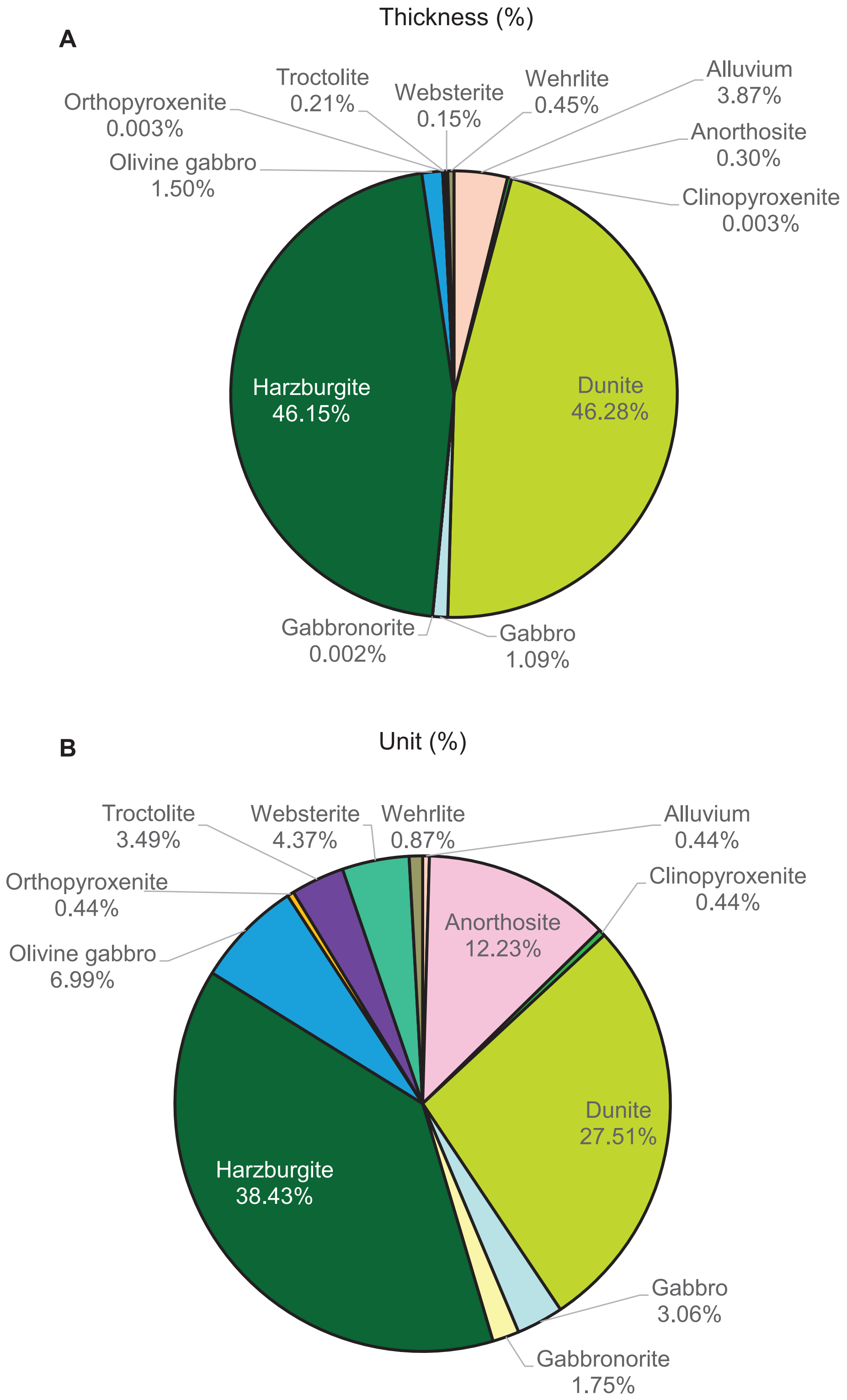

Figure F4. Lithostratigraphic column, sequences, and depths: mode (Ol = olivine, Spl = spinel, Pl = plagioclase, Cpx = clinopyroxene, Opx = orthopyroxene), grain size (GS), and layer thickness (LT), Hole CM2B.

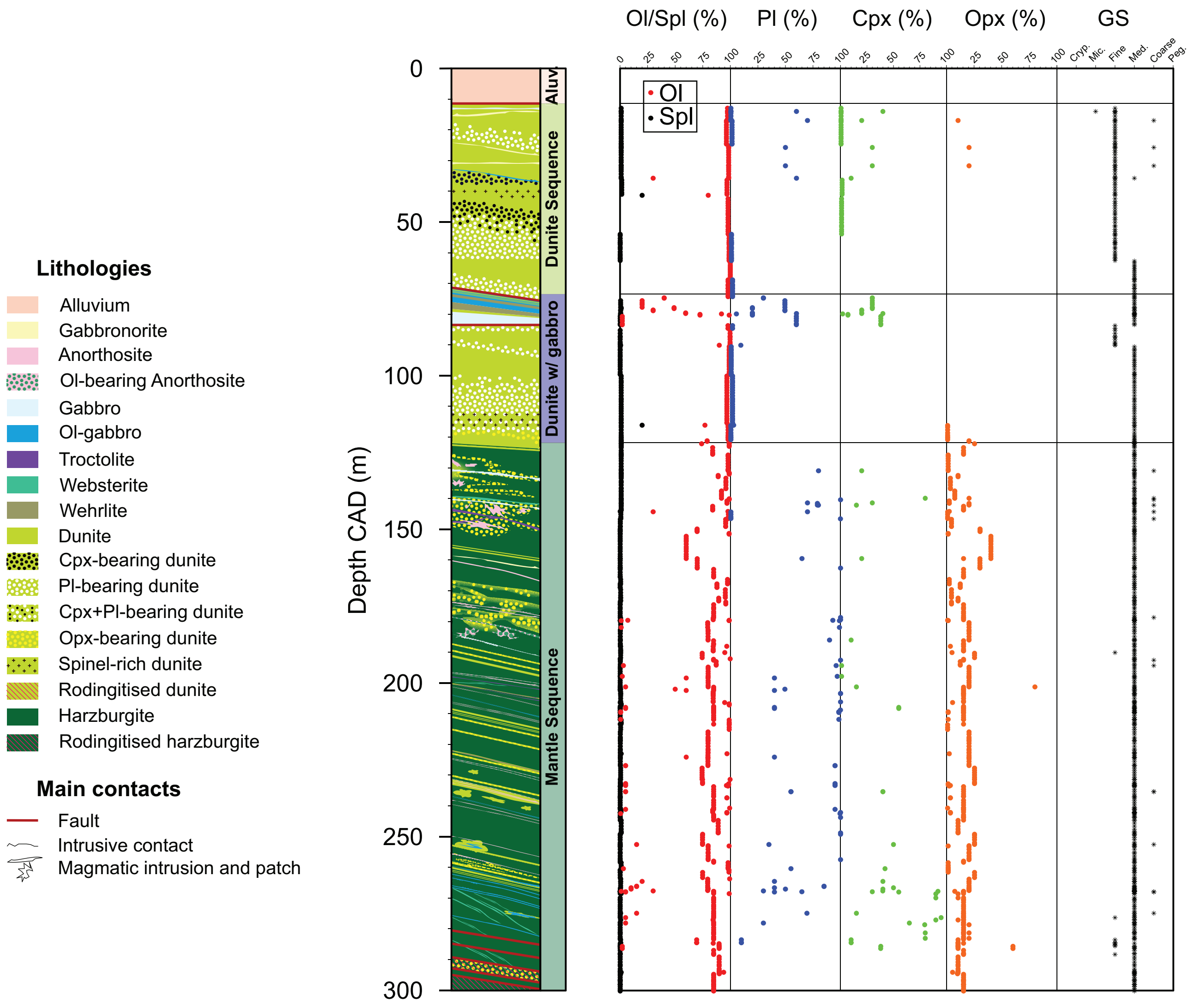

Figure F5. Lithostratigraphic column and pie charts showing unit/subunit counts and cumulative thickness for the lithologic sequences defined in Hole CM2B: (**A**) Dunite Sequence, (**B**) Dunite with Gabbro Sequence, (**C**) Mantle Sequence. Ol = olivine, Pl = plagioclase, Cpx = clinopyroxene, Opx = orthopyroxene.

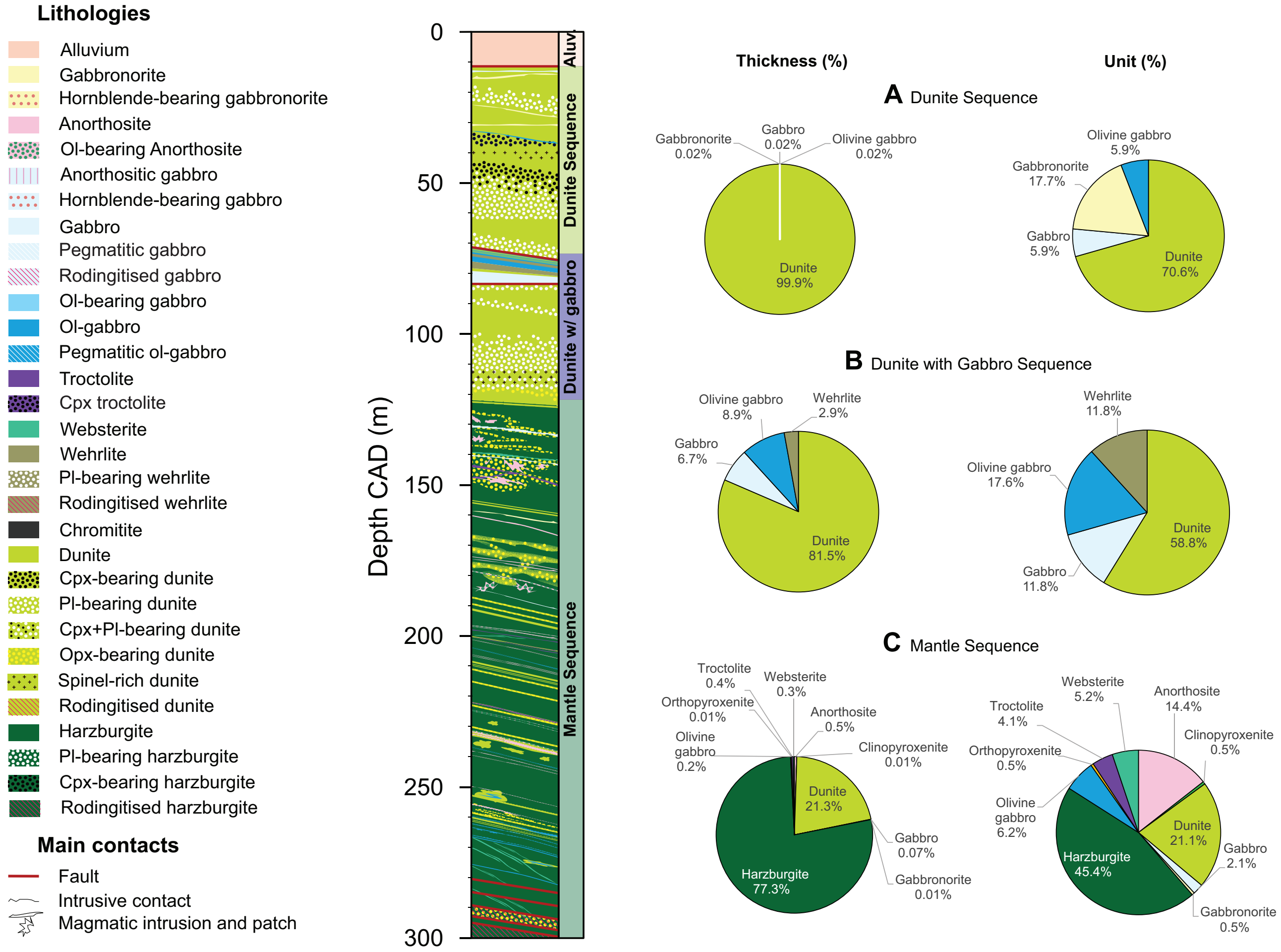

Figure F6. Typical examples of dunite in the Dunite Sequence, Hole CM2B. **A.** Dunite (Subunit 2c). **B.** Plagioclase-bearing dunite (Subunit 2e). **C.** Spinel-rich dunite (Subunit 3h).

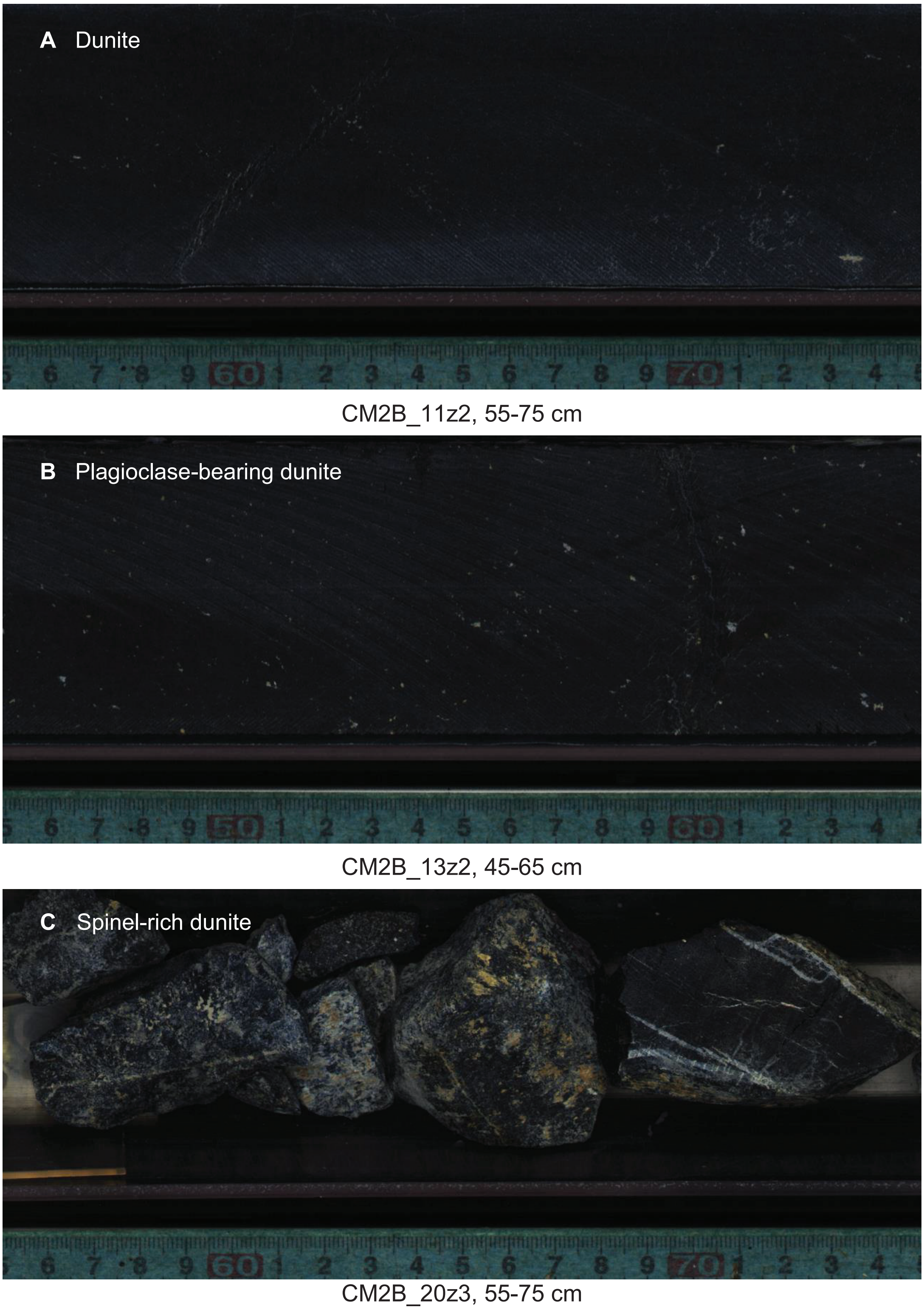

Figure F7. Typical examples of dunites in several sequences, Hole CM2B. **A.** Clinopyroxene-bearing dunite with occasional sulfide-rich bands in the Dunite Sequence (Subunit 3i; yellow arrows = sulfides; green arrow = clinopyroxene-rich band). **B.** Plagioclase-bearing dunite in the Dunite with Gabbro Sequence (Subunit 10c). **C.** Orthopyroxene-bearing dunite in the Mantle Sequence (Subunit 17a).

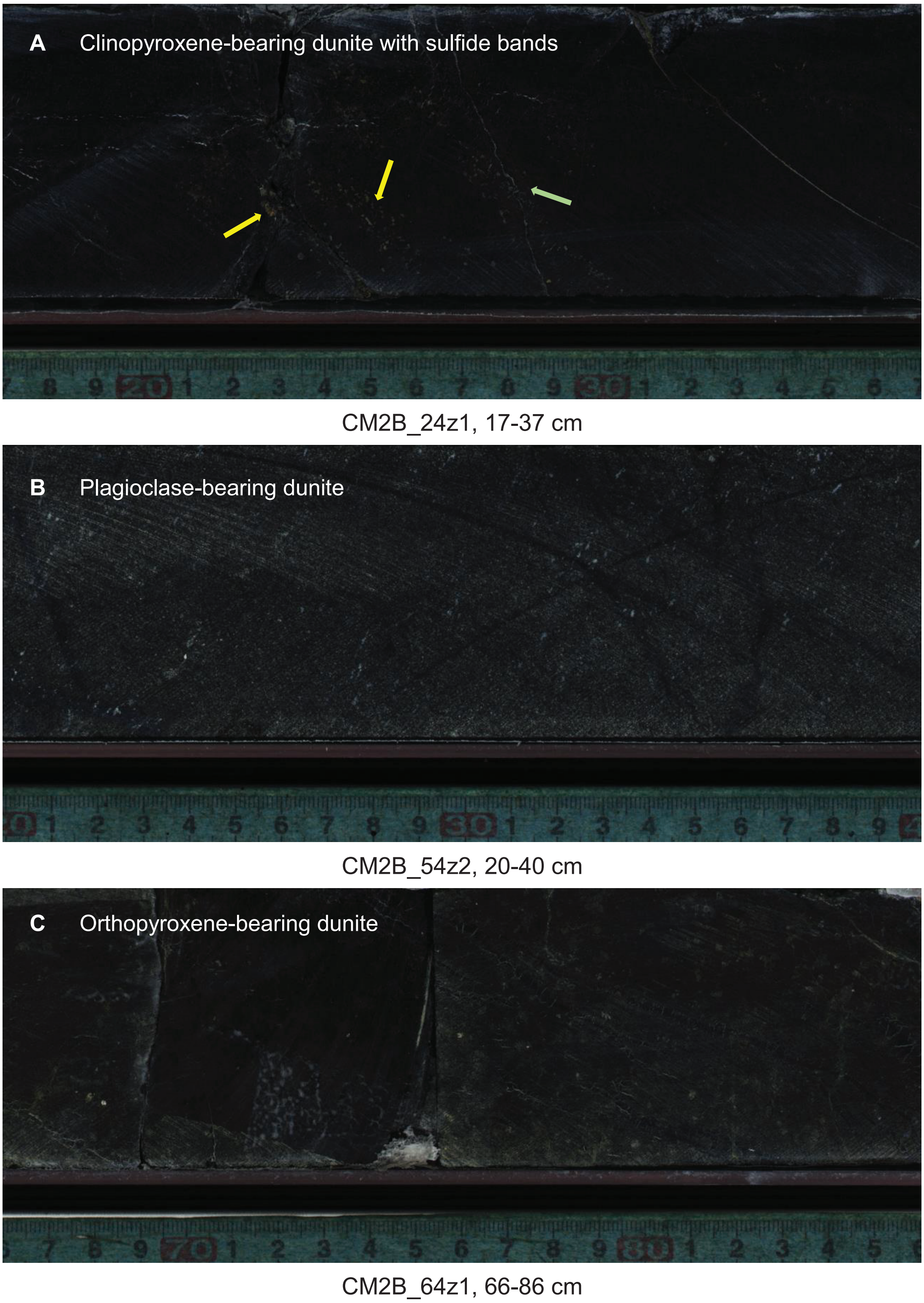

Figure F8. Typical examples of principal rock types in the Mantle Sequence, Hole CM2B. **A.** Orthopyroxene-rich patch in an orthopyroxene-bearing dunite (Unit 29). **B, C.** Harzburgite: (B) Subunit 26e; (C) Subunit 40a.

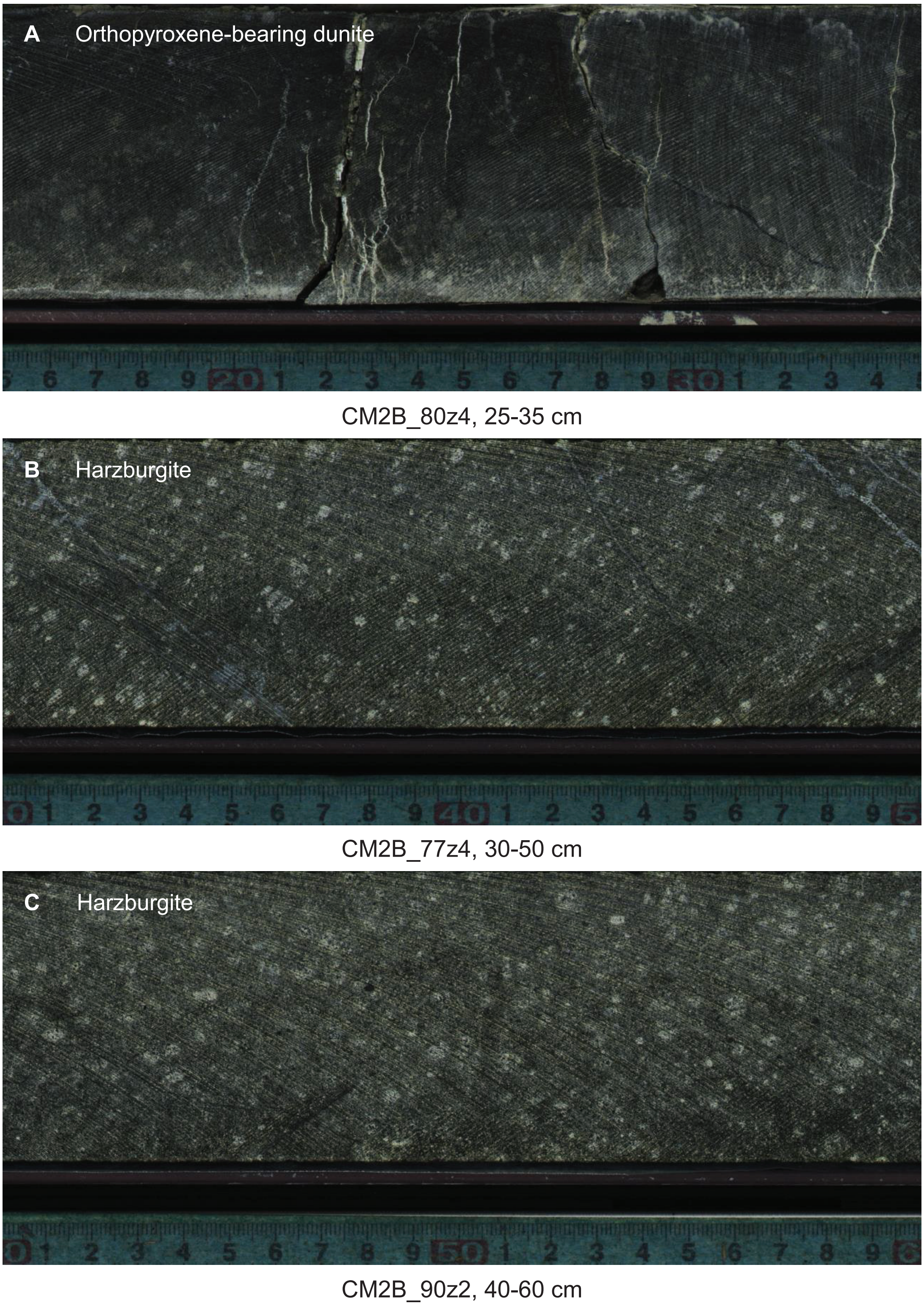

Figure F9. Typical examples of principal rock types, Hole CM2B. **A.** Deformed harzburgite in the Mantle Sequence (Unit 64). **B.** Olivine gabbro in the Dunite with Gabbro Sequence (Subunit 8a). **C.** Olivine gabbro patch in harzburgite in the Mantle Sequence (Subunits 61n, 61o); websterite vein (Subunit 61l) is present above the gabbro patch.

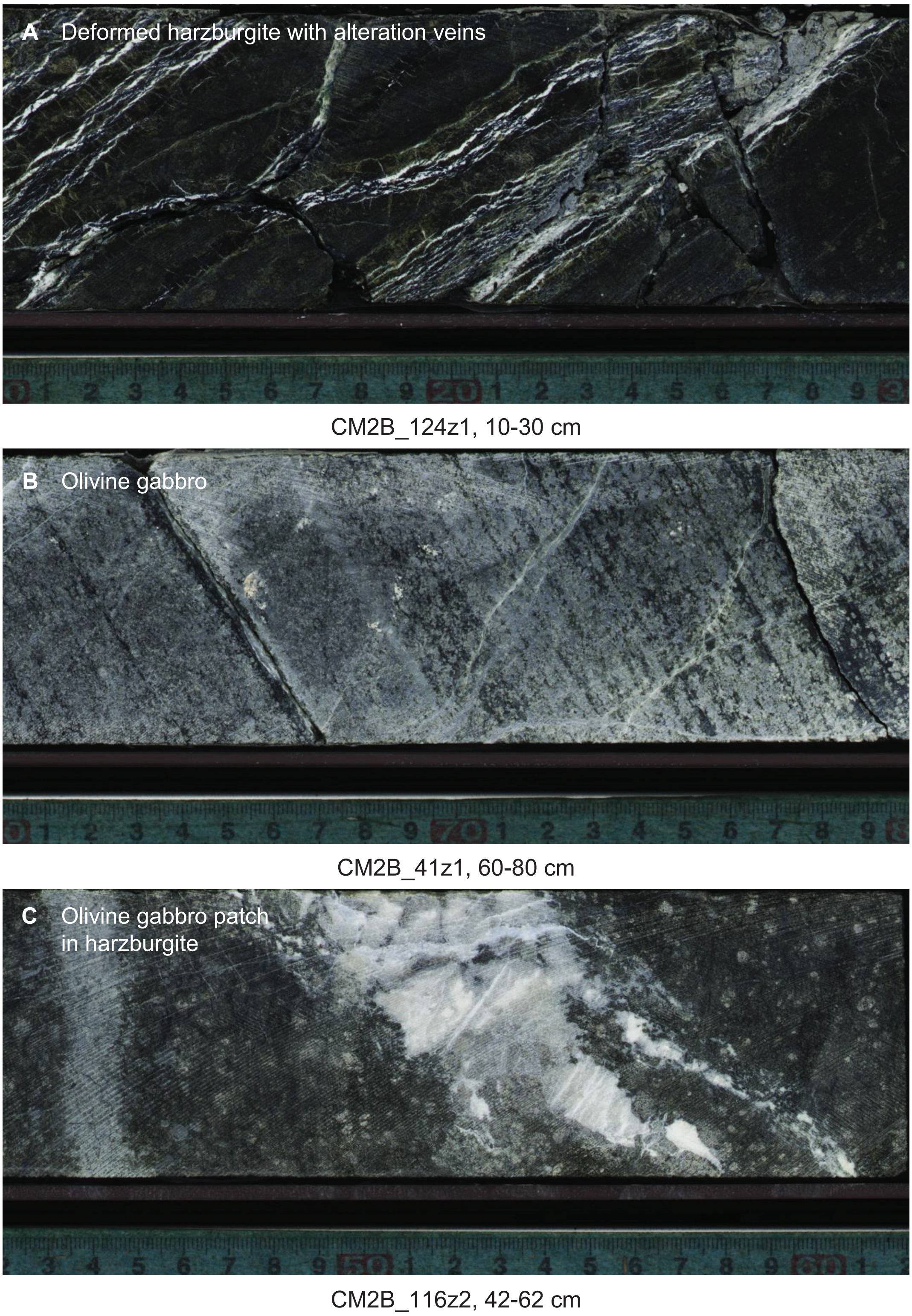

Figure F10. Typical examples of principal rock types, Hole CM2B. **A.** Gabbro in the Dunite with Gabbro Sequence (Subunit 8i). **B.** Altered hornblende-bearing gabbro patch (Subunit 22b) in harzburgite (Subunits 22a, 22c), Mantle Sequence. **C.** Plagioclase-bearing wehrlite with plagioclase-rich bands in the Dunite with Gabbro Sequence (Subunit 8d).

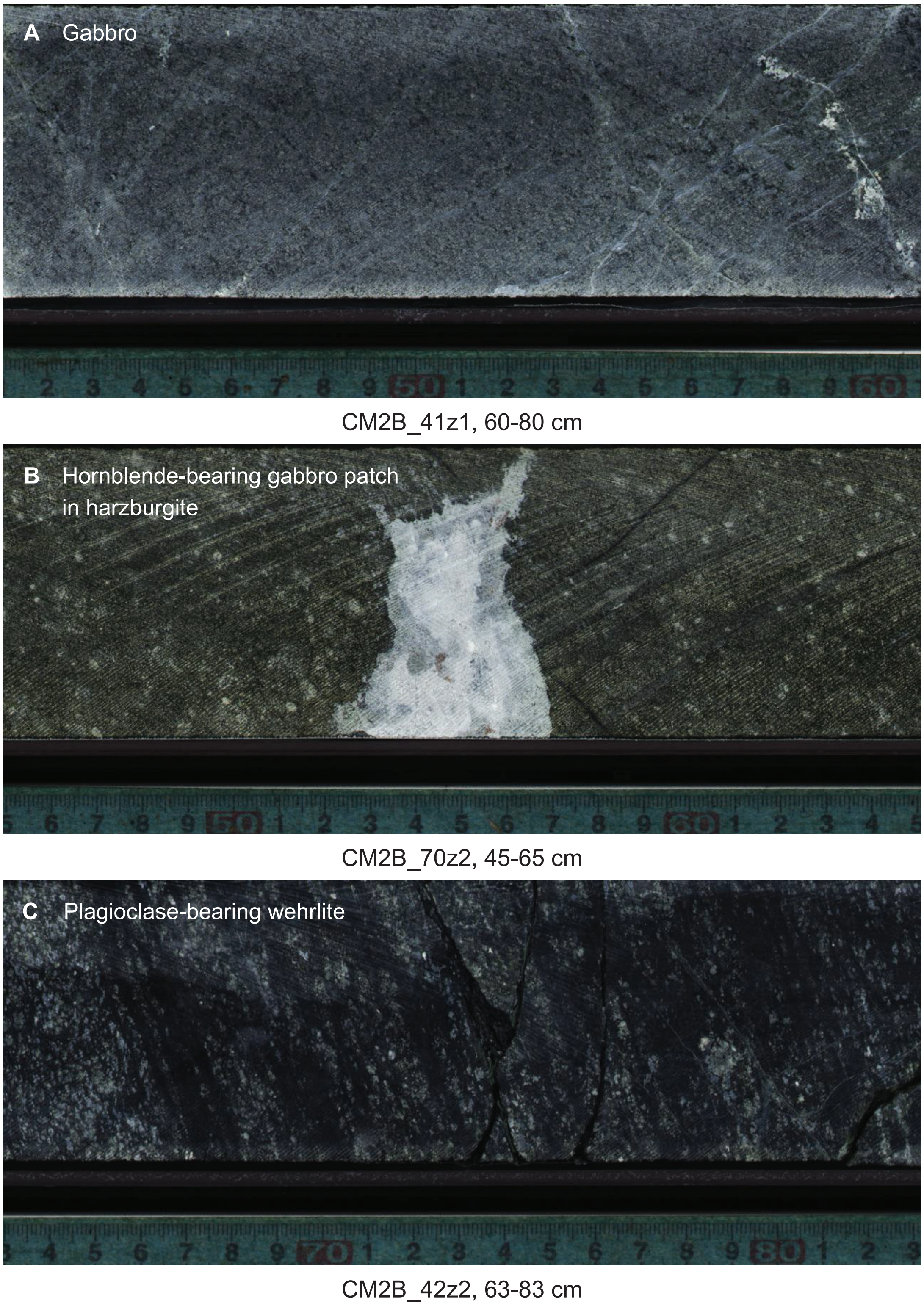

Figure F11. Typical examples of principal rock types in the Mantle Sequence, Hole CM2B. **A.** Rodingitized anorthosite patch (Subunit 21b) in dunite and orthopyroxene-bearing dunite (Subunits 21a, 21c). **B.** Poikilitic clinopyroxene-bearing troctolite patch (Subunit 61j) in harzburgite (Subunits 61i, 61k). **C.** Websterite vein (Subunit 61aa) in harzburgite (Subunits 61z, 61ab).

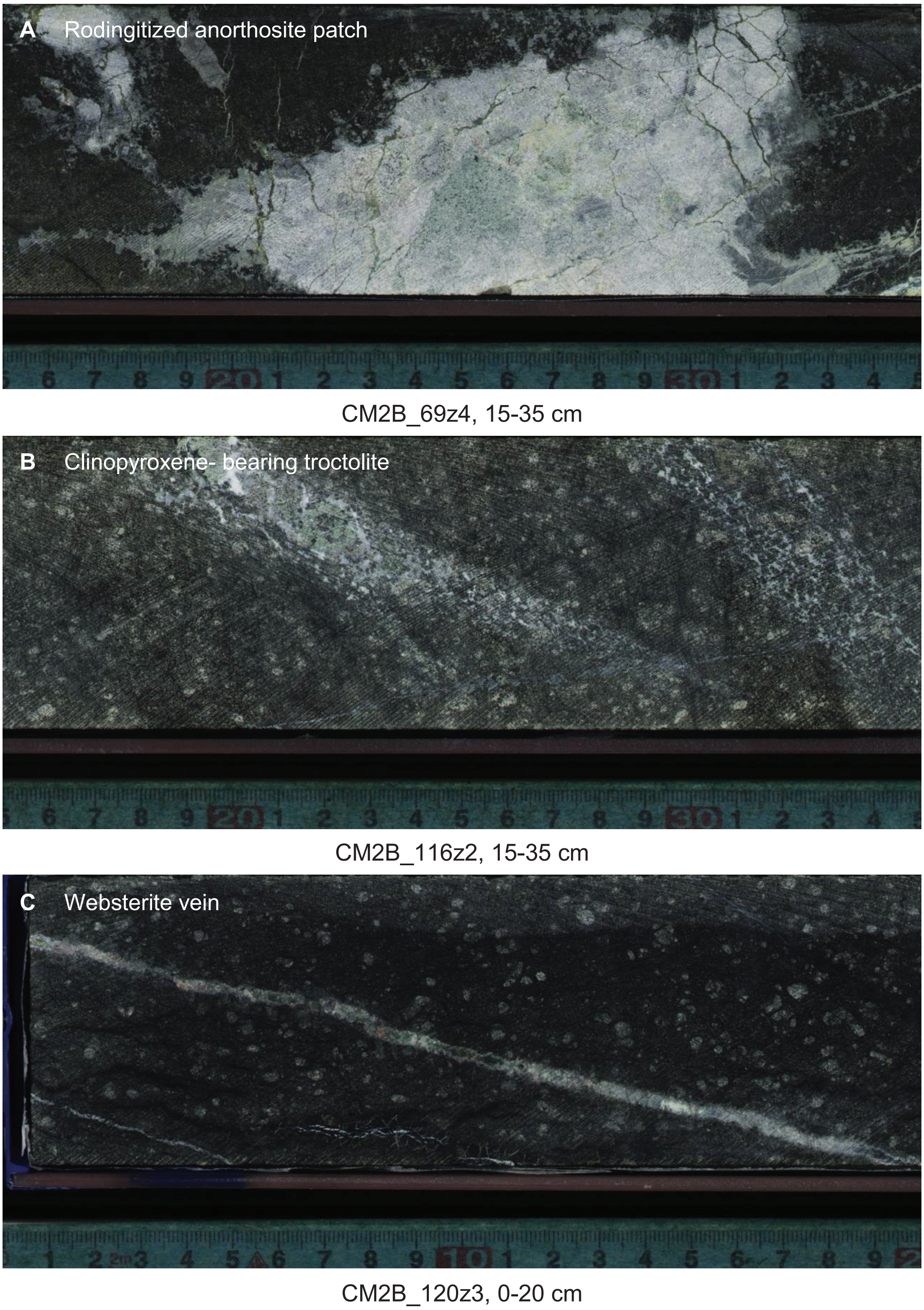

Figure F12. Typical examples of principal rock types, Hole CM2B. **A.** Clinopyroxenite vein (Subunit 61y) in harzburgite (Subunits 61x, 61z), Mantle Sequence. **B.** Gabbronorite vein (Subunit 2d) in dunite and plagioclase-bearing dunite (Subunits 2c, 2e), Dunite Sequence. **C.** Gabbronorite vein (Subunit 26b) in harzburgite (Subunits 26a, 26c), Mantle Sequence.

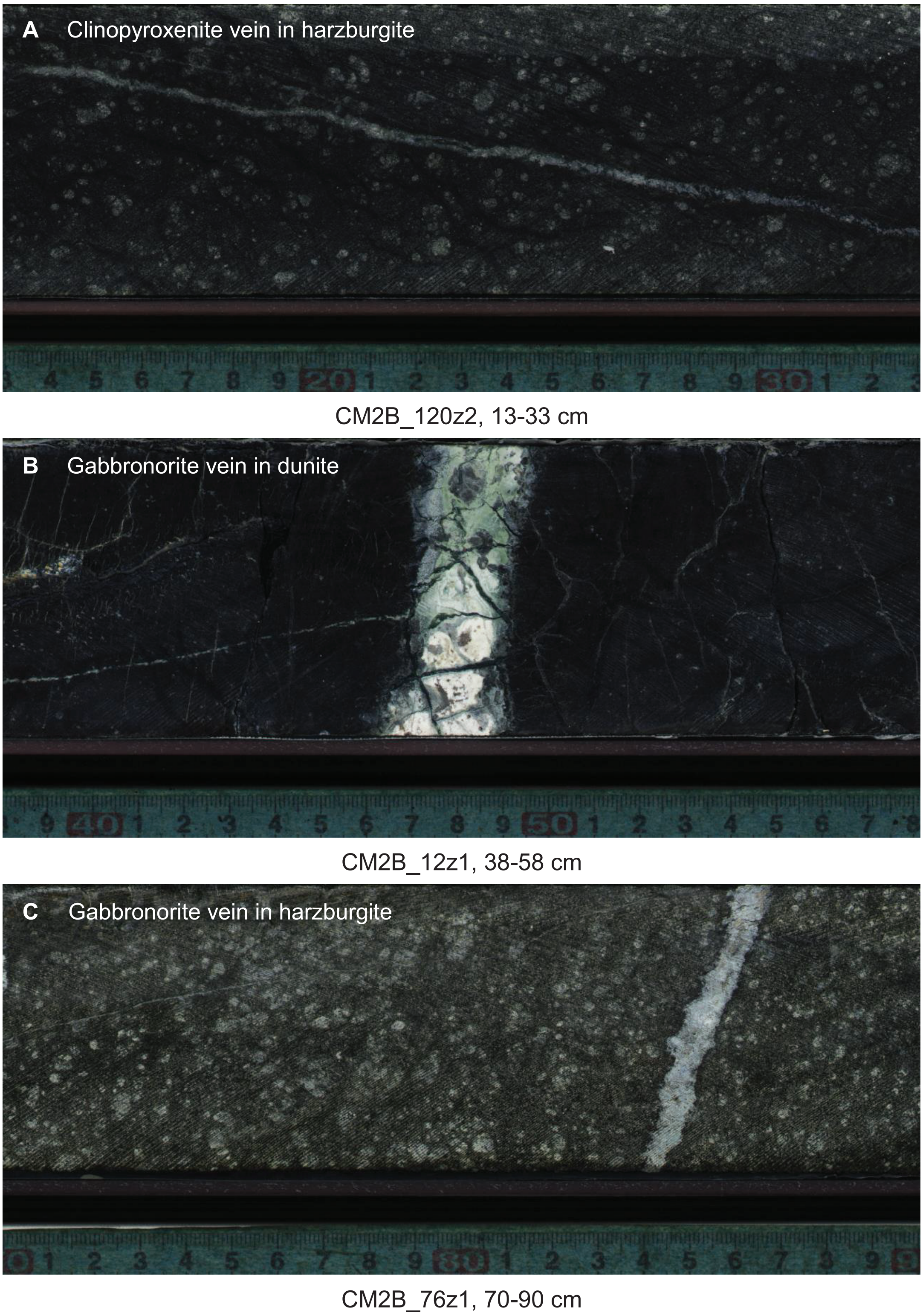

Figure F13. Features related to layering, Hole CM2B. **A.** Strong layering: top of the Dunite with Gabbro Sequence starting with a layered series of alternating olivine gabbros and dunites (the "zebra" rock). **B.** Moderate layering.

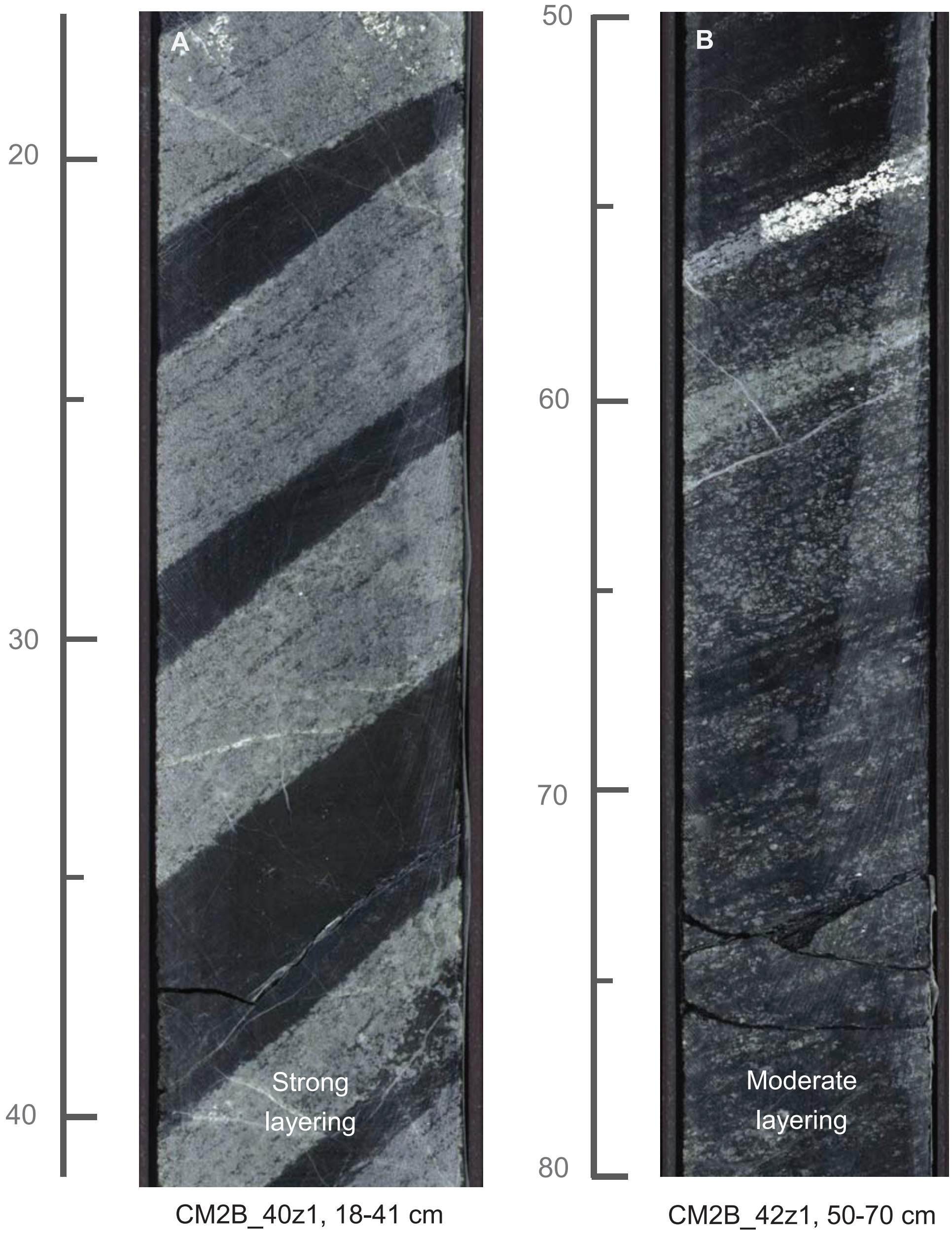

Figure F14. Representative contacts, Hole CM2B. **A.** Dunite Sequence (Unit 6/7). **B, C.** Dunite with Gabbro Sequence (Subunits 8b/8c, 11a/11b). **D–F.** Mantle Sequence (Subunits 11c/12, 21a/21b, 50b/50c).

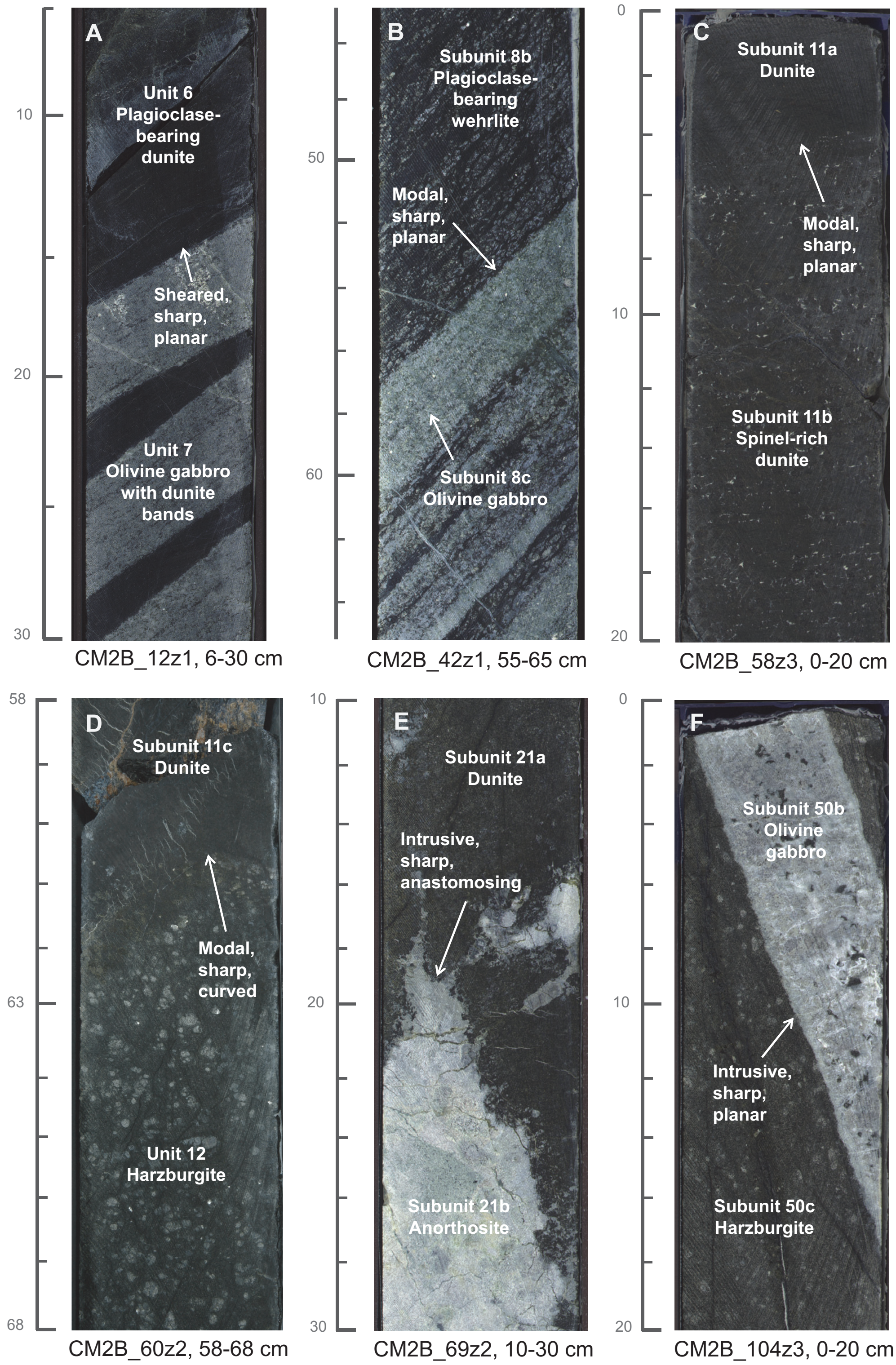

Figure F15. First appearance of mantle peridotite in Hole CM2B. **A, C.** Dunite with texture typical of the Dunite with Gabbro Sequence, now totally altered to serpentinite, characterized by a regular network of equant olivine grains with equigranular grain size distribution. **B, D.** At 23–25 cm, the first dunite with typical mantle texture occurs: dunite with relics of orthopyroxene porphyroclasts (yellow arrows), indicating the first appearance of true mantle rocks in Hole CM2B.

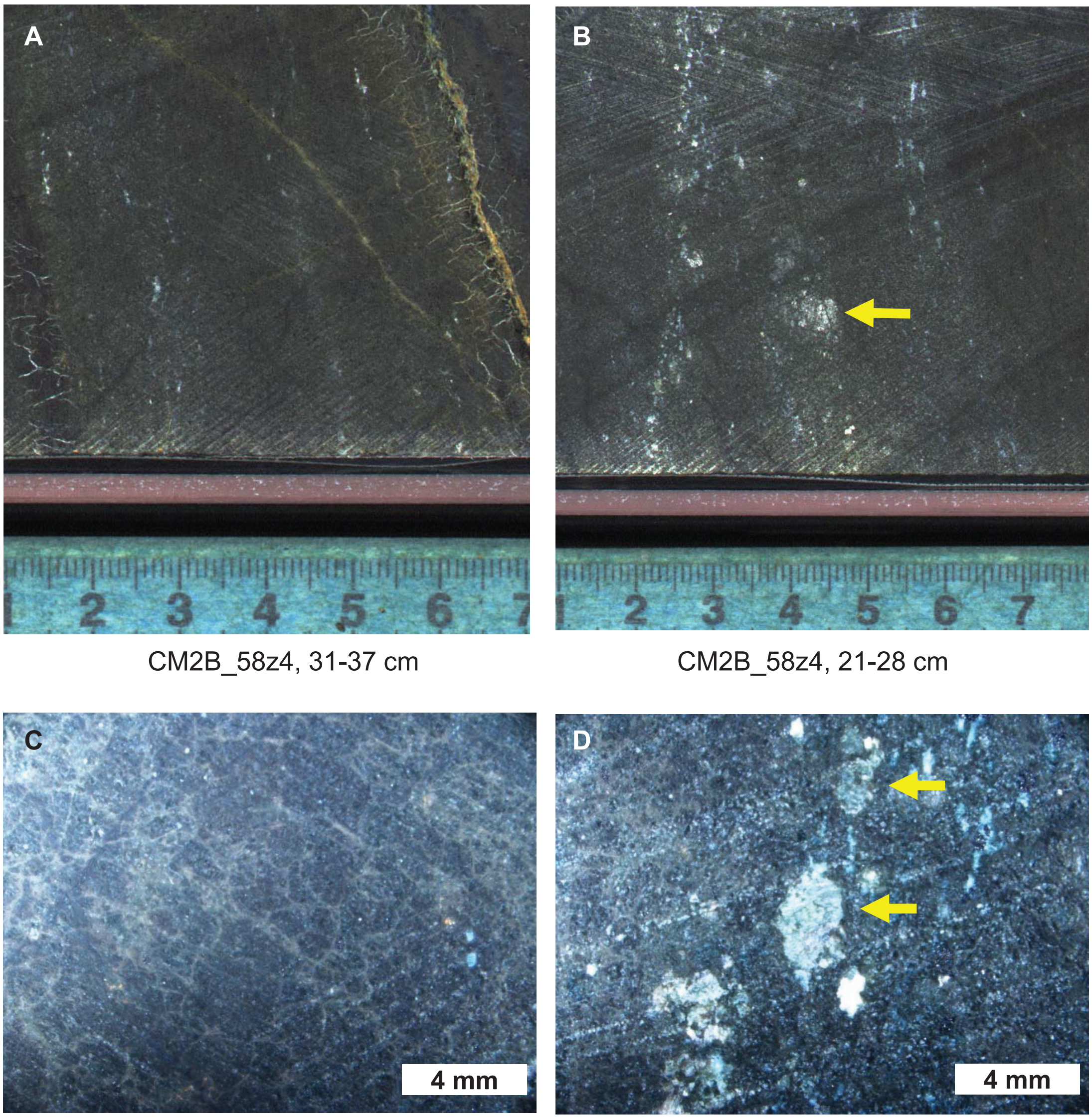

CM2B_58z4, 31-37 cm

CM2B_58z4, 21-28 cm

CM2B_58z4, 33-35 cm

CM2B_58z4, 23-25 cm

Figure F16. Dunite from Dunite with Gabbro Sequence (Subunit 11a: plagioclase-bearing dunite), Hole CM2B. **A.** Whole thin section scan (plane-polarized light [PPL]). **B, C.** Close-up of red box (B: PPL, C: cross-polarized light [XPL]). Spl = spinel, Ol = olivine.

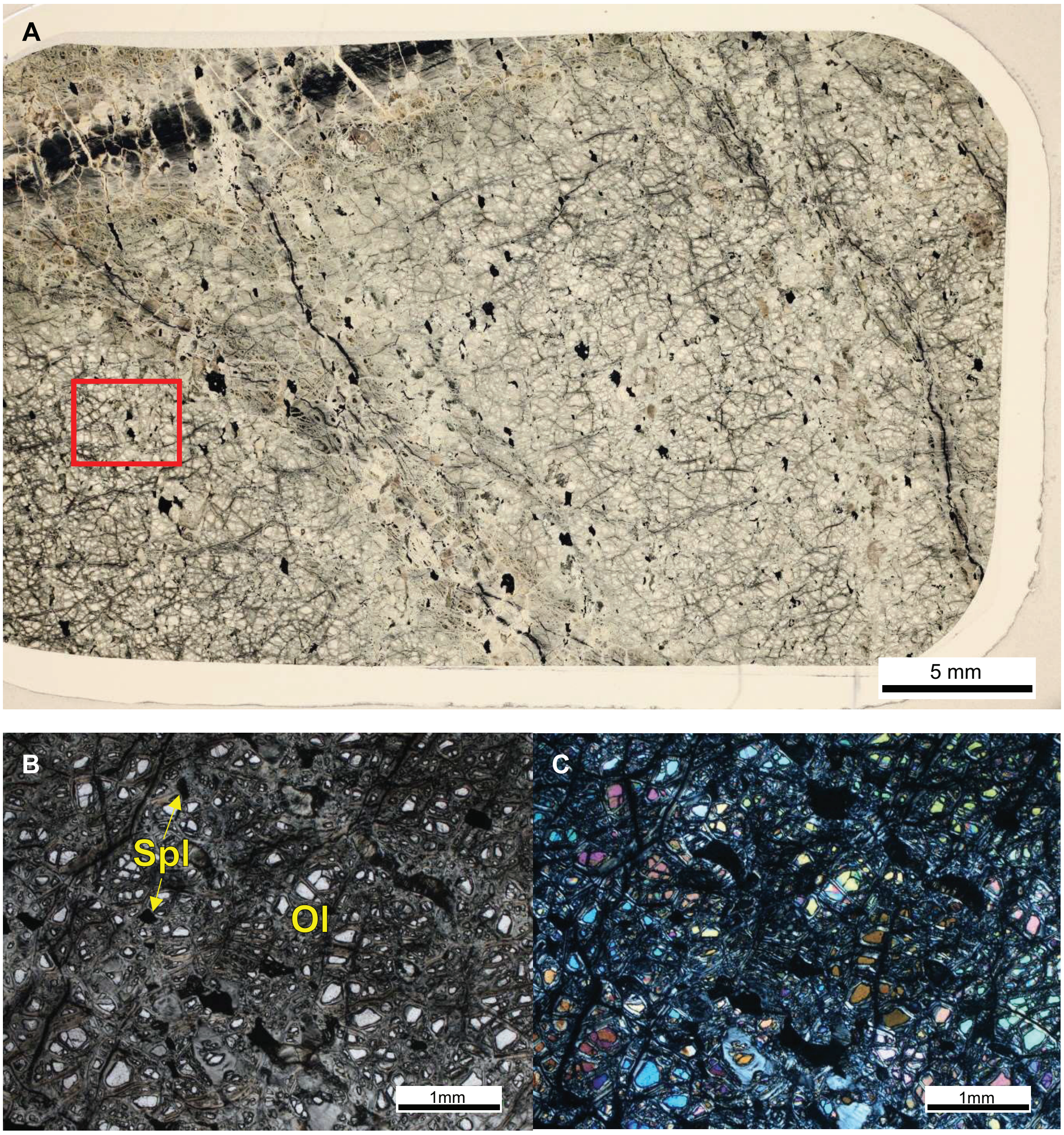

TS_CM2B_53z4_29-34 cm

Figure F17. Dunite from Mantle Sequence (Unit 45), Hole CM2B. **A.** Whole thin section scan (PPL). **B, C.** Close-up of red box (B: PPL, C: XPL). Ol = olivine, Spl = spinel.

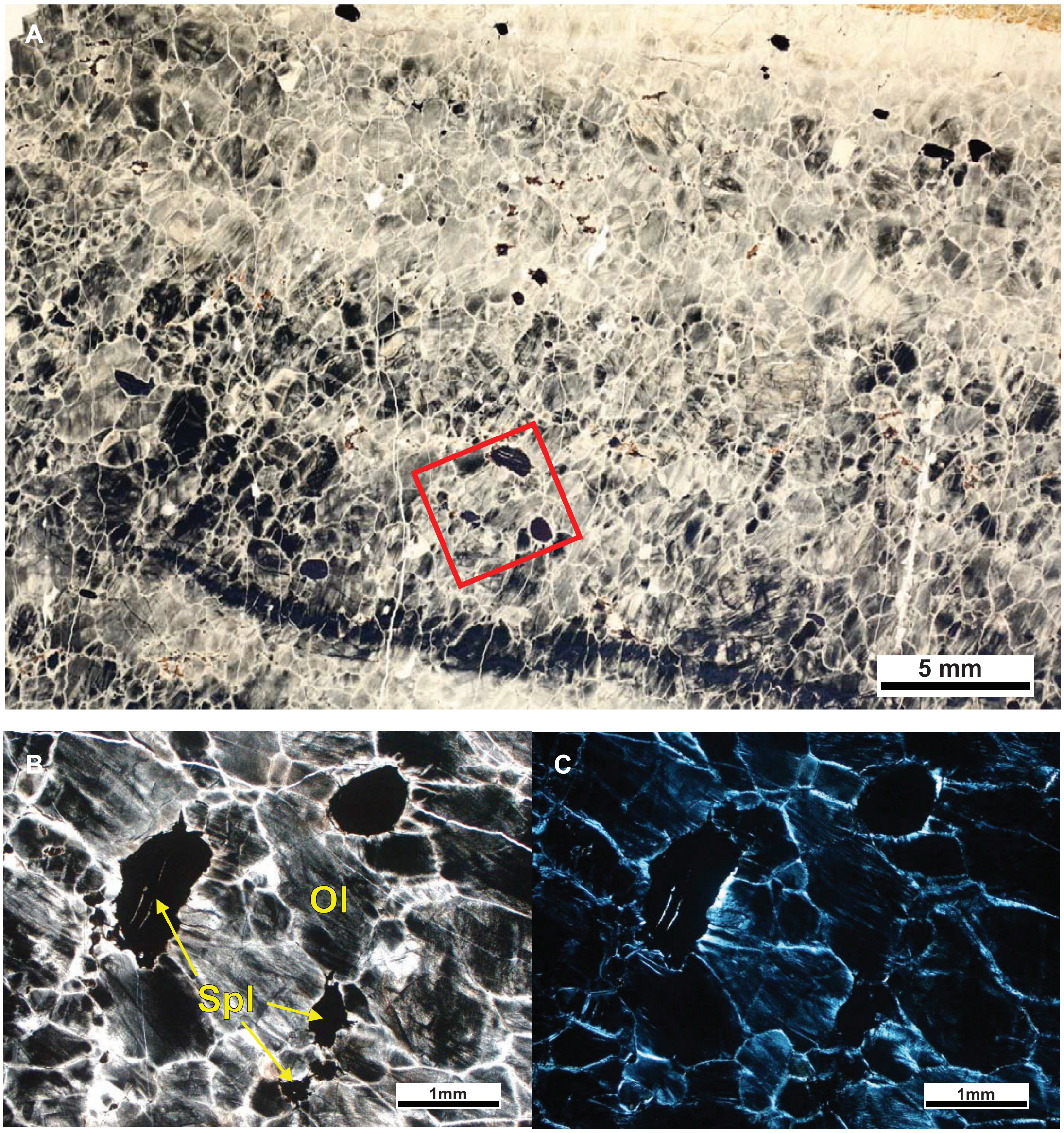

TS_CM2B_96z2_68-71 cm

Figure F18. Harzburgite from Mantle Sequence (Subunit 42k), Hole CM2B. **A.** Whole thin section scan (PPL). **B, C.** Close-up of red box (B: PPL, C: XPL). Ol = olivine, Opx = orthopyroxene, Cpx = clinopyroxene.

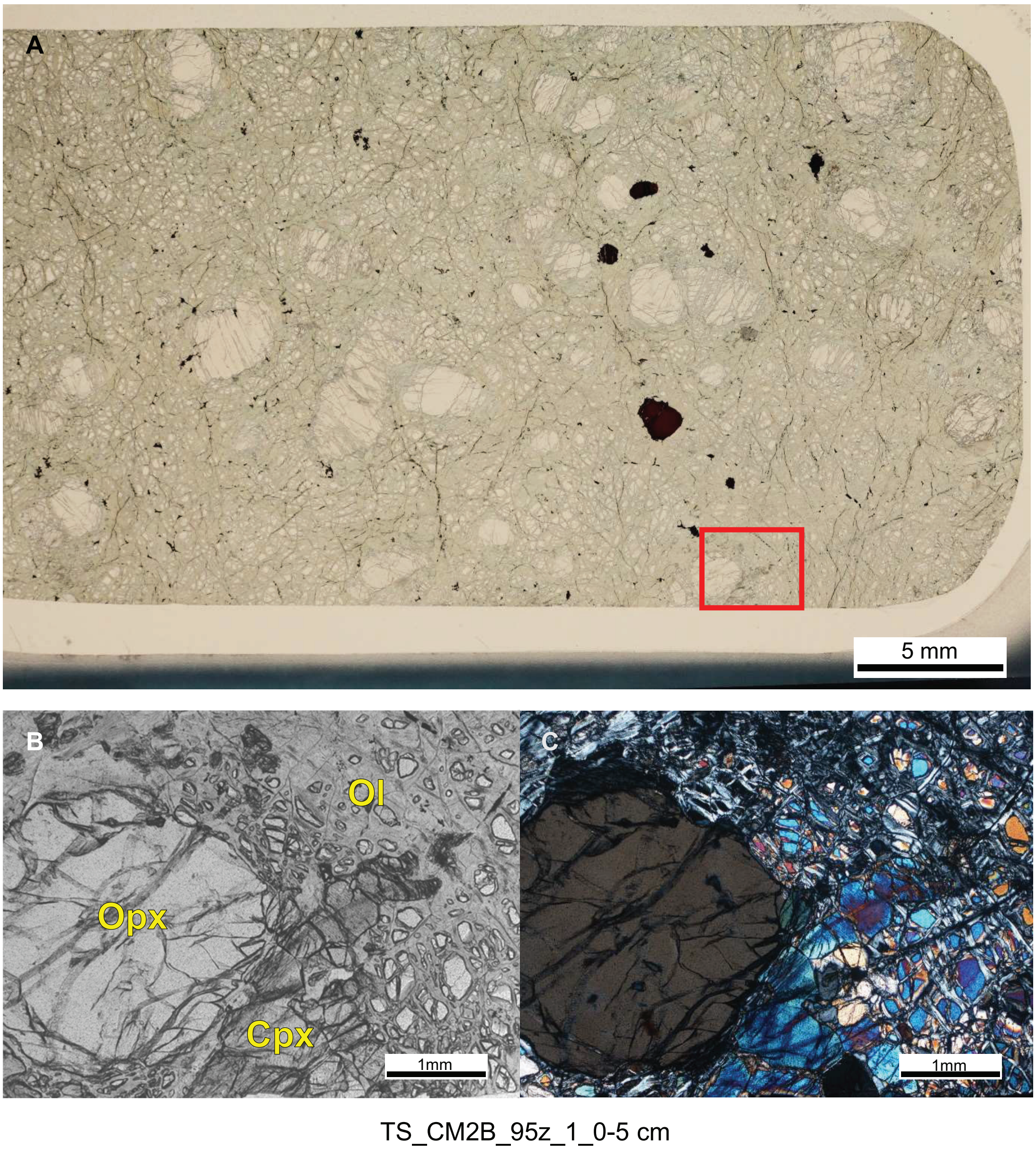

Figure F19. Olivine gabbro in Dunite with Gabbro Sequence (Subunit 8a), Hole CM2B. **A.** Whole thin section scan (PPL). **B, C.** Close-up of red box (B: PPL, C: XPL). Pl = plagioclase, Ol = olivine, Cpx = clinopyroxene.

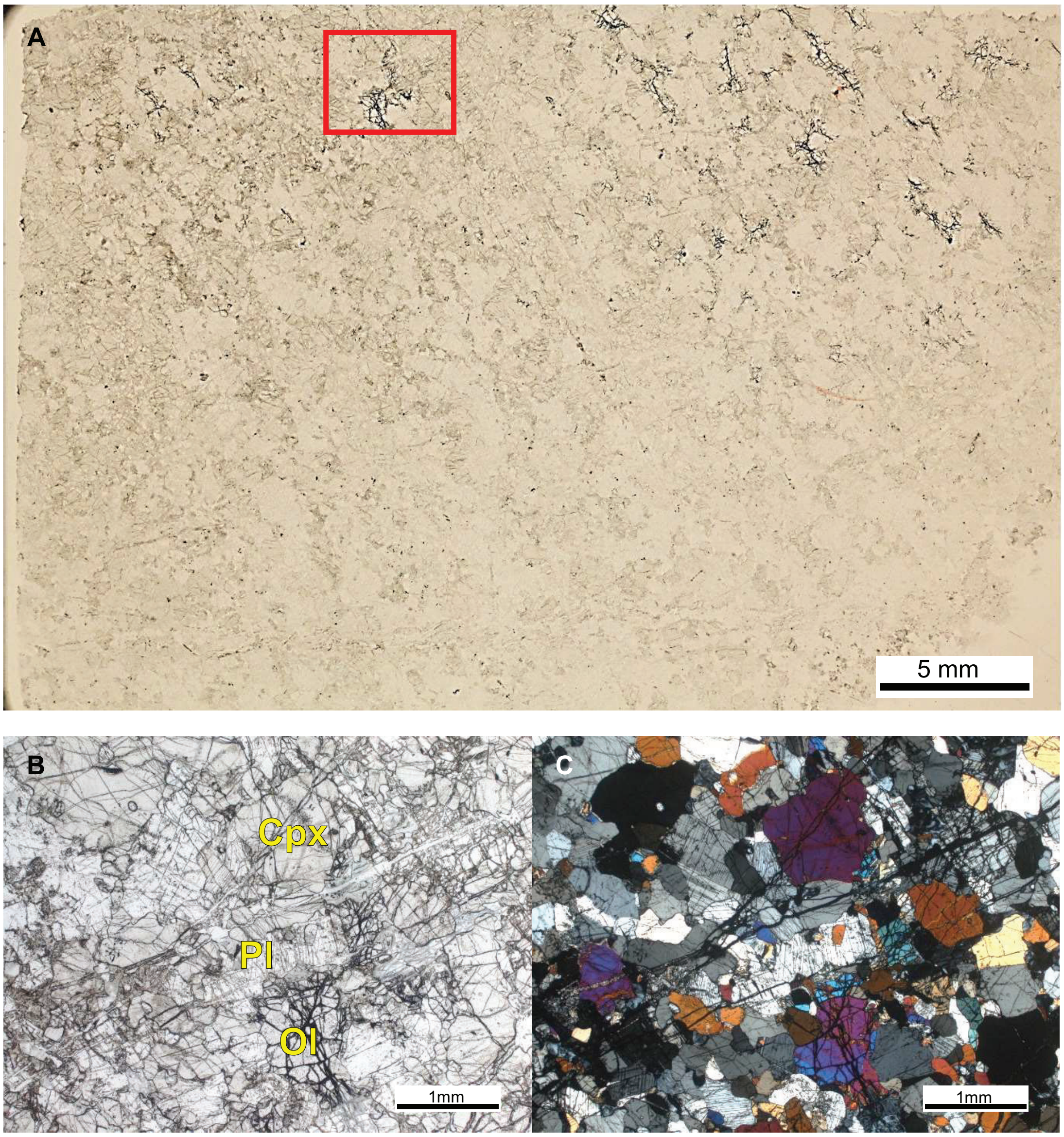

TS_CM2B_41z1_15-18 cm

Figure F20. Gabbro from Dunite with Gabbro Sequence (Subunit 8i), Hole CM2B. **A.** Whole thin section scan (PPL). **B, C.** Close-up of red box (B: PPL, C: XPL). Cpx = clinopyroxene.

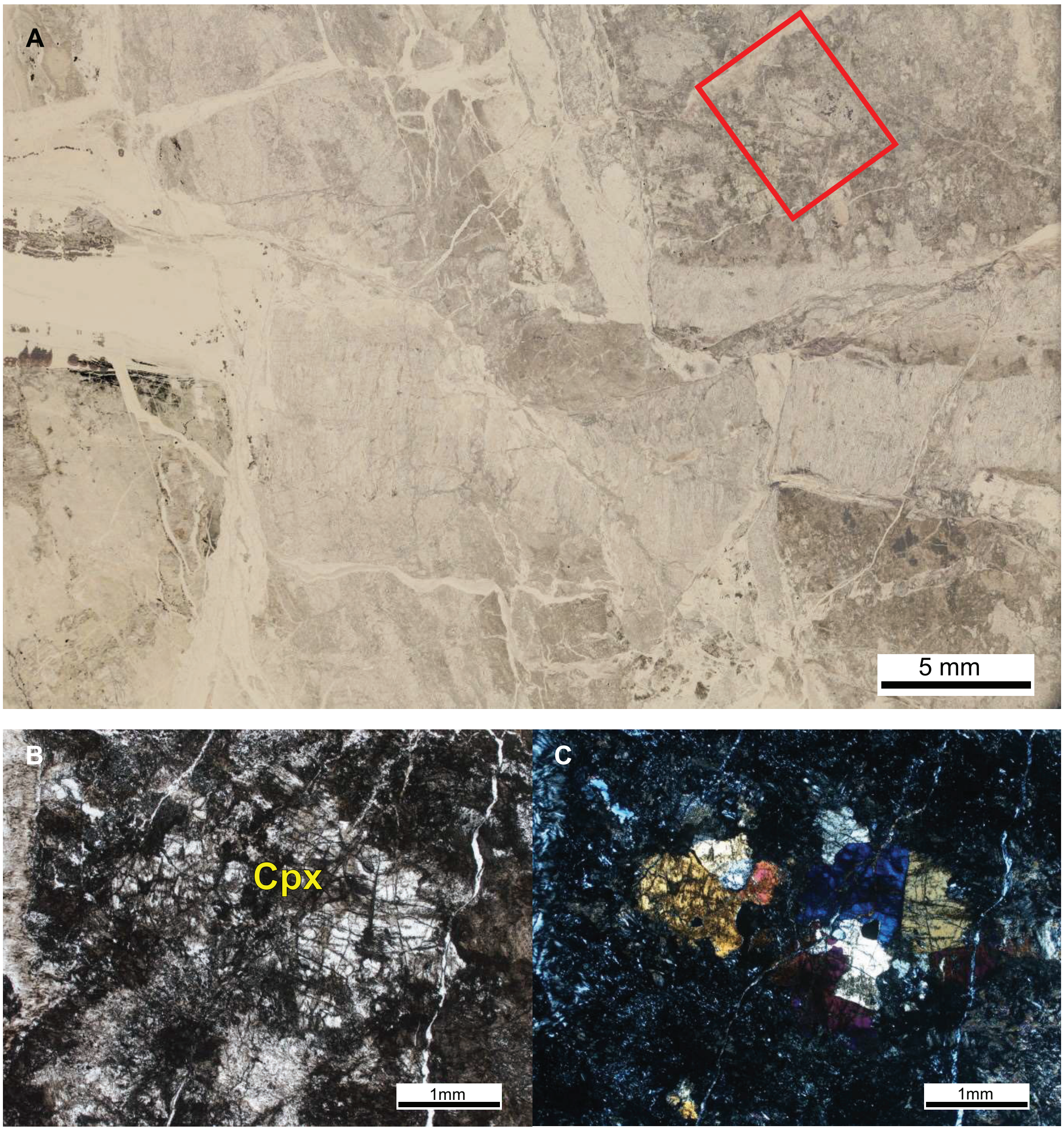

TS_CM2B_44z4_22-25 cm

Figure F21. Wehrlitic patch in dunite from Mantle Sequence (Subunit 21a), Hole CM2B. **A.** Whole thin section scan (PPL). **B, C.** Close-up of red box (B: PPL, C: XPL). Cpx = clinopyroxene, Ol = olivine.

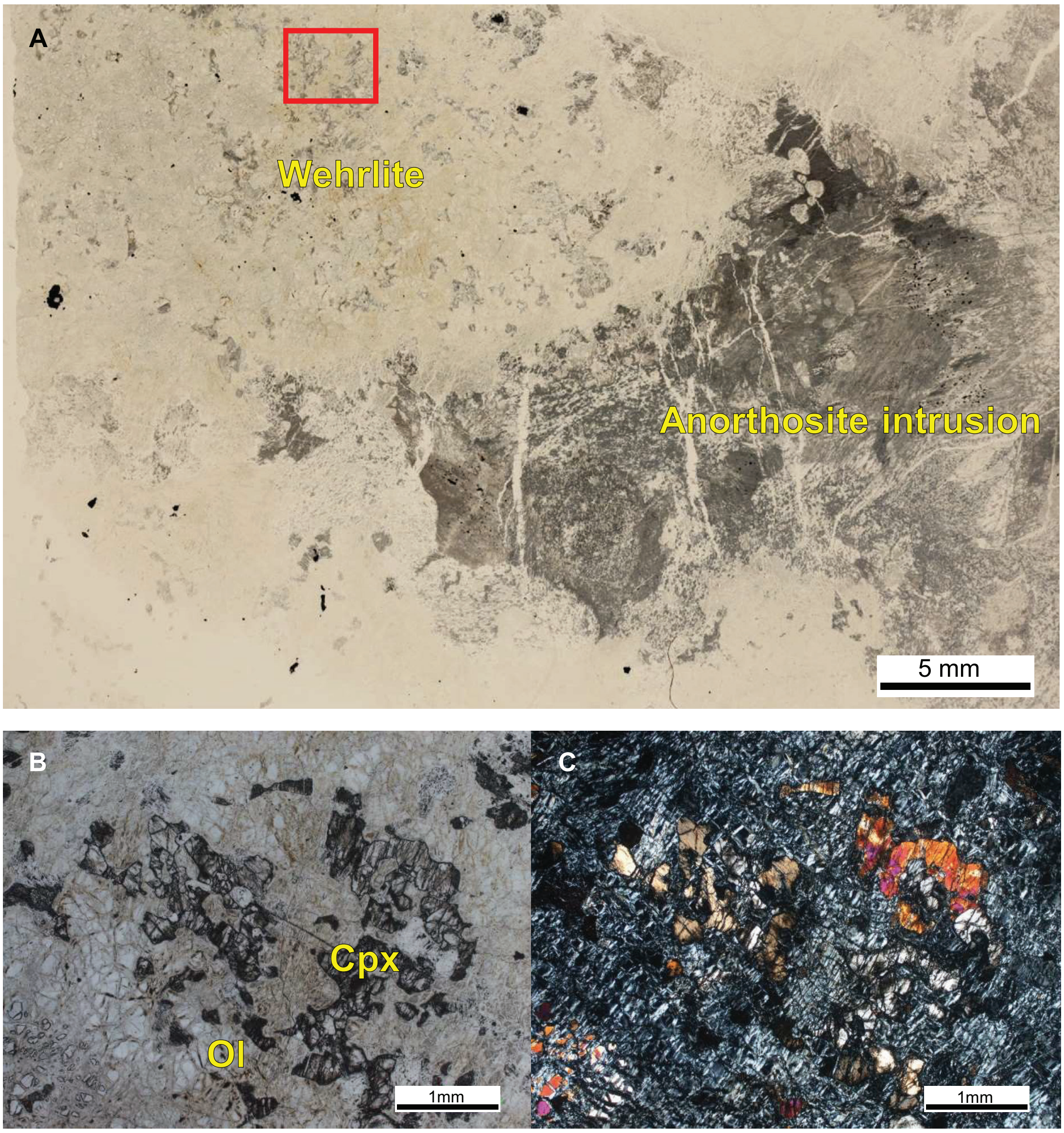

TS_CM2B_69z4_15-19 cm

Figure F22. Troctolite from Mantle Sequence (Subunit 40h), Hole CM2B. **A.** Whole thin section scan (PPL). **B, C.** Close-up of red box indicates (B: PPL, C: XPL). Olivine (Ol) is totally replaced by serpentine and plagioclase (Pl) by greenschist-facies minerals.

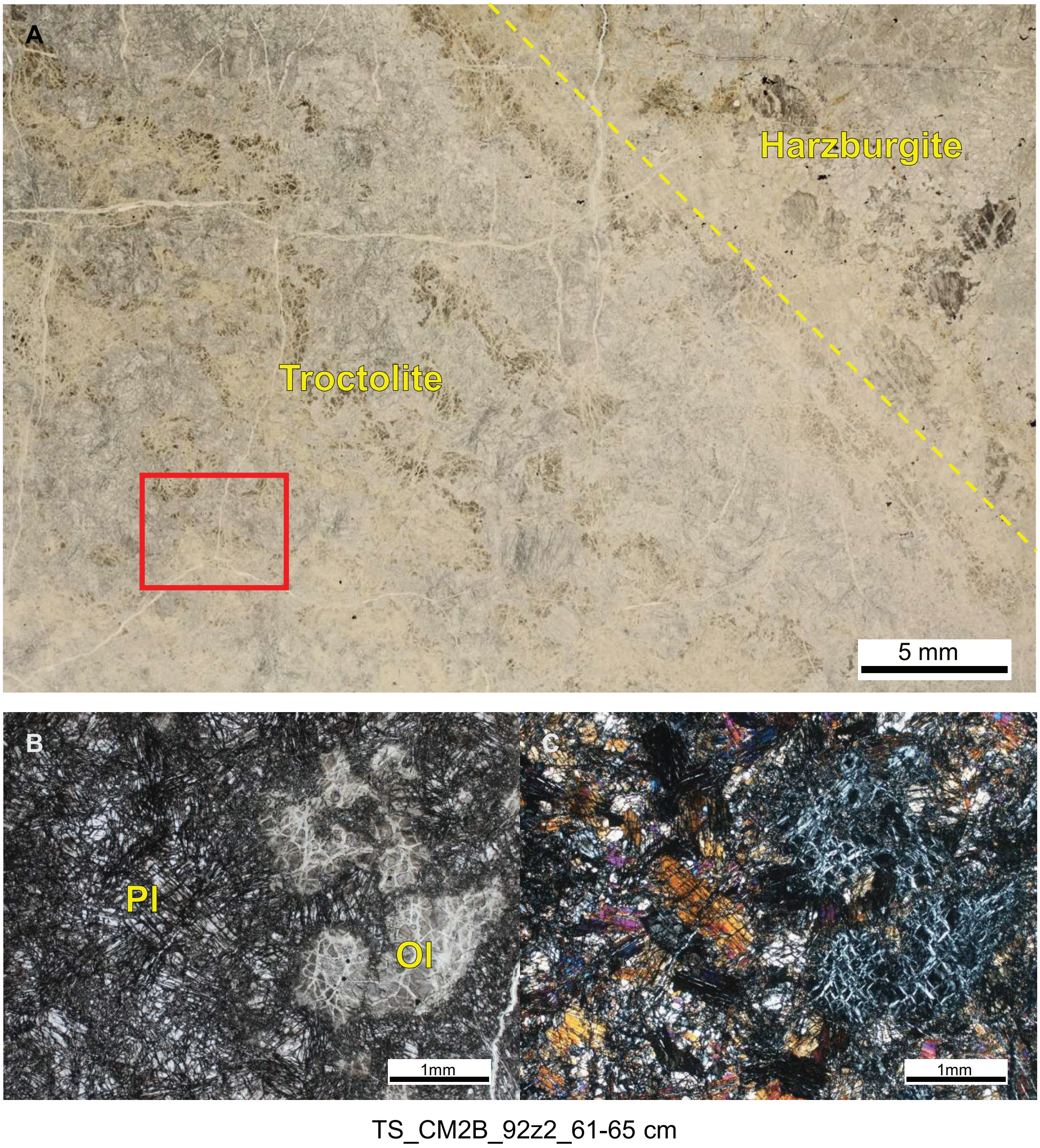

Figure F23. Gabbronorite in Dunite Sequence (Subunit 2d: gabbronorite), Hole CM2B. **A.** Whole thin section scan (PPL). **B–E.** Close-up of red boxes (B, D: PPL, C, E: XPL). Cpx = clinopyroxene, Opx = orthopyroxene.

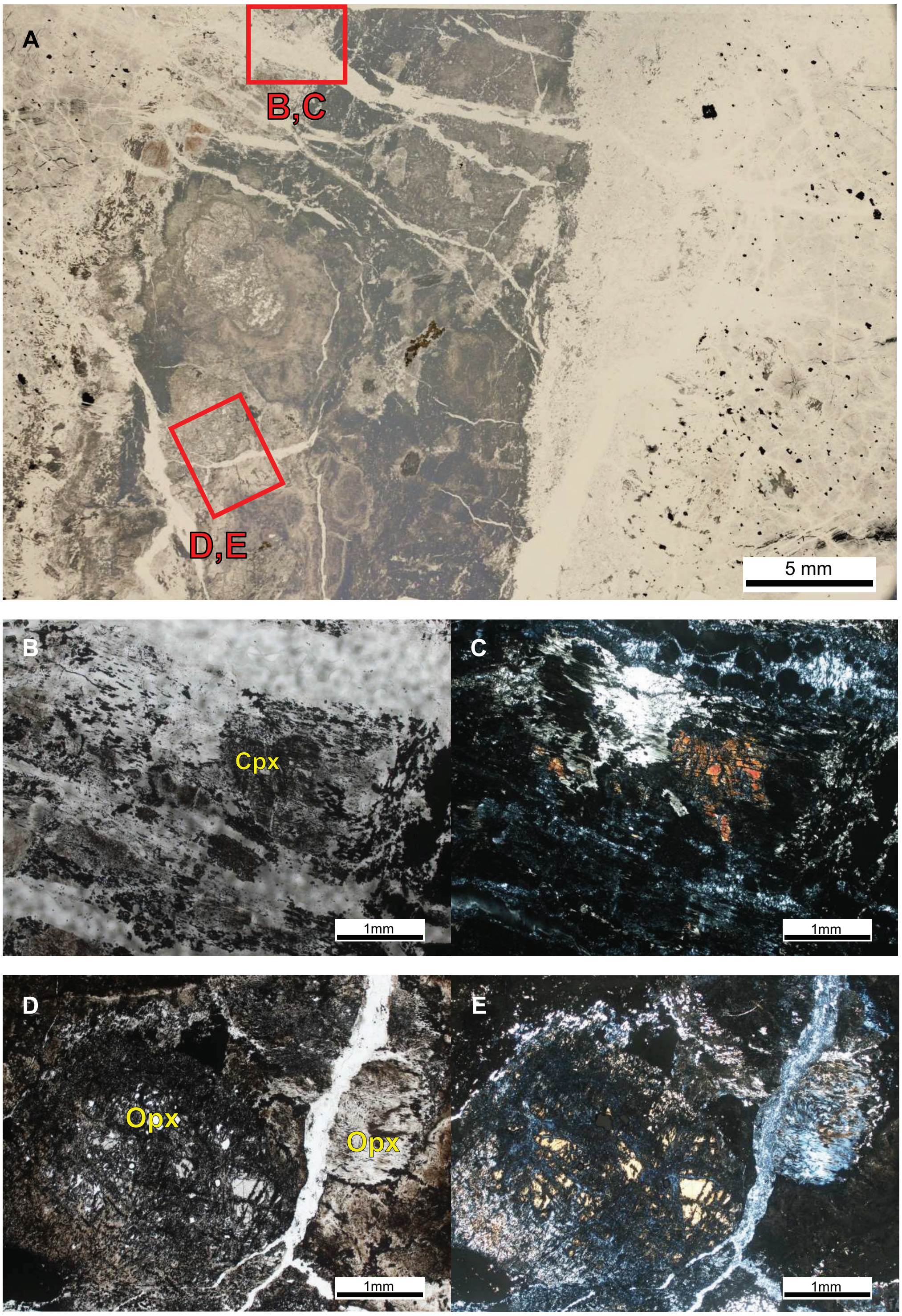

TS_CM2B_12z1_47-51 cm

Figure F24. Fine-grained gabbro in Dunite Sequence, Hole CM2B. (**A**) Core image and photomicrographs under (**B**, **D**) PPL and (**C**, **E**) XPL. cpx = clinopyroxene, chl = chlorite.

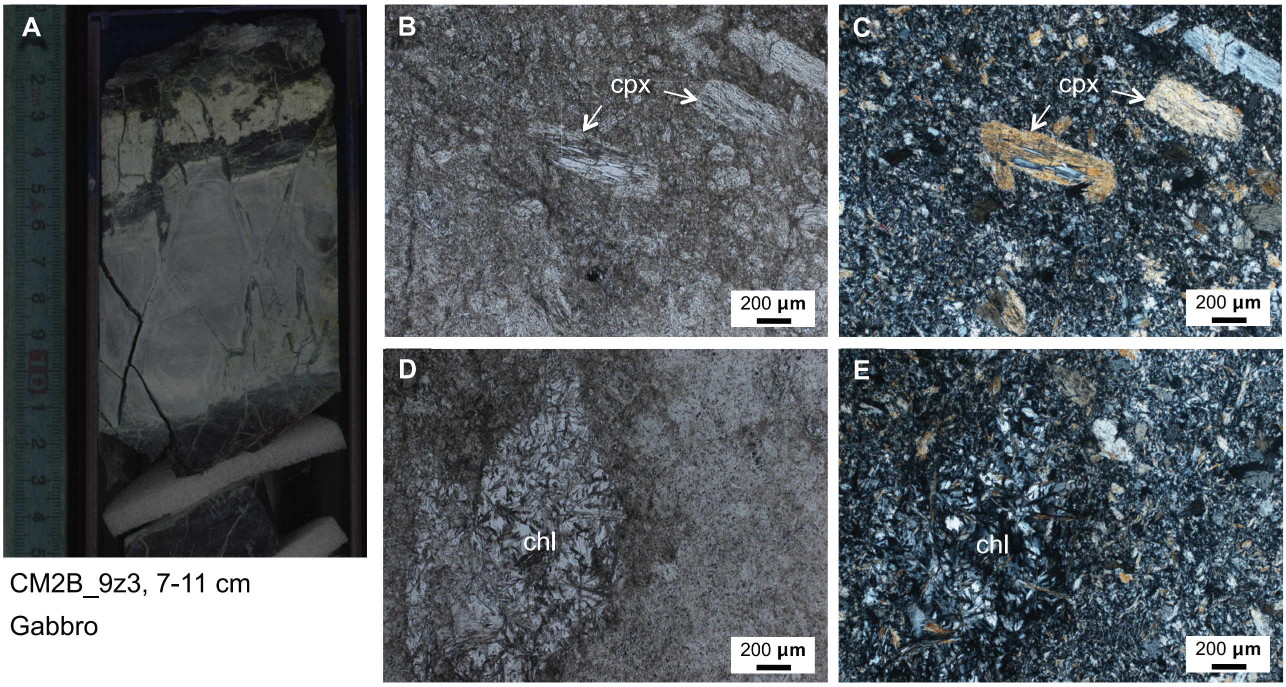

Figure F25. Fine- to medium-grained gabbronorite in Dunite Sequence, Hole CM2B. (**A**) Core image and photomicrographs under (**B**, **D**) PPL and (**C**, **E**) XPL. chl = chlorite.

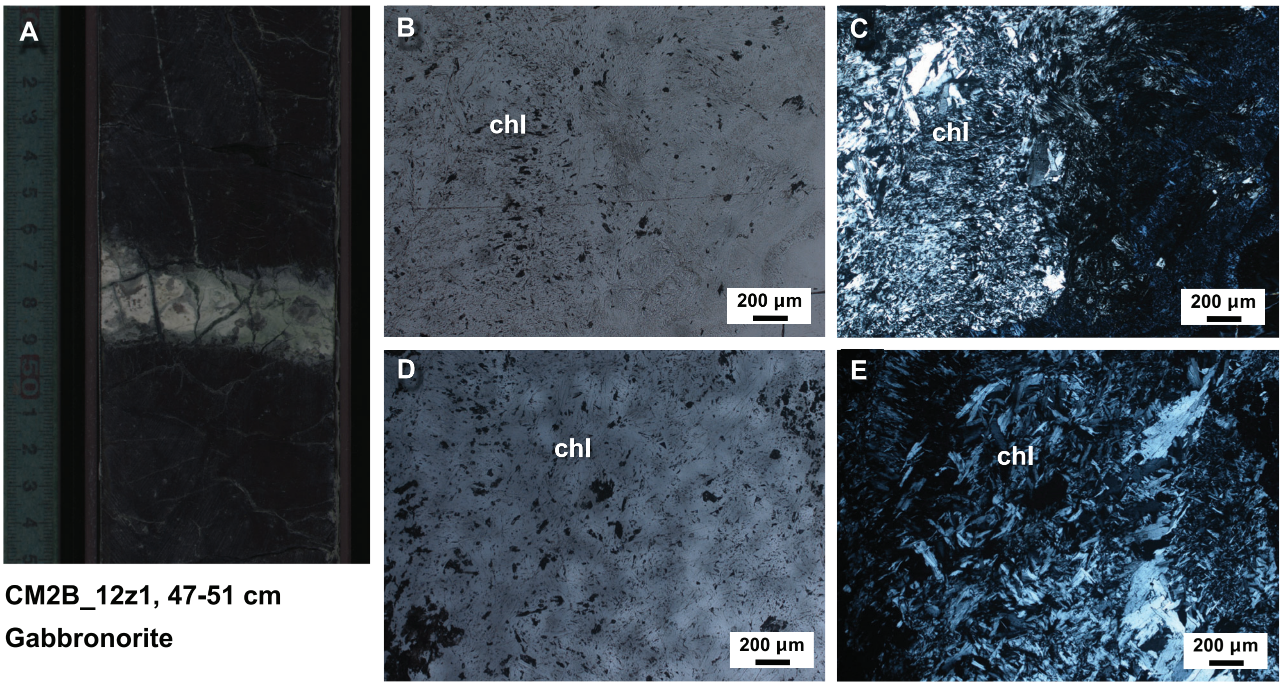

Figure F26. Fine-grained gabbro in Dunite Sequence, Hole CM2B. (**A**) Core image and photomicrographs under (**B**, **D**) PPL and (**C**, **E**) XPL. amp = amphibolite.

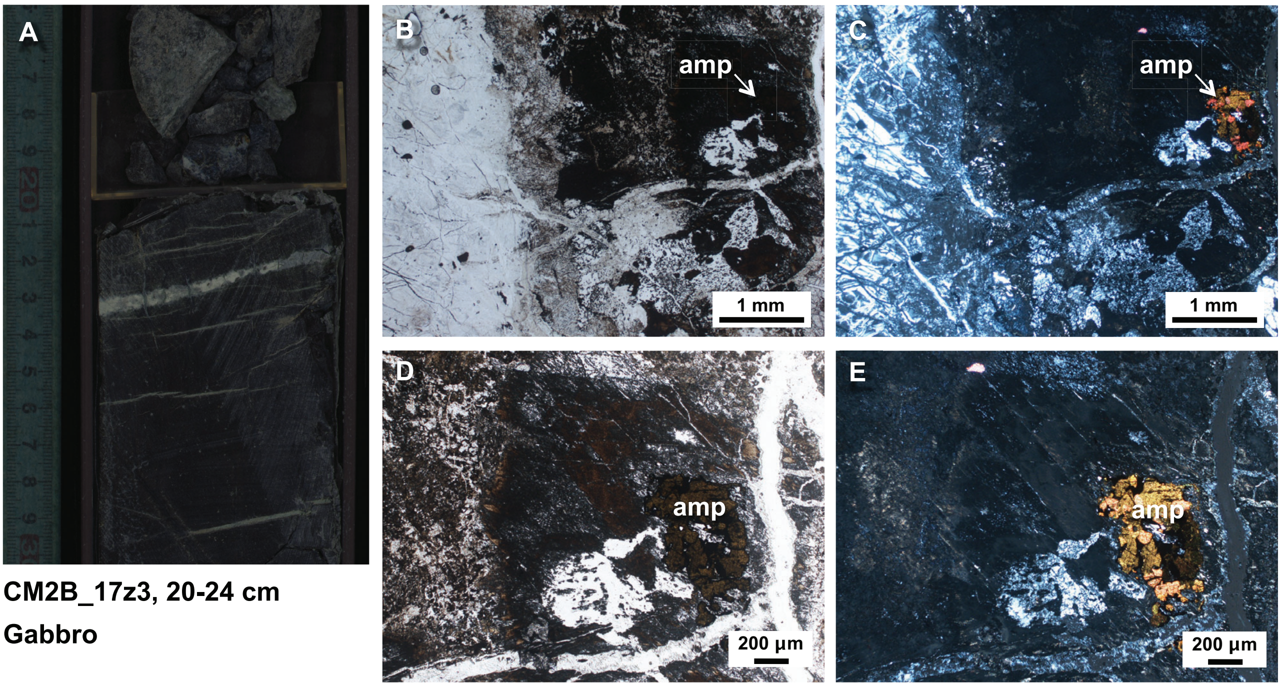

Figure F27. Mylonitic gabbro in Dunite Sequence, Hole CM2B. (**A**) Core image and photomicrographs under (**B**, **D**, **F**) PPL and (**C**, **E**, **G**) XPL. trem = tremolite, chl = chlorite.

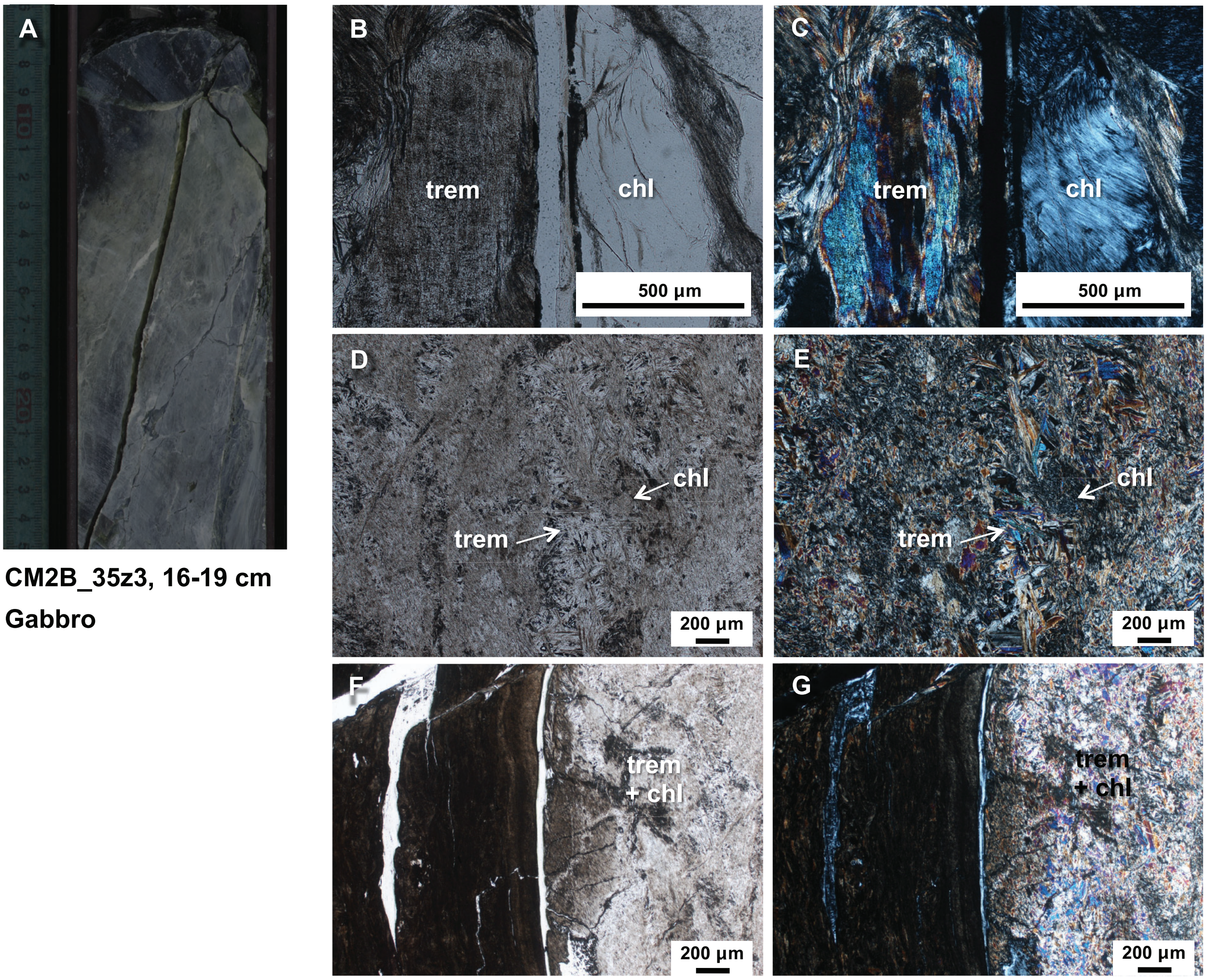

Figure F28. Fine-grained olivine gabbro in Dunite with Gabbro Sequence, Hole CM2B. (**A**) Core image and photomicrographs under (**B**, **D**, **F**) PPL and (**C**, **E**, **G**) XPL. plag = plagioclase, ol = olivine, cpx = clinopyroxene.

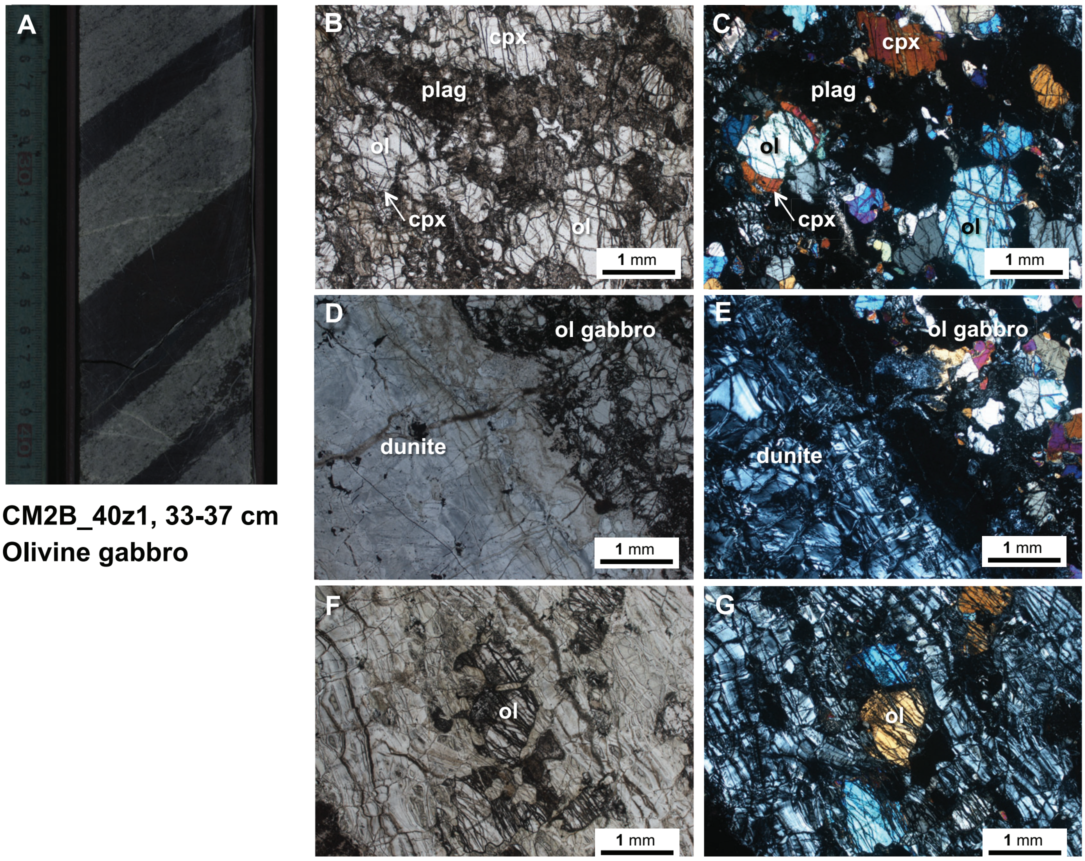

Figure F29. Fine-grained olivine gabbro in Dunite with Gabbro Sequence, Hole CM2B. (**A**) Core image and photomicrographs under (**B**, **D**) PPL and (**C**, **E**) XPL. plag = plagioclase, ol = olivine, cpx = clinopyroxene.

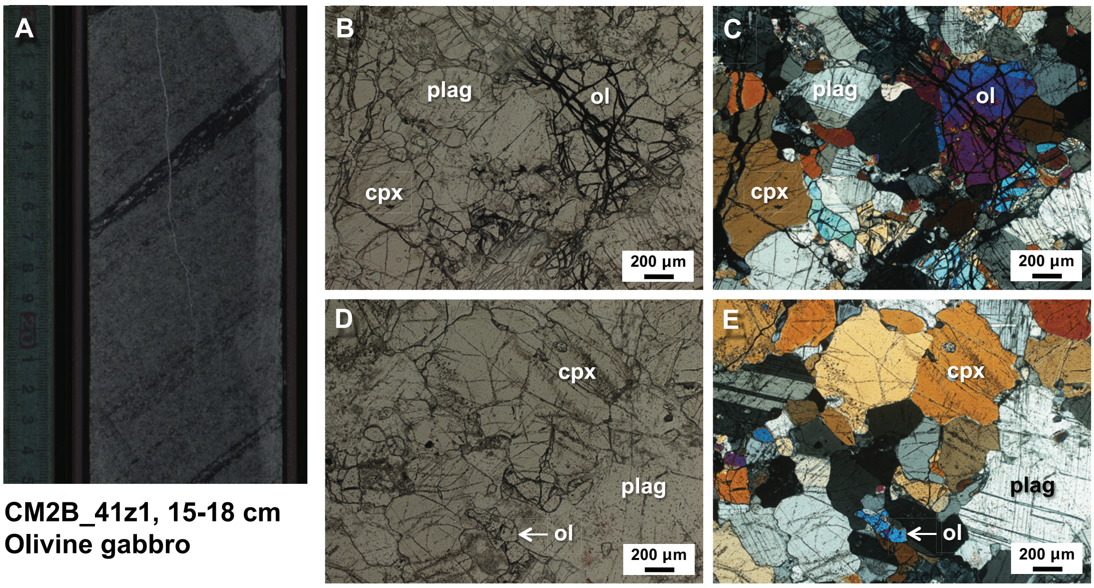

Figure F30. Fine-grained wehrlite in Dunite with Gabbro Sequence, Hole CM2B. (**A**) Core image and photomicrographs under (**B**, **D**) PPL and (**C**, **E**) XPL. ol = olivine, cpx = clinopyroxene.

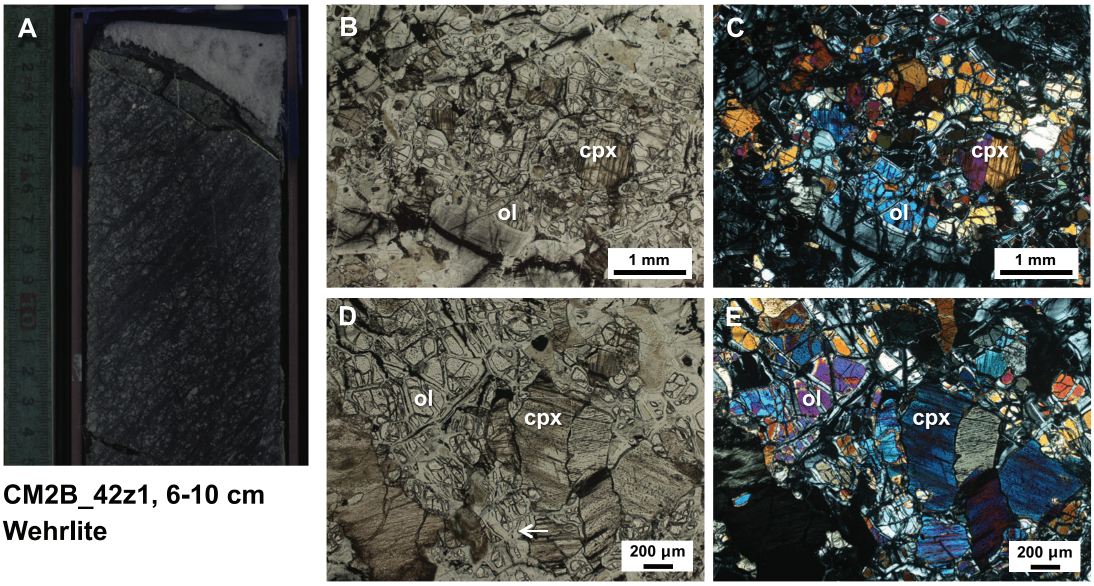

Figure F31. Fine-grained olivine gabbro in Dunite with Gabbro Sequence, Hole CM2B. (**A**) Core image and photomicrographs under (**B**, **D**, **F**) PPL and (**C**, **E**, **G**) XPL. plag = plagioclase, ol = olivine, cpx = clinopyroxene.

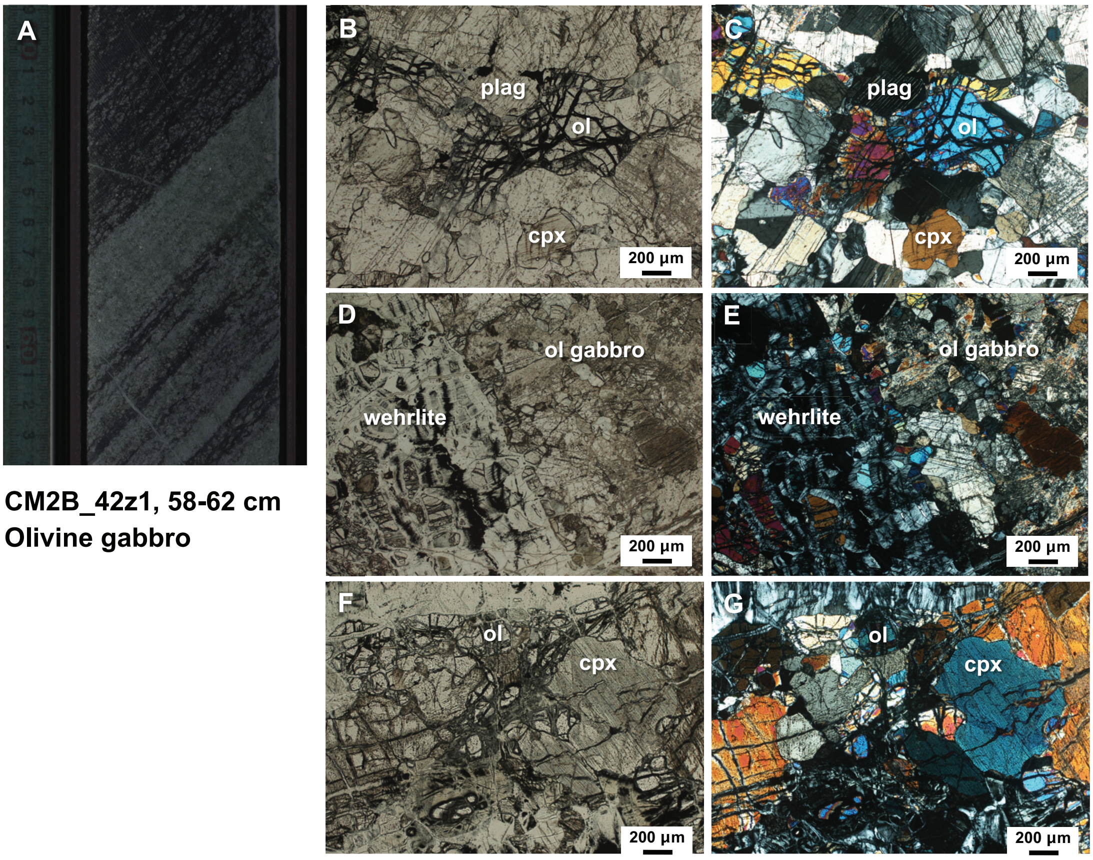

Figure F32. Medium-grained wehrlite in Dunite with Gabbro Sequence, Hole CM2B. (**A**) Core image and photomicrographs under (**B**, **D**) PPL and (**C**, **E**) XPL. cpx = clinopyroxene, ol = olivine.

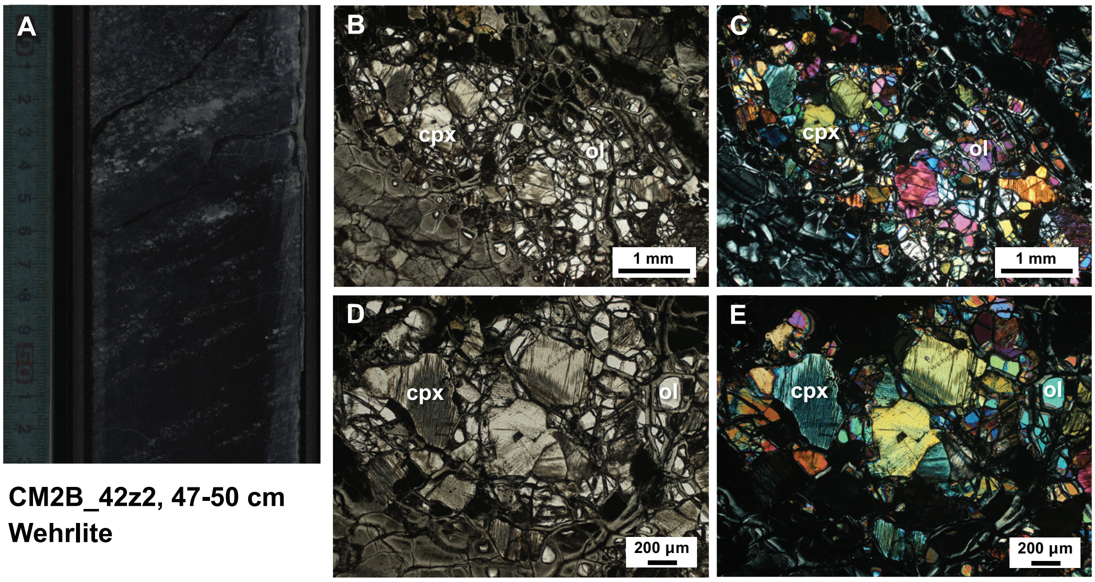

Figure F33. Fine-grained olivine gabbro in Dunite with Gabbro Sequence, Hole CM2B. (**A**) Core image and photomicrographs under (**B**, **D**) PPL and (**C**, **E**) XPL. cpx = clinopyroxene, plag = plagioclase, ol = olivine.

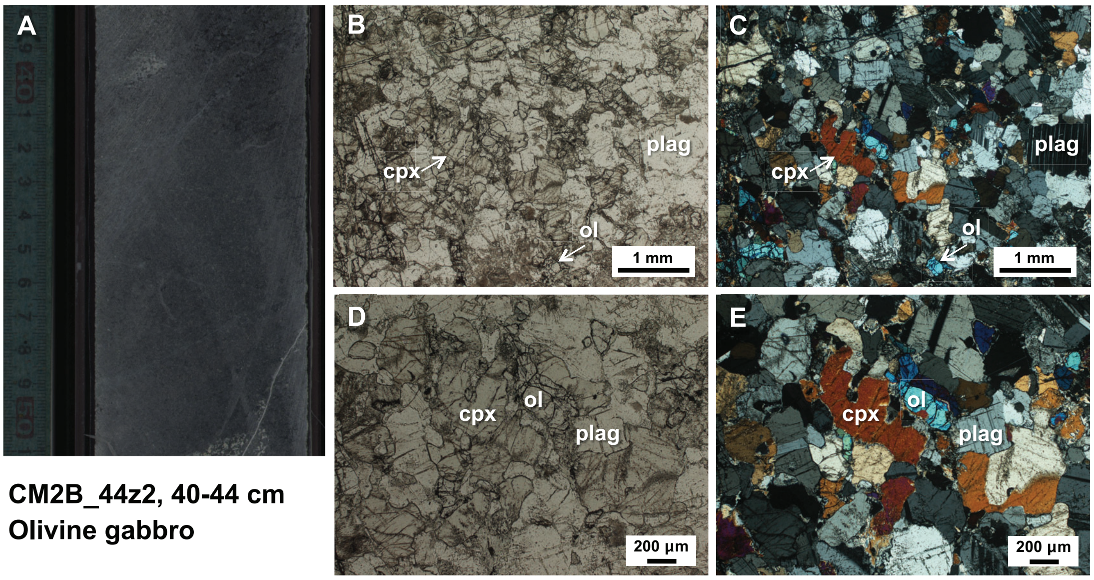

Figure F34. Medium-grained gabbro in Dunite with Gabbro Sequence. (**A**) Core image and photomicrographs. (**B**, **D**, **F**) PPL and (**C**, **E**, **G**) XPL. cpx = clinopyroxene, act = actinolite, srp = serpentinite, prh = prehnite, chl = chlorite.

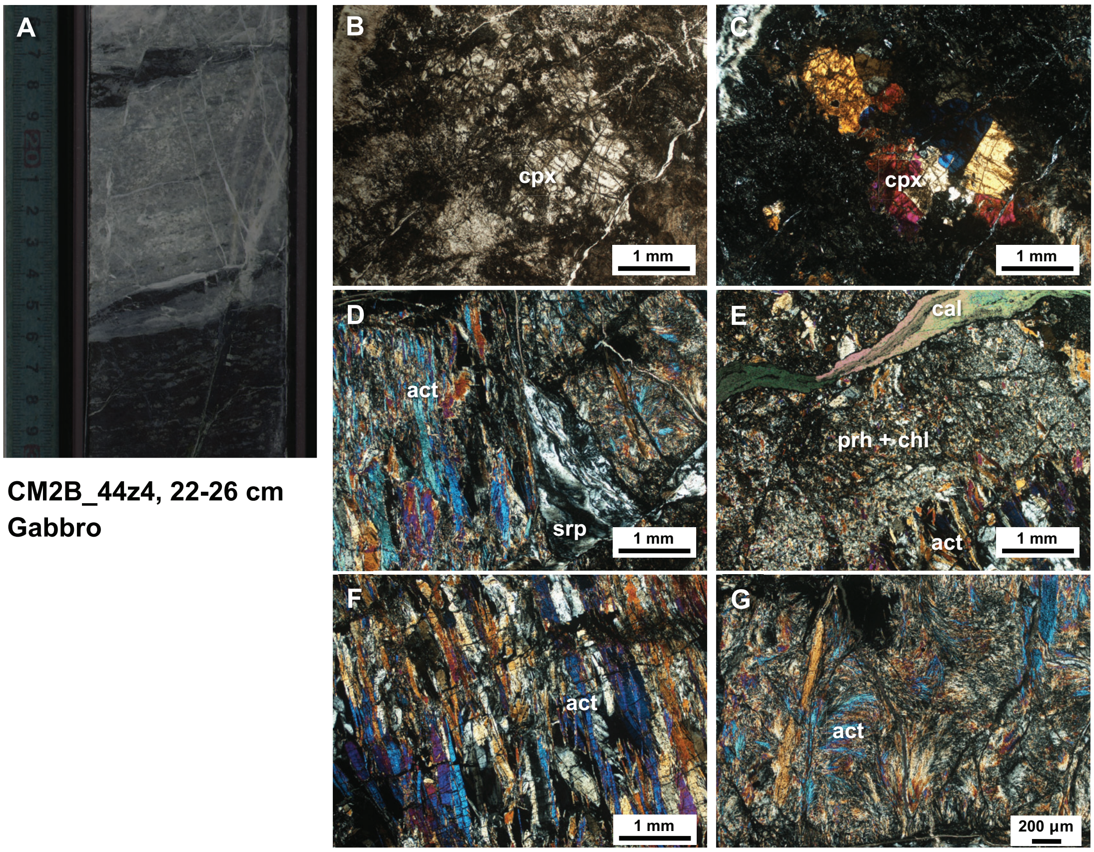

Figure F35. Fine-grained troctolite in Mantle Sequence, Hole CM2B. (**A**) Core image and photomicrographs under (**B**, **D**, **F**) PPL and (**C**, **E**, **G**) XPL. prh = prehnite.

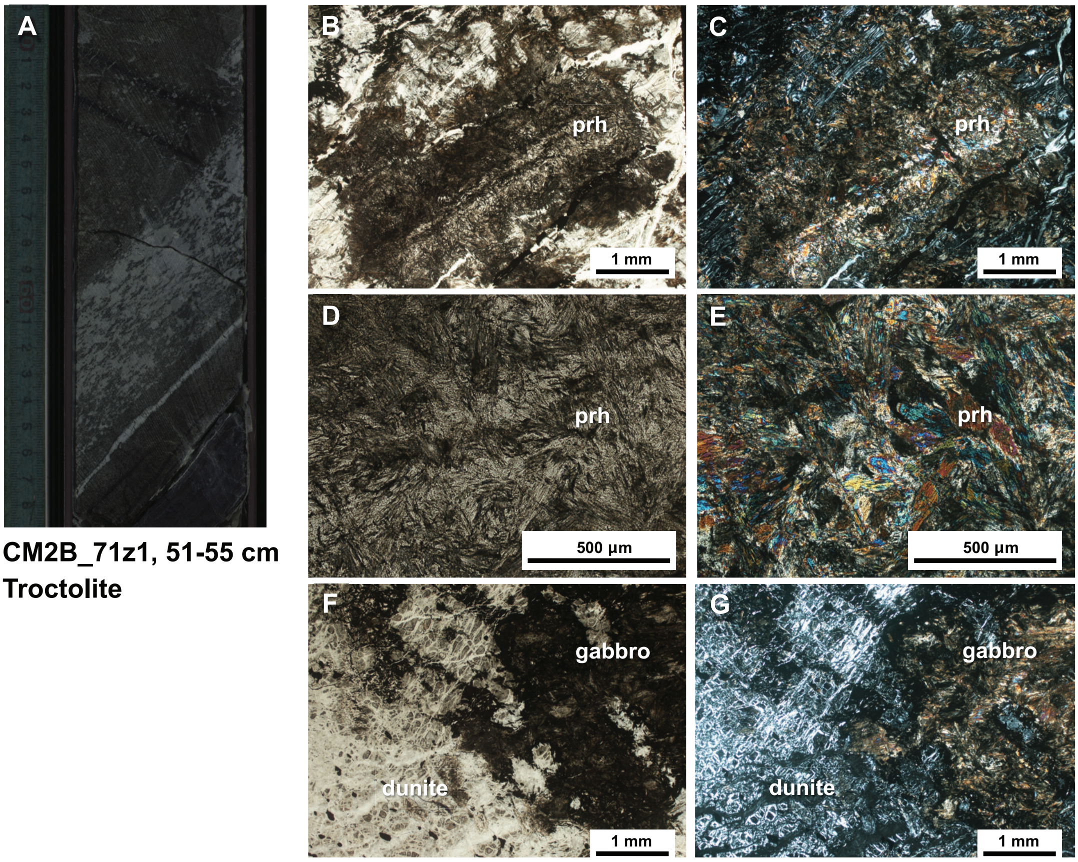

Figure F36. Representative dunite from each lithologic sequence (PPL; all in same orientation, shown in E). **A, B.** Dunite Sequence. **C, D.** Dunite with Gabbro Sequence. **E.** Mantle Sequence. Ol = olivine, Spl = spinel.

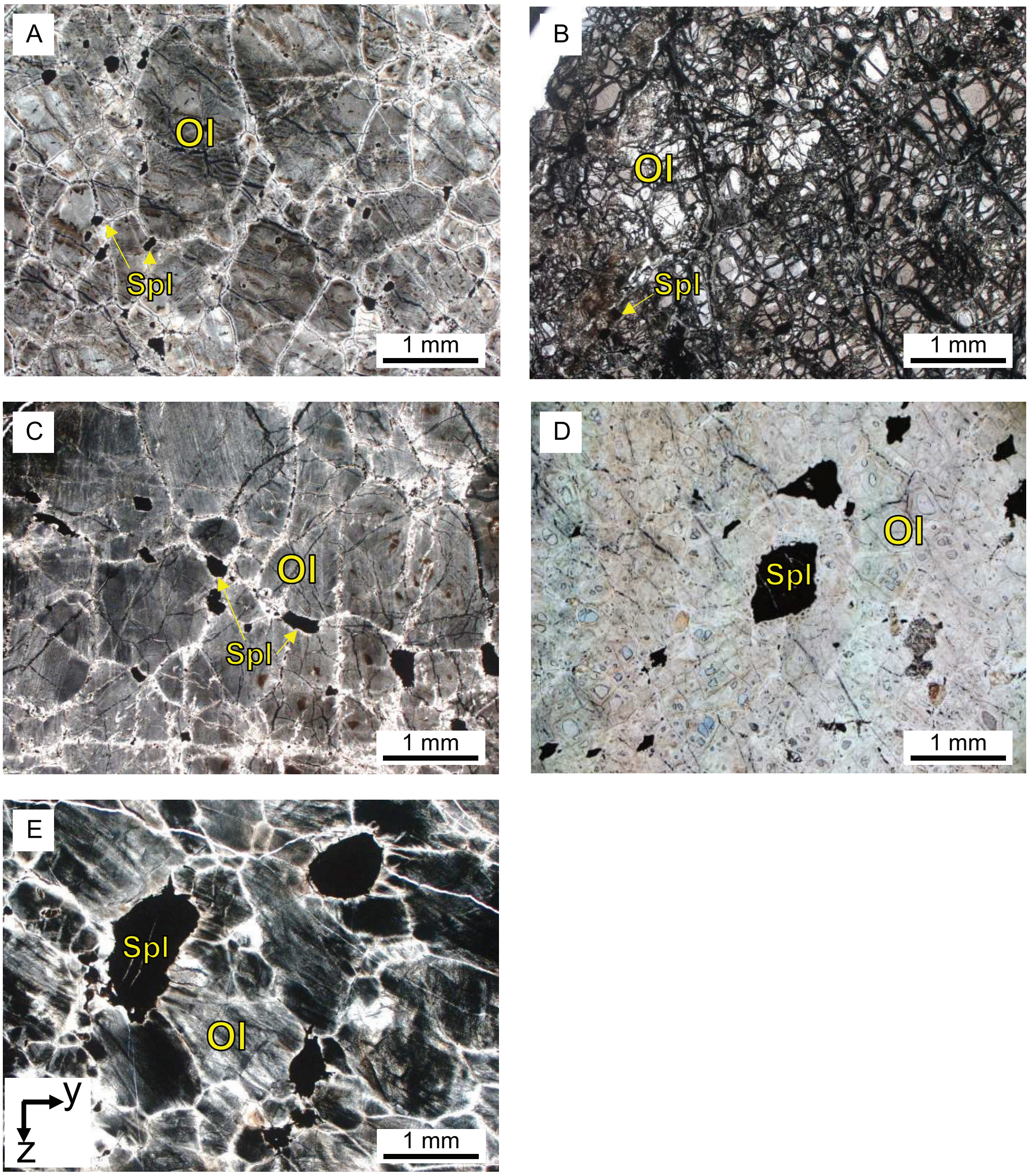

A) TS_CM2B-11z1_34-38 cm
B) TS_CM2B_37_1_51-55 cm
C) TS_CM2B_50z1_32-35 cm
D) TS_CM2B_57z3_50-55 cm
E) TS_CM2B_96z2_68-71 cm

Figure F37. A. Molar Mg/Si vs. Al/Si. Many Hole CM1A and CM2B dunites and harzburgites plot below the terrestrial mantle array of Jagoutz et al. (1979), consistent with some dunites and harzburgites from elsewhere in Oman (Godard et al., 2000; Monnier et al., 2006; Hanghøj et al., 2010). Yellow circle = a Hole CM2B wehrlite. **B.** Normative olivine and pyroxene modes in dunites, harzburgites, and wehrlites from Holes CM1A and CM2B. opx = orthopyroxene, cpx = clinopyroxene.

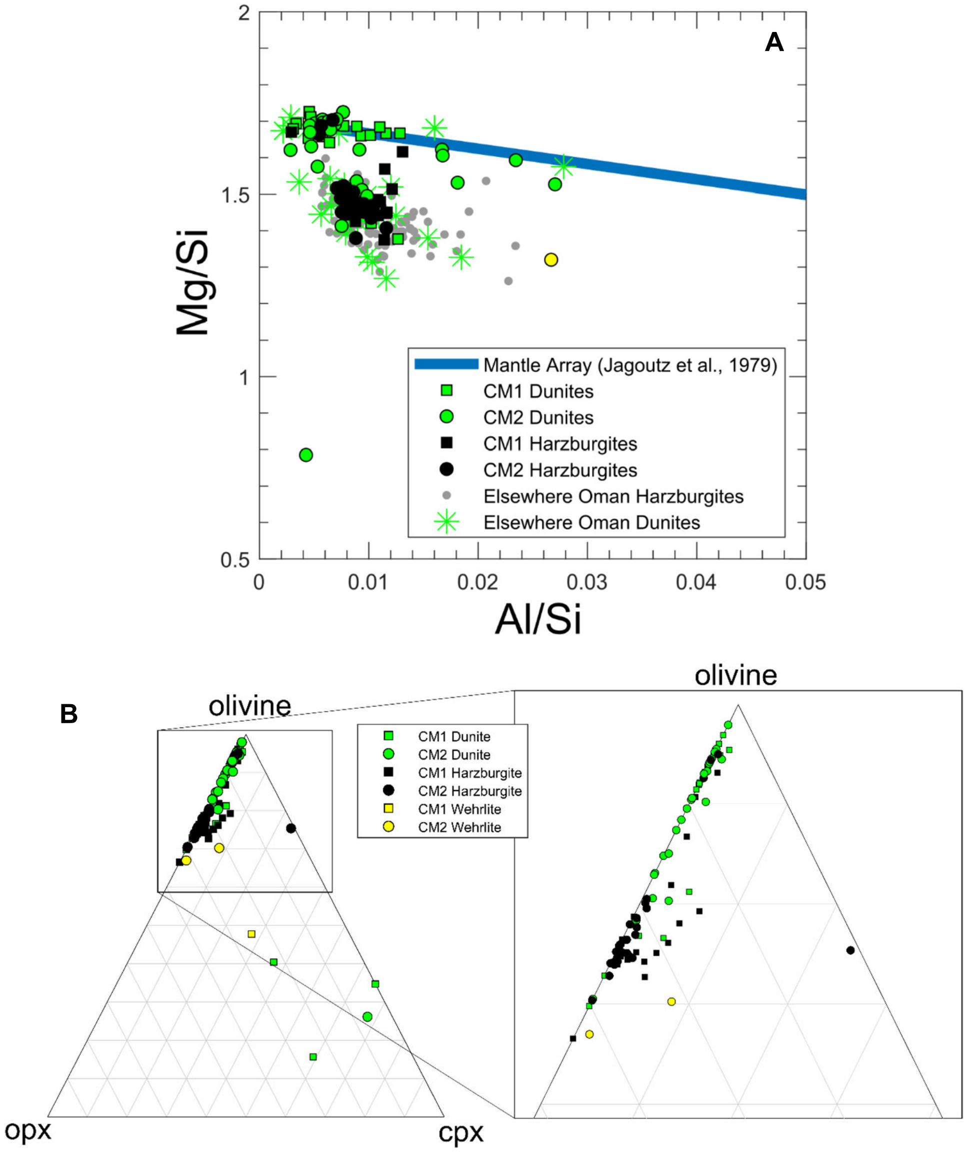

Figure F38. Relative (**A**) olivine, (**B**) orthopyroxene (OPX), (**C**) clinopyroxene (CPX), (**D**) spinel, and (**E**) plagioclase (Plag) mode distributions in Hole CM1A and CM2B peridotites.

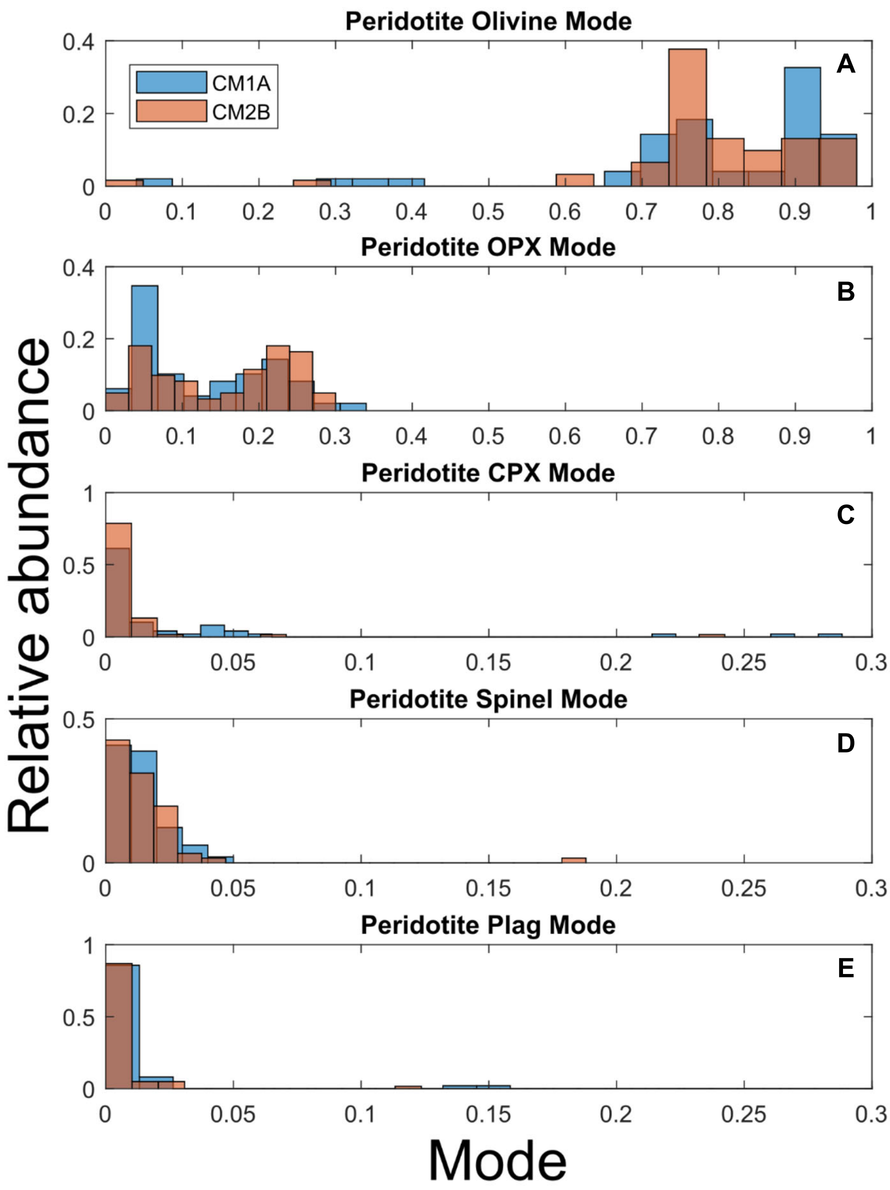

Figure F39. **A.** Orthopyroxene (OPX) vs. olivine modes, Holes CM1A and CM2B. **B.** Clinopyroxene (CPX) vs. olivine modes. **C.** Clinopyroxene + orthopyroxene + feldspar vs. olivine modes. **D.** Clinopyroxene vs. orthopyroxene modes. Many dunites have relatively high orthopyroxene modes, and some harzburgites have low orthopyroxene modes (A). Nearly all peridotites are clinopyroxene poor (D).

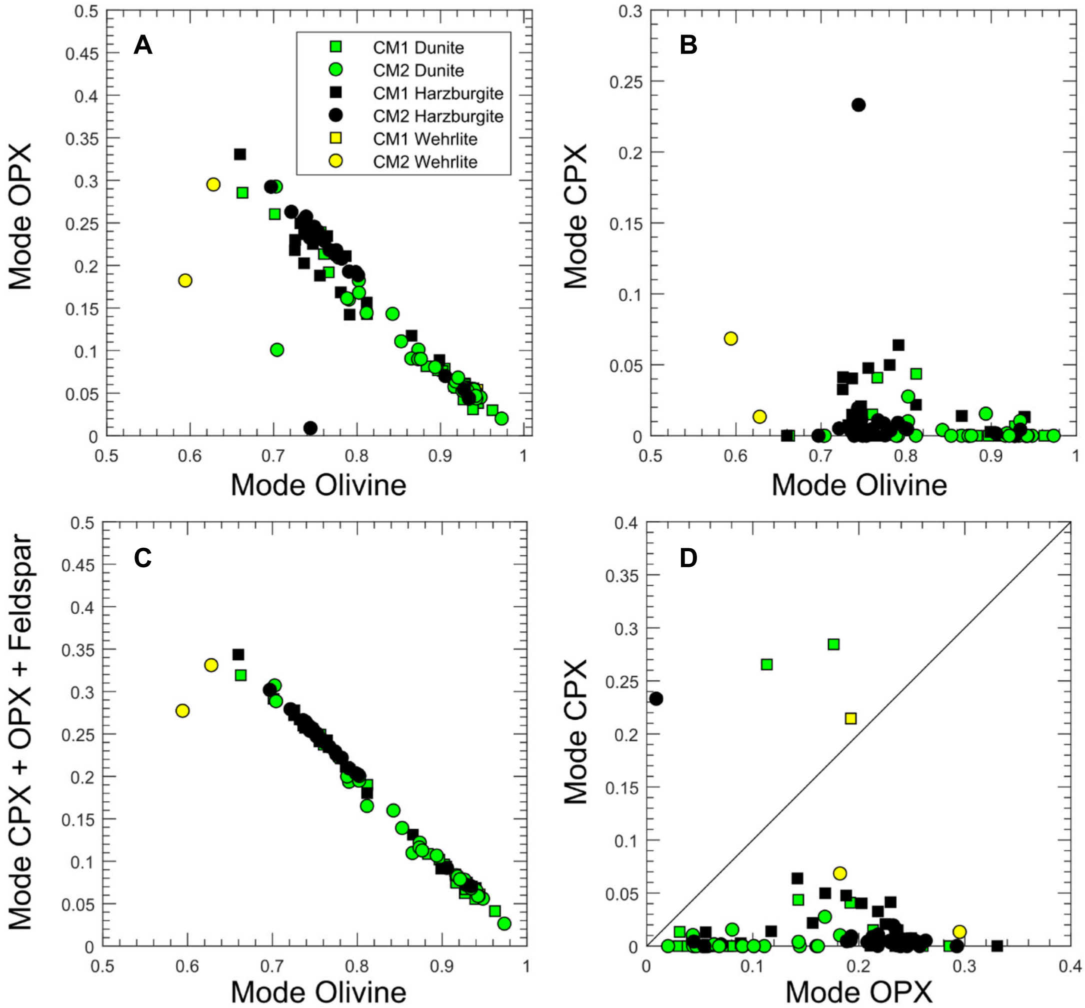

Figure F40. Mineral modes plotted as a function of depth for Holes (**A**) CM2A and (**B**) CM2B. Note the increase in normative pyroxene moving downhole. OPX = orthopyroxene, CPX = clinopyroxene, Plag = plagioclase.

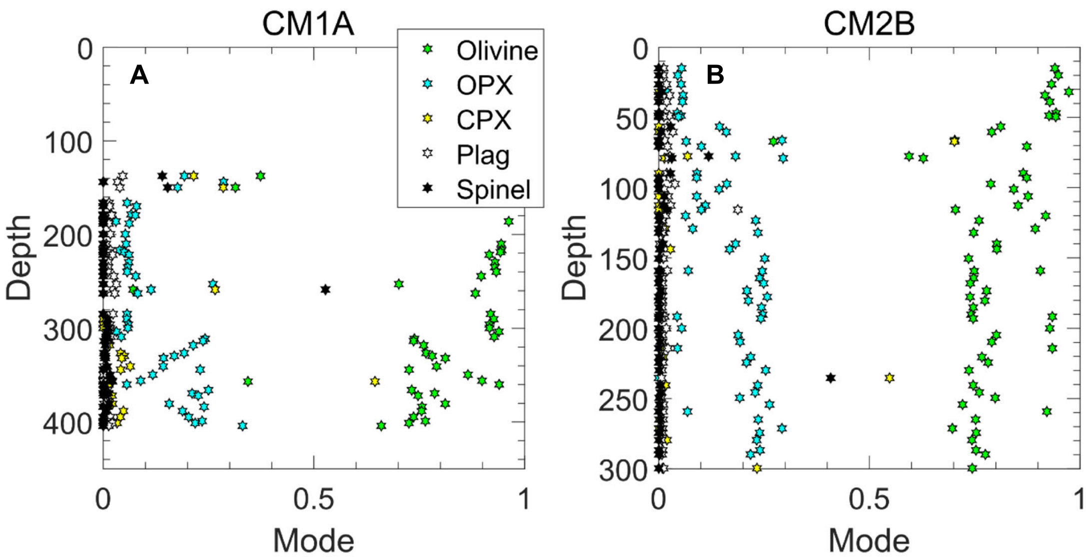

Figure F41. Comparison of lithology logs of both holes transposed into the assumed regional geology of the area around Holes CM1A and CM2B. Macroscopically derived modes for olivine (Ol), plagioclase (Pl), clinopyroxene (Cpx), and orthopyroxene (Opx) are merged (black = Hole CM1A; red = Hole CM2B). Depth was adjusted using the boundary between the Dunite and Dunite with Gabbro Sequence as reference level.

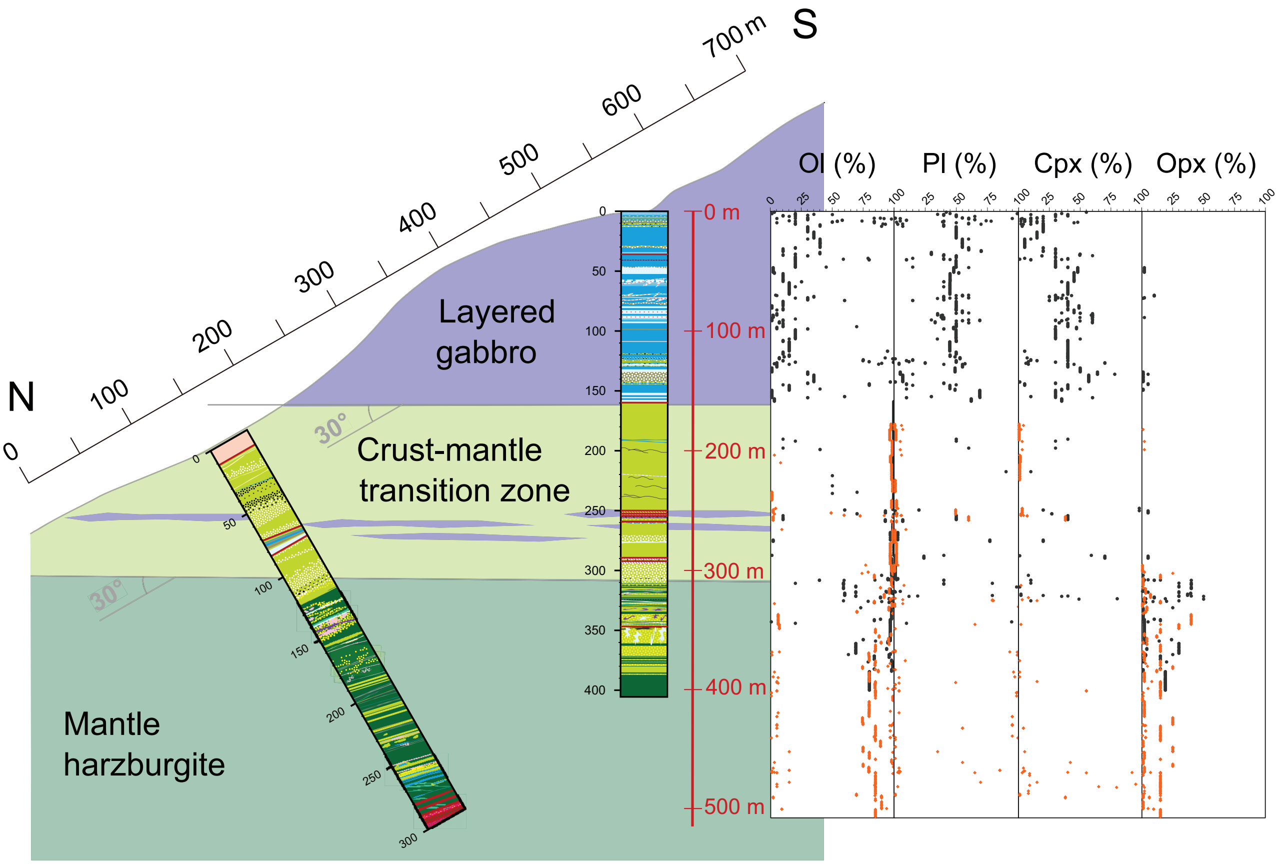

Figure F42. Schematic illustration of Hole CM1A highlighting the 4 principal lithologic sequences and 2 proposed magmatic mechanisms for the formation of the CMTZ: dunite formation by mid-ocean-ridge basalt (MORB) melt-peridotite interaction (left side) and crystal accumulation in primitive MORB (right side). For details see text.

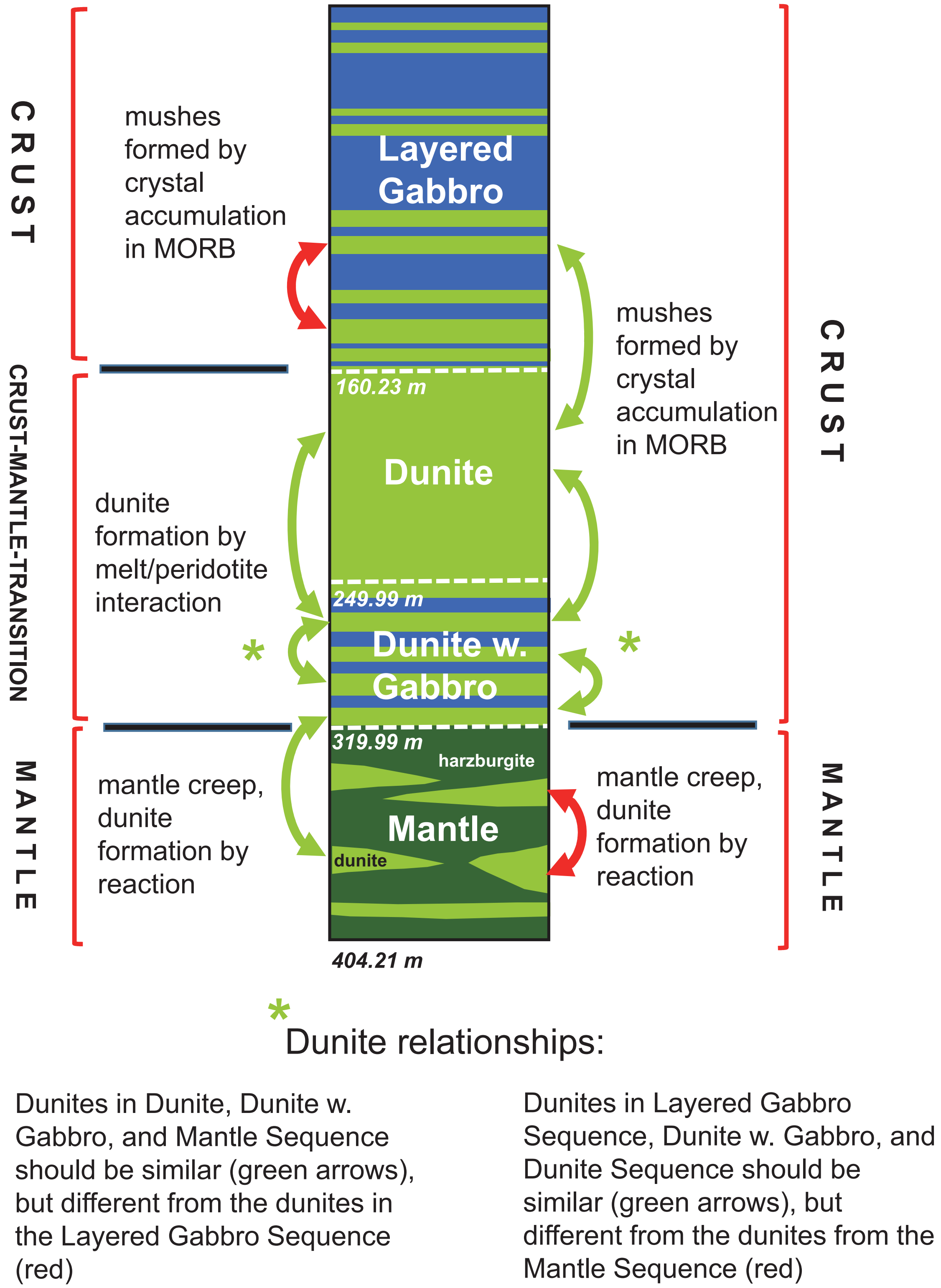

Figure F43. Lithostratigraphic column for Hole CM1A and related downhole plots for selected elements obtained by XRF bulk analyses of massive dunites, which were investigated in detail for relict textures (for details see **Textures of massive dunites** in the **Site CM1** chapter). Light green = dunites from Dunite Sequence; yellow = dunites from Dunite with Gabbro Sequence; dark green = dunites from Mantle Sequence. Note that one analysis marked with an red arrow does not correspond to the assigned thin section. For details see text.

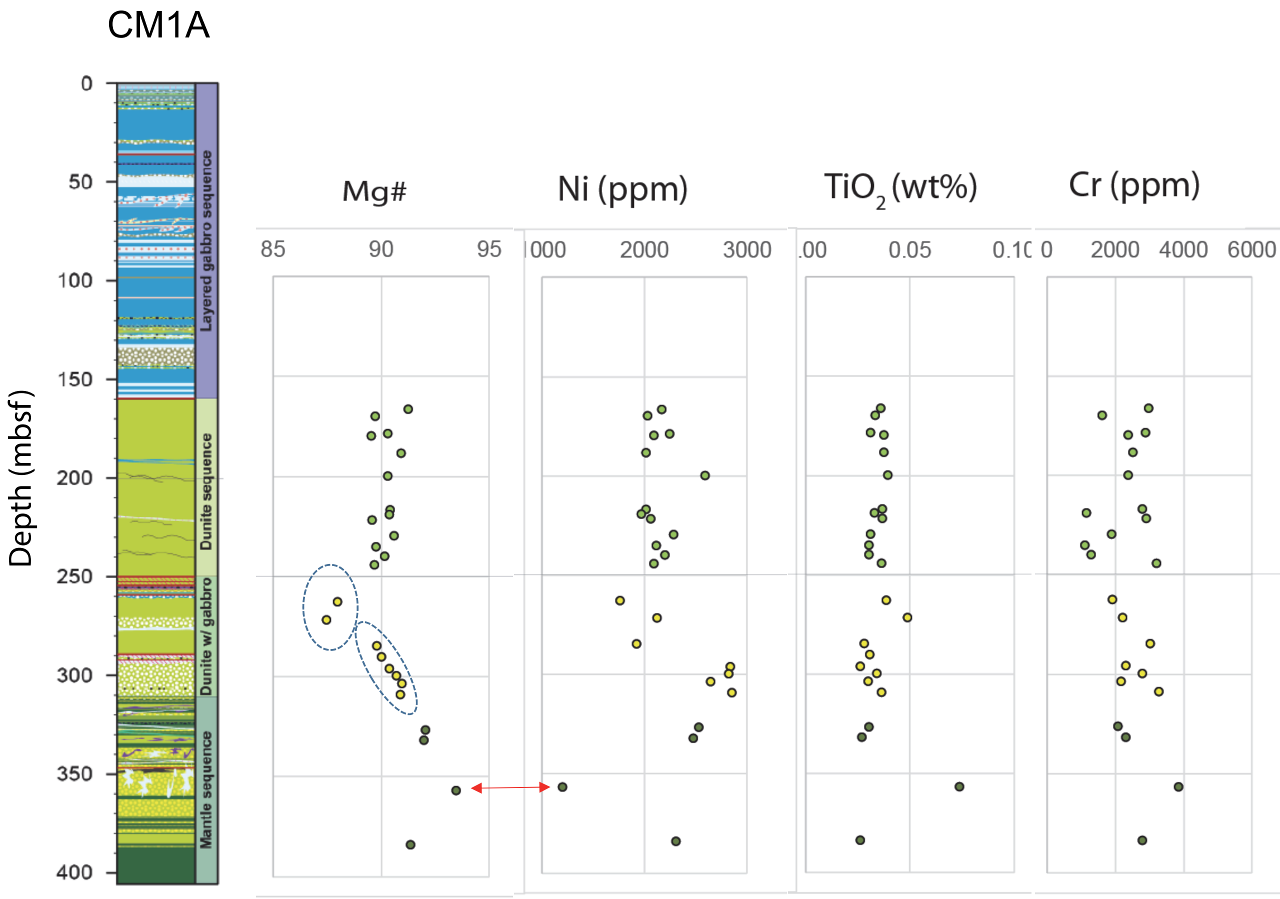

Figure F44. A. Downhole variations in lithology and total alteration, Hole CM2B. **B.** Total alteration intensity in the main lithologic groups. **C.** 10 m running average for background alteration intensity and total alteration intensity. opx = orthopyroxene.

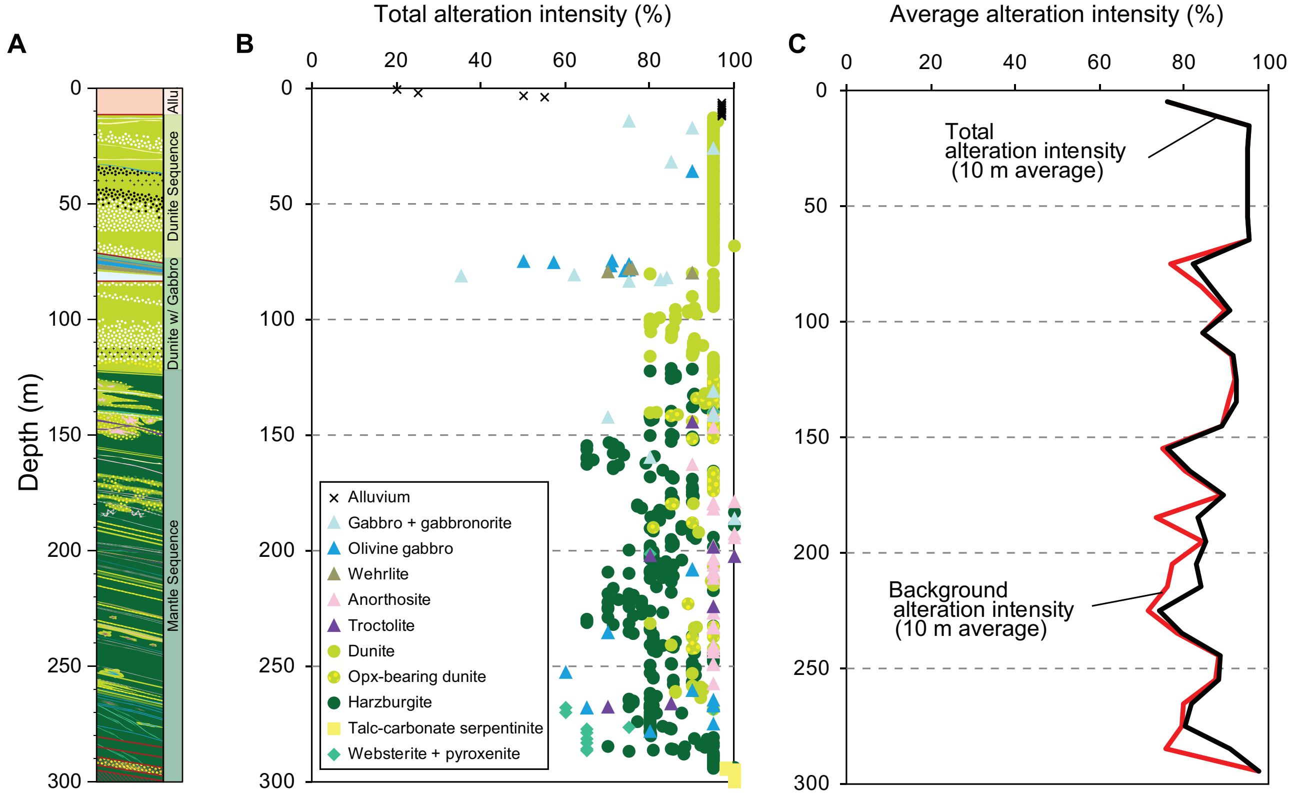

Figure F45. (**A**) Cross-section of CM sites and comparison of downhole plots of total alteration intensity between (**B**) Hole CM1A and (**C**) Hole CM2B.

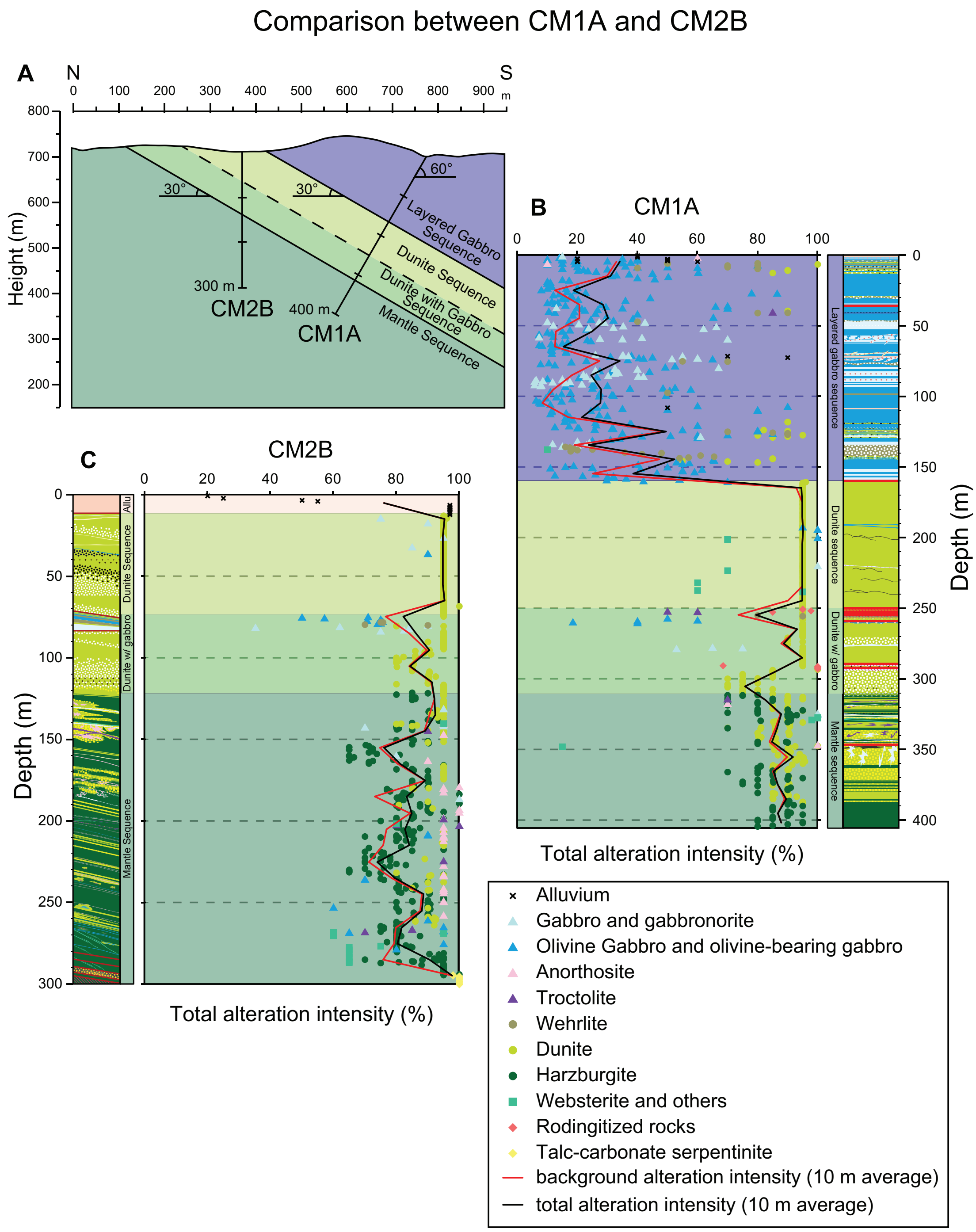

Figure F46. Histograms showing total alteration intensity for the entire Hole CM2B core and variations in background alteration intensity in the main lithologic sequences.

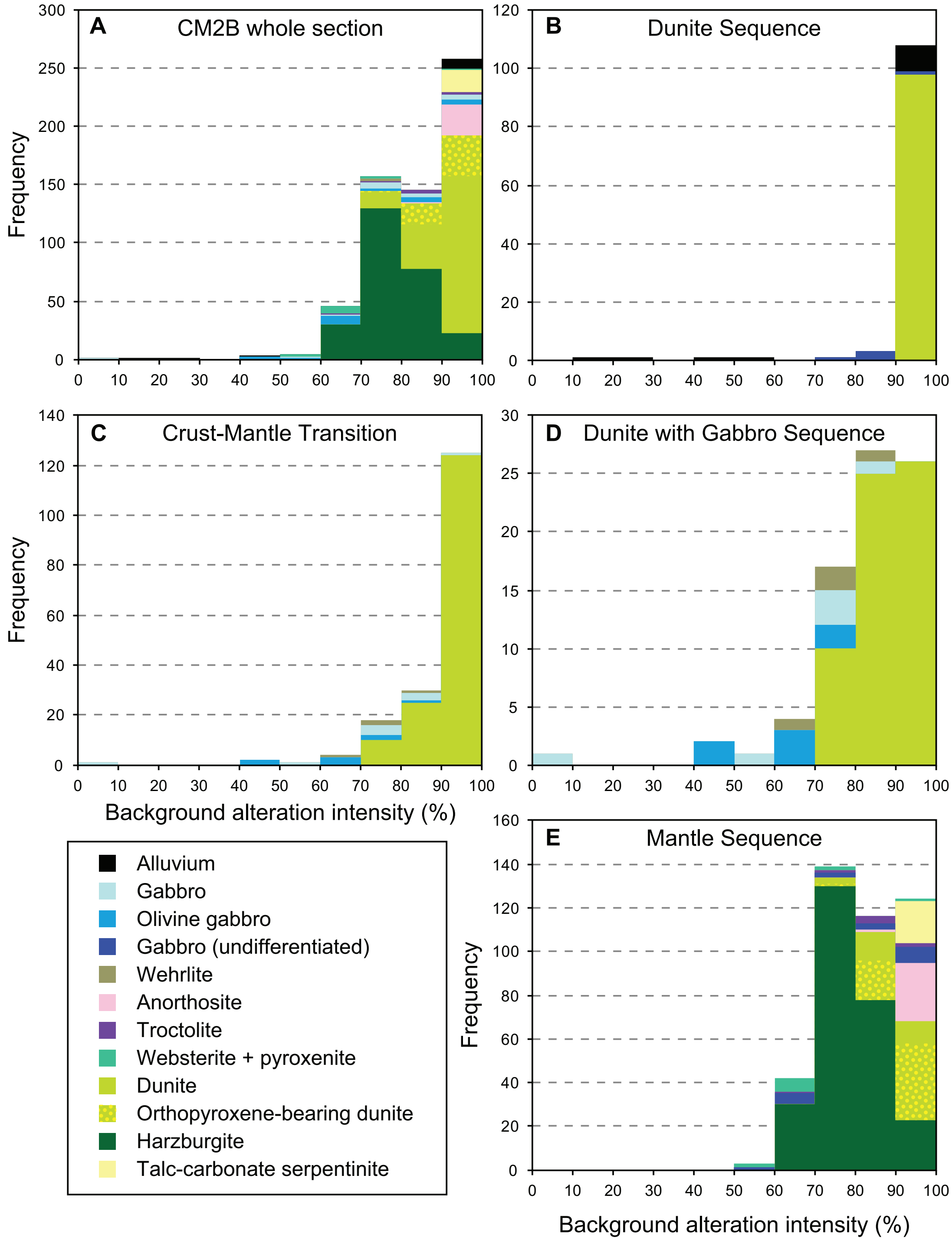

Figure F47. Distribution of secondary minerals in background alteration with depth, Hole CM2B, determined by visual core description and groundtruthed with thin section observations.

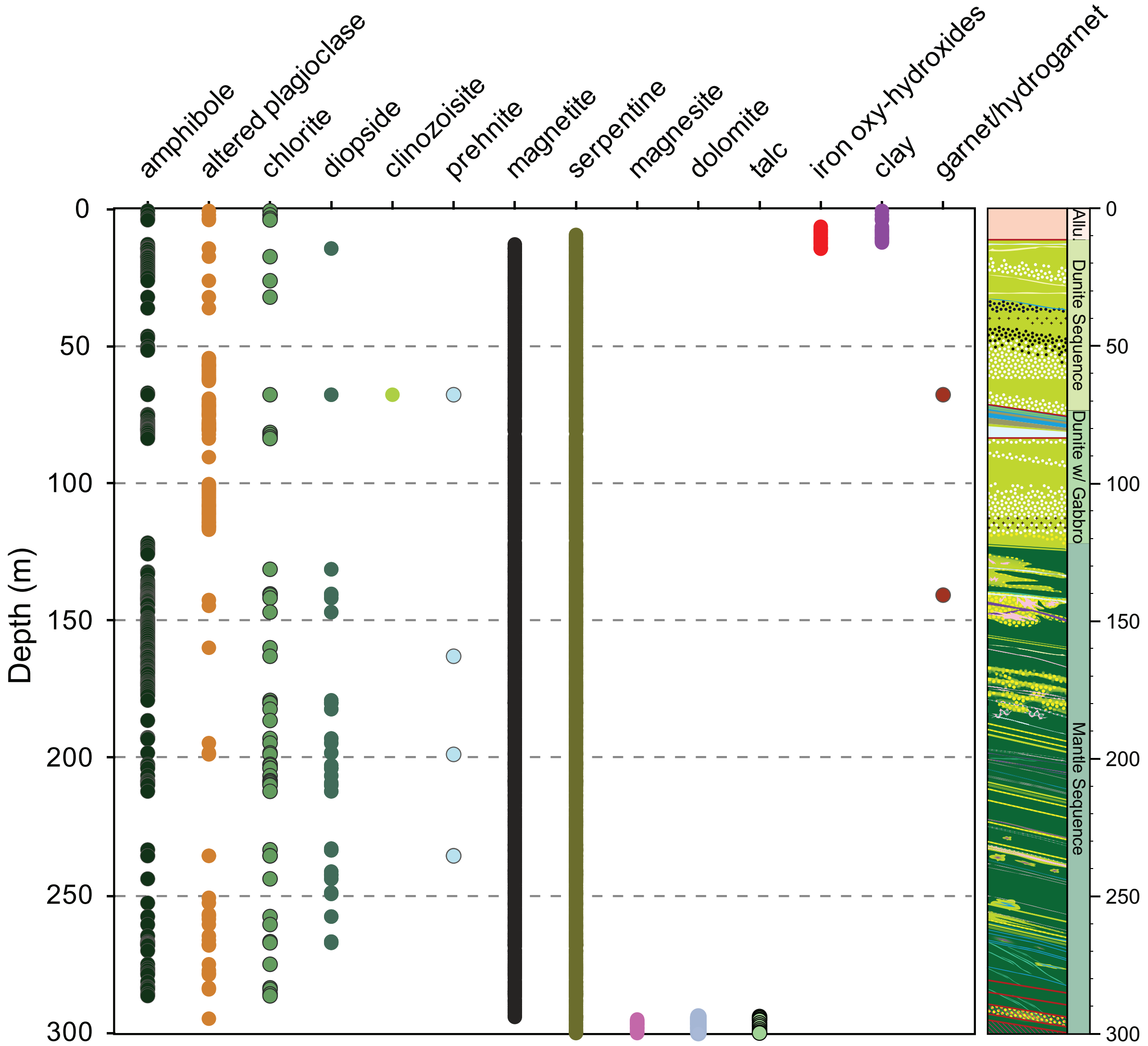

Figure F48. Downhole variation in estimated proportion of vein-filling minerals determined by macroscopic logging, Hole CM2B. Downhole variations in vein intensities are shown in Figure F81. Shown here is the relative abundance of veins per meter, defined as the number of vein entries in the vein log (see Supplemental Table ST6) and takes into account vein networks rather than individual veins. Fine-grained mineral assemblages as replacement of plagioclase were unidentifiable and are plotted as "altered plagioclase."

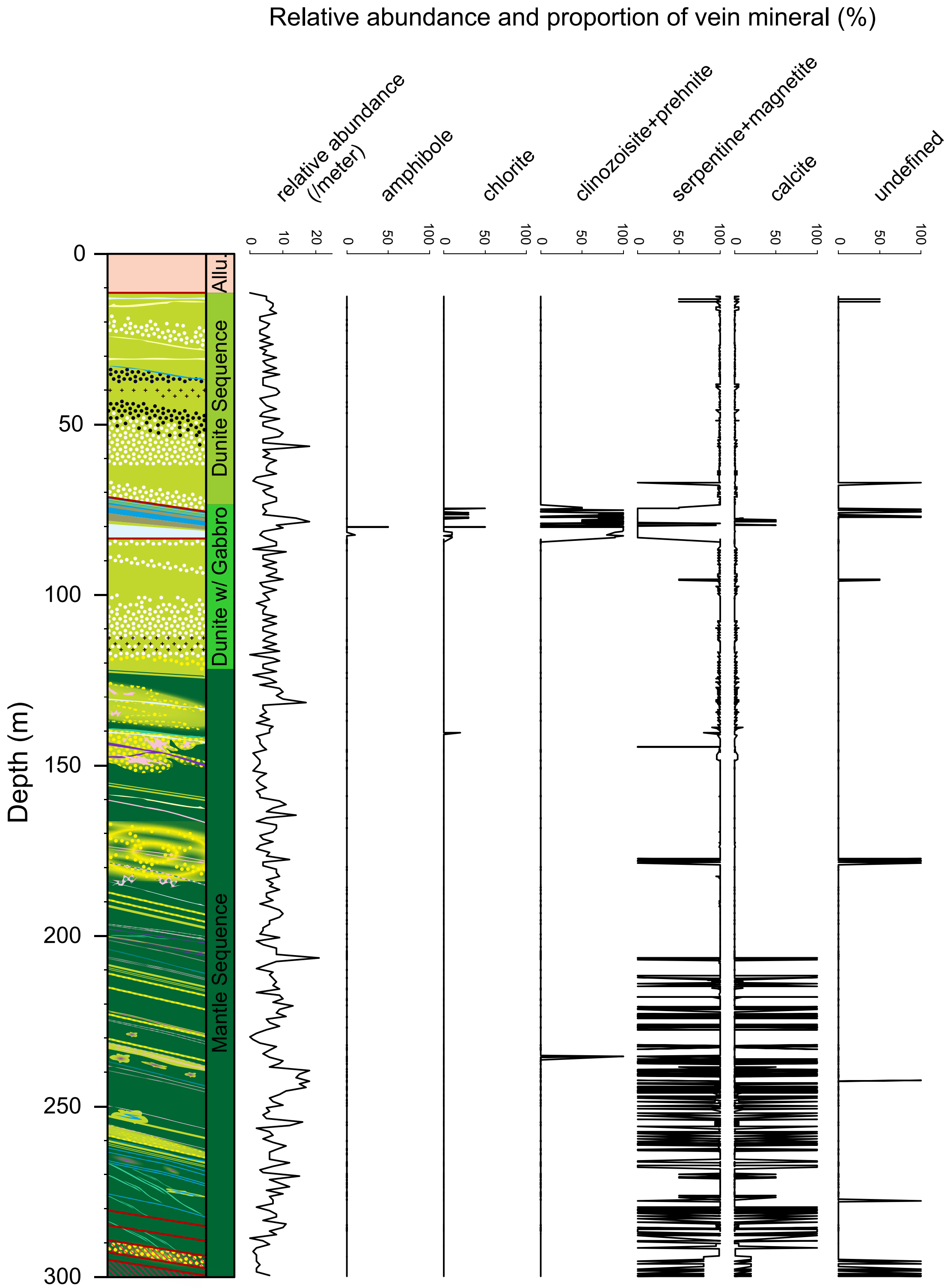

Figure F49. Vein minerals identified by XRD, Hole CM2B. Solid = veins and halos, open = background or patch alteration domains. Mineral abbreviations per Table T5 in the **Methods** chapter.

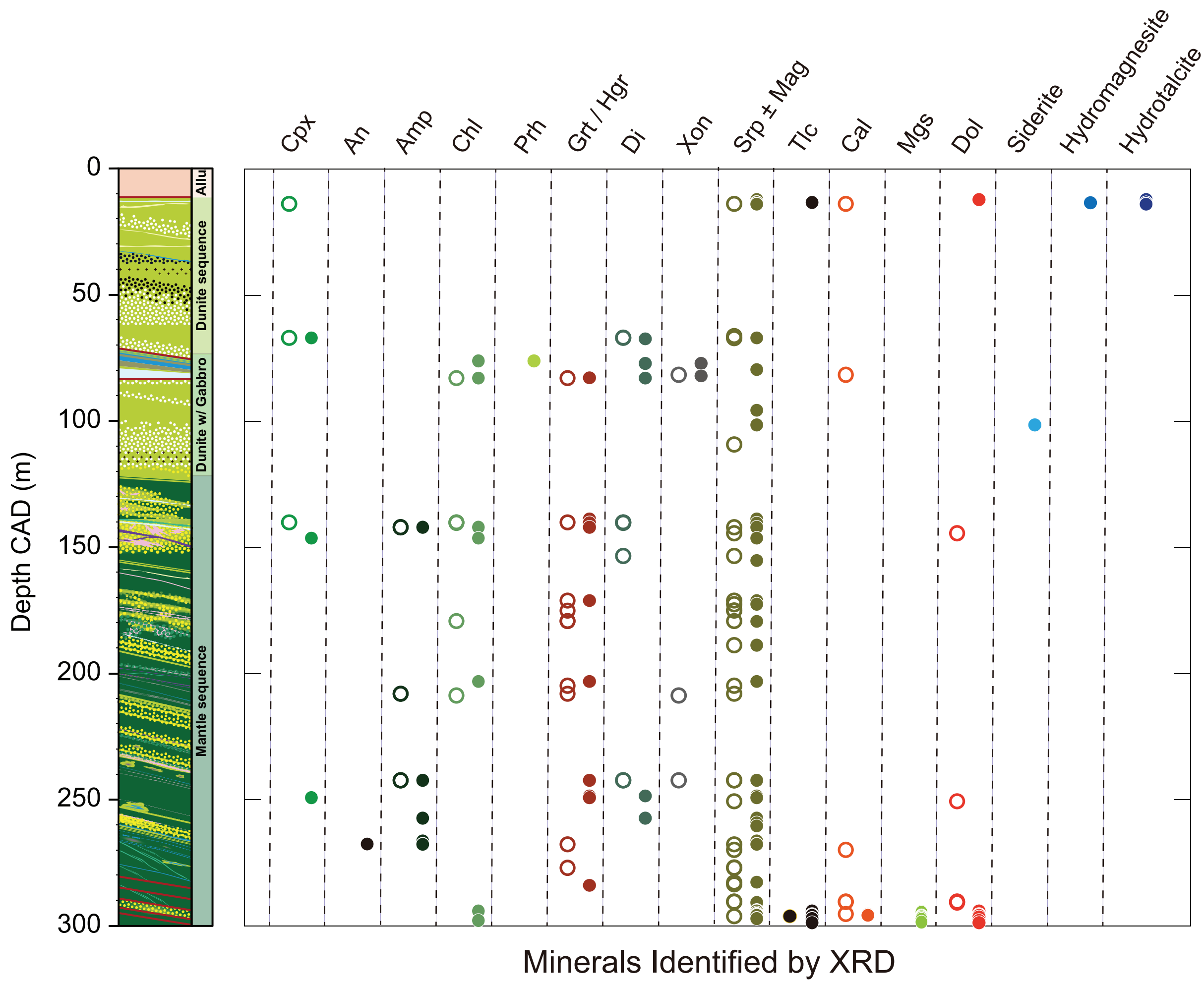

Figure F50. Downhole variations in the proportion of the 4 alteration types within Hole CM2B (main lithologic groups as defined in Fig. F44).

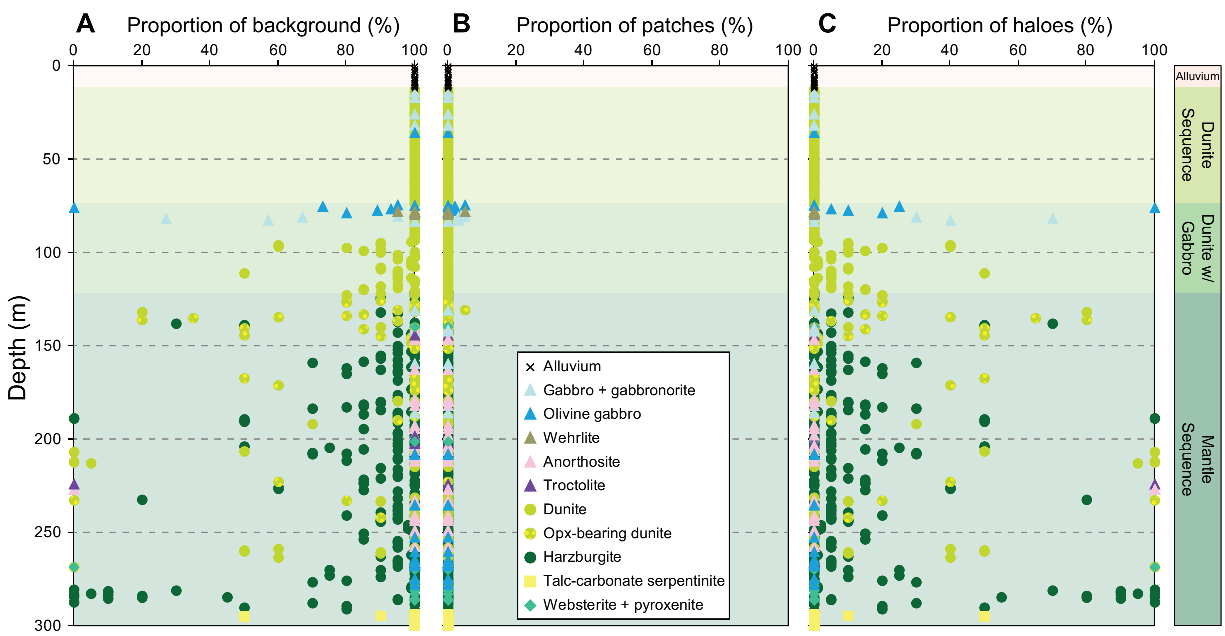

Figure F51. **A.** Characteristic serpentinized dunite in Dunite Sequence, Hole CM2B. **B, C.** Whole thin section scan of zoned alteration from olivine to serpentine (Srp) associated with magnetite-rich serpentine veins along which chrysotile (Ctl) veins developed (B: PPL, C: XPL). Ol = olivine, Px = pyroxene, Mag = magnetite.

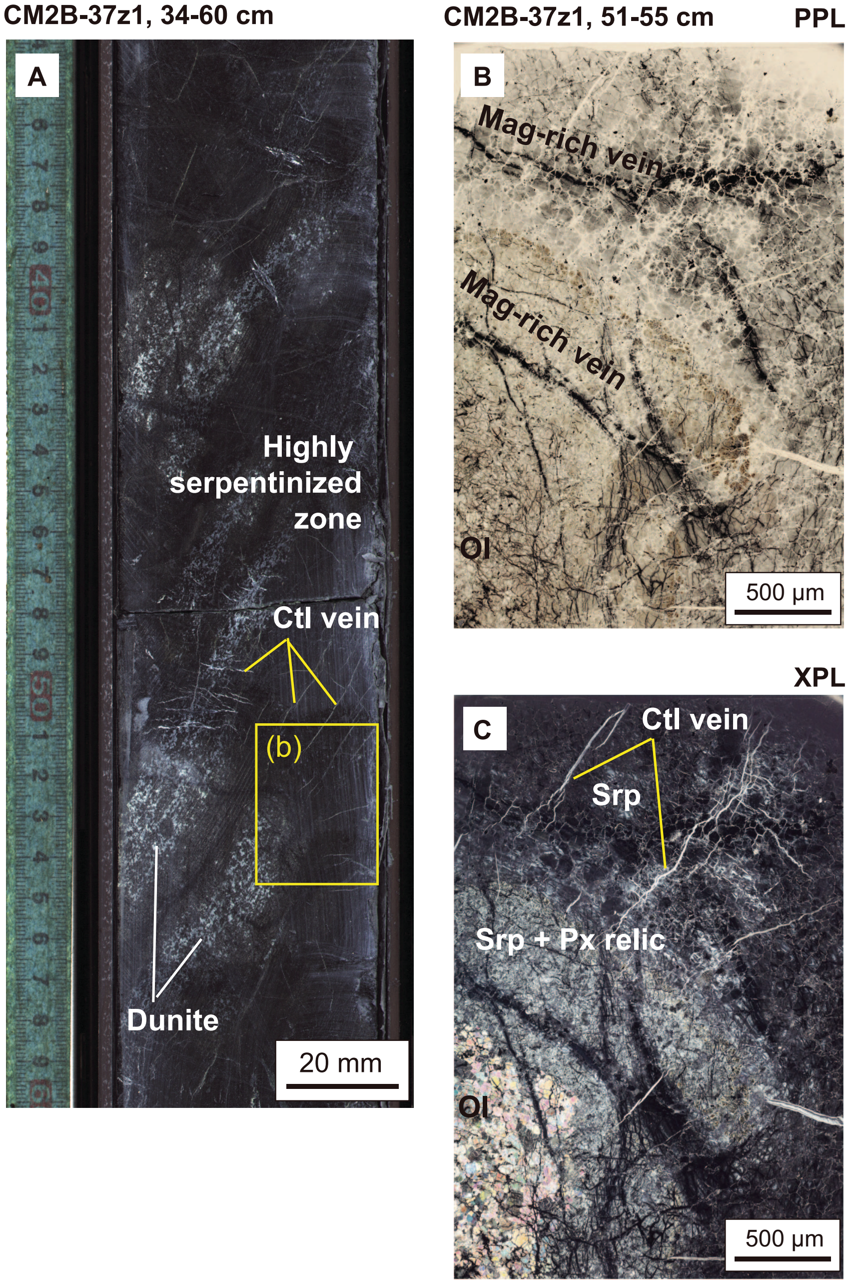

Figure F52. Serpentine and altered plagioclase in Dunite Sequence. **A.** Olivine (Ol) relics surrounded by serpentine (Srp) and altered plagioclase (Pl) in dunite. **B.** Completely serpentinized olivine with interstitial-shaped altered plagioclase in dunite. Spl = spinel.

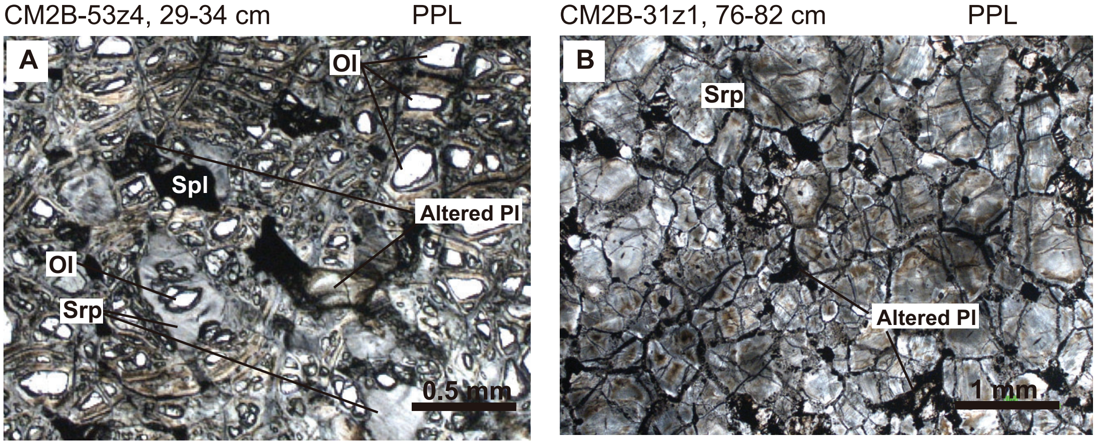

Figure F53. Alteration of characteristic magmatic veins in Dunite Sequence. **A.** Gabbroic vein in serpentinite. **B.** Whole thin section scan of gabbroic vein in serpentinite (Srp); chlorite (Chl) is developed at the boundary between serpentinite and gabbroic vein. The vein is mainly composed of altered plagioclase (Pl) and is cut by magnetite (Mag)-rich serpentine vein. Px = pyroxene.

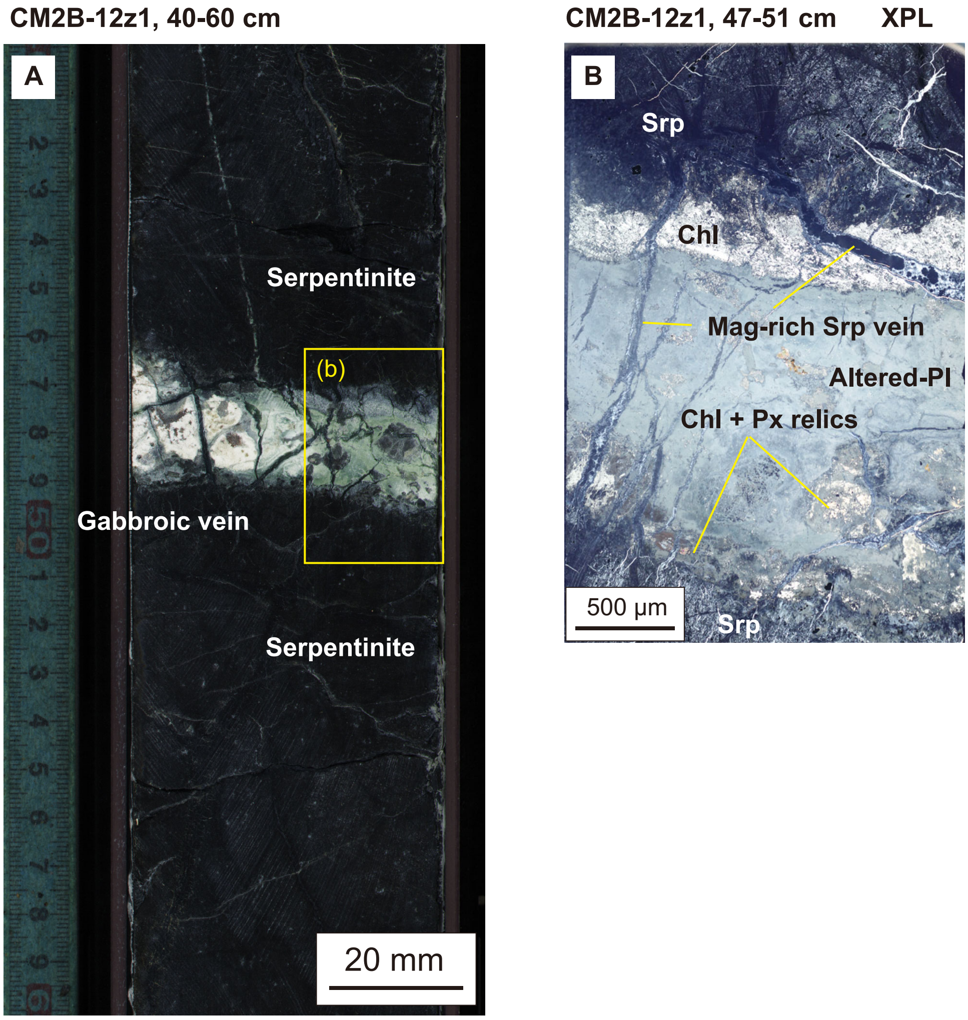

Figure F54. Alteration features of gabbro-dunite in Dunite Sequence. **A.** Gabbro-dunite layer. Prehnite (Prh) is observed in gabbro layer. **B.** Whole thin section scan shows chlorite (Chl)-formed boundary between serpentinite (Srp) and gabbroic vein. Chlorite (and serpentine) formed between clinopyroxenes (Cpx) in gabbro layer (box = photomicrograph location). **C, D.** Alteration features of olivine (serpentine) and plagioclase (chlorite) between clinopyroxenes. **E.** Lowermost part of the gabbro-dunite layered zone. **F.** Whole thin section scan showing actinolite (Act) formed along calcite (Cal) veins. Prehnite and chlorite formed around actinolite (box = photomicrograph location). **G, H.** Actinolite-prehnite-chlorite vein across altered plagioclase-clinopyroxene layer and serpentine layer.

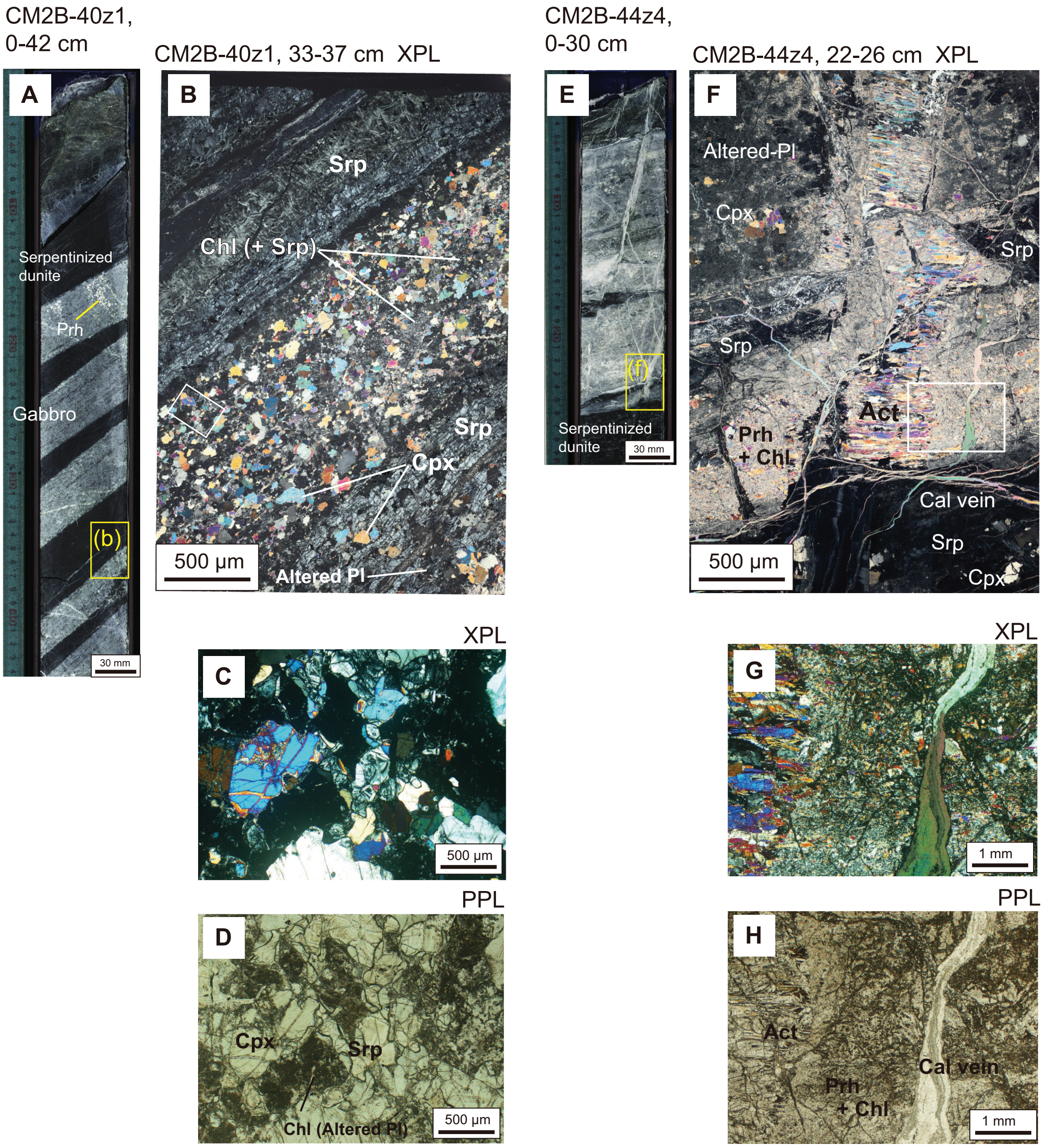

Figure F55. Vein generations in Dunite Sequence. **A.** Serpentine vein generations in dunites. **B.** Close-up showing V1: serpentine ± magnetite vein network as a mesh texture; V2: banded serpentine ± magnetite vein cuts the mesh texture; V3: chrysotile ± calcite vein cuts the V1 and V2 vein networks; V4: fractured cross-fiber serpentine vein cuts V1, V2, and V3 veins. **C.** Vein network in gabbro. **C.** Close-up showing extensively haloed vein network containing prehnite (Prh) + chlorite (Chl) + clinozoisite (Czo).

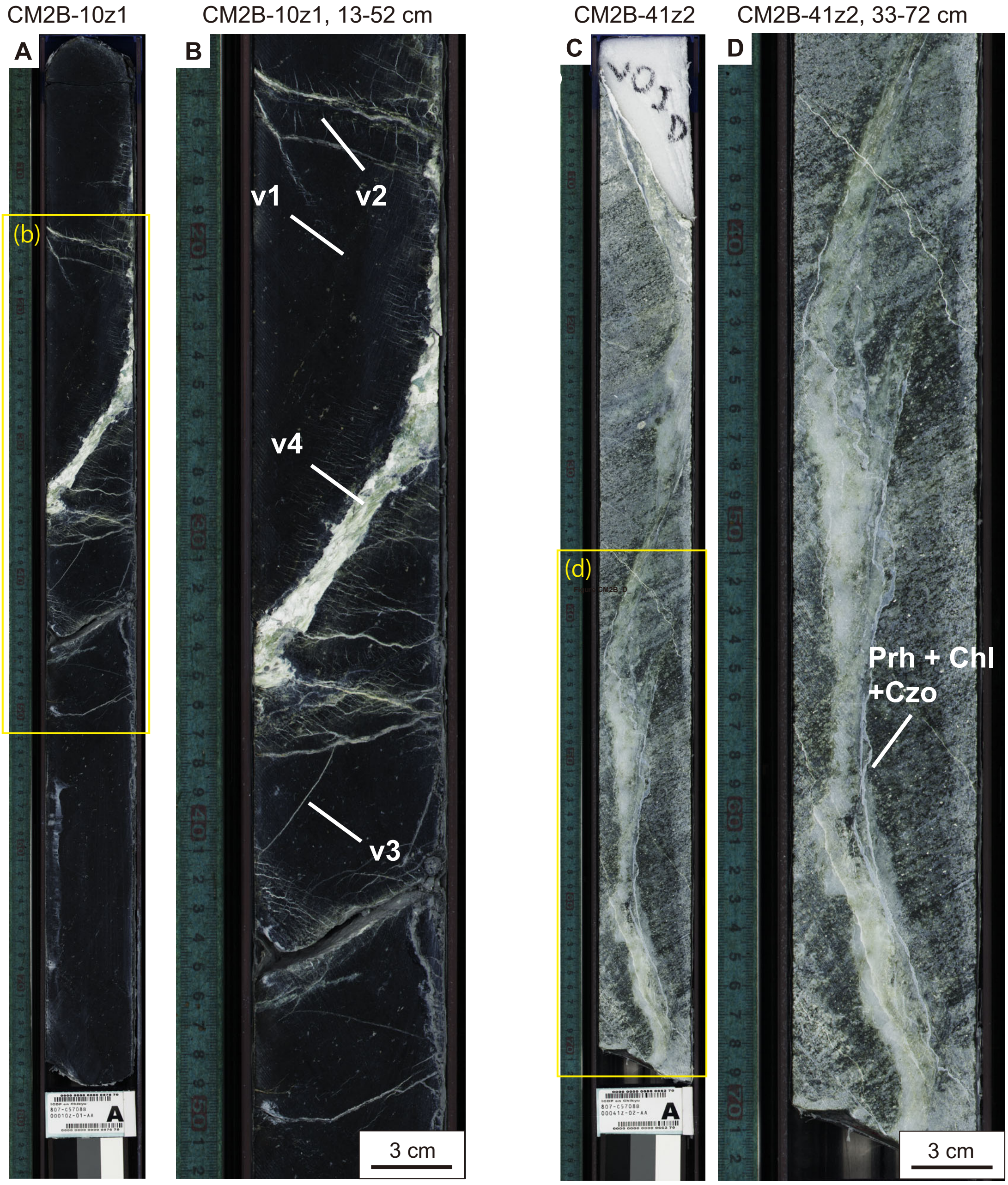

Figure F56. Typical XRD results from Dunite Sequence, Hole CM2B. **A.** Sampled intervals marked by red boxes. **B.** Close-up of interval 94Z-3, 5–12 cm. Arrow = XRD sampling point. **C.** XRD diffractogram shows peaks of serpentine, amphibole, and grossular. **D.** Close-up of interval 94Z-3, 55–65 cm. Arrow = XRD sampling point. **E.** XRD diffractogram shows peaks of xonotlite and chlorite.

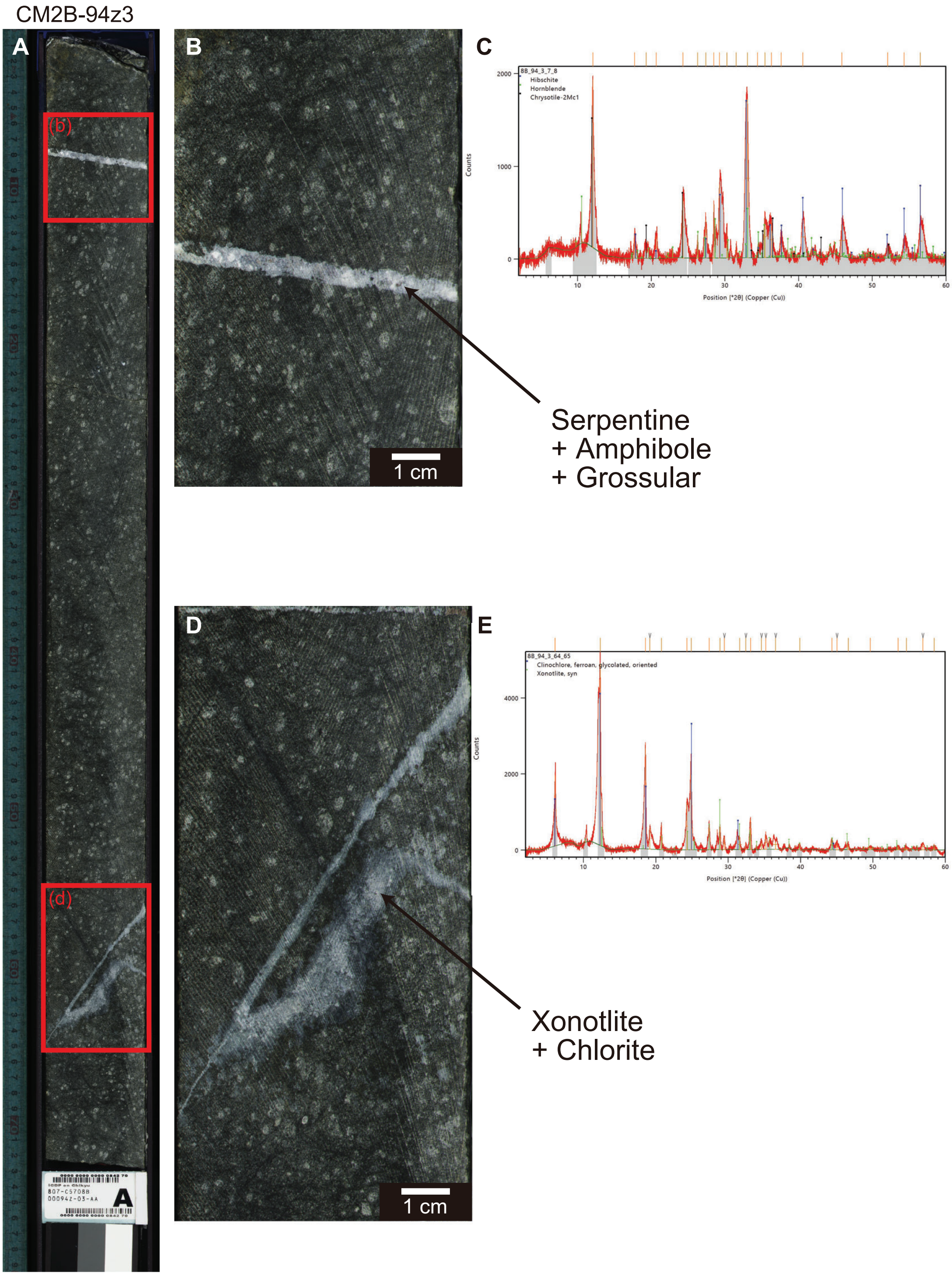

Figure F57. Harzburgite alteration in Mantle Sequence, Hole CM2B, shown in core photos (left) and XCT images (right). **A.** Less-altered harzburgite. **B.** Serpentinized harzburgite. **C.** Extensively veined harzburgite. Red in XCT image corresponds to high-density magnetite-rich serpentine veins. **D.** Talc-magnesite serpentinite altered from harzburgite (gray in core image) with carbonate veins (white). Yellow and pale yellow in XCT image reflect moderate-density magnesite and dolomite, respectively.

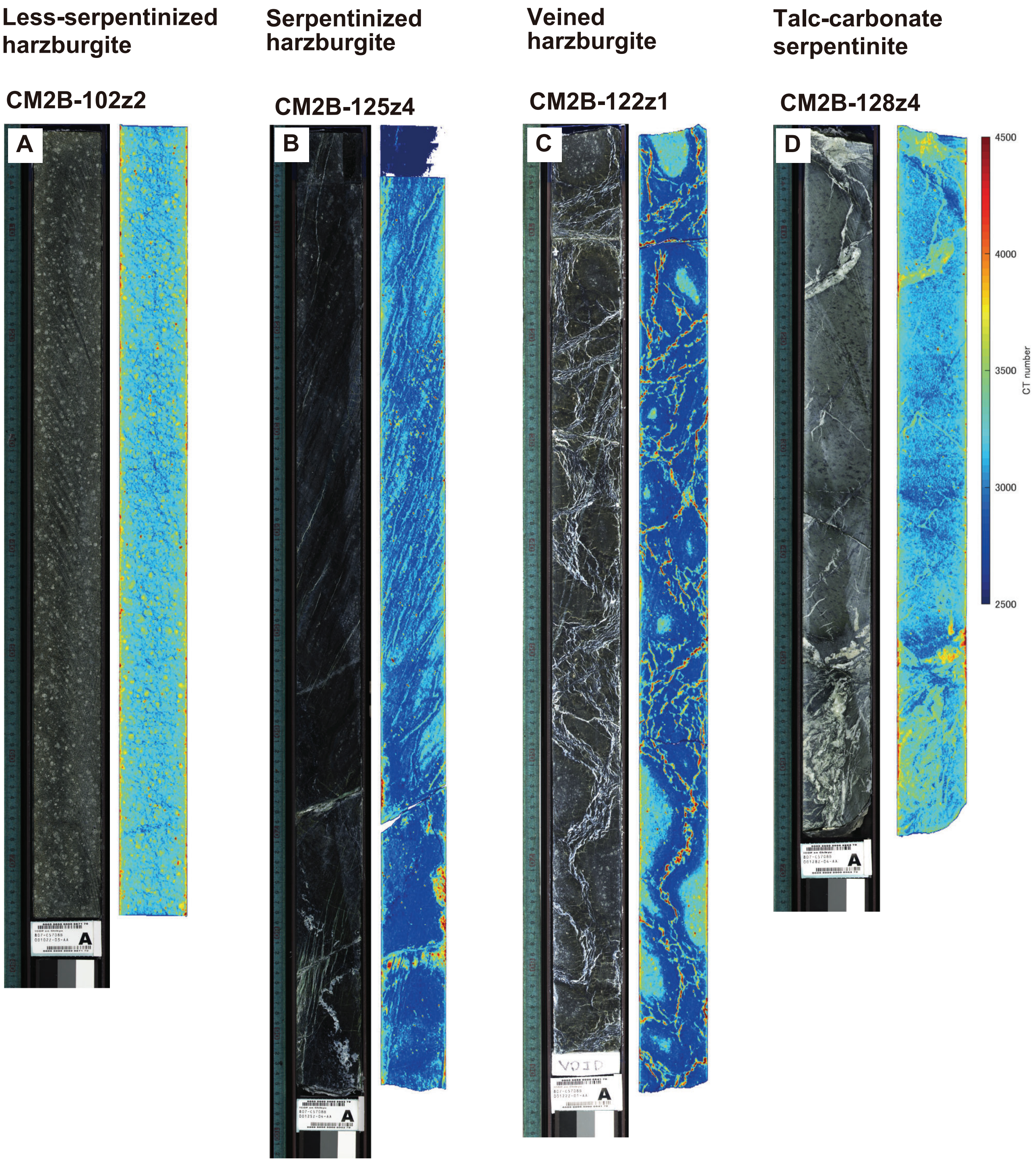

Figure F58. Serpentinized harzburgites and serpentinites in Mantle Sequence, Hole CM2B. **A, B.** Serpentine (Srp) in mesh texture after olivine (Ol); (Spl = spinel, Opx = orthopyroxene). **C.** Orthopyroxene with talc (Tlc) rim in mesh texture after olivine. **D.** Altered orthopyroxene in serpentine. **E, F.** Altered orthopyroxene with talc rim in serpentine with talc. **G, H.** Contact between talc-magnesite (Mgs) and magnesite-serpentine mixtures.

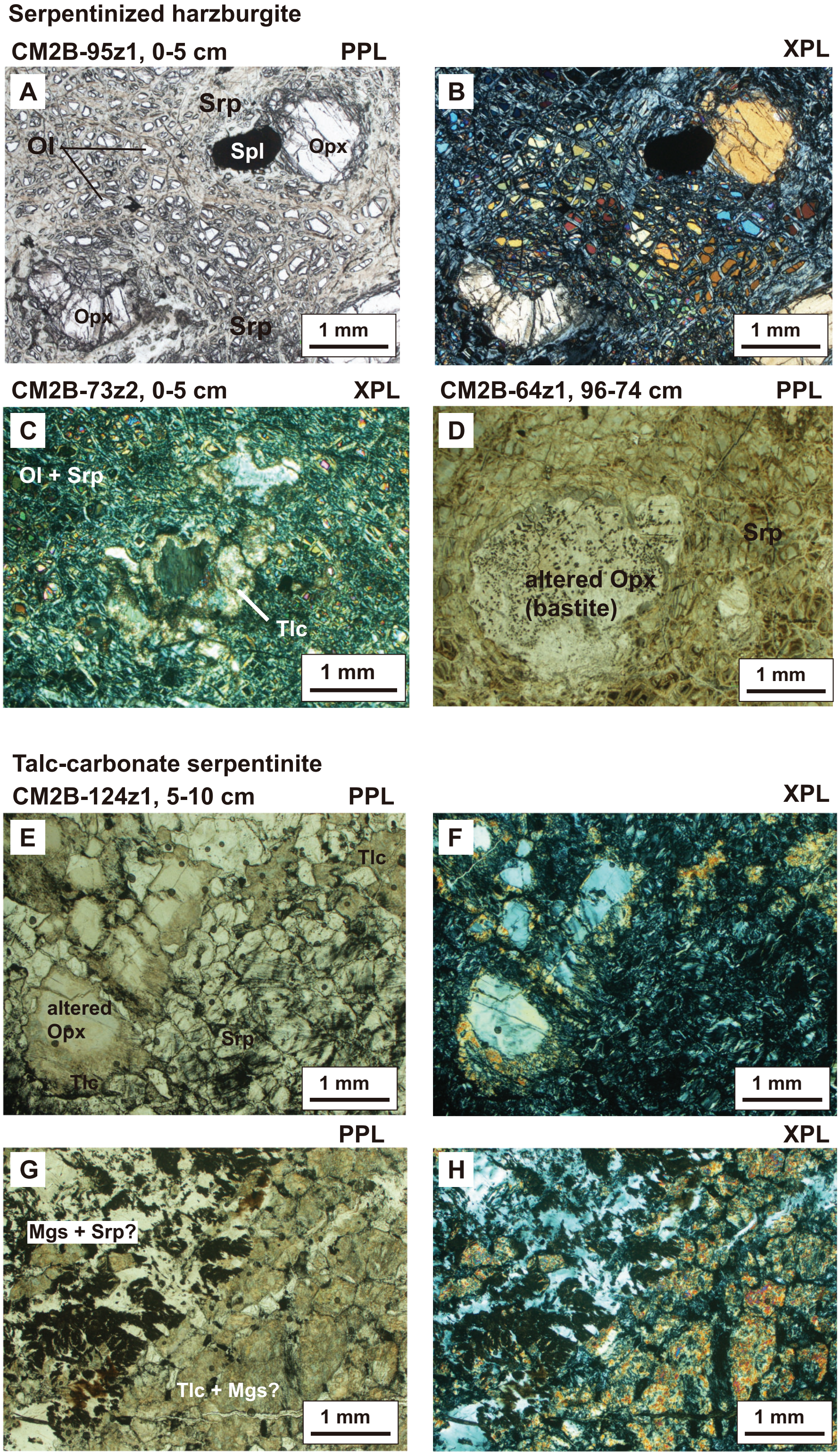

Figure F59. Magnetite-rich serpentine vein-related alteration halos in Dunite and Mantle Sequences, Hole CM2B. Alteration halos in dunite in the upper Dunite Sequence are rarely identified (cf. Fig. F44), whereas they are well identified in harzburgite and dunite below Core 51Z (Fig. F54). **A–C.** Serpentinized dunite in Dunite Sequence; (A) core photo, (B) XCT image: red indicates high-density magnetite-rich vein; (C) close-up of alteration halos. Red arrows = magnetite (Mag)-rich serpentine (Srp) veins. Chrysotile (Ctl) veins crosscut alteration halos. **D.** Photomicrograph showing relationship between magnetite-rich serpentine veins, alteration halo, and chrysotile veins. **E–G.** Veined serpentinized harzburgite in Mantle Sequence; (E) core photo, (F) XCT image (red color indicates high-density magnetite-rich serpentine vein); (G) close-up of alteration halos. Chrysotile veins are aligned along magnetite-rich serpentine veins and alteration halos. Less-altered harzburgite spots (seen in F) formed by network-like veins in harzburgite.

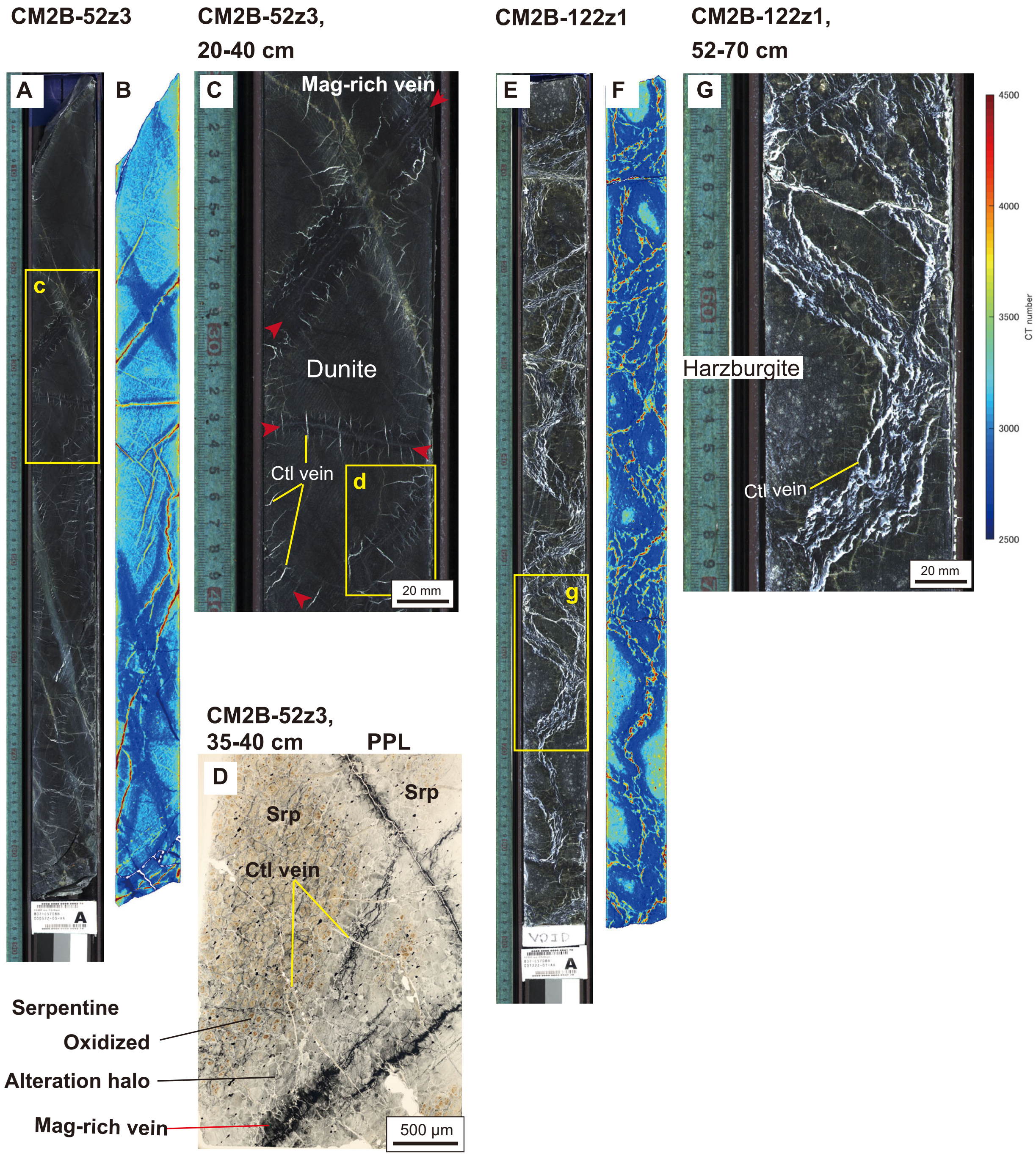

Figure F60. Alteration of magmatic vein in harzburgite and dunite from Mantle Sequence. **A.** Troctolite layer in highly serpentinized dunite. **B.** Whole thin section scan showing serpentinized dunite and troctolite. Actinolite (Act) and altered plagioclase (Pl) aggregates in troctolite layer and serpentine (Srp) are cut by magnetite (Mag)-rich serpentine vein. **C.** Troctolite, websterite, and olivine gabbro veins in harzburgite. **D, E.** Whole thin section scans showing troctolite vein in harzburgite. Olivines (Ol) in clinopyroxene (Cpx) partly altered to serpentine and brown-color altered plagioclase are observed at the boundary between harzburgite and troctolite vein. Opx = orthopyroxene.

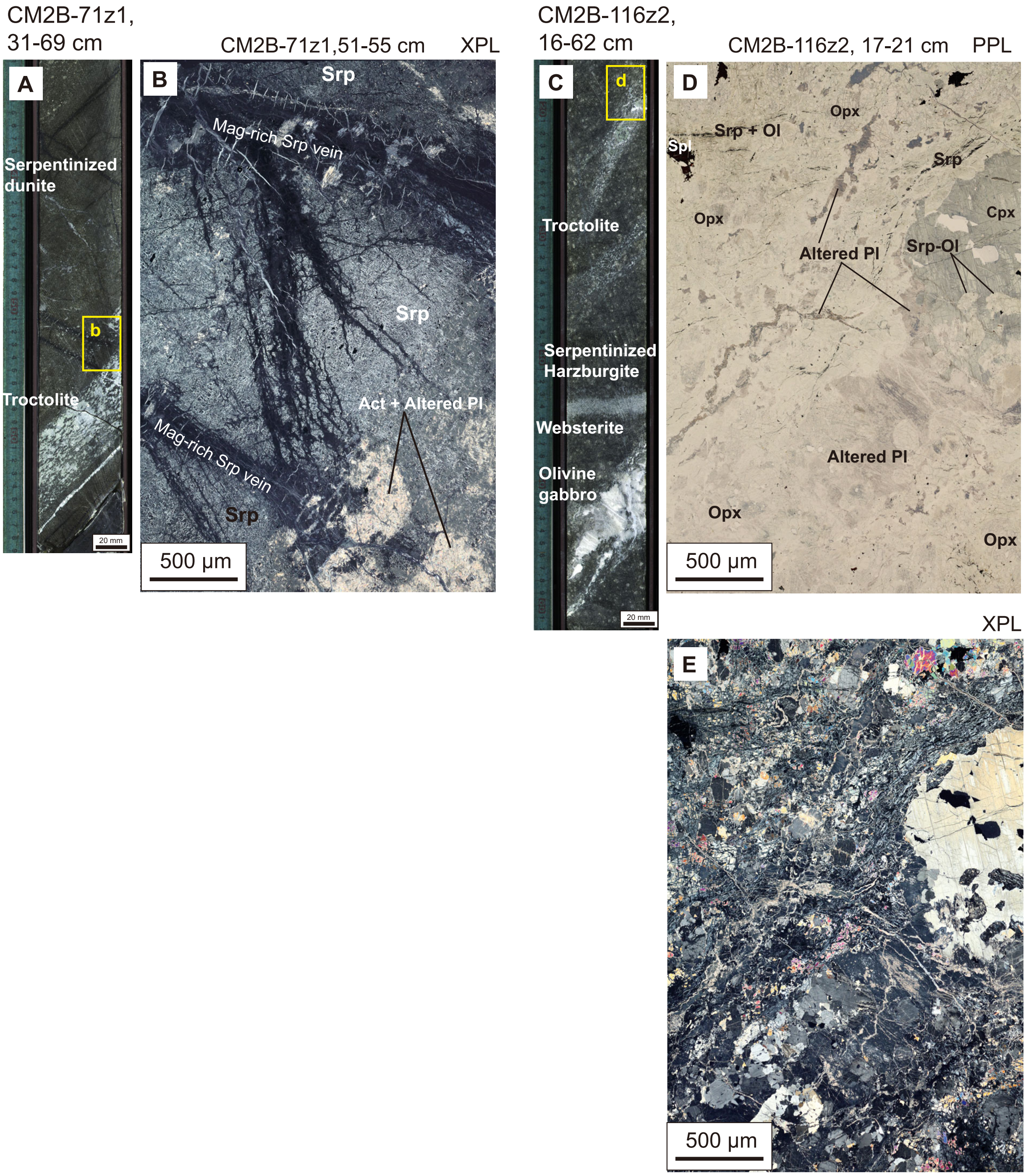

Figure F61. Alteration of rodingite and diopsidite veins in serpentinized dunite in Mantle Sequence. **A, B.** Irregular-shaped diopsidite in serpentinized dunite. Diopside-chlorite-uvarovite (Di-Chl-Uva) formed after gabbroic rock (anorthosite defined as an igneous unit). **C.** Diopsidite vein in serpentinized dunite. Diopsidite formed after gabbroic rock (anorthosite defined as an igneous unit).

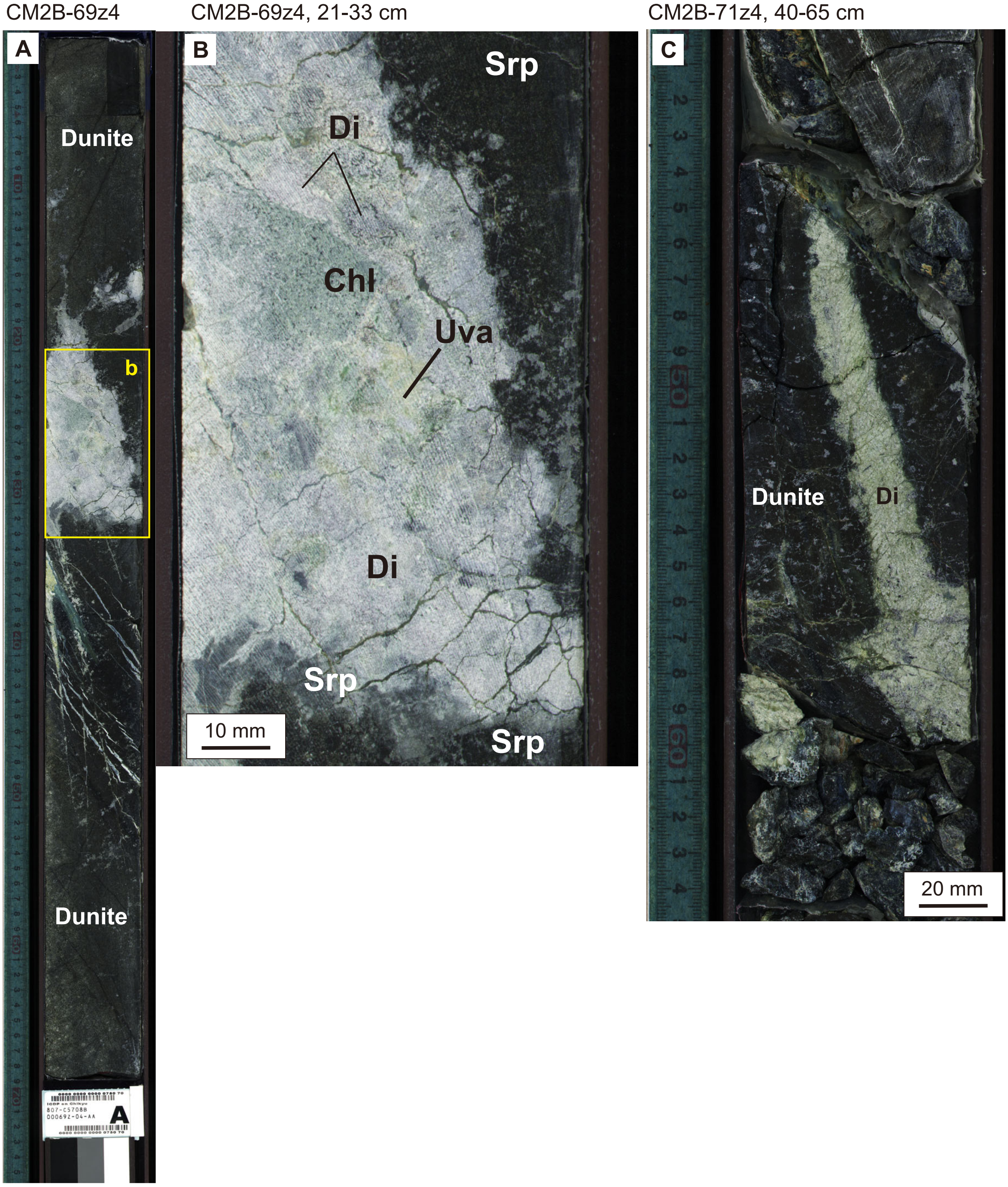

Figure F62. Transitional interval from serpentinized harzburgite to talc-carbonate-serpentinite in Mantle Sequence. **A.** Serpentine (Srp), chlorite (Chl), dolomite (Dol), calcite (Cal), magnesite (Mgs), and talc (Tlc) assemblage (confirmed by XRD). Spl = spinel. **B.** Close-up showing talc-calcite-serpentine dominant interval.

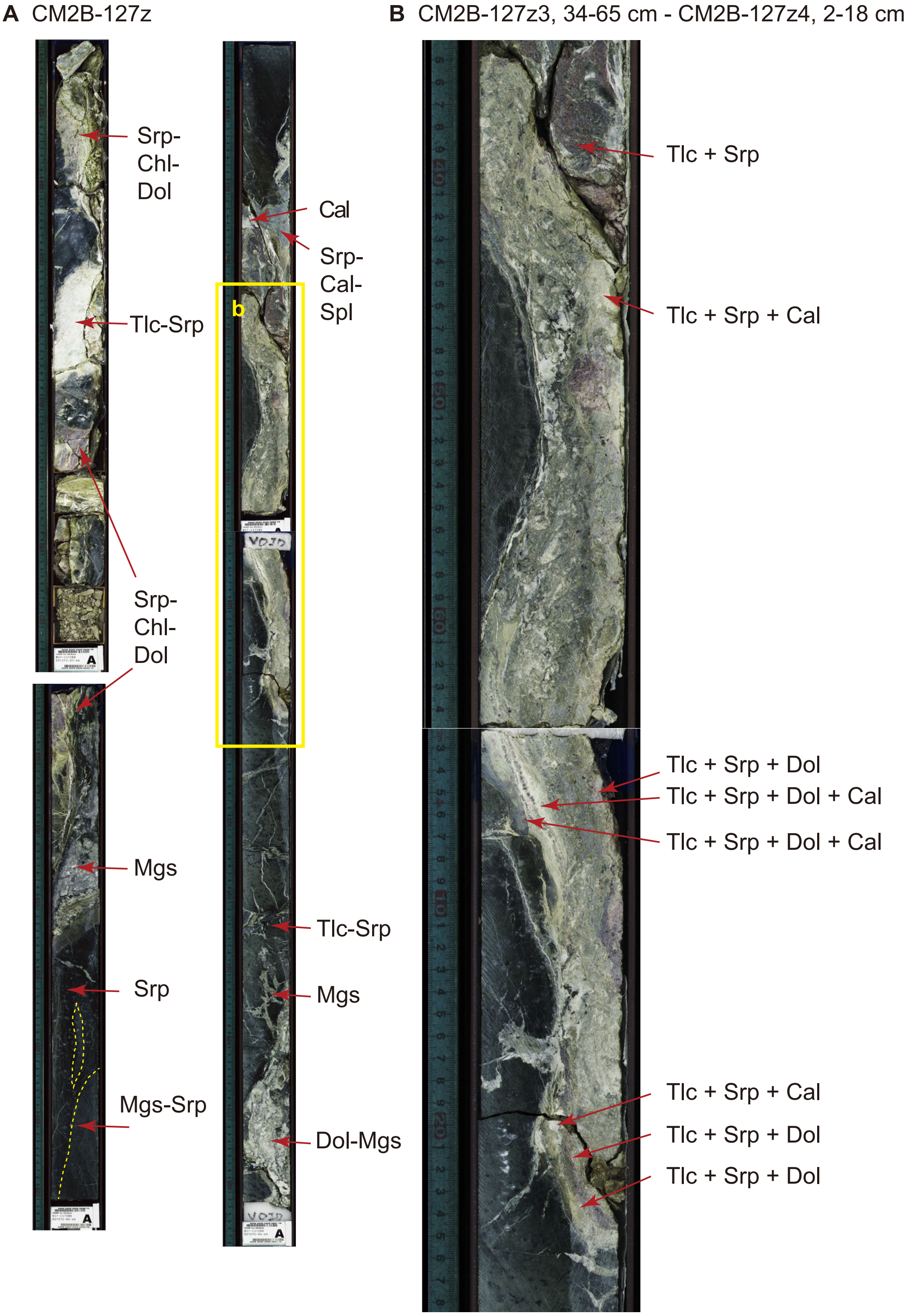

Figure F63. Transitional interval from serpentinized harzburgite to talc-carbonate-serpentinite in Mantle Sequence, Hole CM2B. **A.** Serpentine (Srp), chlorite (Chl), dolomite (Dol), calcite (Cal), magnesite (Mgs), and talc (Tlc) assemblage (confirmed by XRD). **B.** Close-up showing feather-like texture composed of serpentine and magnesite.

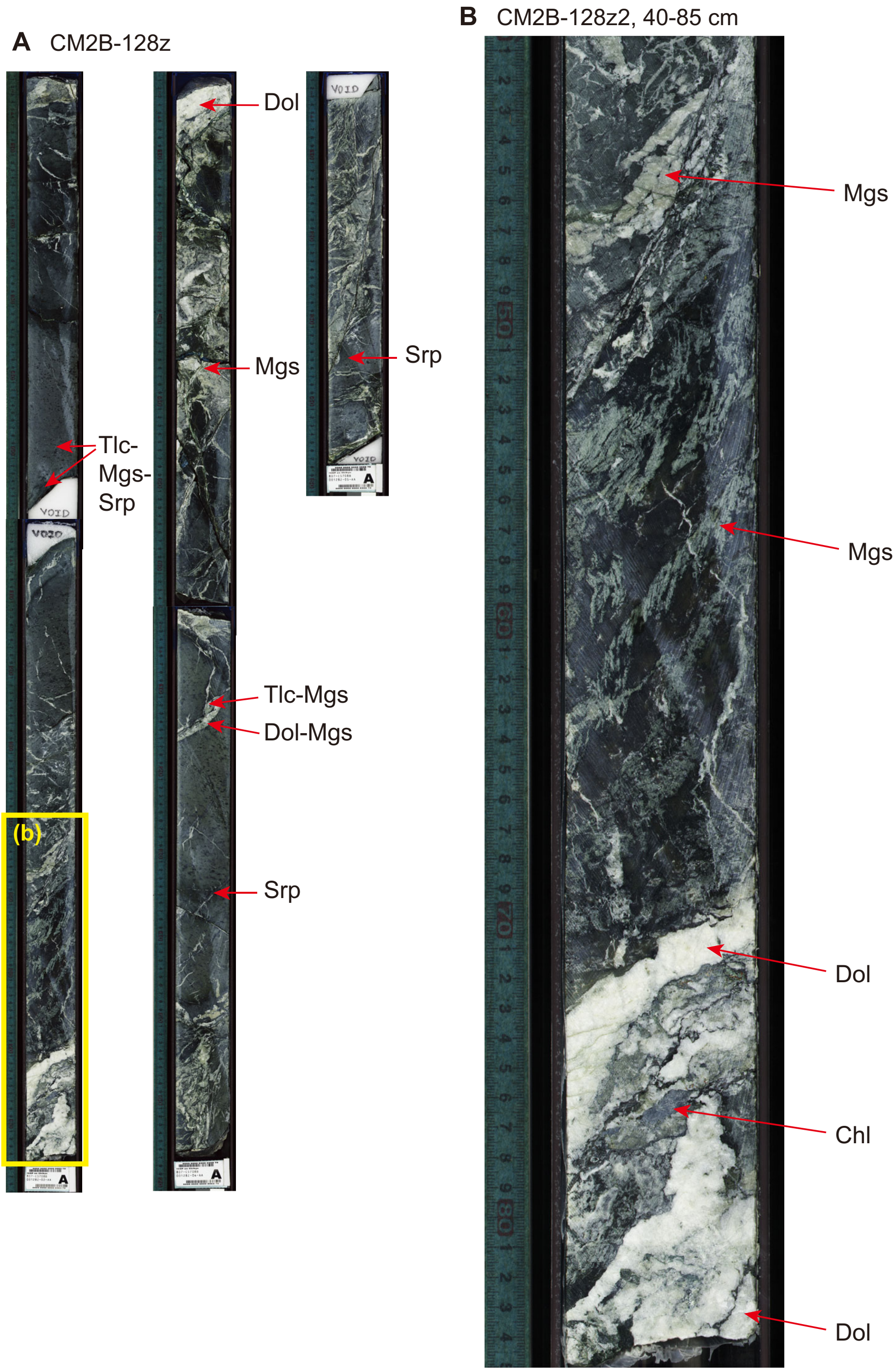

Figure F64. Vein types observed in harzburgites from Mantle Sequence, Hole CM2B. **A.** V1 and V2 serpentine (Srp) veins are not clearly visible macroscopically; V3 magnetite (Mag)-rich serpentine veins with wide serpentine ± magnetite halo; V4 slip-fiber fractured serpentine vein; bluish green serpentine vein following the center of V3 magnetite-rich serpentine vein; V5 white serpentine (chrysotile) ± calcite (Cal) vein network following earlier vein pathways; V6 calcite vein network following earlier vein pathways in the lower part of the section and forming polygonal structures in the upper part. **B.** XCT scan of clearly visible high-density (red) magnetite-rich center of the serpentine vein (V3).

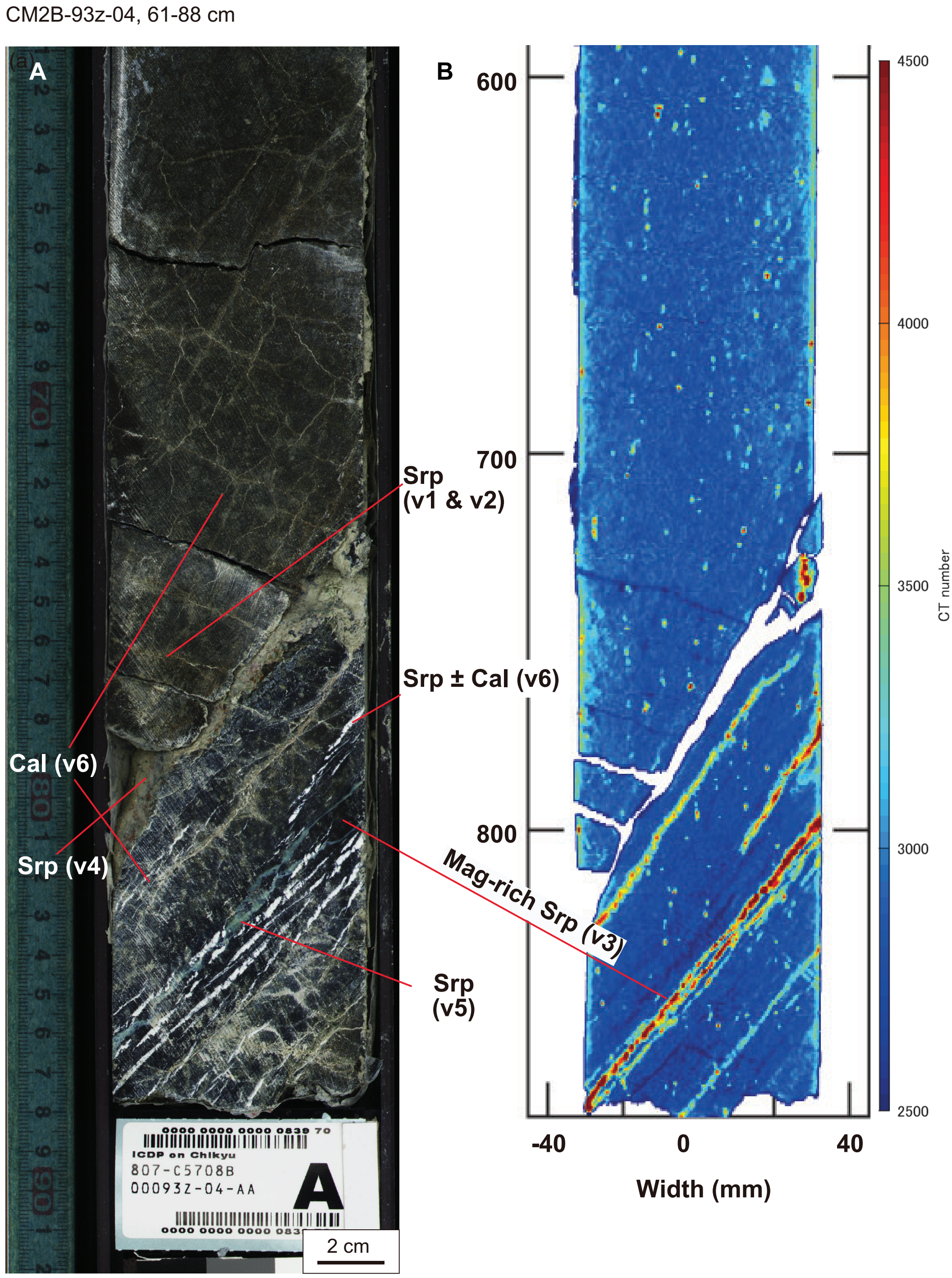

Figure F65. Vein types observed in harzburgites from Mantle Sequence, Hole CM2B. **A.** Massive bluish green serpentine (Srp) veins are dislocated and overprinted by patchy chrysotile (Ctl) + calcite (Cal) veins. **B.** Slip-fiber serpentine vein overprints the magnetite (Mag)-rich serpentine vein and is overprinted by chrysotile + calcite vein network. **C.** Magnetite-rich serpentine vein network is crosscut by chrysotile + calcite veinlets.

Figure CM2B_D_F22

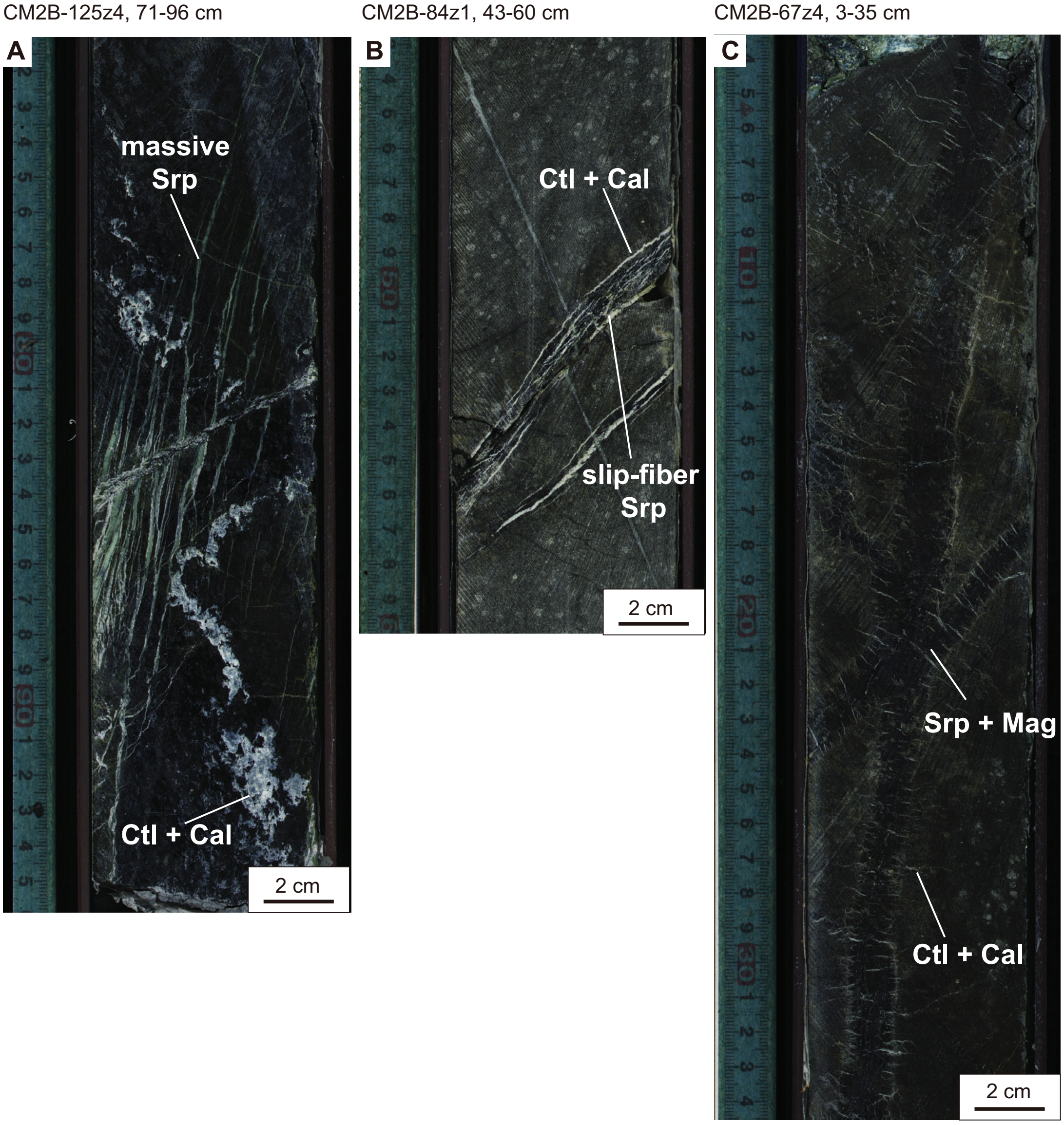

Figure F66. Forms of chrysotile + calcite vein "swarm" networks observed in harzburgites from Mantle Sequence, Hole CM2B. **A.** Magnetite-rich serpentine vein (Srp + Mag) is partially overprinted by chrysotile (Ctl) + calcite (Cal) "swarm" vein network. **B.** Chrysotile + calcite "swarm" vein network extending through section. **C.** Extensive network of chrysotile + calcite veins.

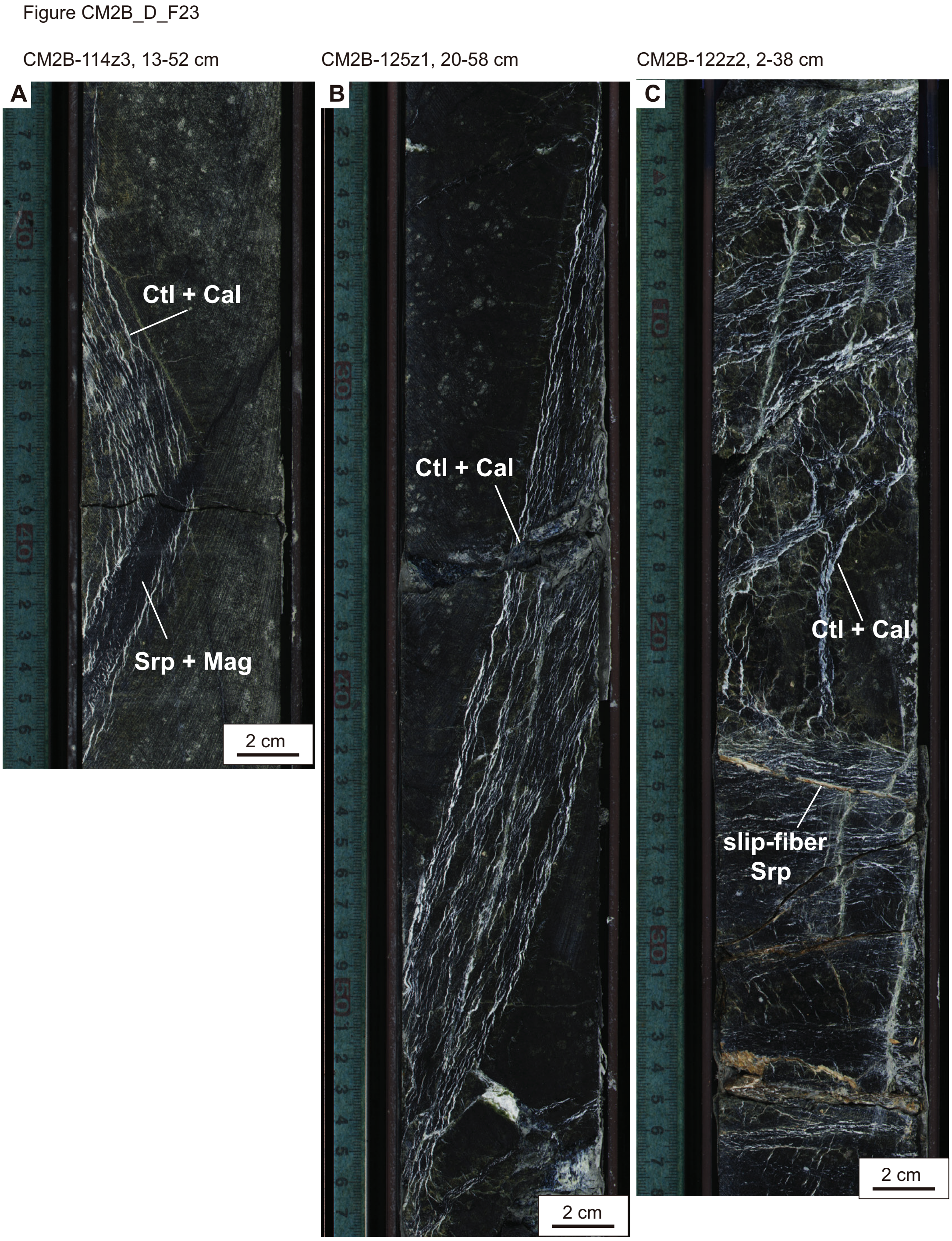

Figure F67. Vein types observed in Mantle Sequence, Hole CM2B. **B.** Pinkish serpentine (Srp) + diopside (Di) vein is cut by xonotlite (Xon) white vein in altered dunitic patch. Green amphibole (Amp) + garnet (Grt) vein cuts the dunitic patch in the lower part. **B.** White calcite (Cal) vein cuts the serpentine (Srp) + calcite (Cal) + spinel (Spn) patch in the upper part of the section, and talc (Tlc) + serpentine patch in the lower part of the section. Dol = dolomite, Mgs = magnesite.

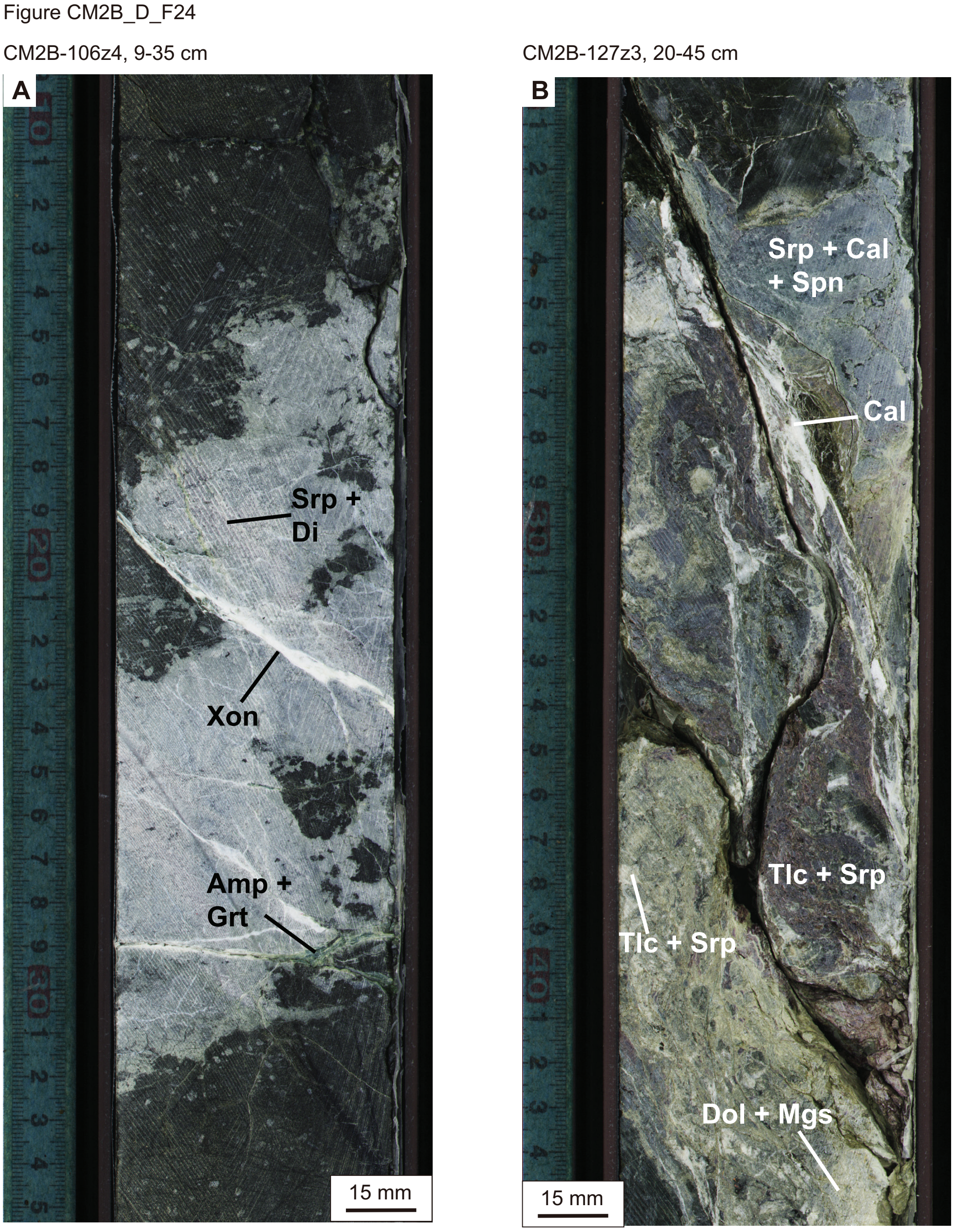

Figure F68. (**A**) *P-T* and (**B**) isobaric T-X_{CO2} diagrams in H_2O-saturated CaO-MgO-SiO_2-H_2O-CO_2 system calculated with the use of Perple_X ver. 6.7.9 (Connolly, 2009) with hp11ver.dat dataset (Holland and Powell, 2011). Abbreviation of minerals is consistent with Whitney and Evans (2011).

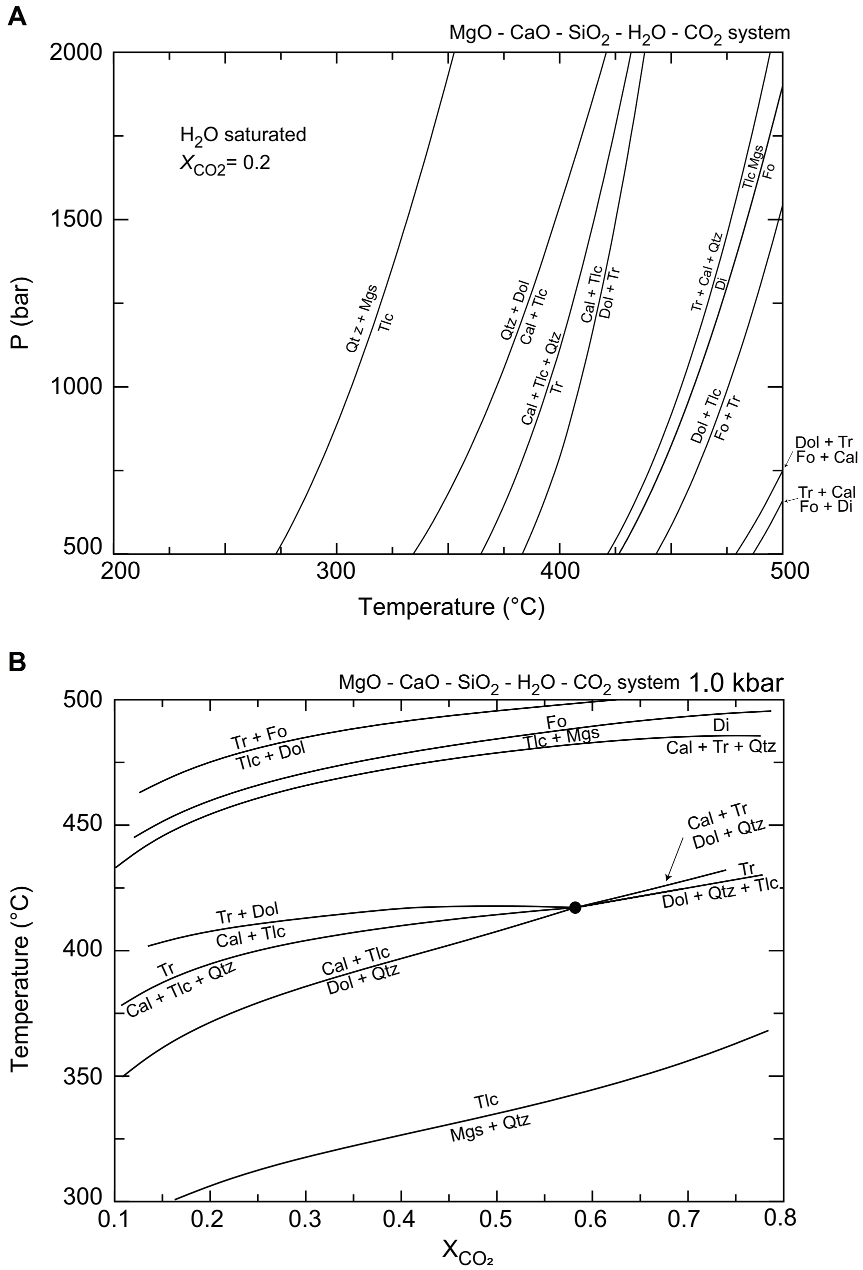

Figure F69. Downhole variation of total alteration intensity compared with that of magnetic susceptibility. Black arrows and green arrows indicate shear zones and veined harzburgite zones, respectively. High-MS pulses in the Mantle Sequence are mainly located in magnetite-rich serpentine veined harzburgite. Dunite intervals at 205 and 210 m are probably harzburgite-dominant intervals (not dunite intervals) with magnetite-rich serpentinite veins. Magnetite after spinel in highly altered halo along vein may effectively cause high magnetic susceptibility. Halos related to magnetite-rich serpentine veins are not clearly visible above 94.5 m (Core 51Z) because of high serpentinization of the background dunite (see Fig. F58).

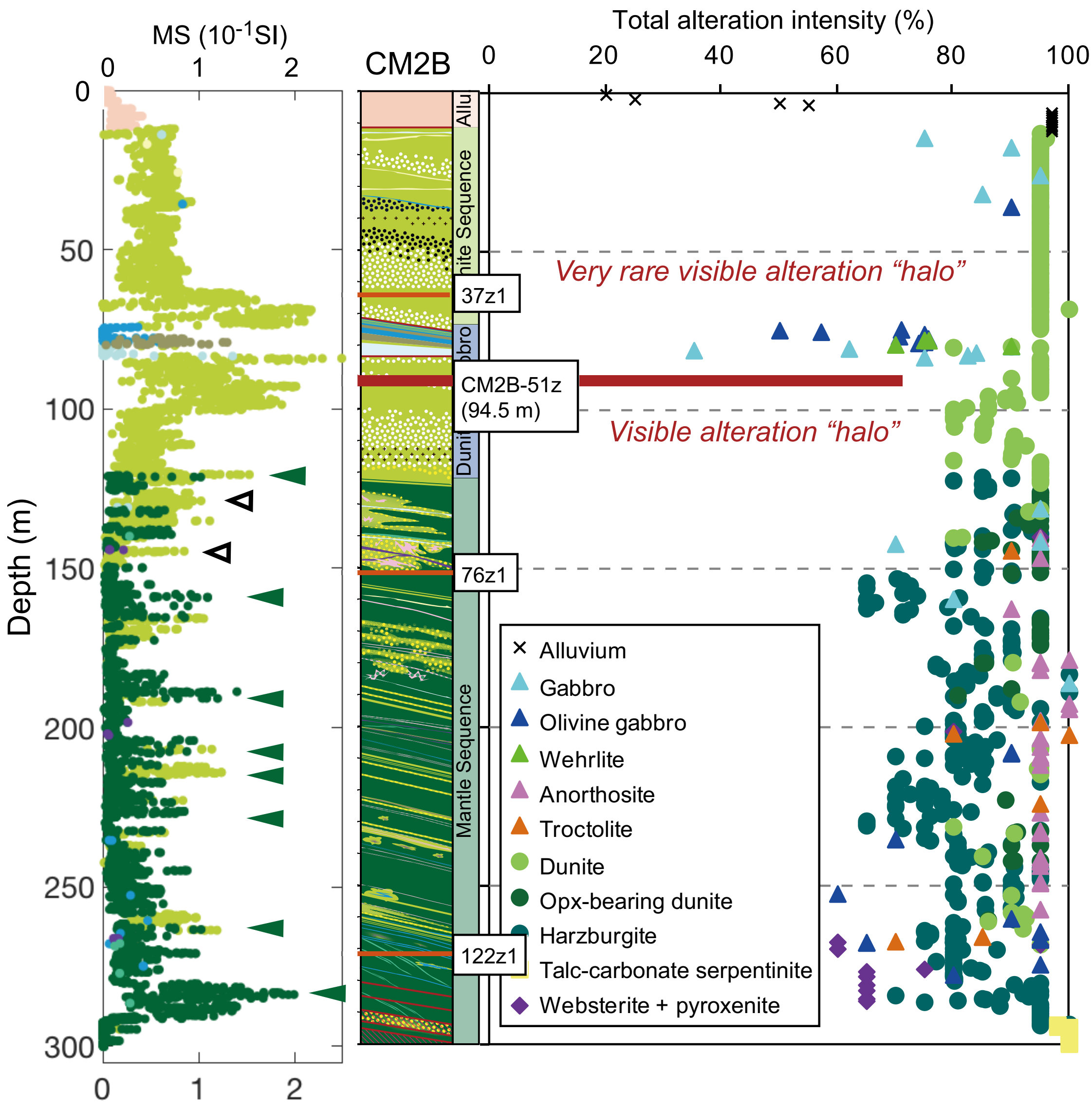

Figure F70. Lithologic contacts. **A.** Gradational contacts between dunite and harzburgite. **B.** Sharp contacts between gabbro and dunite in Dunite with Gabbro Sequence.

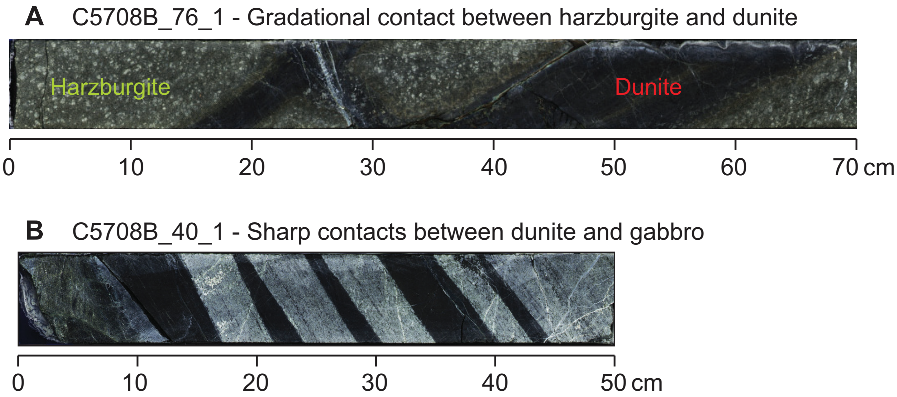

Figure F71. Gabbro igneous Unit 8 in Dunite with Gabbro Sequence.

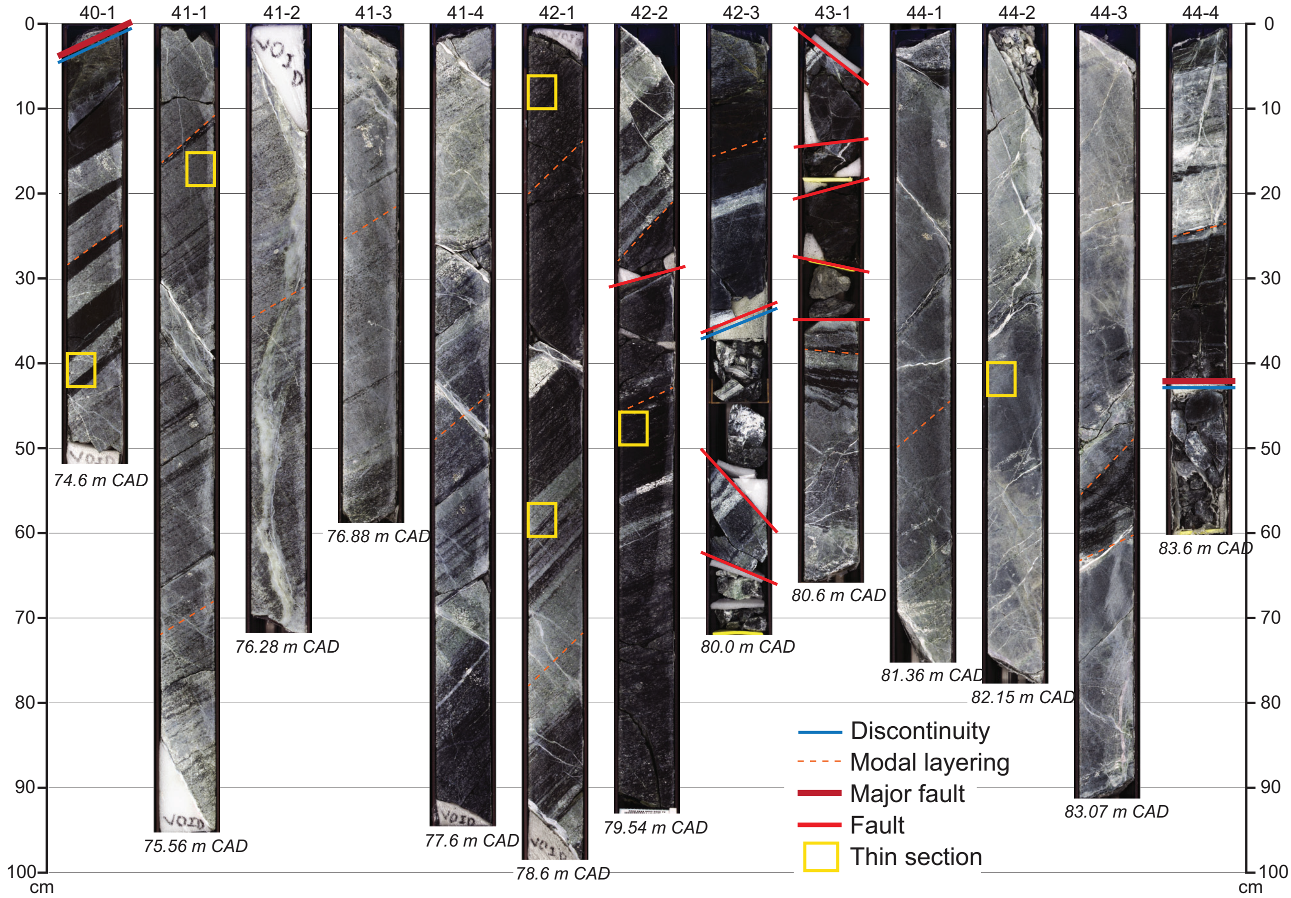

Figure F72. Dip angle of lithologic contacts and veins (in the CRF). **A.** Dip angle. **B.** Contacts and associated anorthosite veins in the gabbroic layers. Dashed red line highlights the trend of variation of the dip with depth in the gabbros; the dotted and solid red lines denote the location of minor and major faults. **C.** Frequency diagram of the gabbroic vein dip angle, with bins of 10°. Dotted line illustrates the distribution of dips expected for randomly oriented veins in a core.

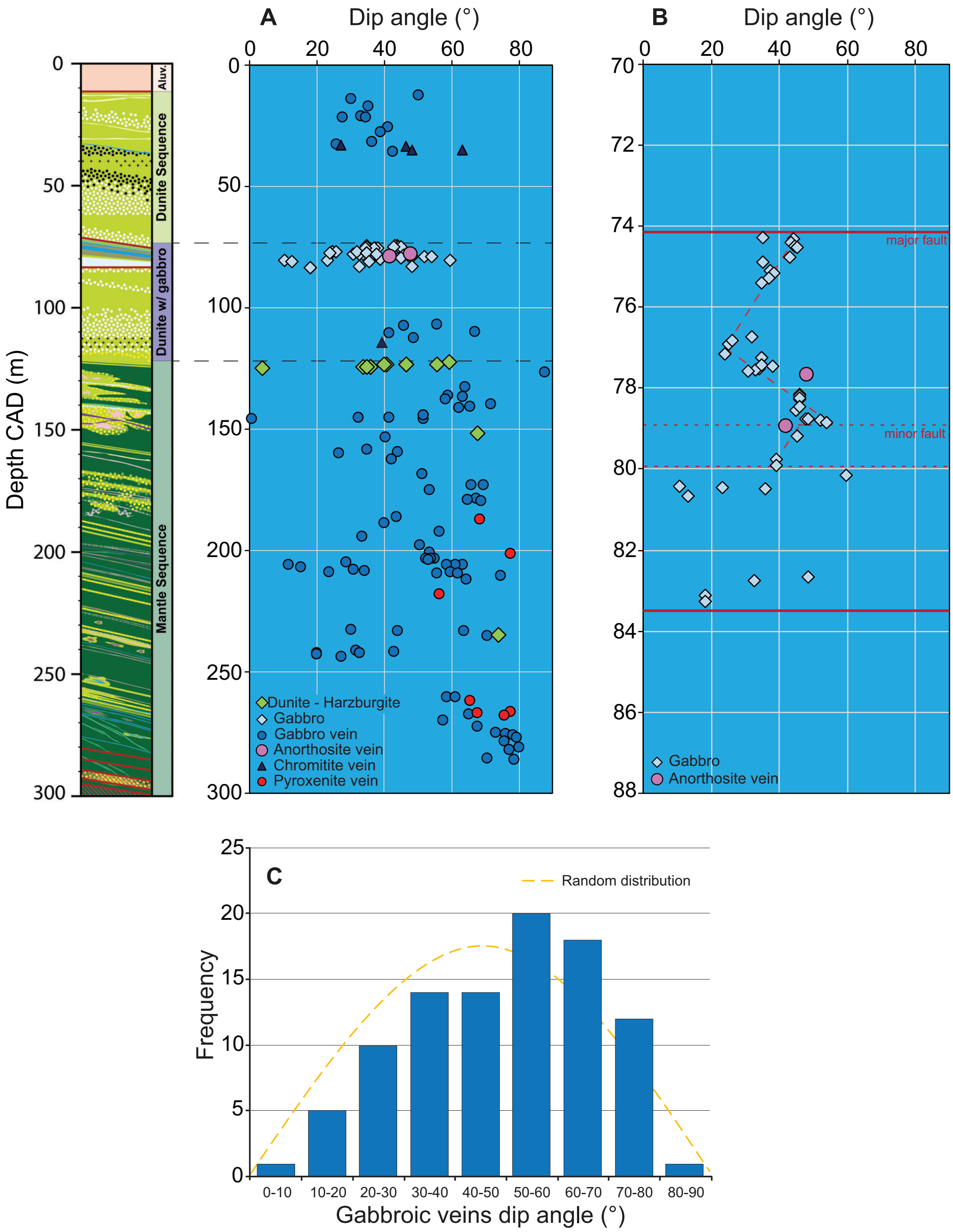

Figure F73. Images of the variability of discrete intrusions within dunite and harzburgite. **A.** Millimeter-thick gabbroic vein in dunite. **B.** Centimeter-thick gabbroic vein in dunite. **C.** Gabbroic veins and patches in harzburgite. **D.** Pyroxenite layer and gabbroic vein in harzburgite. **E.** Pyroxenite layer and gabbroic patch in impregnated harzburgite. **F.** Chromitite vein in dunite (highlighted in red by high-density contrast on the micro-CT scan). **G.** Chromitite patches in dunite (highlighted in red by high-density contrast on the micro-CT scan).

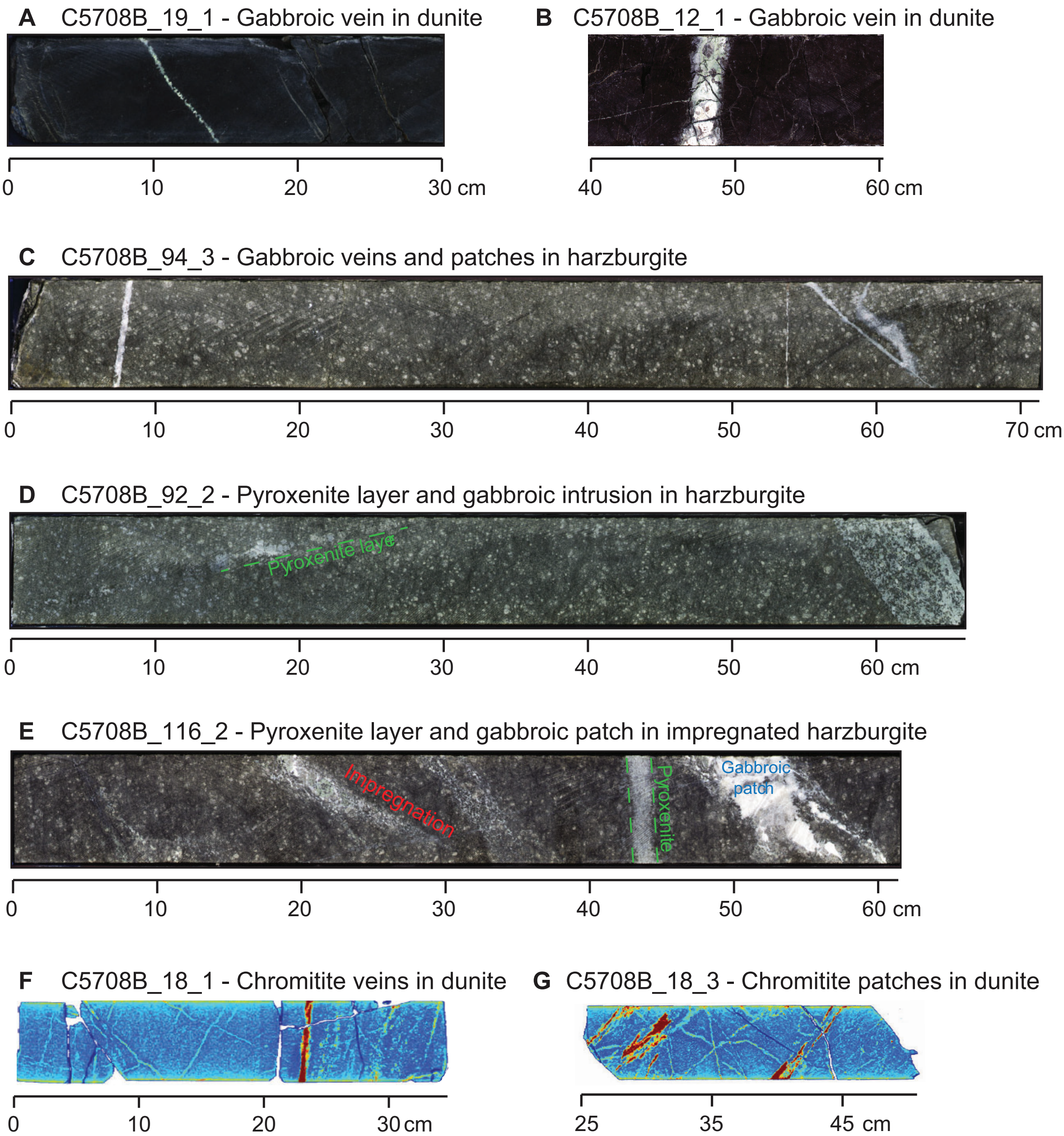

Figure F74. Downhole and frequency diagrams of dunite layer thickness. **A.** Layer thickness. Symbols mark the top of dunite layers. The depth extent of dunite layers thicker than 5 m are highlighted by green bands. **B.** Dunite layer thickness at the transition between Dunite with Gabbro Sequence and Mantle Sequence. **C.** Dunite layer thickness frequency with bins of 0.2 m. **D.** Frequency diagram of the natural logarithm of dunite layer thickness.

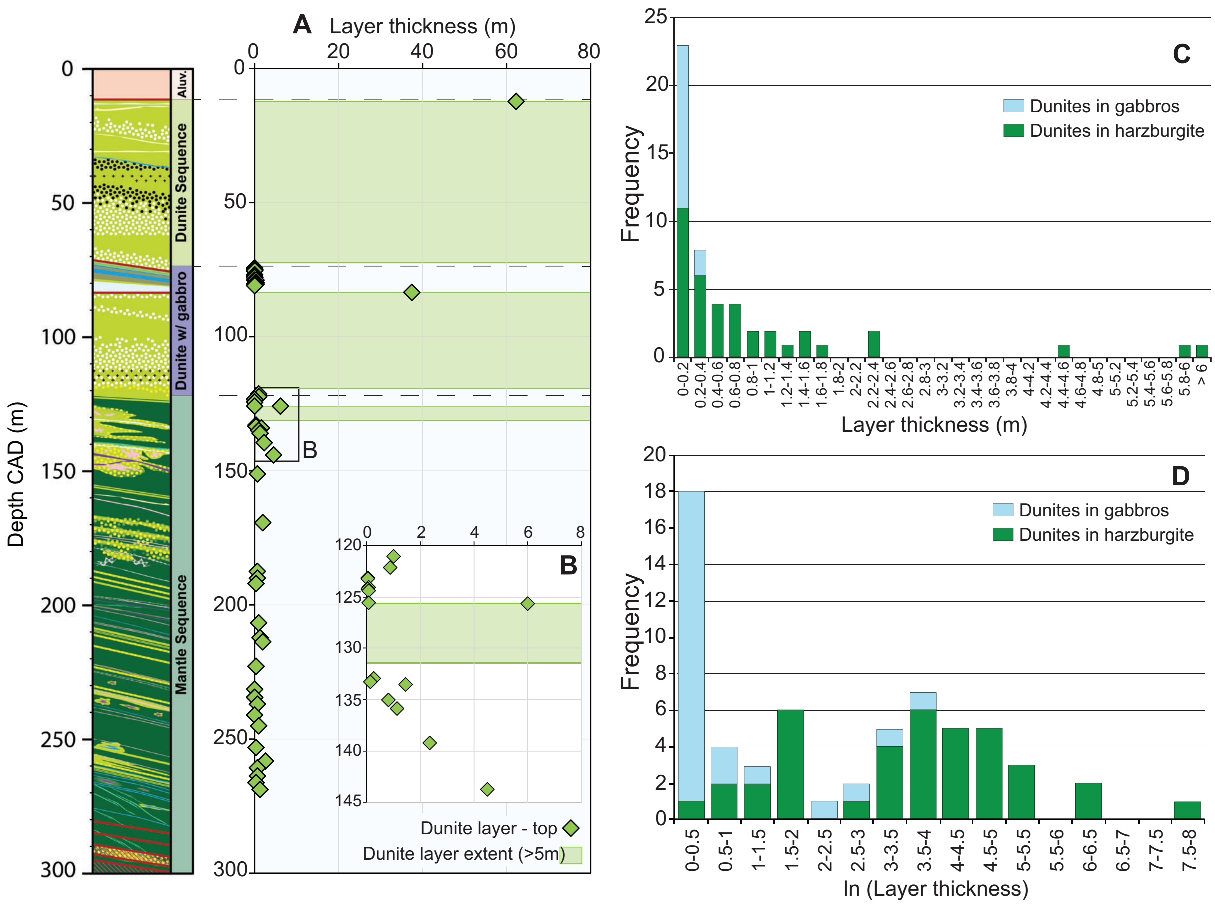

Figure F75. Layering and foliation. **A.** Spinel (highlighted in red by high-density contrast on the micro-CT scan) and plagioclase impregnation in dunite. **B.** Modal layering in gabbro. **C.** Modal layering and brittle deformation in gabbro. **D.** Modal layering in gabbro. **E.** Impregnation plagioclase layering in dunite. **F.** Impregnation plagioclase trails in dunite.

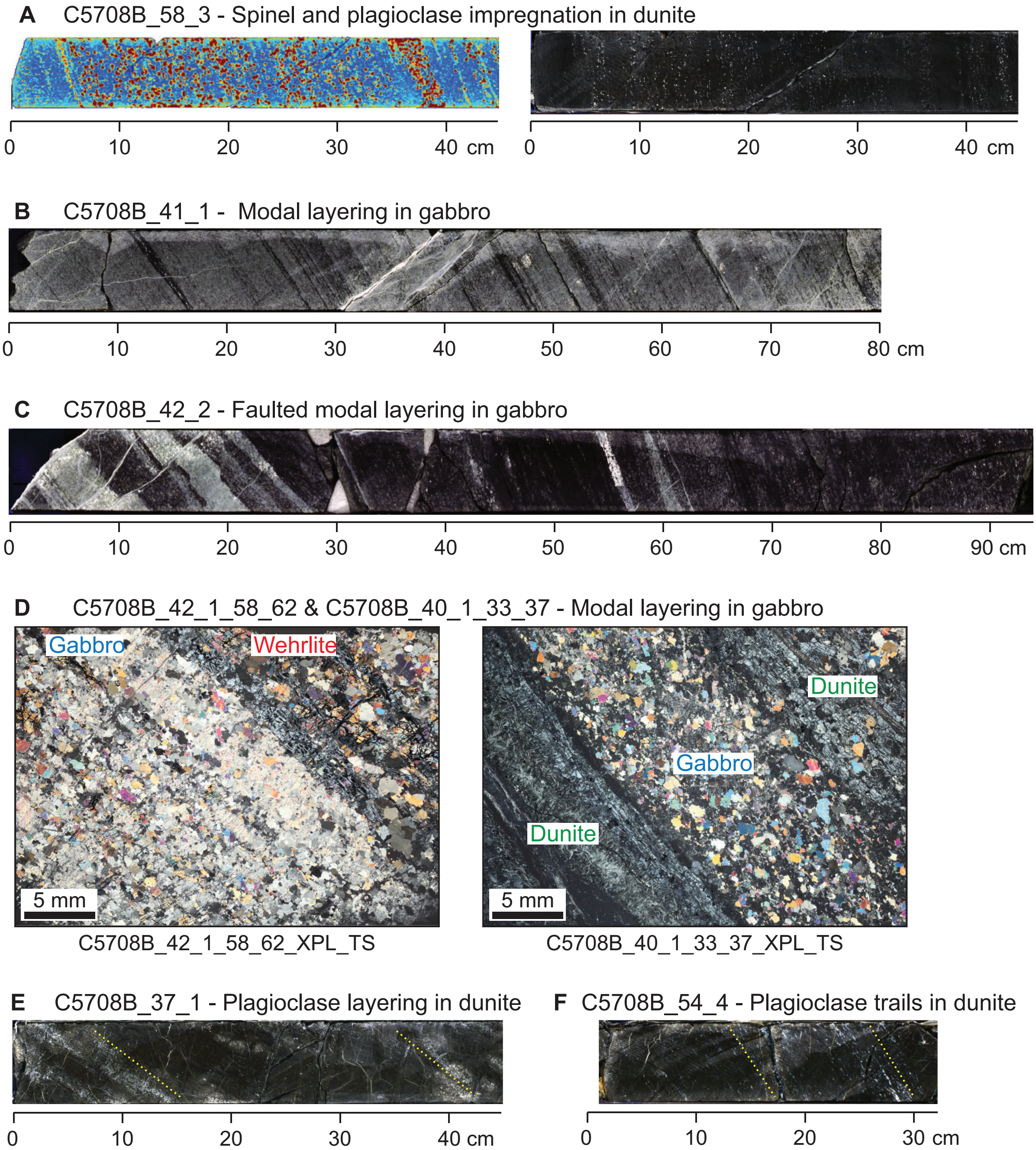

Figure F76. A. Layer thickness in the gabbroic sequence. Symbols mark the top of gabbro layers. The depth extent of gabbro layers thicker than 1 m are highlighted by blue bands. **B.** Frequency diagram of the gabbro layer thickness with bins of 5 cm. **C.** Frequency diagram of the natural logarithm of gabbro layer thickness.

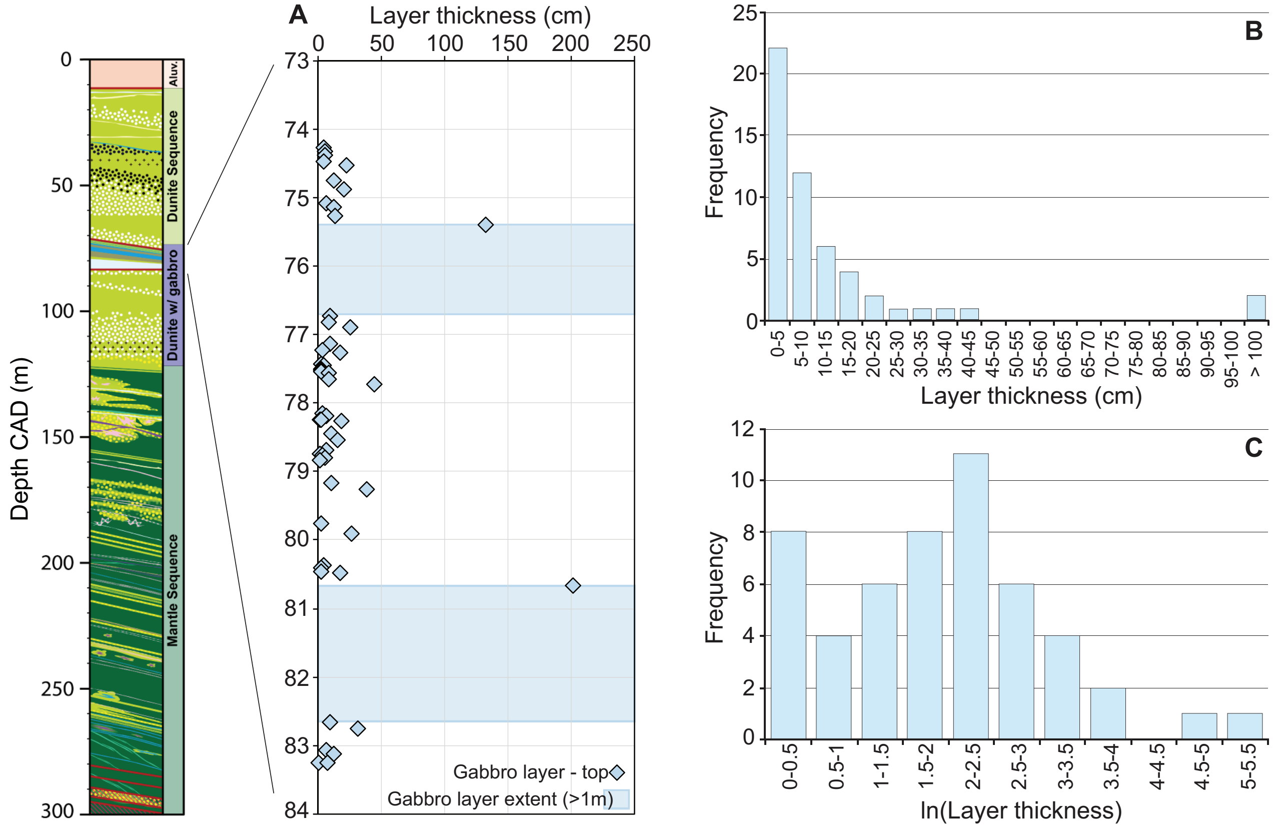

Figure F77. **A.** Vein thickness. The symbols mark the top of gabbroic veins. **B.** Frequency diagram of the gabbroic veins thickness with bins of 5 cm. **C.** Frequency diagram of the natural logarithm of gabbroic veins thickness.

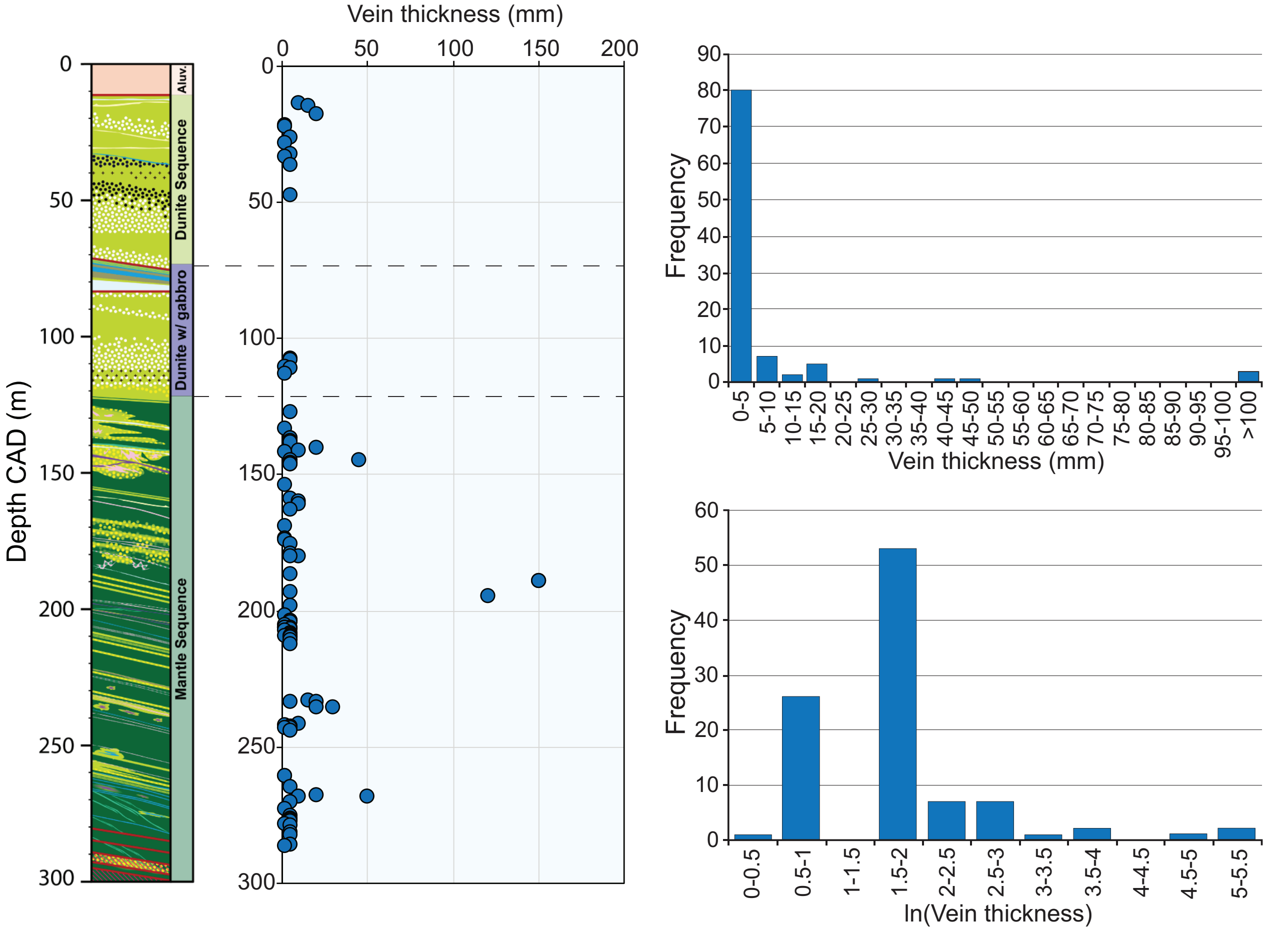

Figure F78. **A.** Dip angle of plagioclase impregnation foliation in dunite and harzburgite and harzburgite foliation. **B.** Crystal-plastic intensity of foliation in dunites and harzburgites: 0 = undeformed-protogranular, 1 = weakly foliated (porphyroclastic), 2 = moderately foliated (porphyroclastic), 3 = protomylonite, 4 = mylonite, 5 = ultramylonite, 6 = pseudotachylite.

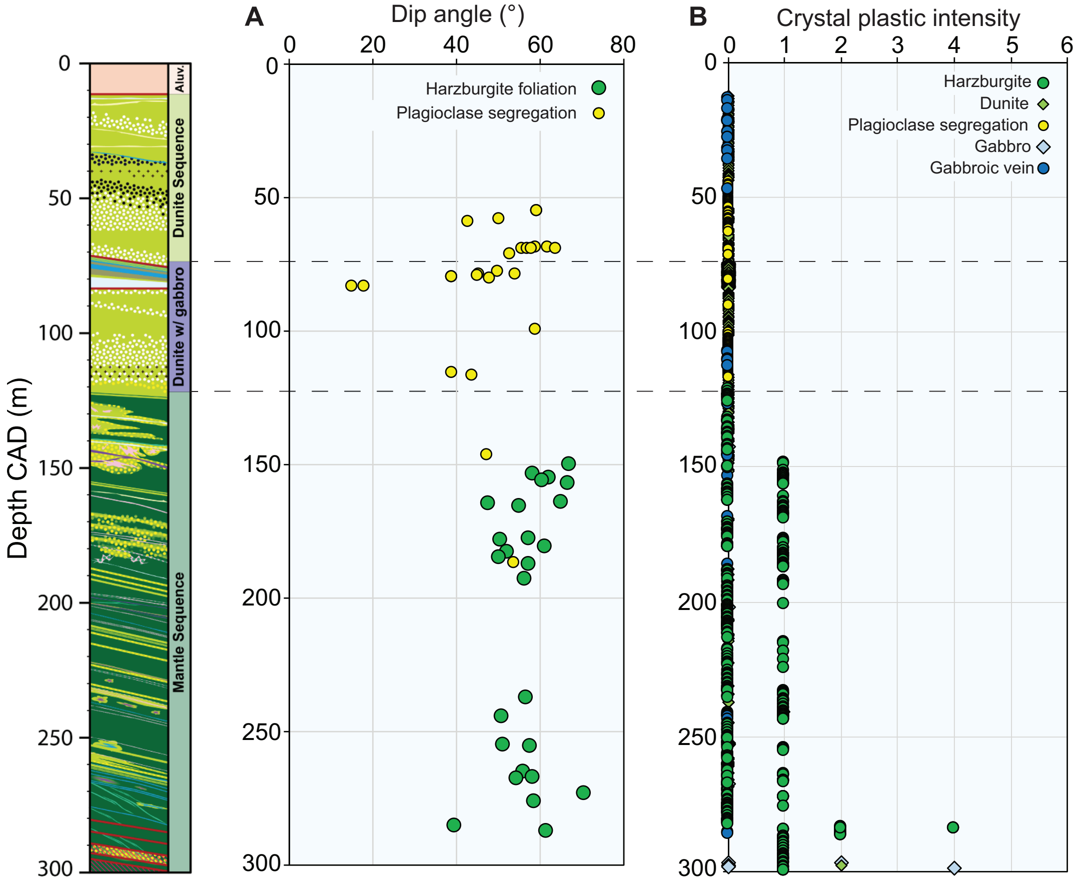

Figure F79. Microstructures, Hole CM2B. **A.** Coarse undeformed dunite showing spinel lineation. **B.** Finer grained dunite showing elongated olivines and shape-preferred orientation. **C, D.** Deformed olivine grains in dunite. Arrows = subgrain boundaries.

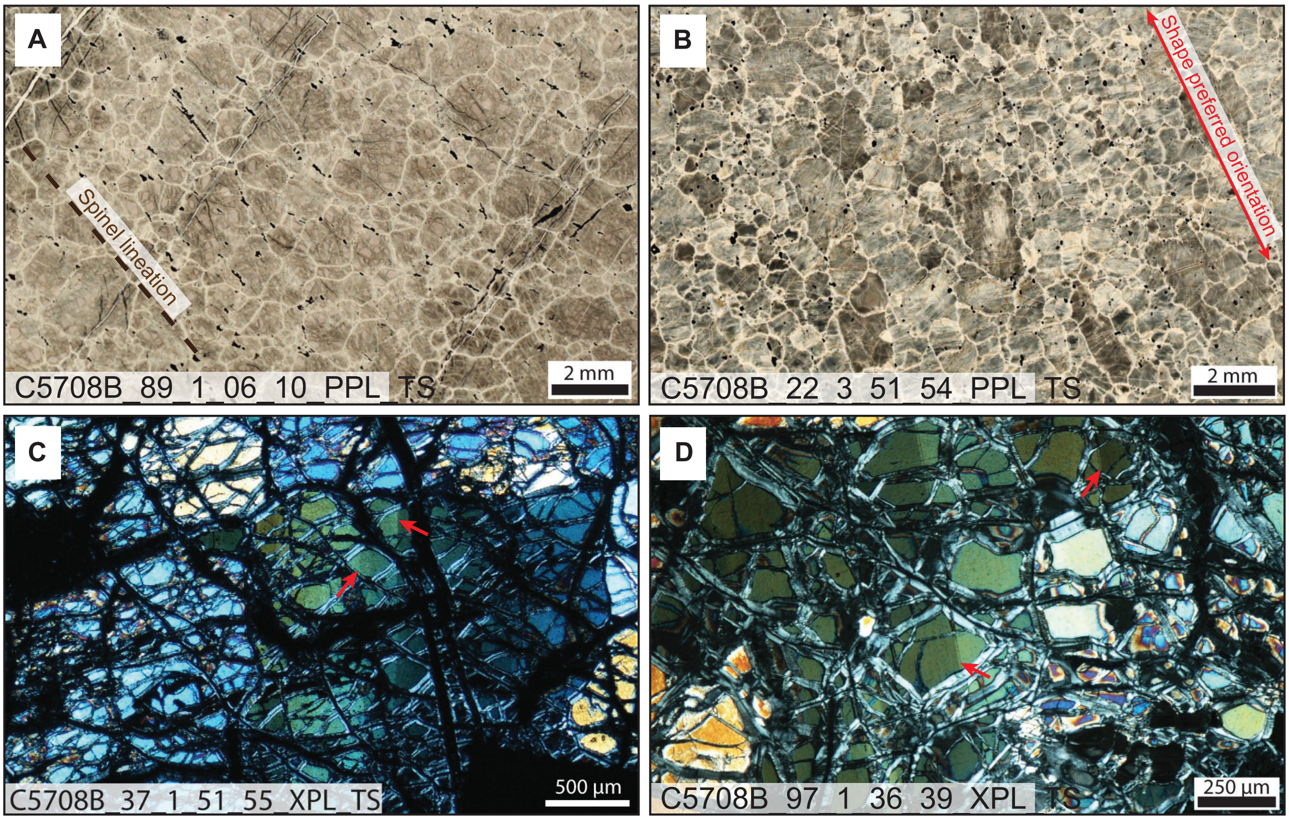

Figure F80. Microstructures, Hole CM2B. **A.** Undeformed harzburgite. **B.** Deformed harzburgite with crystal-plastic fabric shown by orthopyroxene and spinel. **C.** Protomylonite in impregnated harzburgite layer. **D.** Kinked porphyroclastic orthopyroxene grain. **E.** Recrystallized porphyroclastic orthopyroxene crystal. **F.** Spinel-rich impregnated layer with altered plagioclase crystals in the spinel pressure shadow (red arrows).

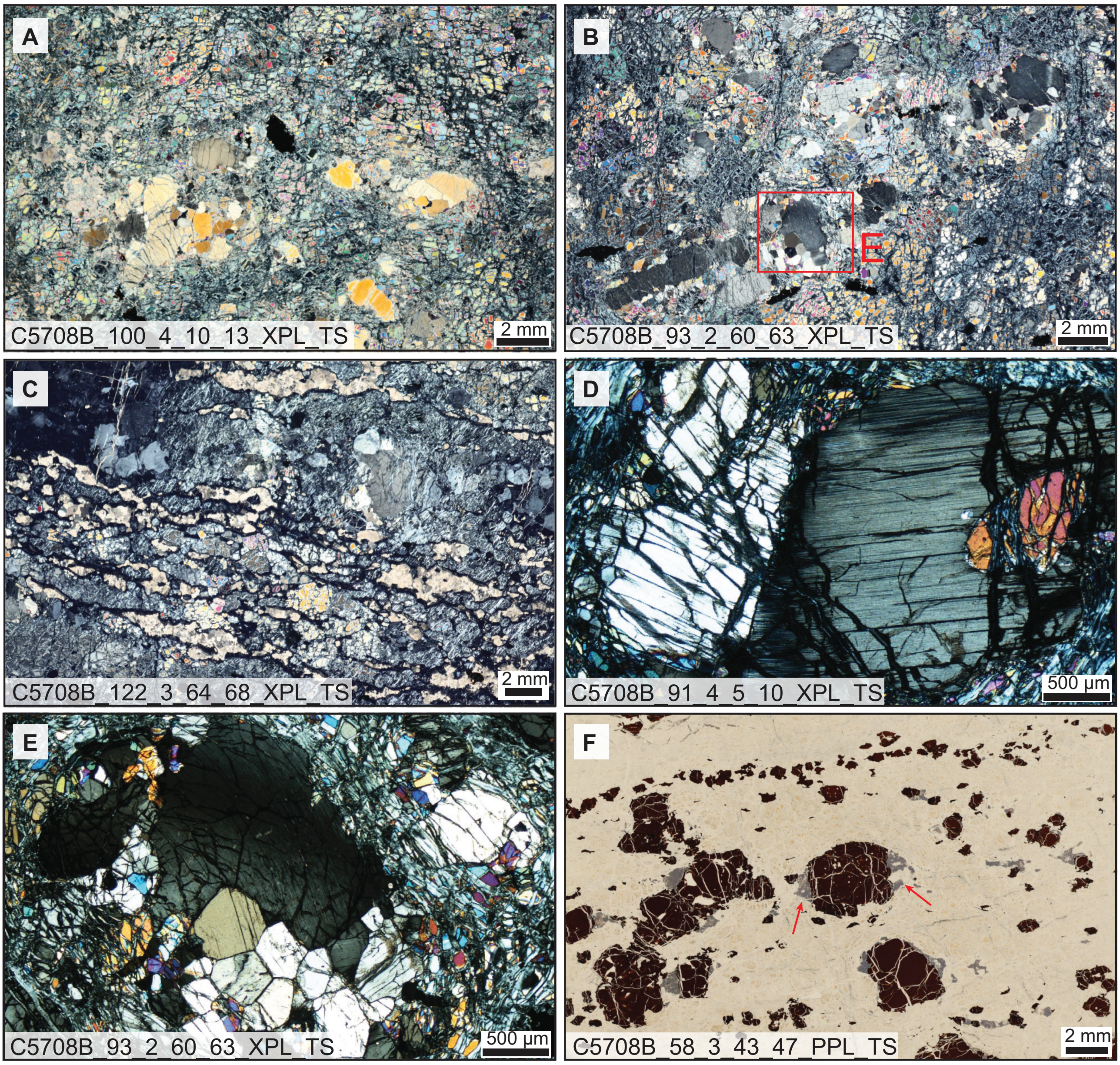

Figure F81. Smoothed downhole plots of fracture density, deformation intensity, and vein density and depths of fault zones, Hole CM2B.

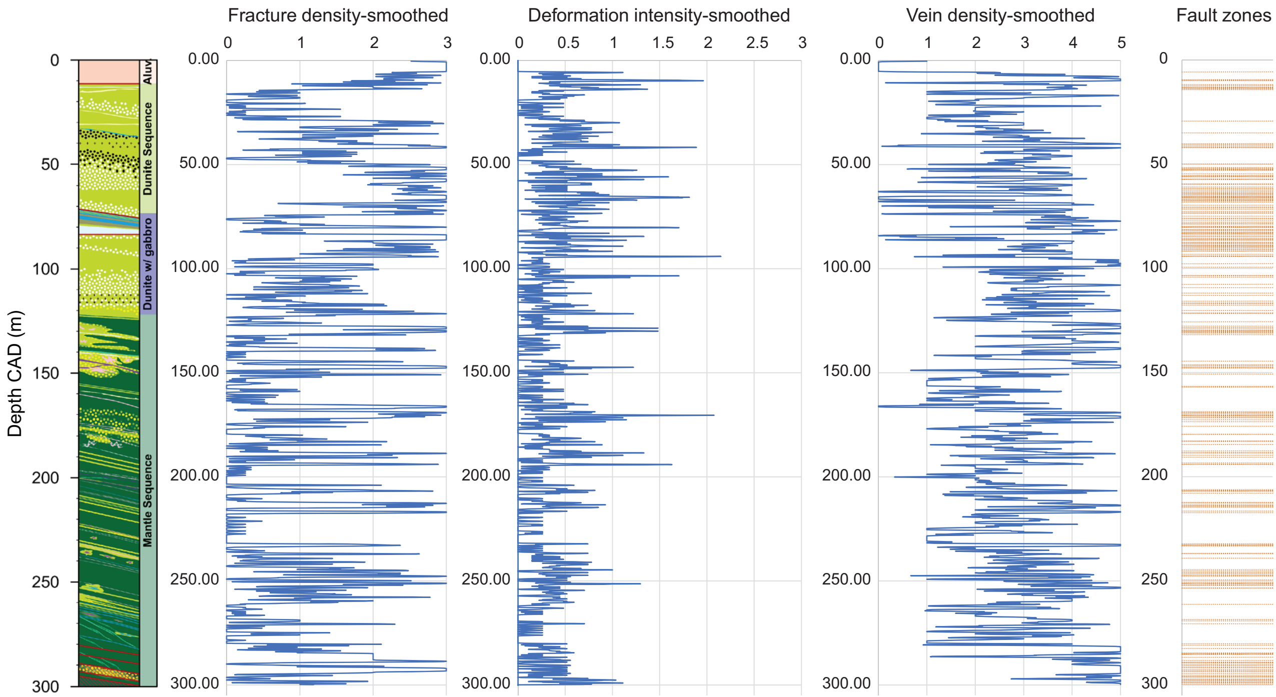

Figure F82. Cohesive cataclasite and semibrittle deformation, Hole CM2B. **A, B.** Deformed vein material showing semibrittle microstructures in foliated cataclasite and localized fault surface at the interface between diopsidite (light material in B; identified by XRD) and serpentinite (box = location of photomicrograph). **C–E.** Sheared vein cuts across both mafic layer and ultramafic layers: (D) synchronous formation of amphibole (tremolite) and serpentine vein; subsequent shear along the vein involves semibrittle deformation of chlorite and serpentine is then (E) crosscut by later brittle displacement and carbonate veins.

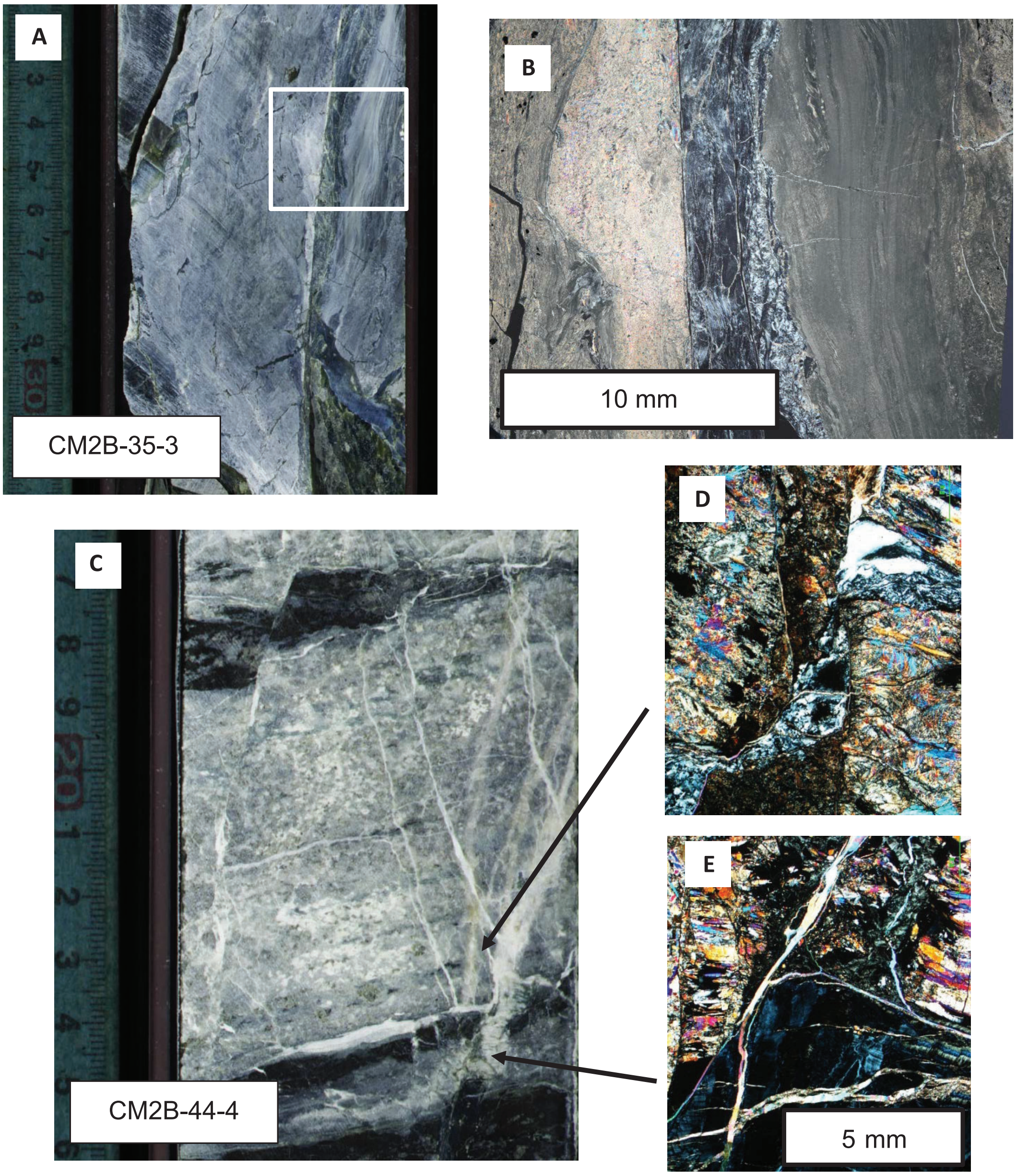

Figure F83. Cohesive cataclasite and semibrittle deformation in carbonated harzburgite, Hole CM2B. **A, B.** Deformed vein material showing crystal-plastic deformation microstructures in carbonate (subgrain boundaries, recrystallized grains) and talc (foliation wrapping around carbonate). **C, D.** Brittle overprint of ductile deformation microstructures.

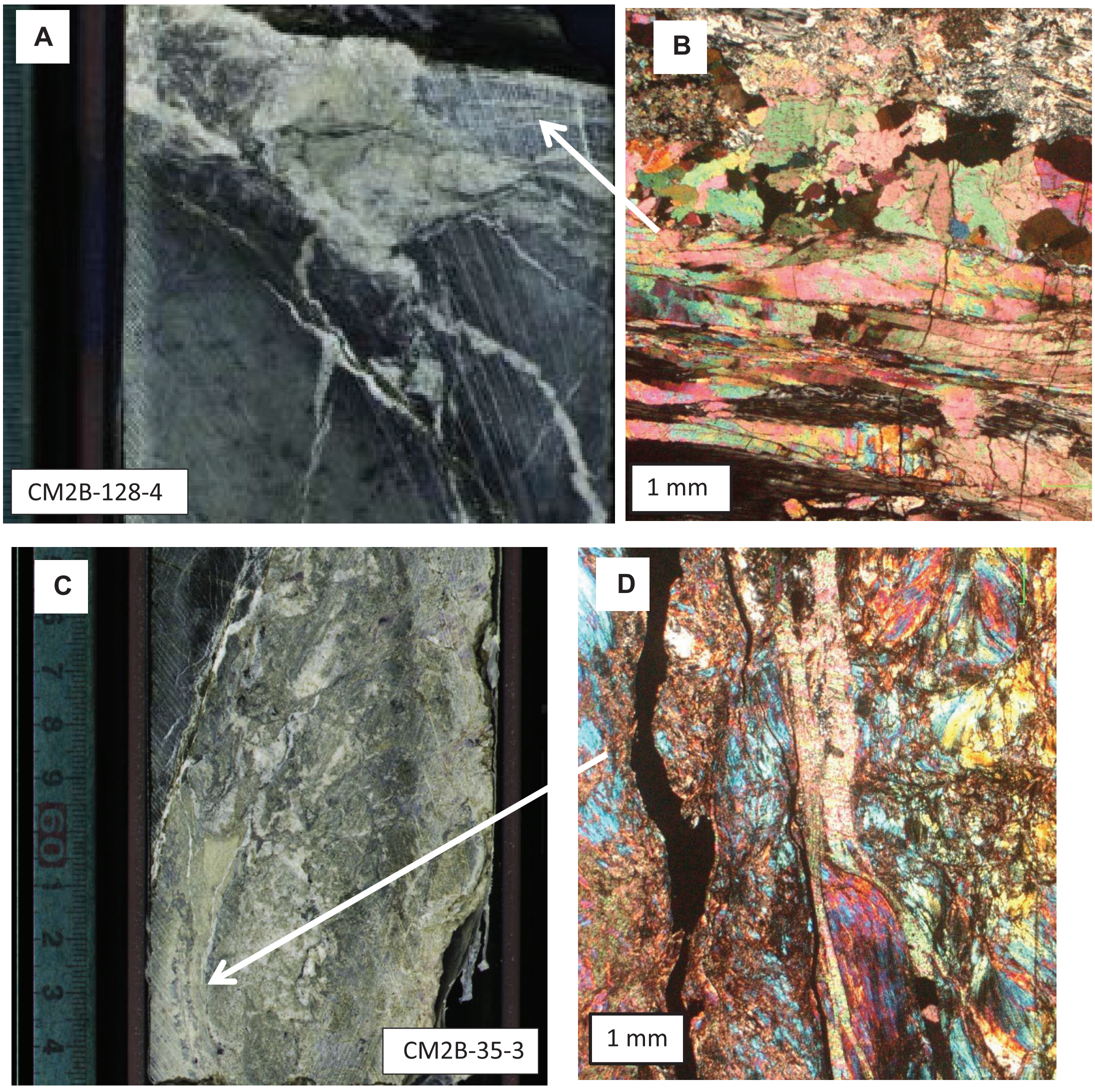

Figure F84. **A, B.** Serpentine vein-related brittle deformation in harzburgite, Hole CM2B. Deformation microstructures are illustrated for region of V3 veins. **C, D.** Localized cataclastic overprint of vein-related deformation (box = location of photomicrograph). Fractured and rotated clasts in D exhibit microstructures similar to those shown in C.

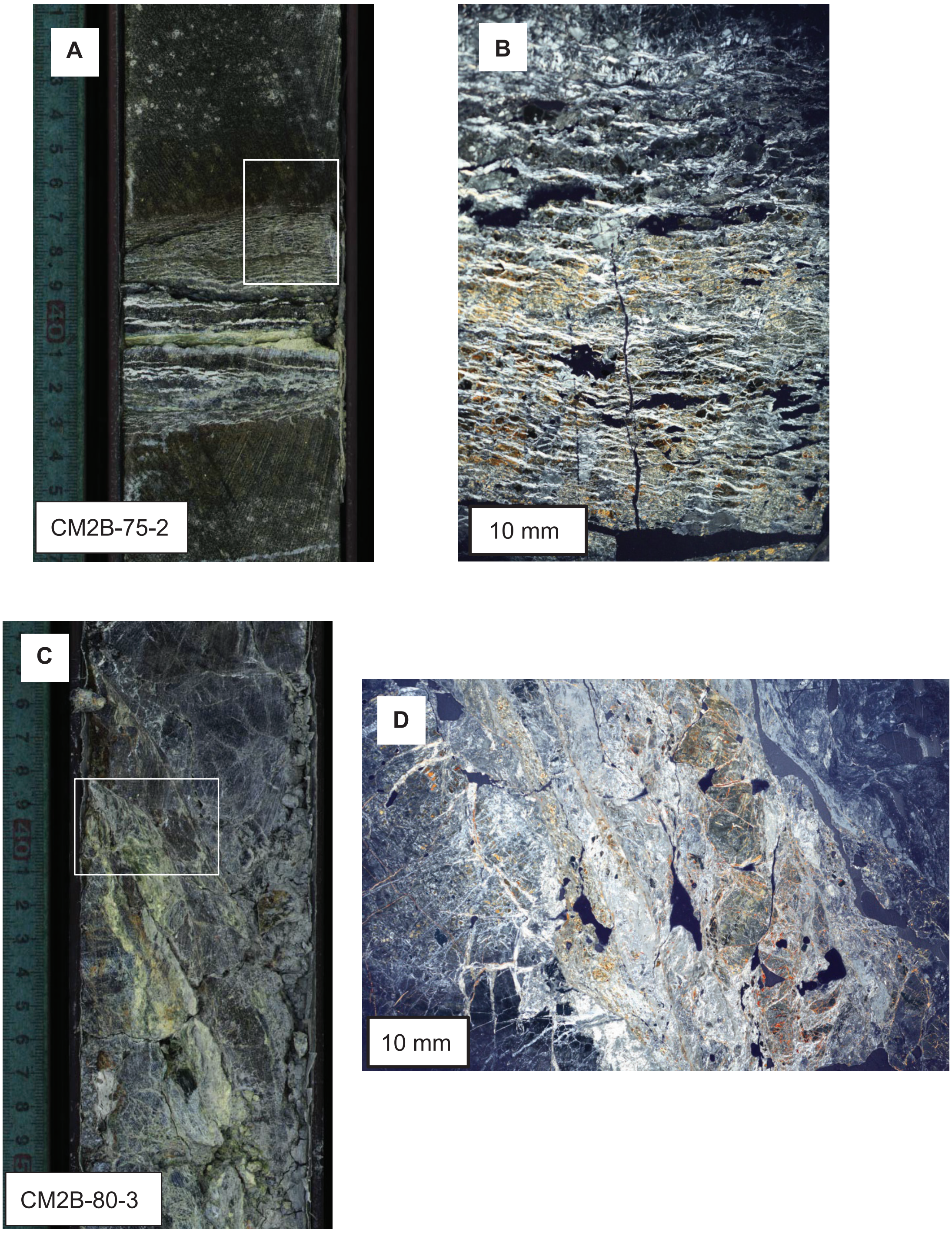

Figure F85. Incohesive cataclasite in dunite, Hole CM2B. The angular clasts are semicohesive cataclastic material comprising serpentinized dunite in a matrix is clay-like gouge.

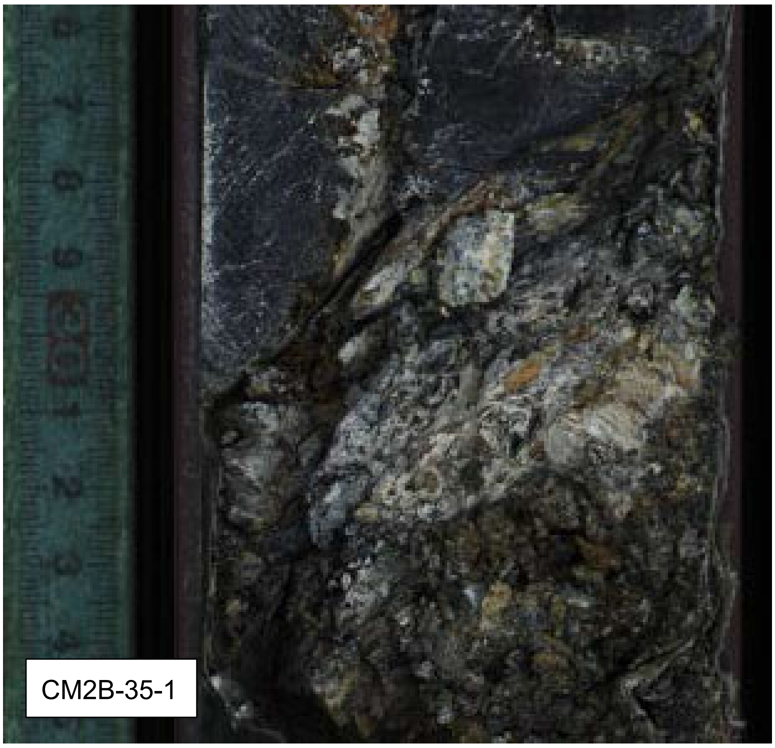

Figure F86. Downhole distribution of various fault types as interpreted from the core, Hole CM2B. **A.** Discontinuities between sections of core. **B.** Location of fault zones measured in the core and as shown in Figure F69. **C–F.** Interpreted depths and thicknesses of various fault zone types: (C) cohesive cataclasite; (D) fault/vein fracture network; (E) incohesive cataclasite; (F) surface-related deformation, (G) fault zone intensity index.

Figure F87. Distribution of dunite and harzburgite, fault zone intensity index (FZII), and identification of most significant faults, Hole CM2B (orange = zones with FZII > 0.2). The included table provides statistics on the percentages of dunite and harzburgite exhibiting FZII > 0.2.

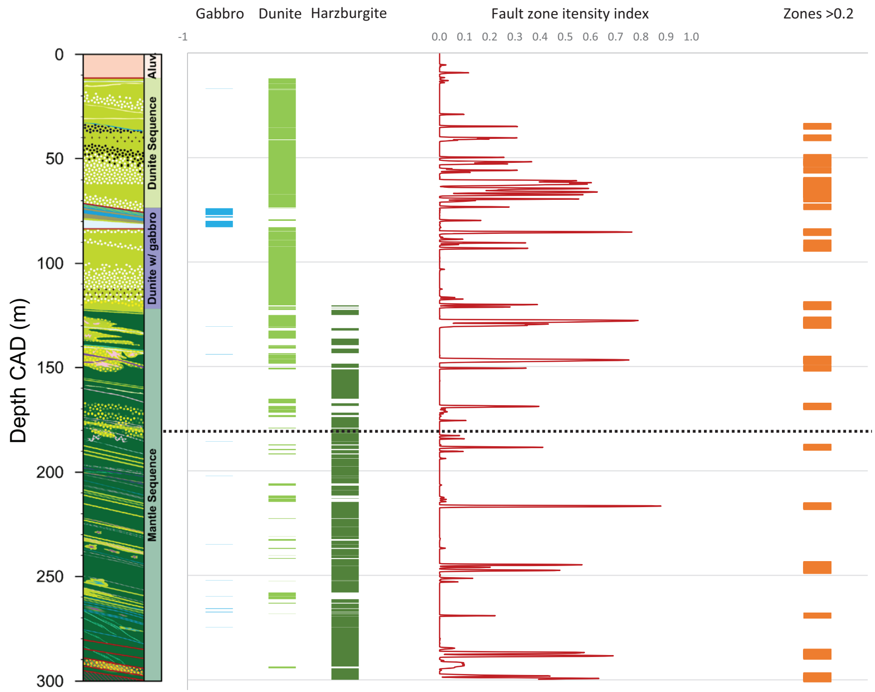

Deformation greater than 0.2

Deformation >0.2 per lithology		
	0 – 180 m	***180 – 300 m***
Dunite	99%	0%
Harzburgite	0%	100%
Anorthosite	1%	0%
Total	17.0 m	6.6 m

- 23.6 m of CM2B consists of fault zones with an intensity index greater than 0.2.
- In the upper 180 m there is a total of 17.0 m of fault zone (>0.2), with the majority (99%) of these occurring in the dunites.
- Below 180 m this correlation breaks down, with 100% of the 6.6 m of fault zone (>0.2) occurring in the harzburgites.

Figure F88. **A.** Crosscutting relationships of V2–V3 vein generations in the ultramafic sequences, Hole CM2B. **B.** V1: black serpentine veins; V2: black serpentine-magnetite veins; V2.5: grey serpentine veins; V3: 1 mm wide chrysotile veins; V5a: 0.1 mm wide chrysotile-carbonate veins. **C.** Crosscutting relationships (PPL). **D, E.** Mutually crosscutting relationships between V3 and V4 veins; (D) 1–4 mm wide V4 vein (green serpentine) crosscuts a V3 chrysotile vein with an offset of ~ 2 cm; (E) the V4 vein (green serpentine) contains a V3 chrysotile vein, indicating precipitation of the V3 vein by reactivation of the V4 vein. (Continued on next page.)

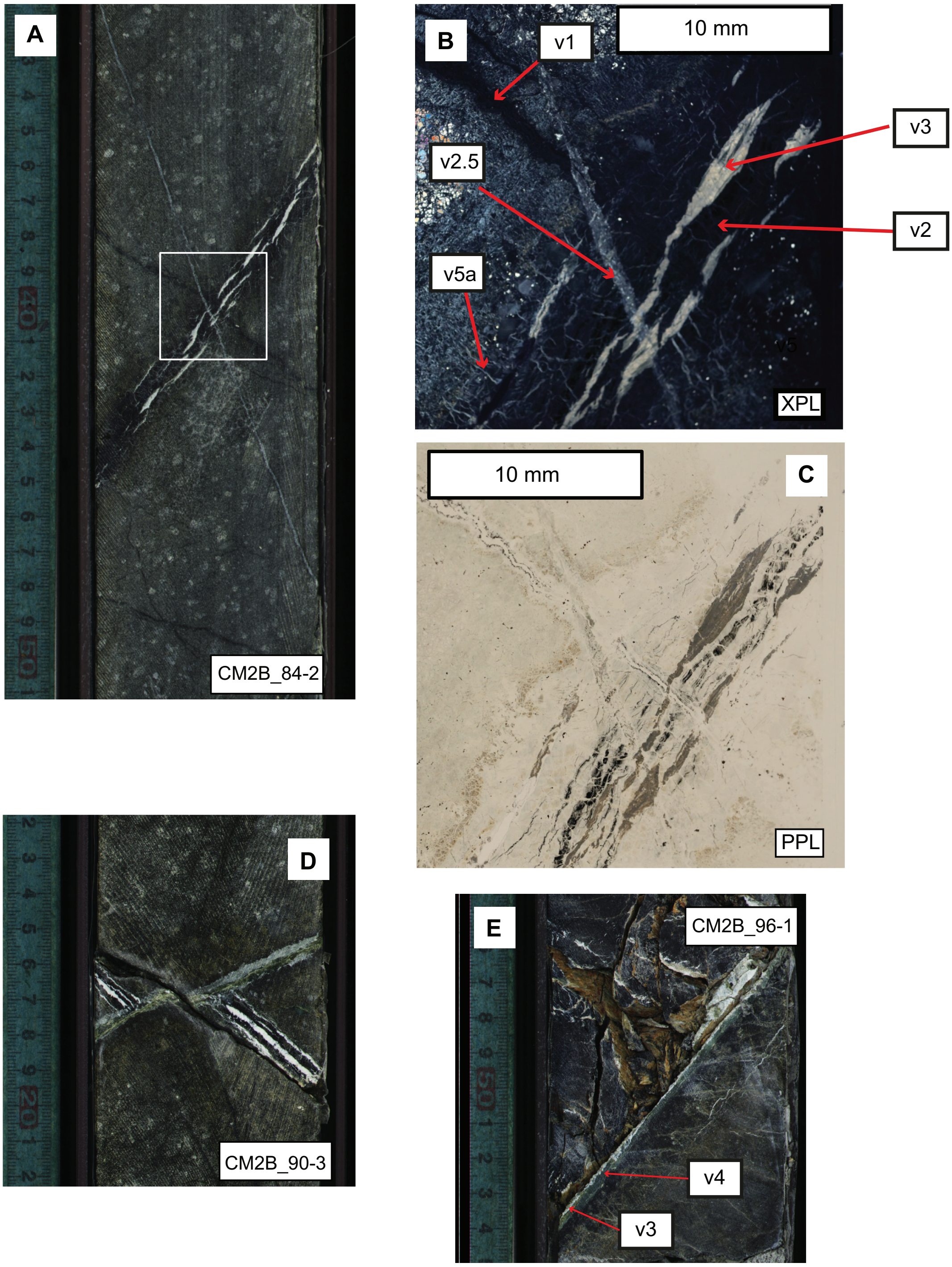

Figure F88 (continued). **F.** Schematic diagram of crosscutting relationships of all observed veins.

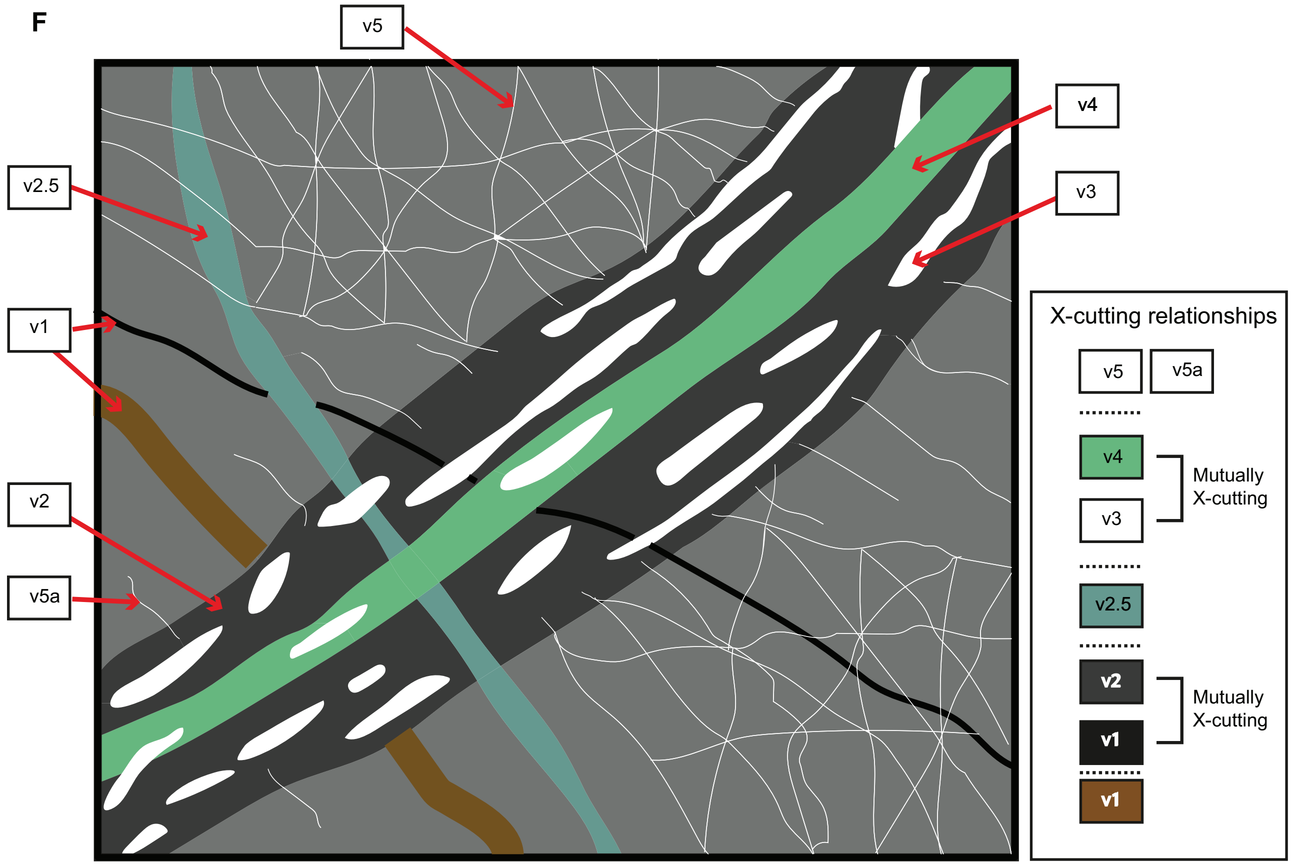

Figure F89. Downhole plot of vein dip angle (denoted with vein generation) compared with fault zone intensity index (FZII). In the middle diagram, the average vein dips of V1 and V2 veins are illustrated for intervals defined by the location of faults with FZII > 0.5 (shown as dashed lines).

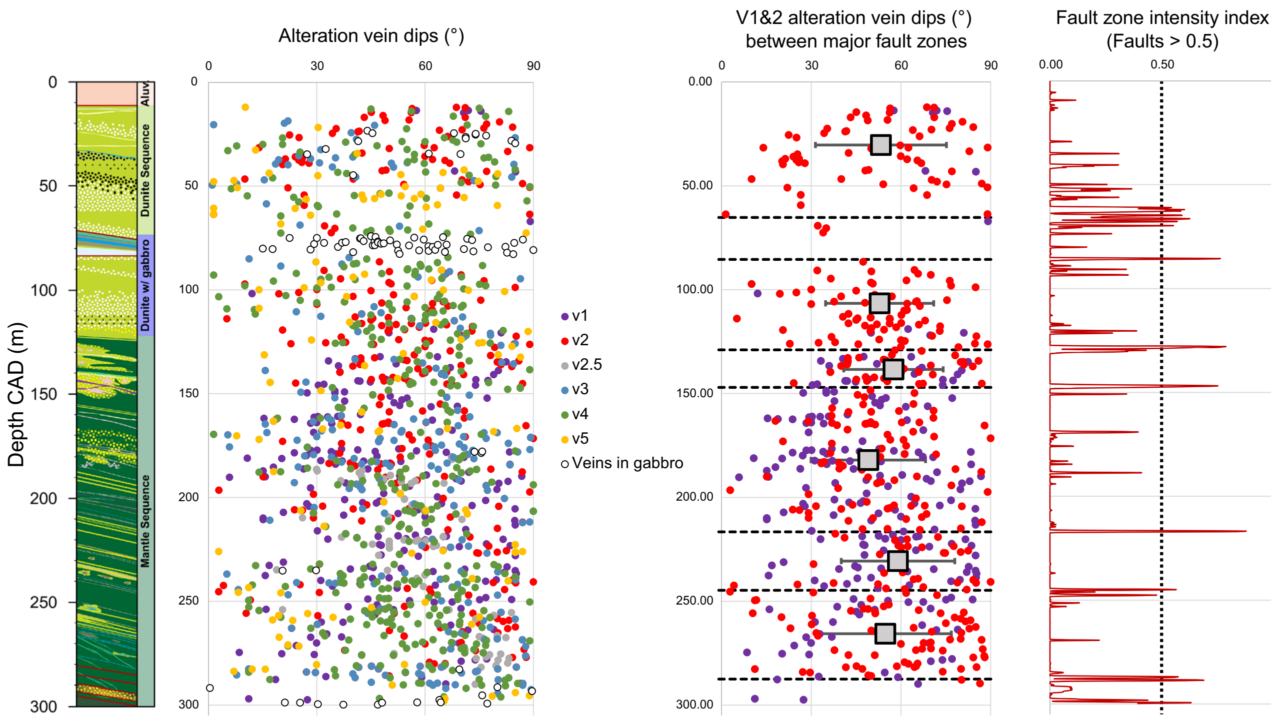

Figure F90. Histograms showing the distribution of vein dips, separated by vein generation. Dotted lines illustrate the distribution of dips expected for randomly oriented fractures in a core.

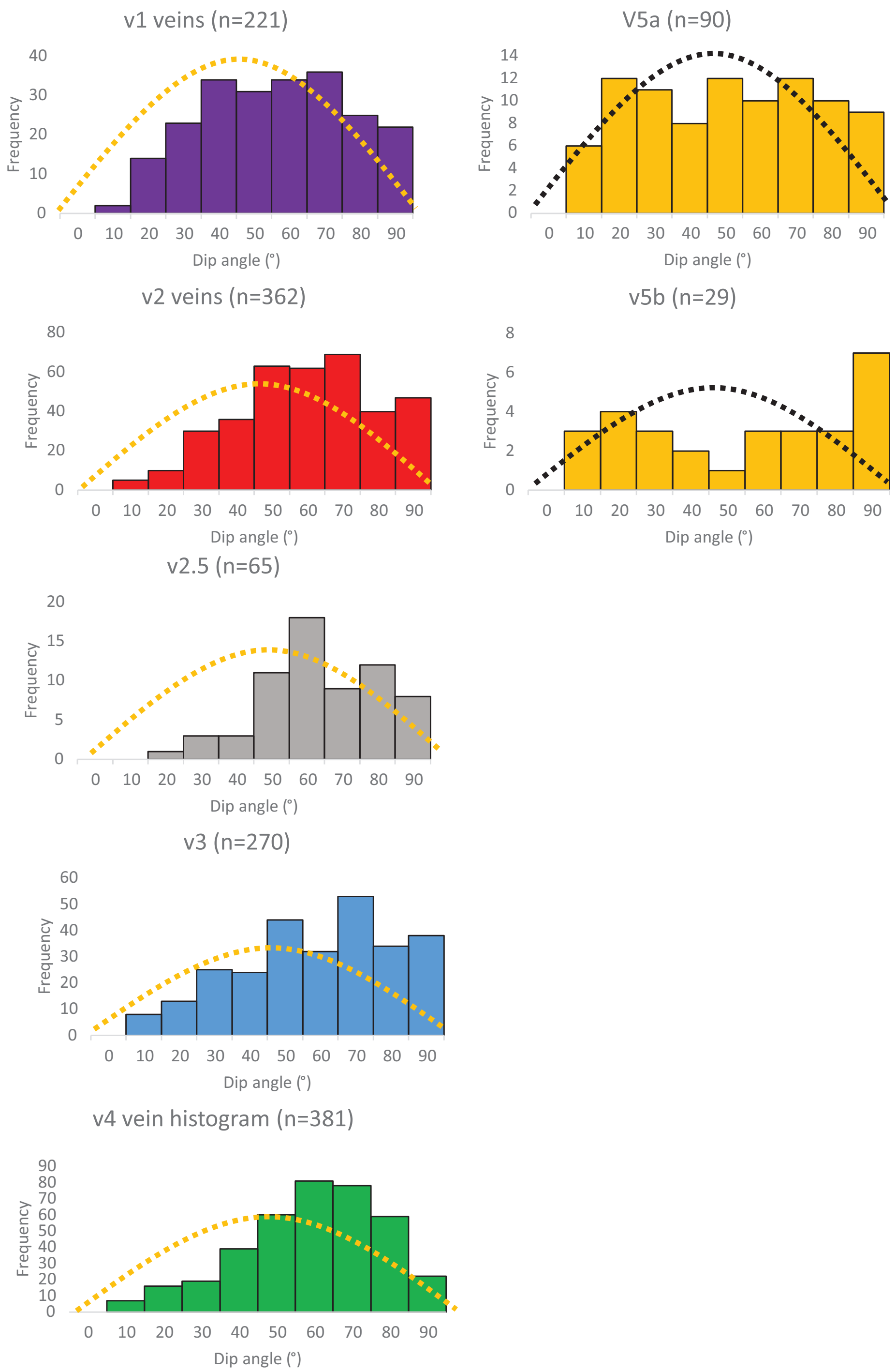

Figure F91. Downhole plots of dip angles for fault zones, extensional fractures (by vein generation; yellow = fractures without vein material and for which vein material could not be identified), and slickensides identified on V2, V3, and V4 vein surfaces.

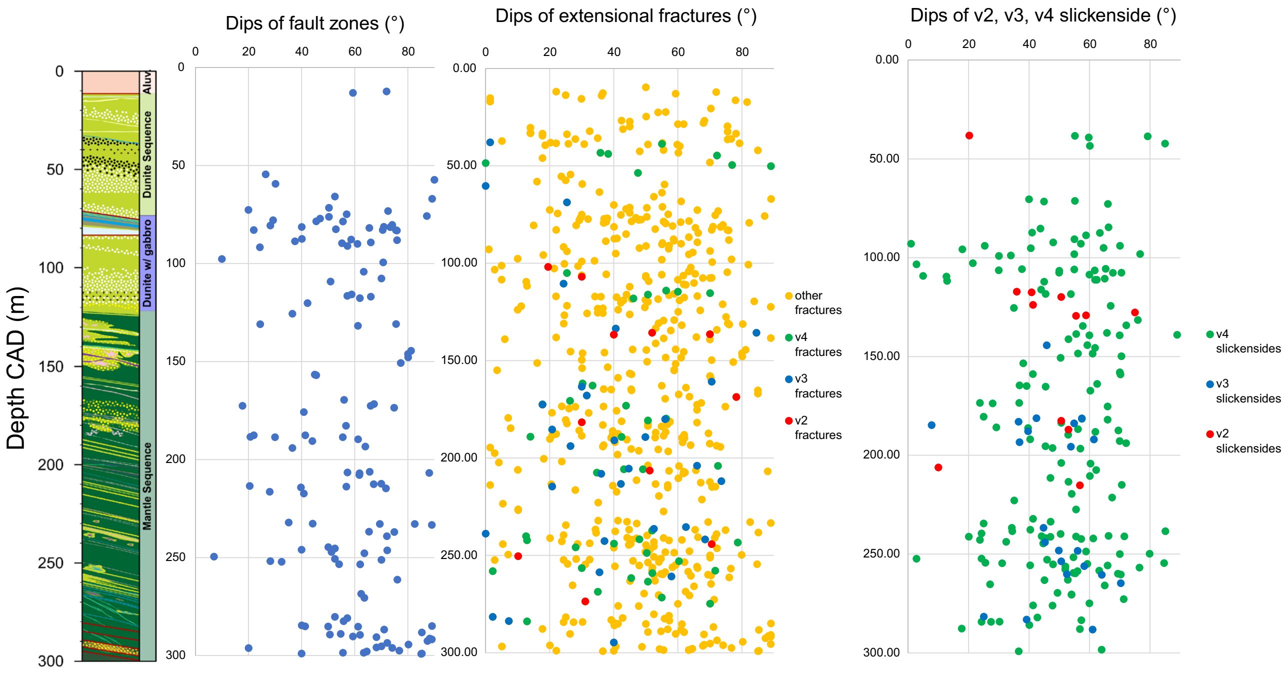

Figure F92. Histograms showing the distribution of dips for extensional fractures (by vein generation), slickensides (by vein generation), and all extensional fractures, slickensides, and faults.

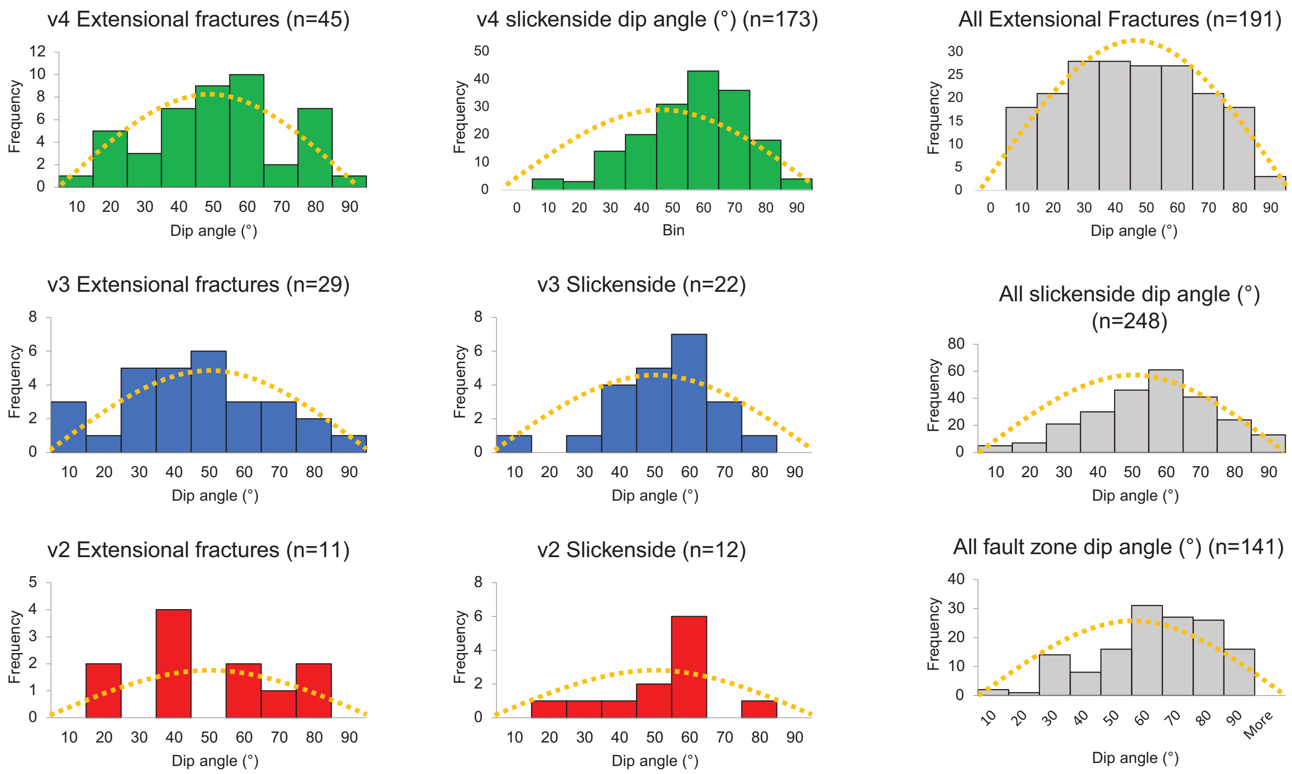

Figure F93. Downhole plot of slickenline plunge by sense of shear (other = both strike slip [at low plunges] and those for which shear sense could not be determined). Histograms for slickenline plunge are shown, denoted by the vein generation for the surface they on which they were identified. Histograms for all slickenline plunges and all fault zone plunges are also shown.

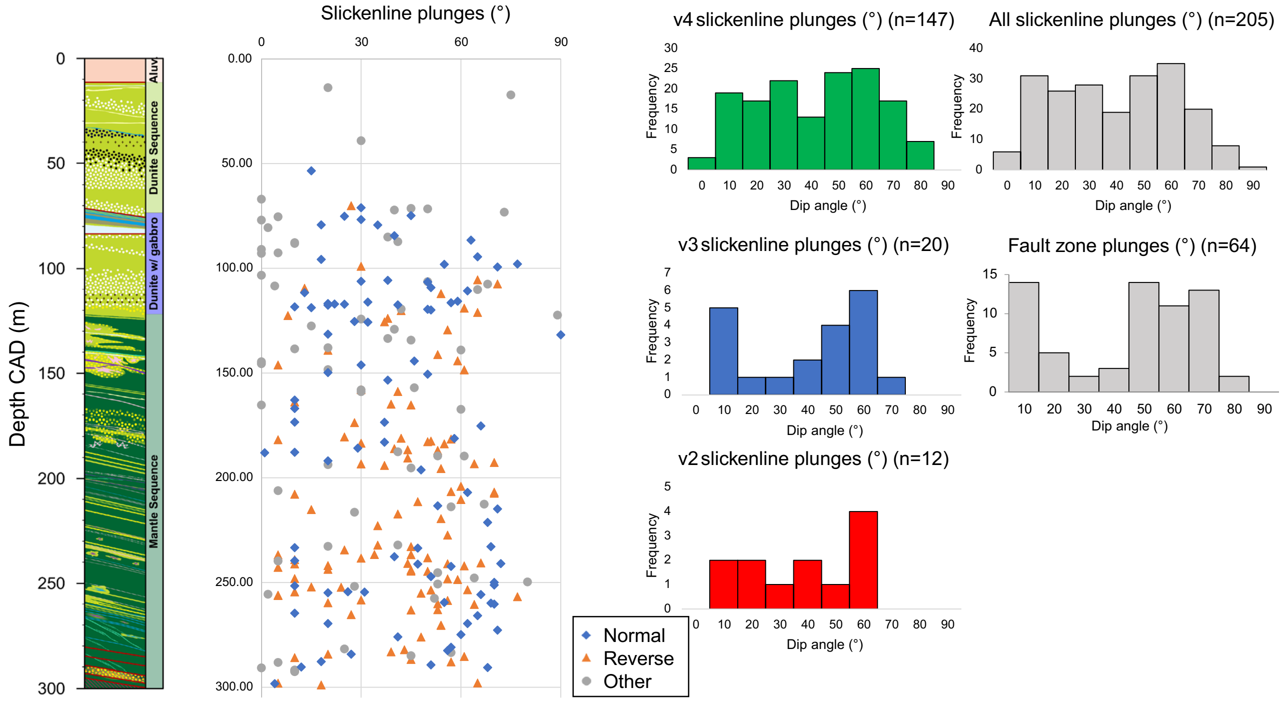

Figure F94. Lower hemisphere stereonet plots showing the orientations of structural features in (**A, B**) the longest continuous core interval (173–213 m); (**C, D**) the entire data set for Hole CM2B. (A) Pole to planes for fault zones, slickensides on V3 veins, slickensides on V4 veins, harzburgite foliation, and magmatic veins. (B) Poles to planes to slickensides on V3 and V4 veins, denoted by sense of shear. (C) Contoured plot of poles to planes of all V4 veins. (D) Contoured plot of poles to planes of all slickensides on V4 veins.

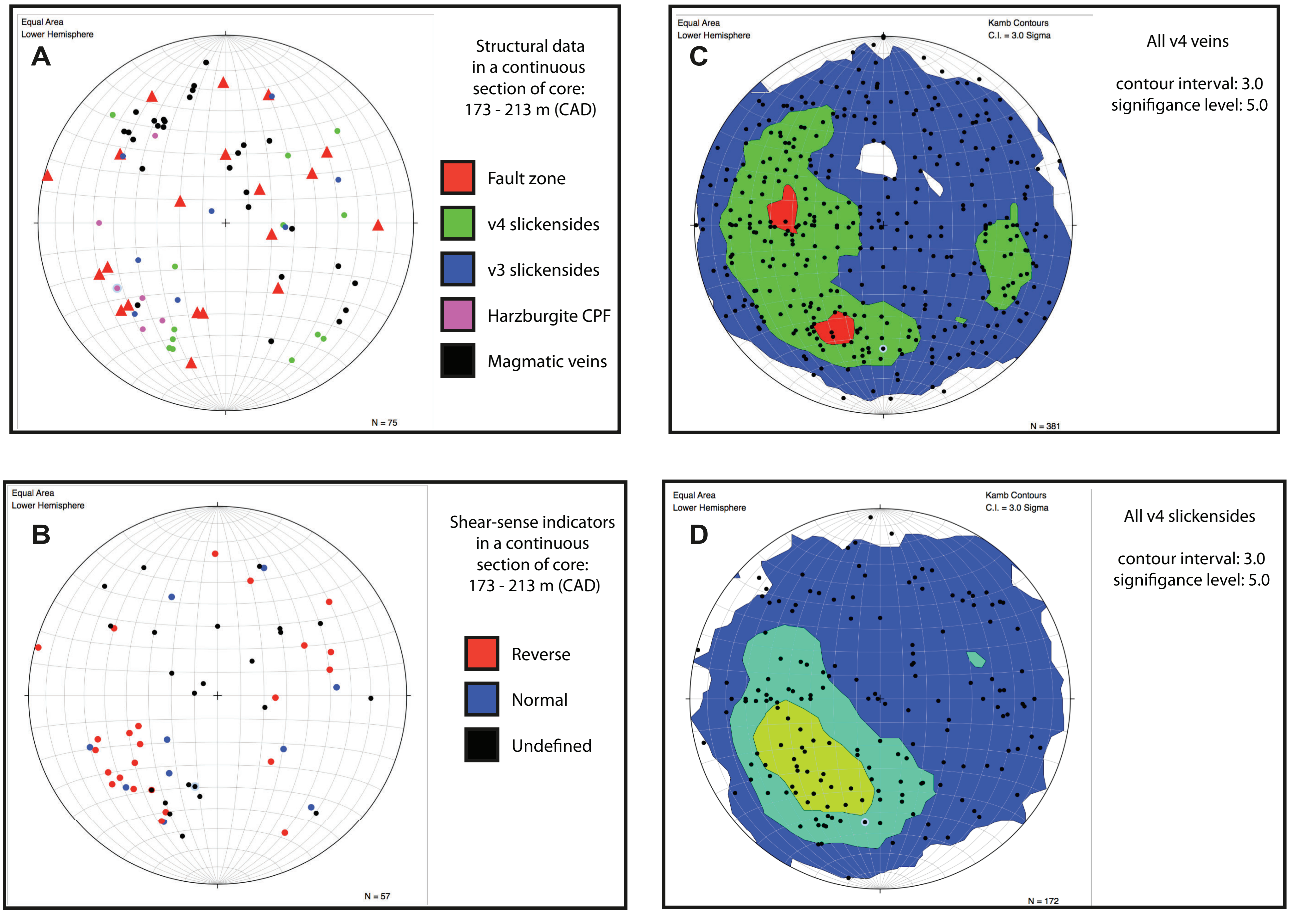

Stereonet 3D © Cardozo, N. and Allmendinger, R.W., 2016

Figure F95. Schematic cross-section of structural relationships based on correlation of observations from Holes CM1A and CM2B.

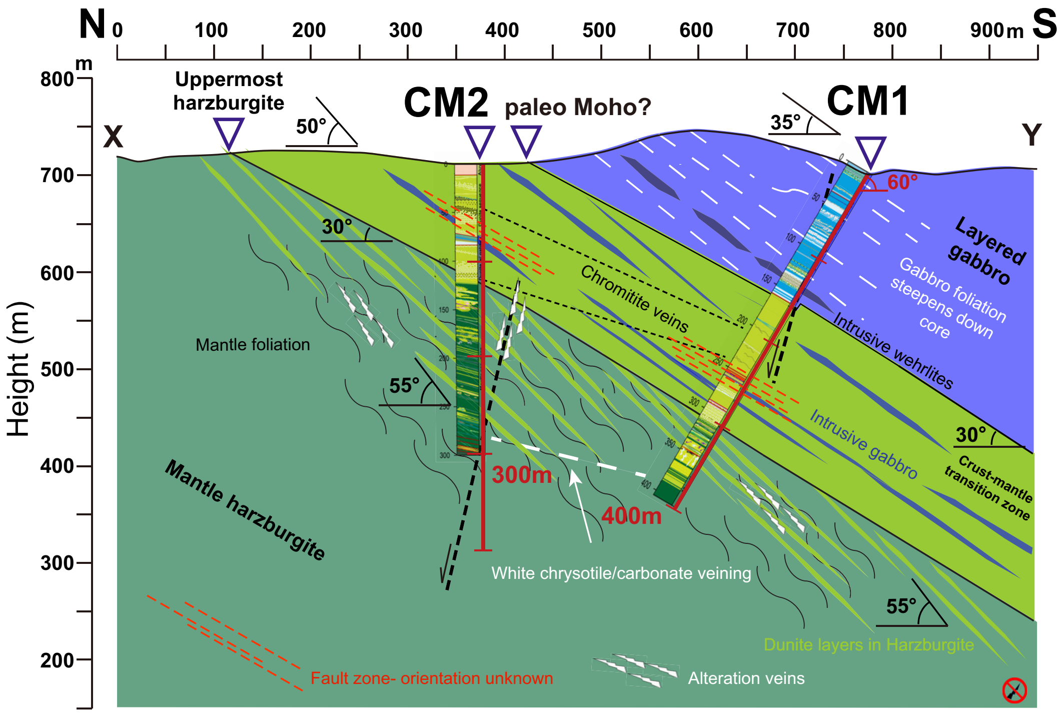

Figure F96. LOI vs. (**A, B**) inorganic carbon, (**C, D**) CO_2, and (**E, F**) H_2O contents, Hole CM2B.

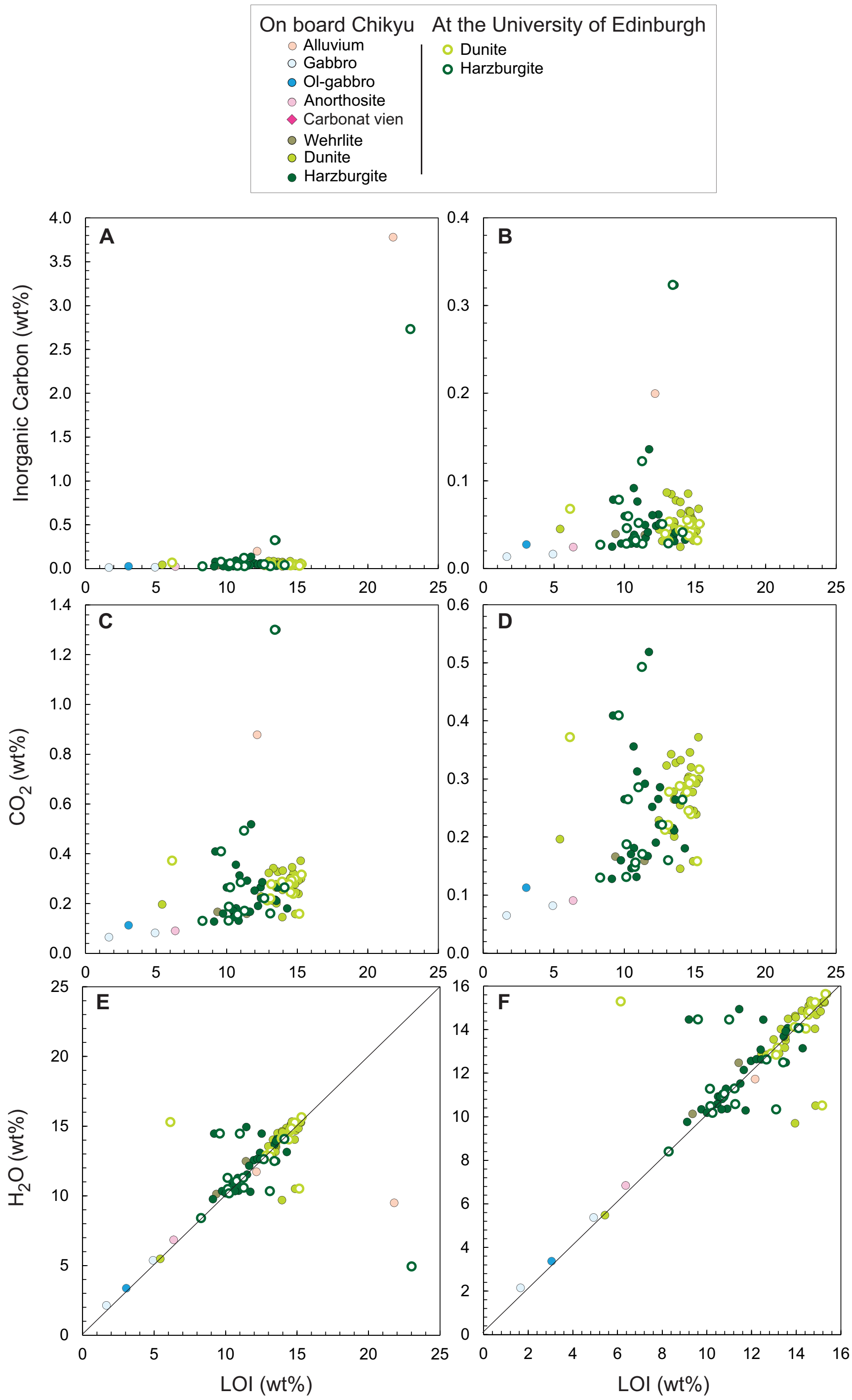

Figure F97. Downhole plots of lithology, LOI, Mg# (cationic Mg/[Mg + Fe], calculated assuming all Fe as FeO), and major element oxides, Cr, and Ni in whole-rock samples, Hole CM2B.

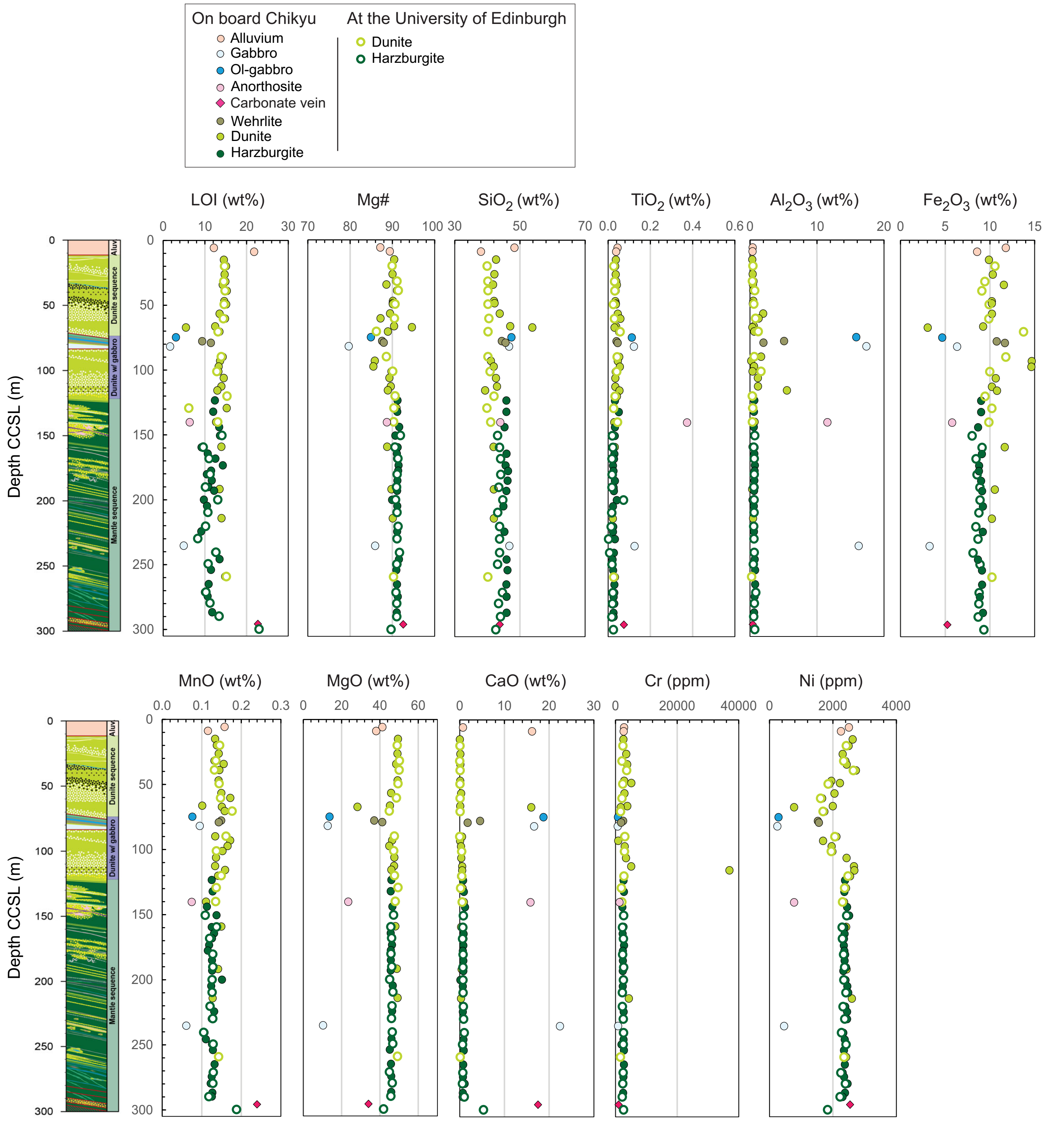

Figure F98. Whole-rock major and minor compositions vs. Mg# (cationic Mg/[Mg + Fe], calculated assuming all Fe as FeO), Hole CM2B.

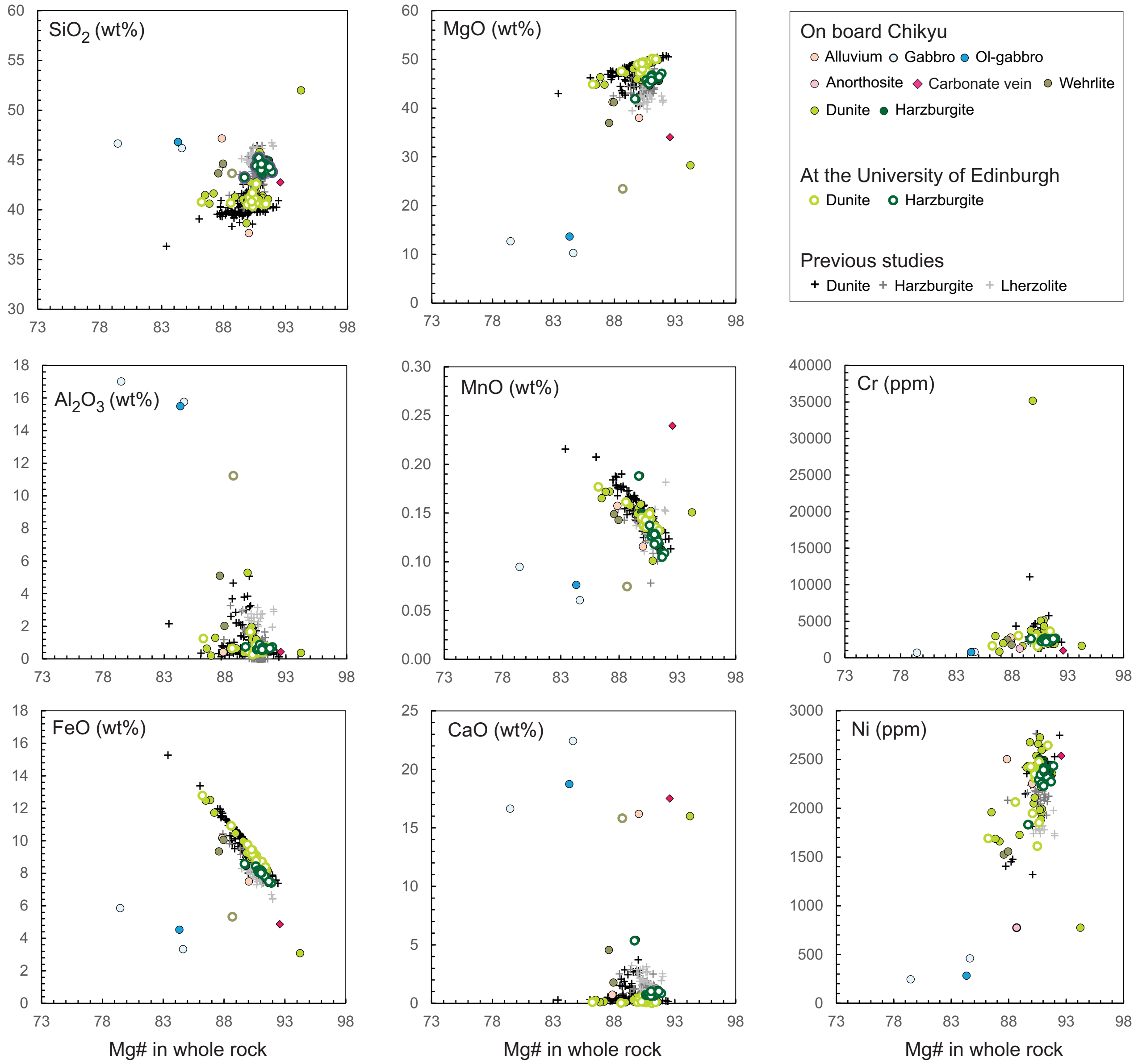

Figure F99. Whole-rock major compositions in Hole CM2B samples compared to other dunites, harzburgites, and lherzolites from the Oman ophiolite (Godard et al., 2000; Gerbert-Gaillard, 2002; Takazawa et al., 2003; Monnier et al., 2006; Hanghøj et al., 2010; Khedr et al., 2014; Nicolle et al., 2016; Rospabé et al., 2018). Top: MgO/SiO_2 vs. Al_2O_3/SiO_2. Middle: total iron as FeO vs. MgO. Bottom: Al_2O_3 vs. CaO. Compositions are recalculated on a volatile-free basis. Gray bar in top panel represents the silicate Earth differentiation trend (or "terrestrial array") (Jagoutz et al., 1979). Dashed lines in middle and lower panels represent constant Mg# and Al_2O_3/CaO ratios, respectively.

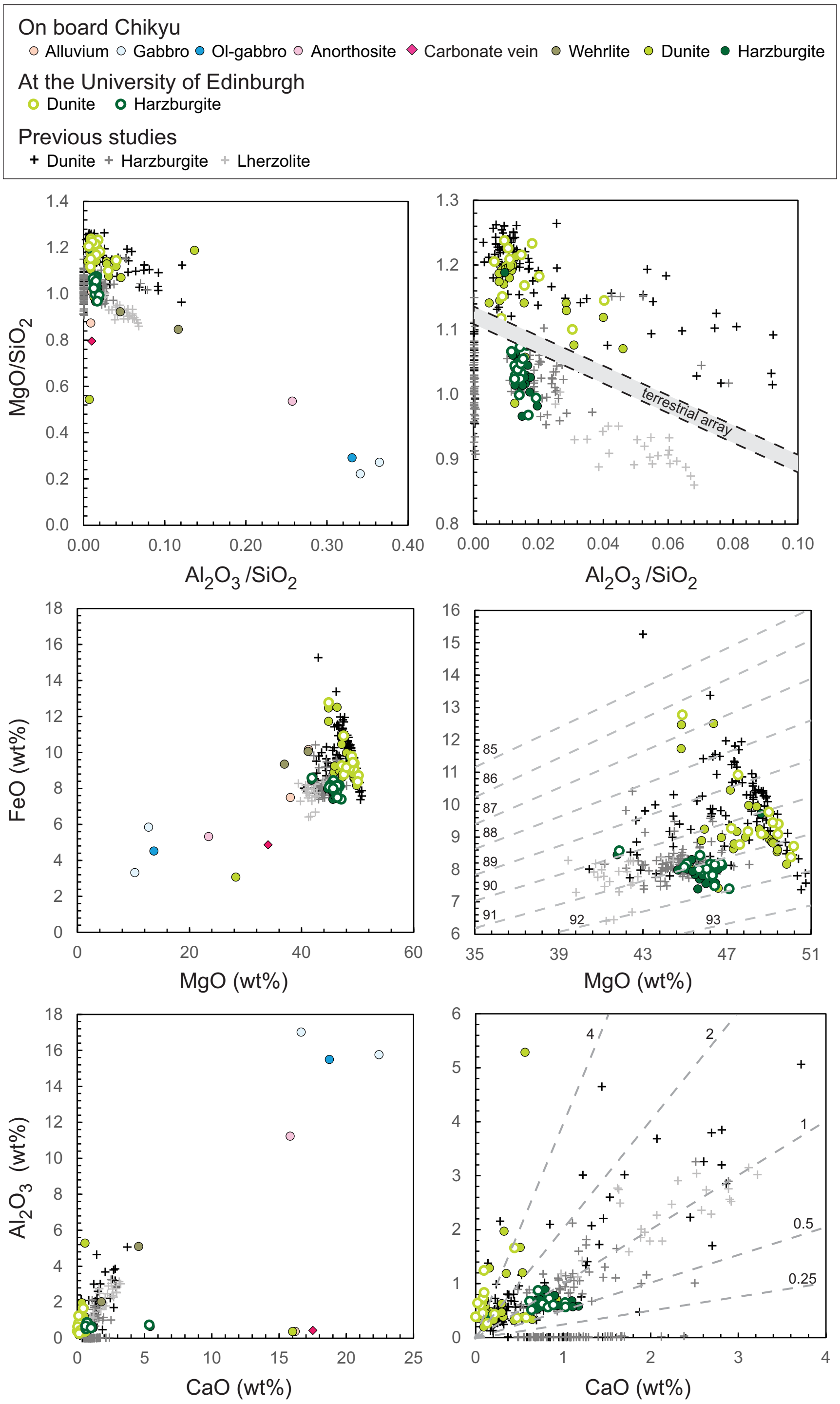

Figure F100. (**A**) Chondrite-normalized REE and (**B**) primitive mantle–normalized multielement patterns of gabbro, olivine gabbro, and dunite, Hole CM2B. Normalizing chondrite and primitive mantle values are from Barrat et al. (2012) and Sun and McDonough (1989), respectively.

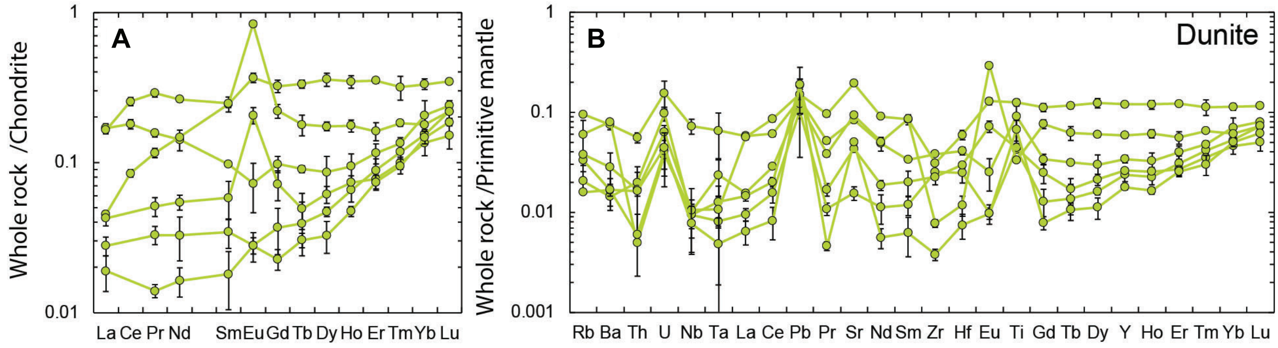

Figure F101. (**A**) Chondrite-normalized REE and (**B**) primitive mantle–normalized multielement patterns of orthopyroxene and clinopyroxene, Hole CM2B. Normalizing chondrite and primitive mantle values are from Barrat et al. (2012) and Sun and McDonough (1989), respectively.

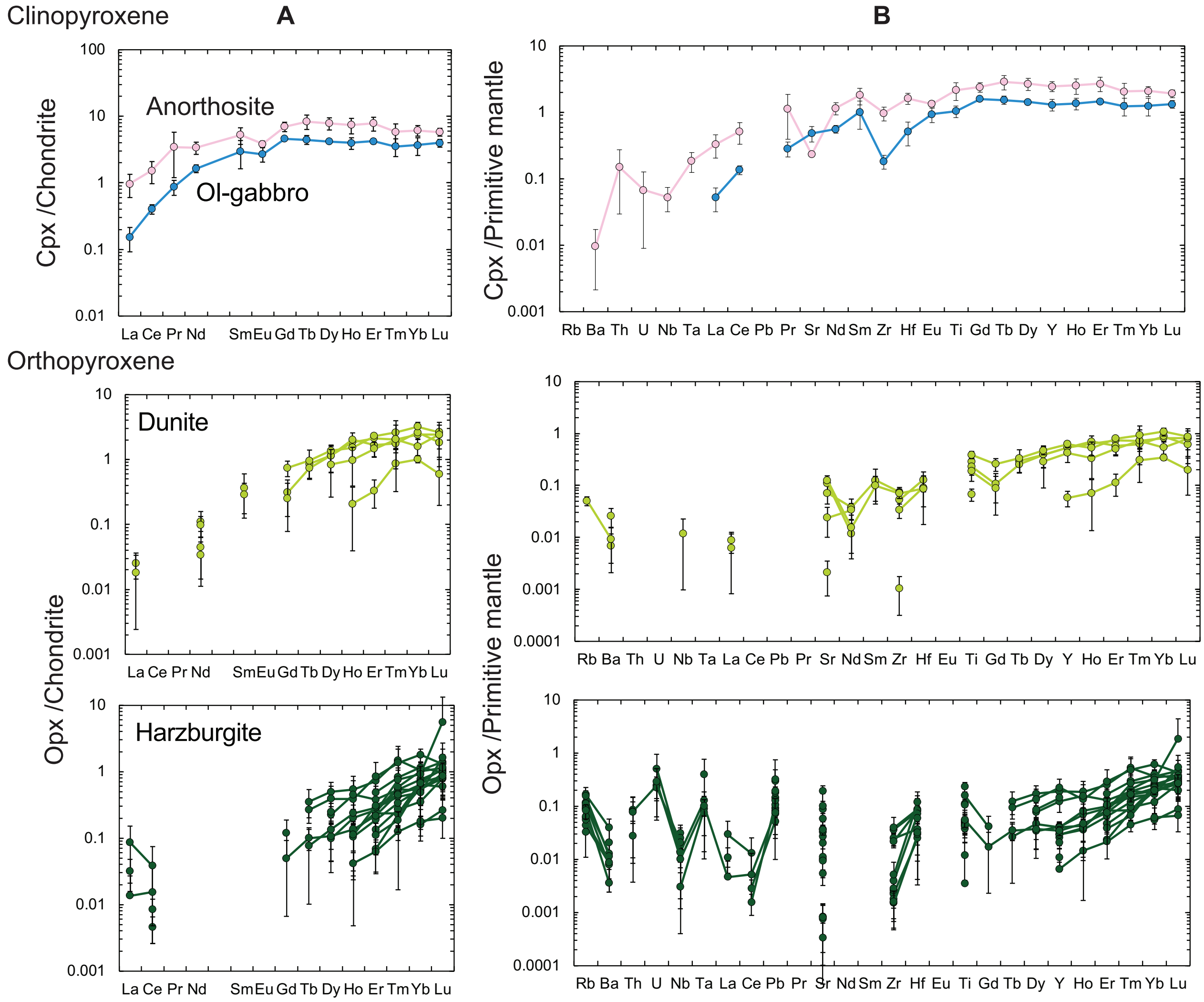

Figure F102. NRM intensity, bulk magnetic susceptibility, and Koenigsberger ratios, Hole CM2B.

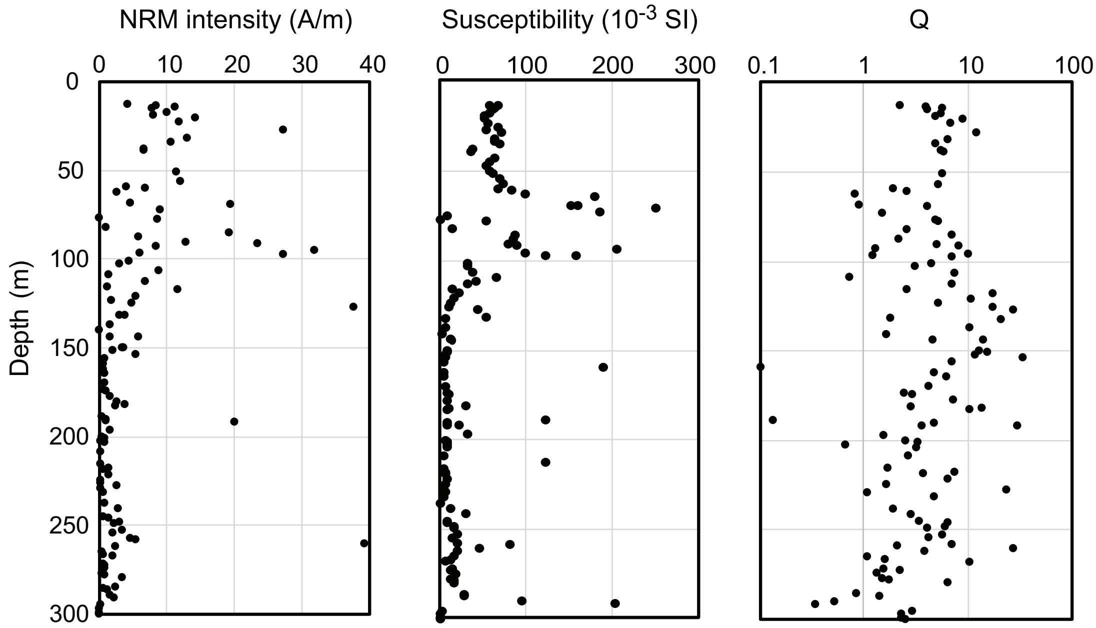

Figure F103. Inclinations of NRM, ChRM, and soft-components isolated from principal component analysis, Hole CM2B.

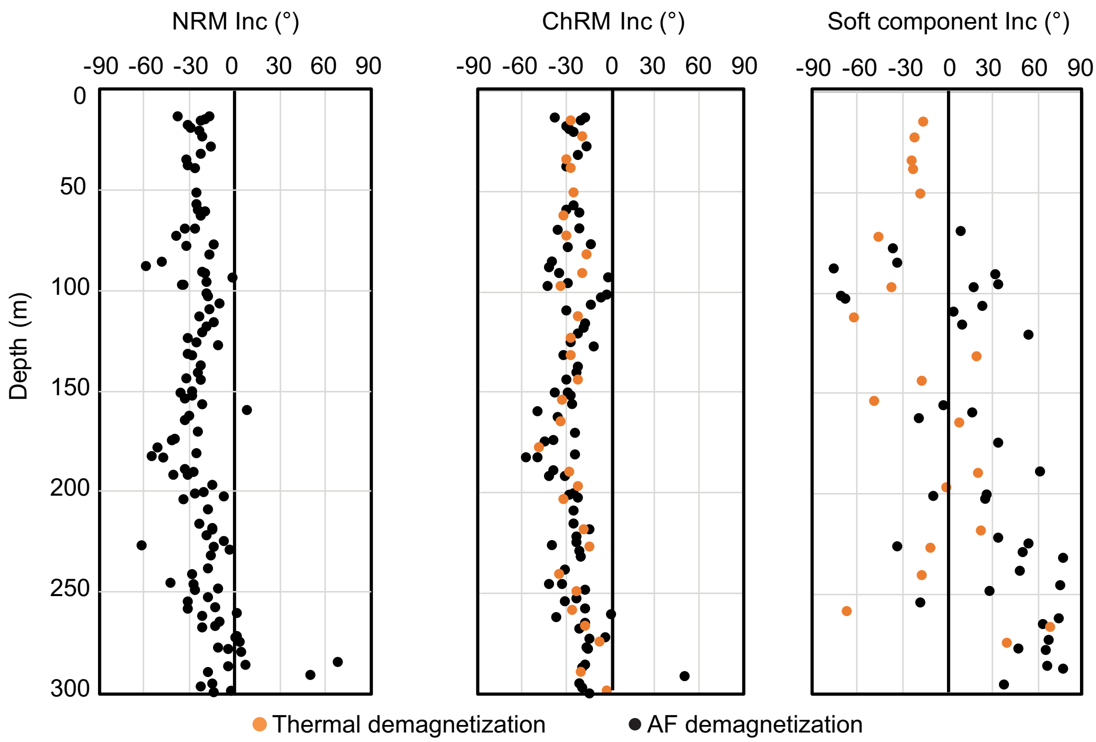

Figure F104. Orthogonal vector diagrams displaying representative behavior of (**A**) magnetic remanence directions during progressive AF demagnetization of samples and (**B**) changes in normalized remanence intensity as a function of demagnetization field, Hole CM2B.

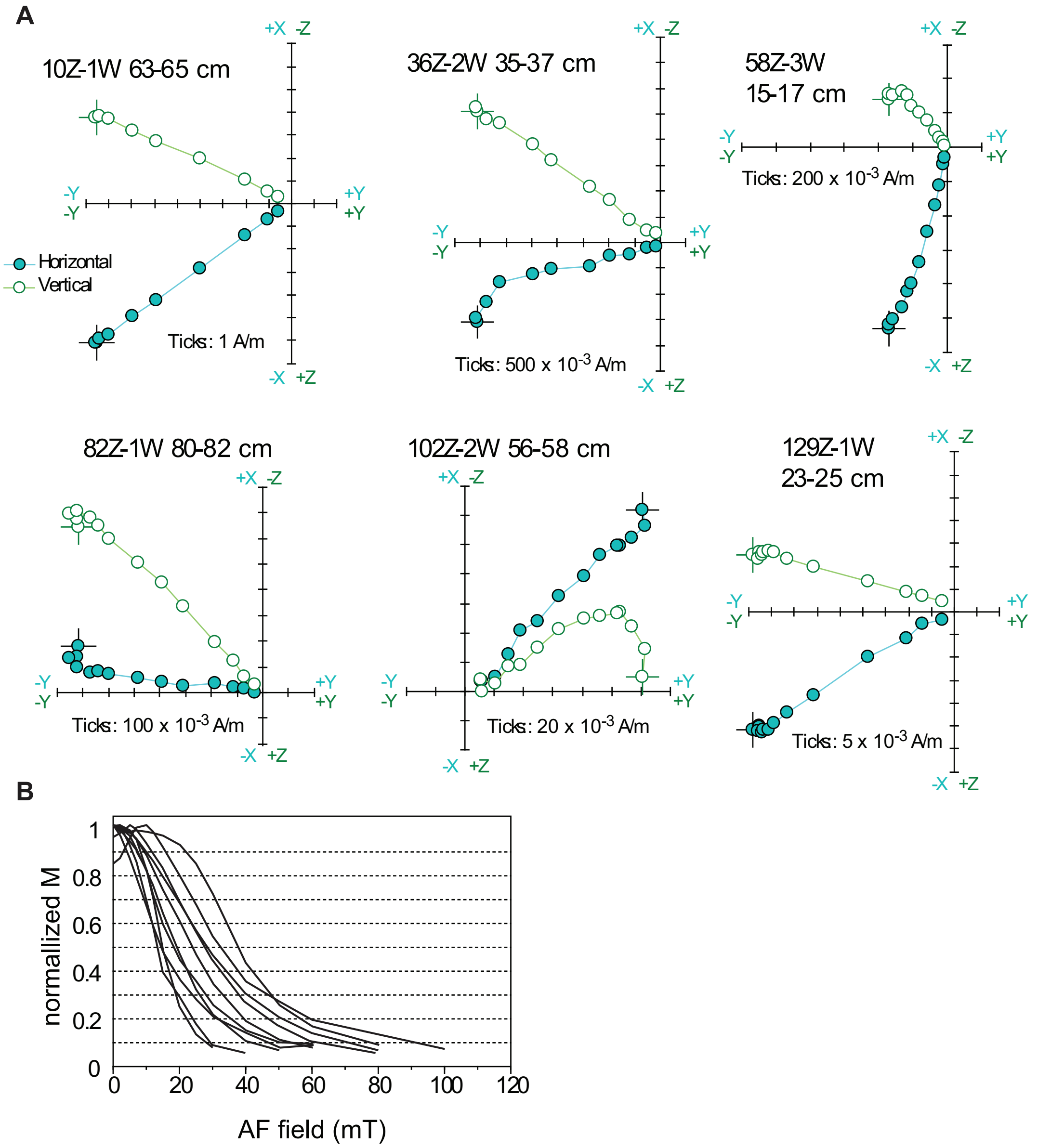

Figure F105. Orthogonal vector diagrams displaying representative behavior of (**A**) magnetic remanence directions during progressive thermal demagnetization of samples and (**B**) changes in normalized remanence intensity as a function of temperature, Hole CM2B.

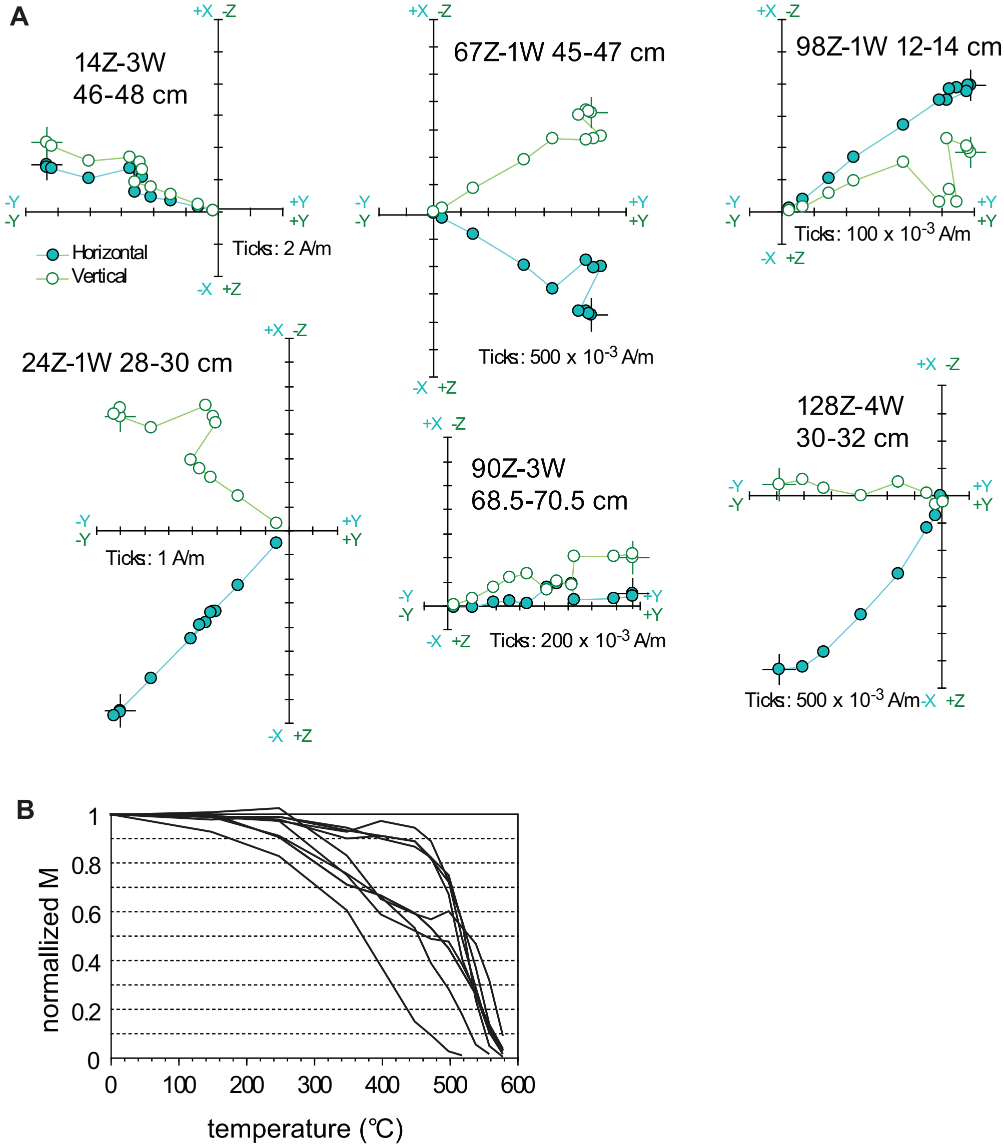

Figure F106. Downhole plots of median destructive field (MDF) and median destructive temperature (MDT) from demagnetization experiments, Hole CM2B.

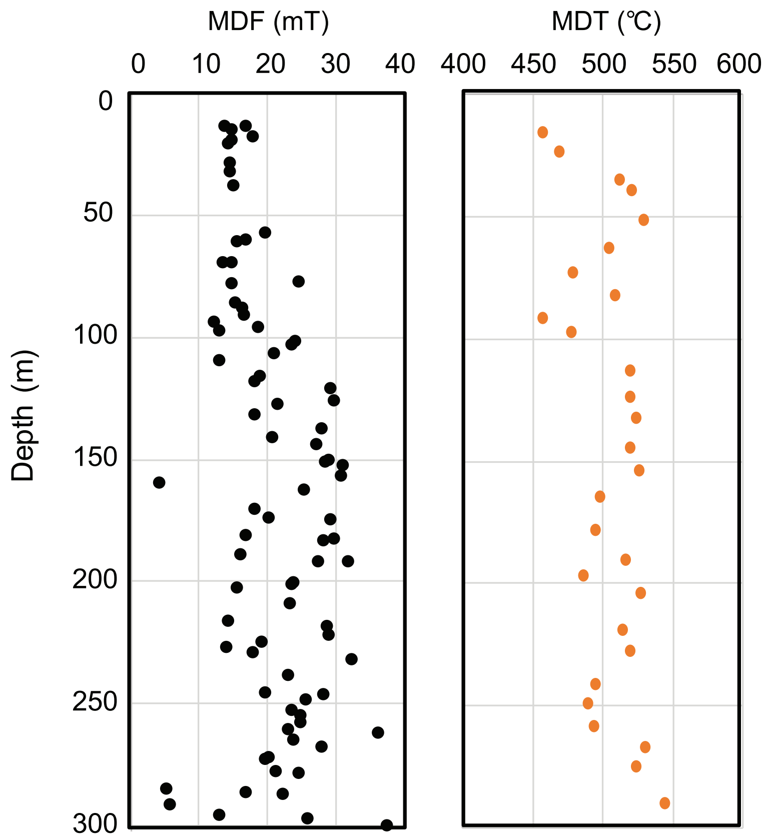

Figure F107. **A.** Magnetic anisotropy intensity (P'), shape parameter (T), and K_{max}, and K_{min} inclinations. **B.** Degree of anisotropy as a function of bulk susceptibility. **C.** Shape parameter T vs. degree of anisotropy of magnetic susceptibility.

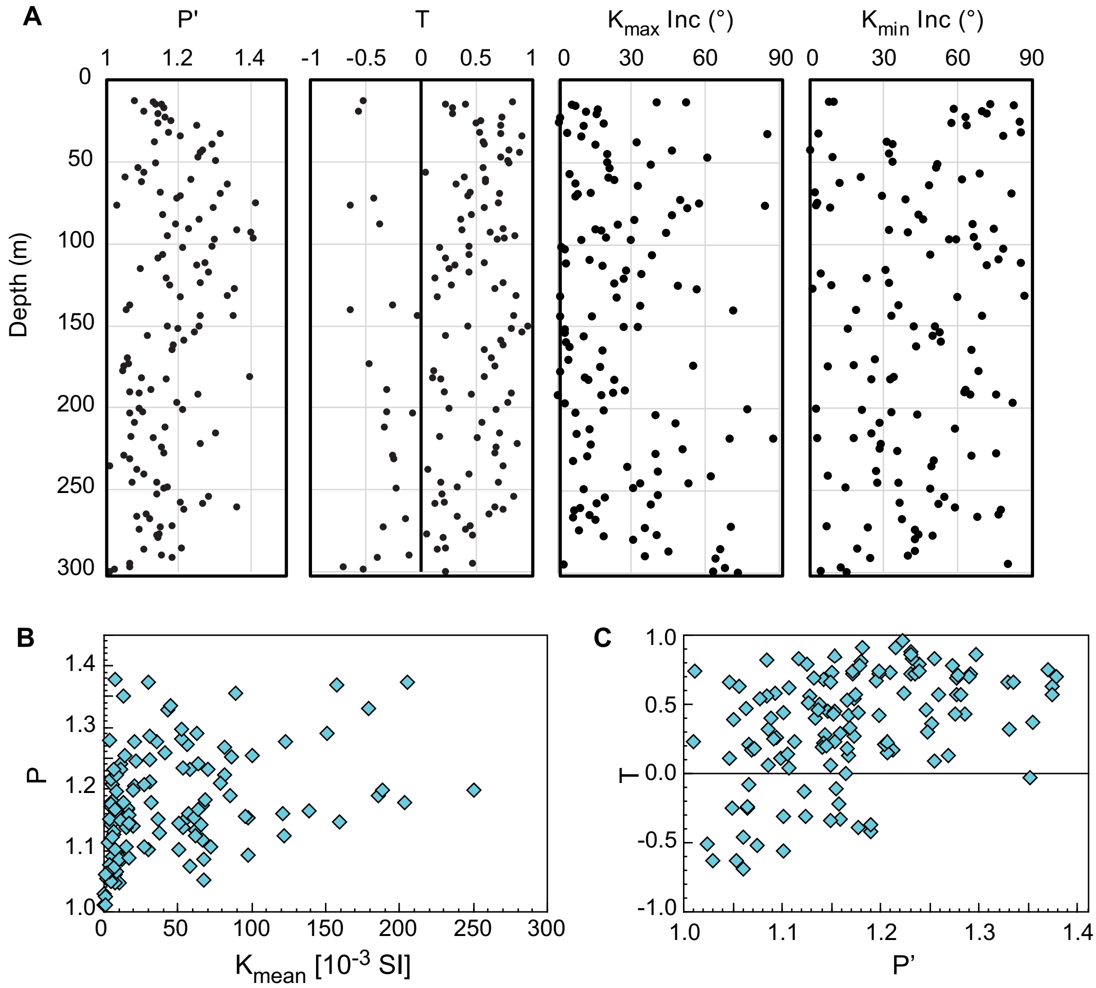

Figure F108. Contoured stereoplots of principal susceptibility axes from AMS analyses plotted on lower hemisphere equal-area projections in the core reference frame, Hole CM2B.

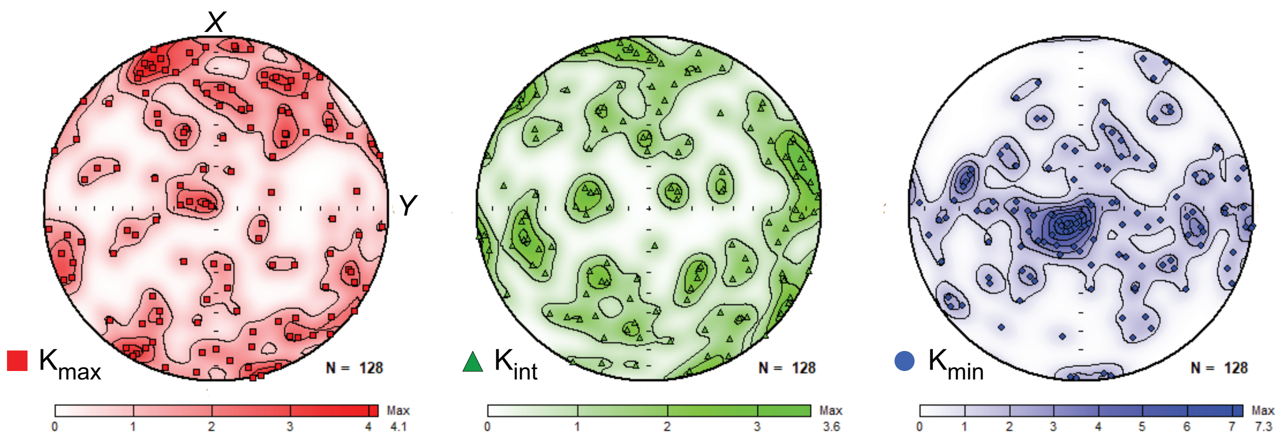

Figure F109. A downhole plot of (**A**) Hole CM2B lithology, (**B**) GRA density, (**C**) magnetic susceptibility, (**D**) electrical resistivity, (**E**) NGR, (**F**) average (blue) and mode (red) of CT numbers in each section, Hole CM2B. Edged symbols in B are bulk density data from discrete sample measurements.

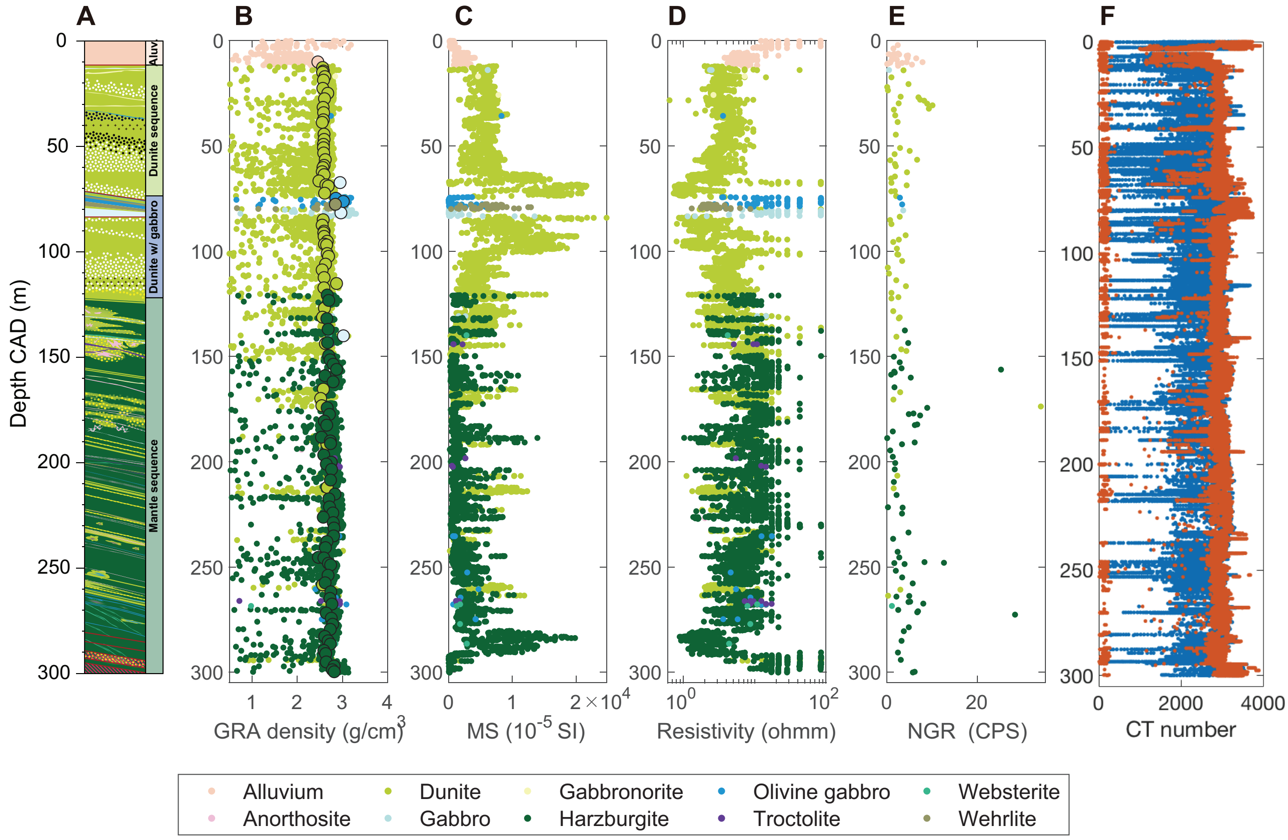

Figure F110. Examples of MSCL-I image, average and mode of CT numbers, and CT image from Hole CM2B. **A.** Alternating layers of dunite and gabbro. **B.** Cr-spinel layer in Dunite Sequence. **C.** Intact harzburgite. **D.** Carbonated harzburgite.

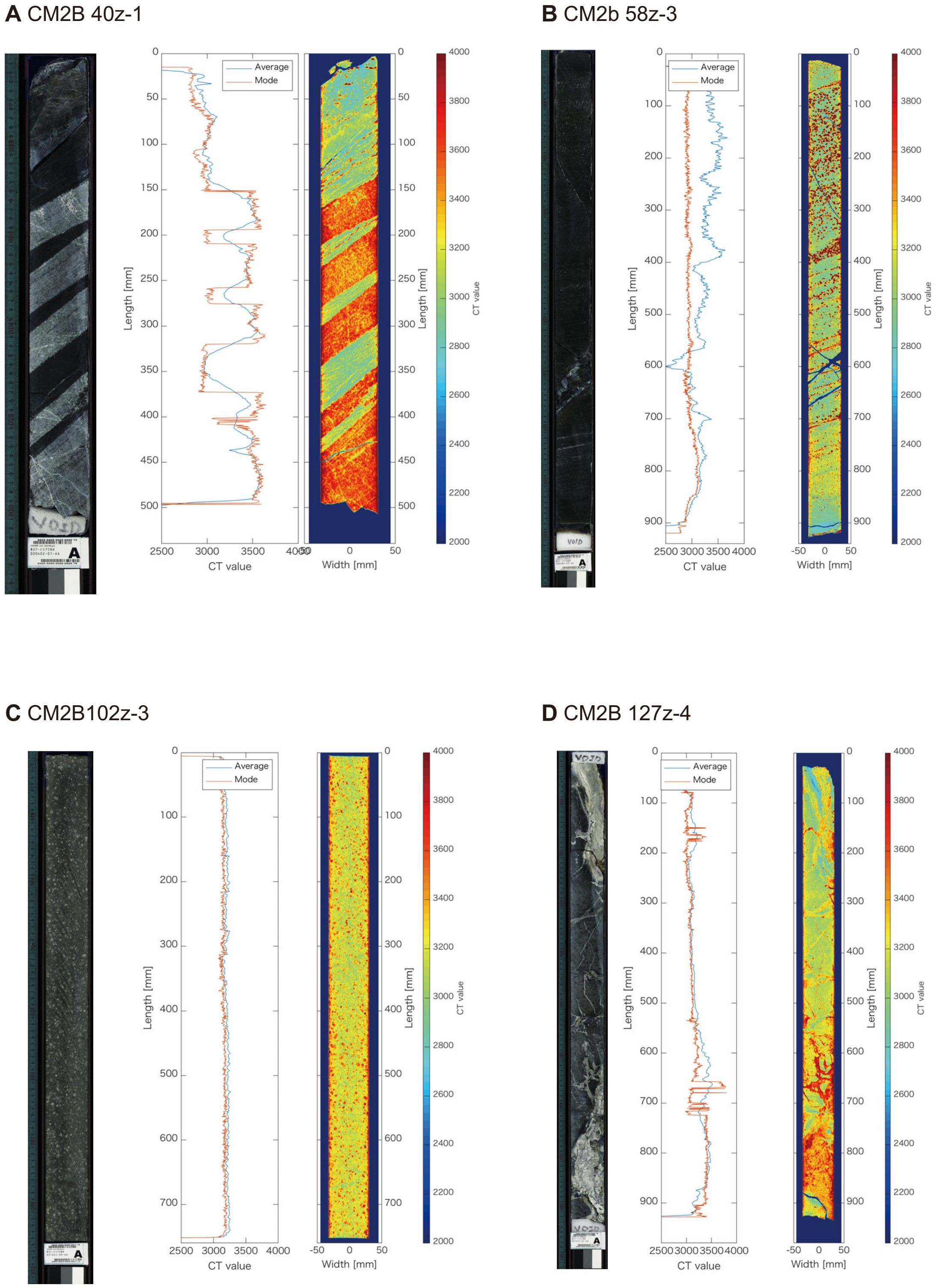

Figure F111. A–C. Correlations between XCT number and GRA density, Hole CM2B, (A) all lithologies, (B) lithologies excluding dunite and harzburgite, (C) dunite and harzburgite. **D–F.** Correlations between whole-round MS and the inverse of whole-round resistivity (i.e., electrical conductivity), (D) all lithologies, (E) lithologies excluding dunite and harzburgite, and (F) dunite and harzburgite.

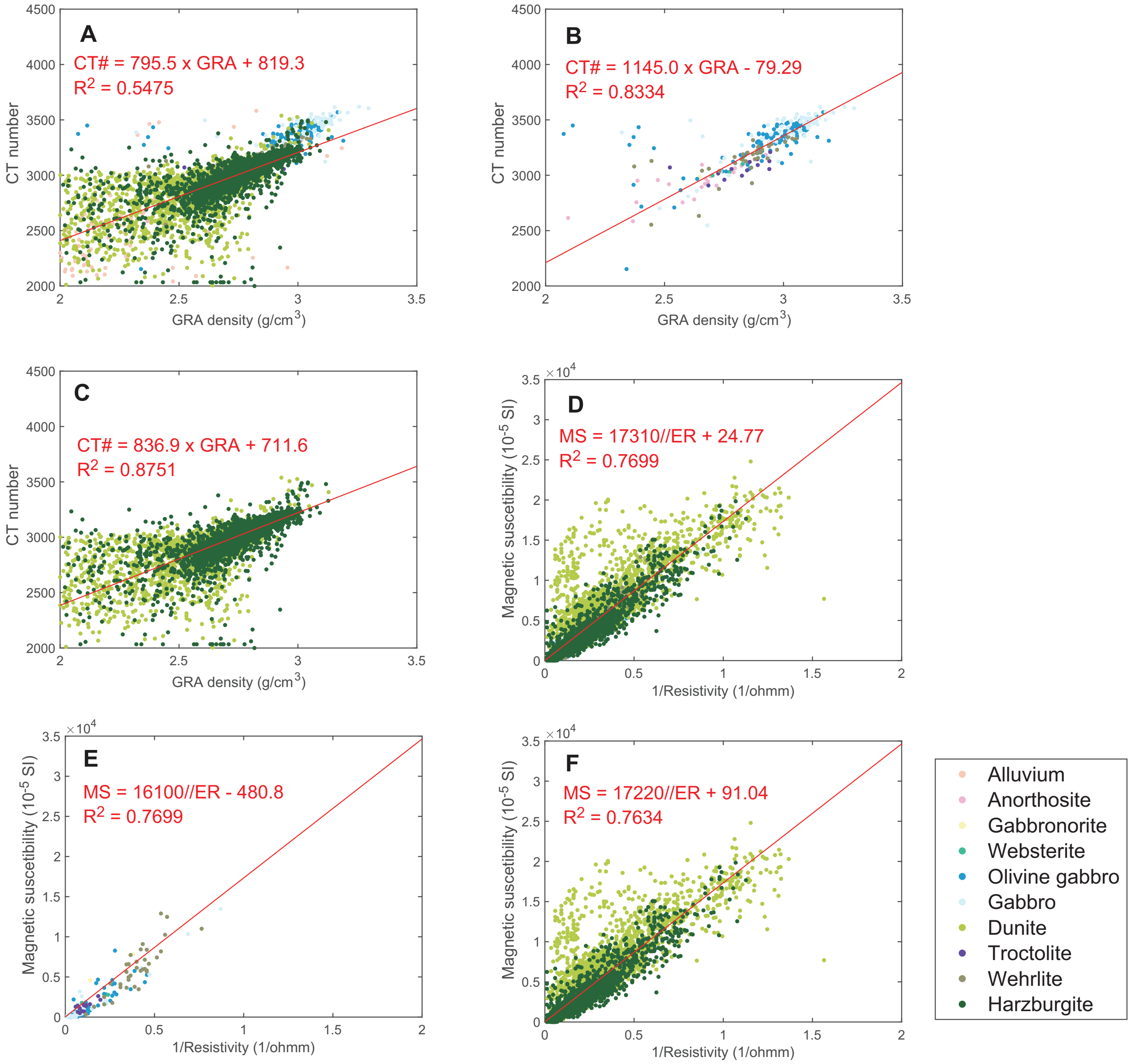

Figure F112. Downhole plot of half-round core measurements, Hole CM2B. Color spectrometry (**A**) L*, (**B**), a*, (**C**) b* and (**D**) point magnetic susceptibility.

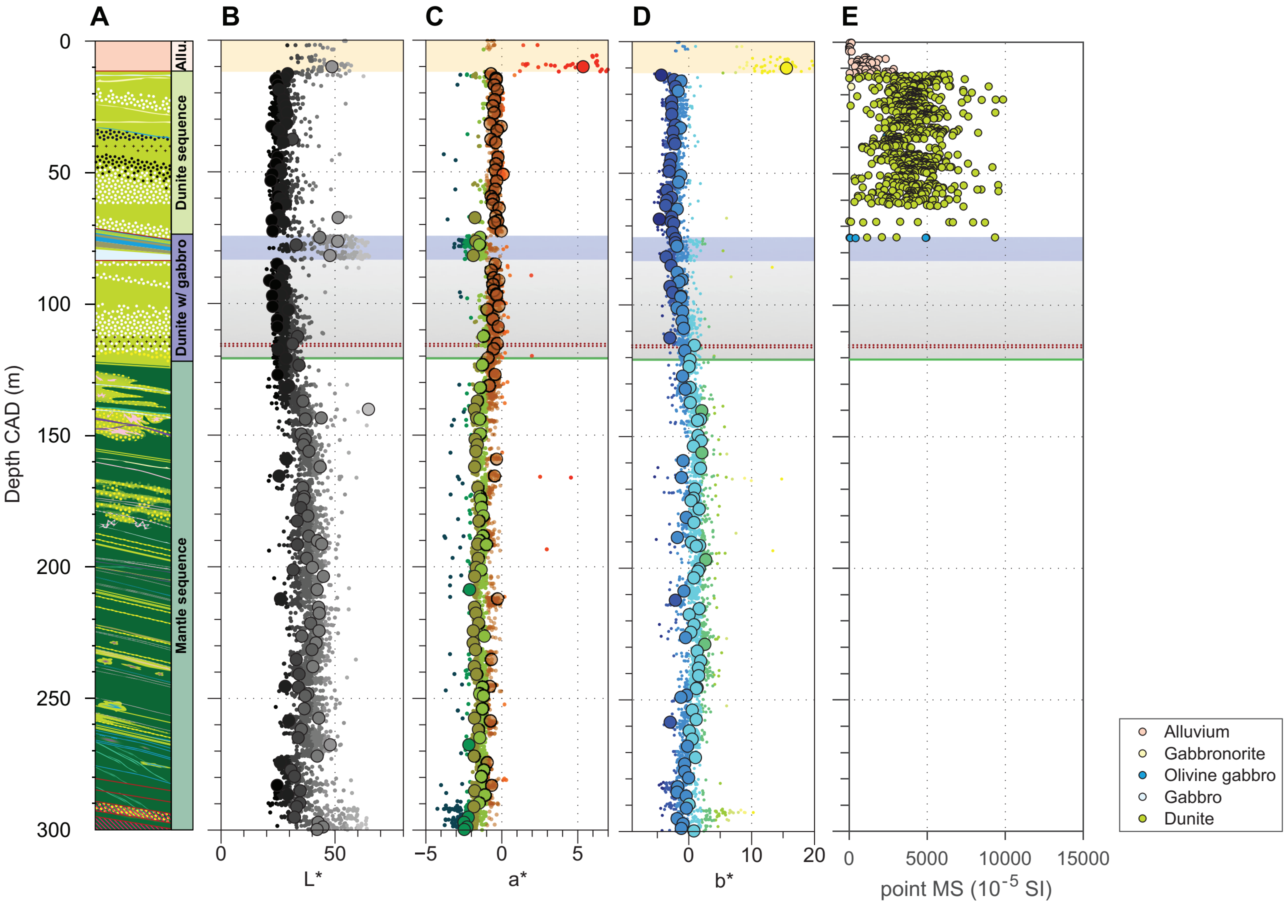

Figure F113. Downhole plots of discrete sample measurements of physical properties. (**A**) *P*-wave velocity, (**B**) bulk density, (**C**) grain density, (**D**) porosity (linear plot), (**E**) porosity (logarithmic plot), (**F**) electrical resistivity (logarithmic plot), (**G**) thermal conductivity, and (**H**) bulk magnetic susceptibility, Hole CM2B. Solid horizontal = sequence boundaries, brown horizontal dotted line = spinel-ridge layer in Dunite Sequence. Hatching: orange = alluvium zone, purple = gabbro intrusion, gray = dunite with gabbro intervening zone.

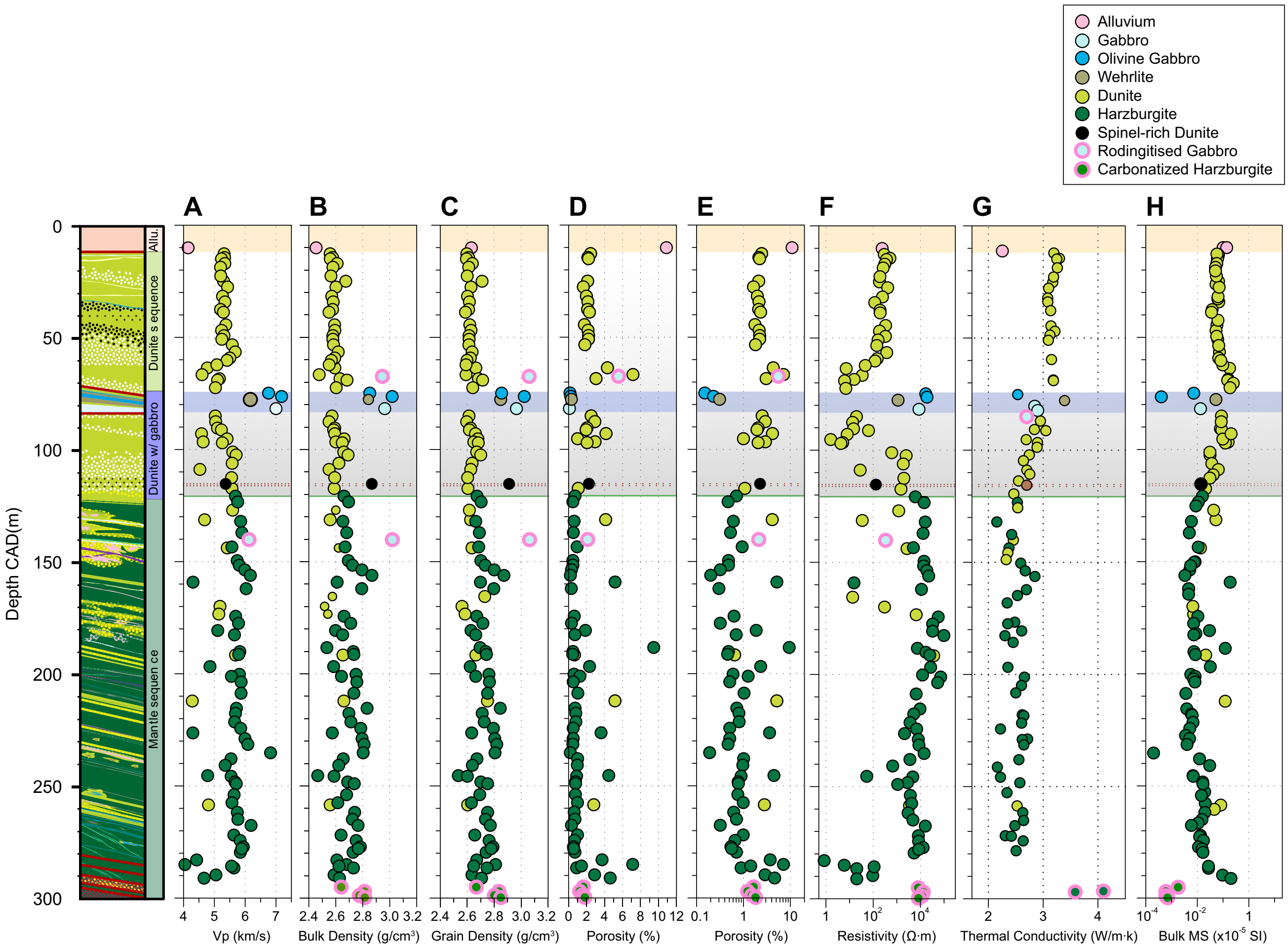

Figure F114. Relationships between *P*-wave velocity and porosity of minicube samples by lithology plotted on (**A**) linear scale and (**B**) logarithmic scale of the horizontal axes, Hole CM2B. Hole CM1A data are also plotted for comparison.

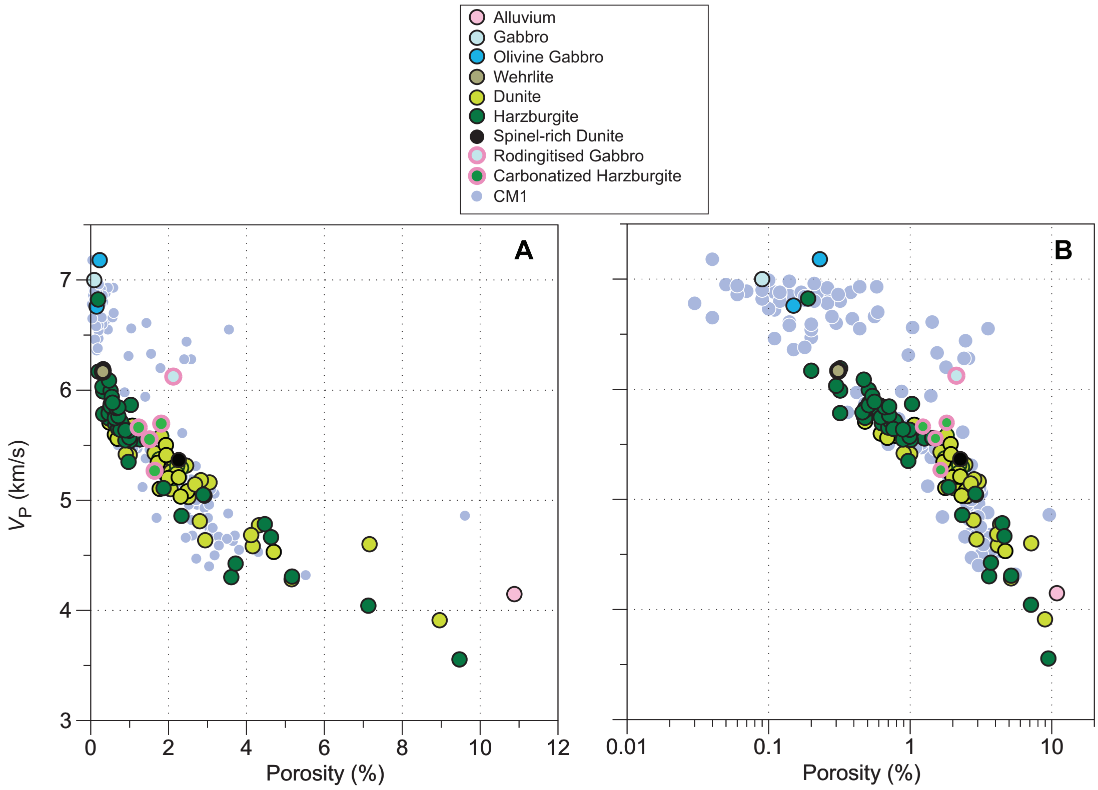

Figure F115. Relationship between *P*-wave velocity and (**A**) bulk density and (**B**) grain density, Hole CM2B. Hole CM1A data are also plotted for comparison.

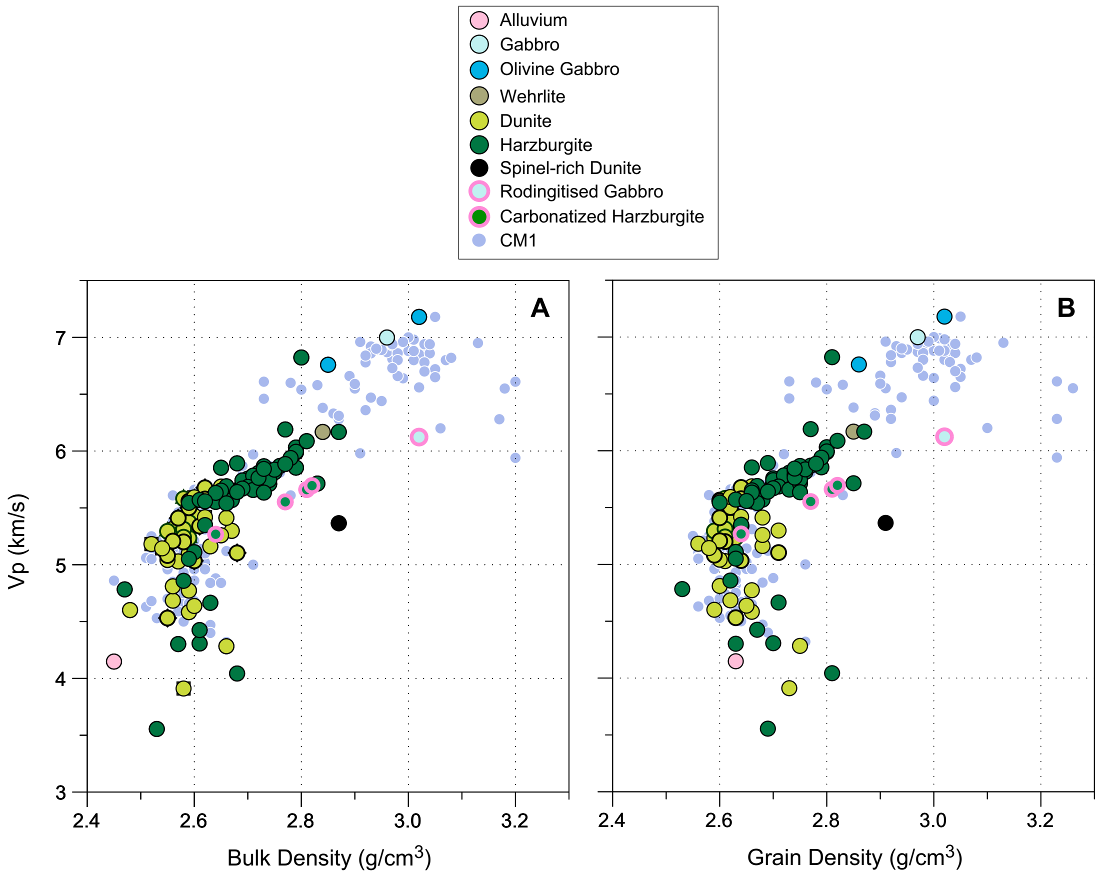

Figure F116. Relationship between (**A**) bulk density and porosity and (**B**) grain density and porosity, Hole CM2B. Hole CM1A data also plotted for comparison.

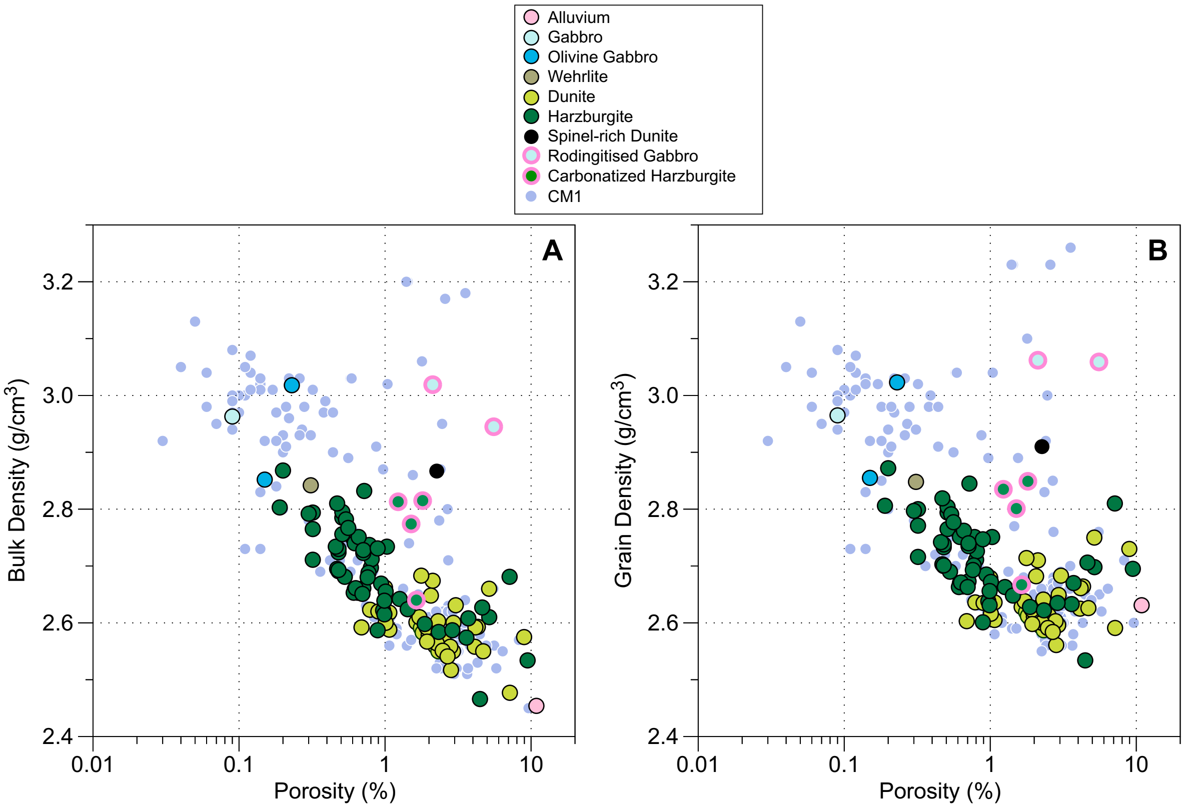

Figure F117. Downhole plot of (**A**) *P*-wave velocity and (**B**) resistivity with color scale of porosity, Hole CM2B. The color of each point represents the degree of porosity for each sample as shown on the corresponding color scale bar. The lowest porosity is in the gabbro zone at ~80 m depth. Deeper, lower porosity tends to show an inverse correlation with velocity and resistivity.

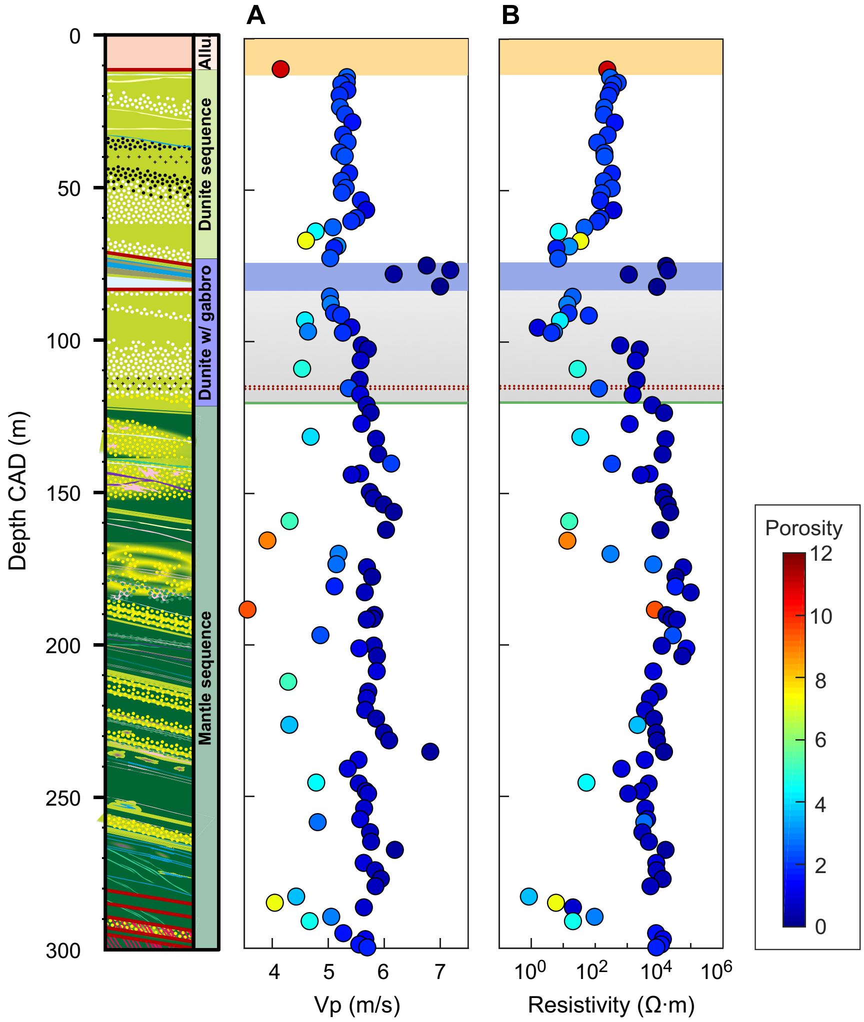

Figure F118. Correlation between bulk magnetic susceptibility and electrical resistivity of the minicube samples, Hole CM2B. Red line = fitting line of $R = 0.014 \times B^{-3.4}$ ($R^2 = 0.61$), where R = resistivity and B = bulk magnetic susceptibility of minicubes.

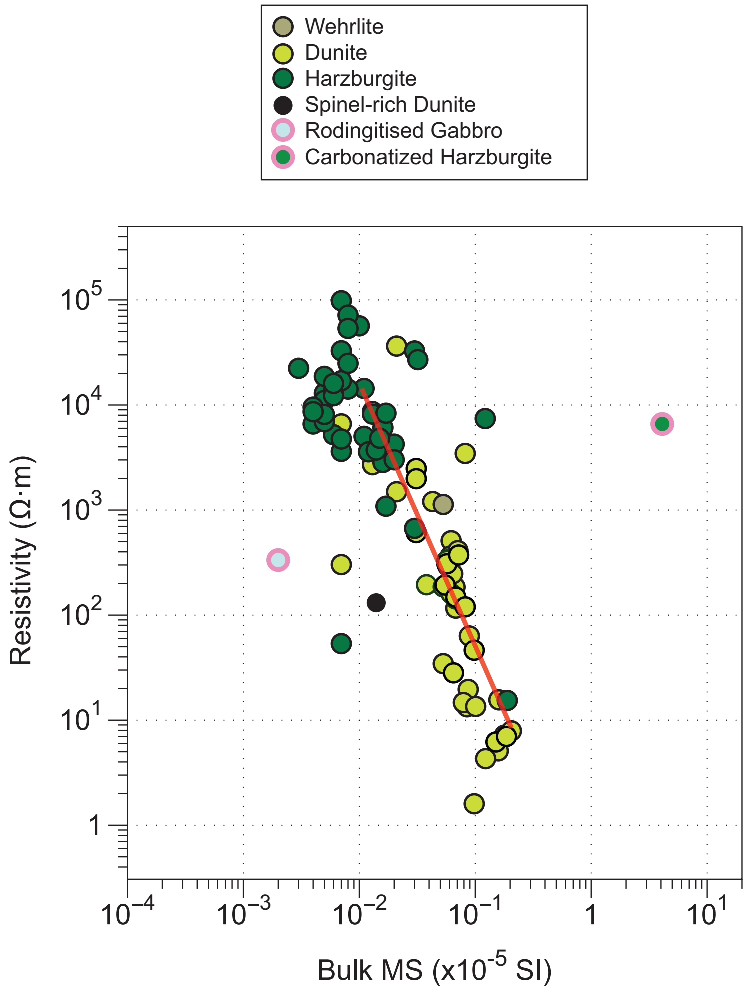

Figure F119. A. Intrinsic specific energy (strength) with a strength color-coded background from Hole CM2B upper section (117.14–144.24 m). **B.** Profile of ultrasonic velocities V_P and V_S overlaid on the strength values (V_P = gray dots, V_S = red dots, strength = blue).

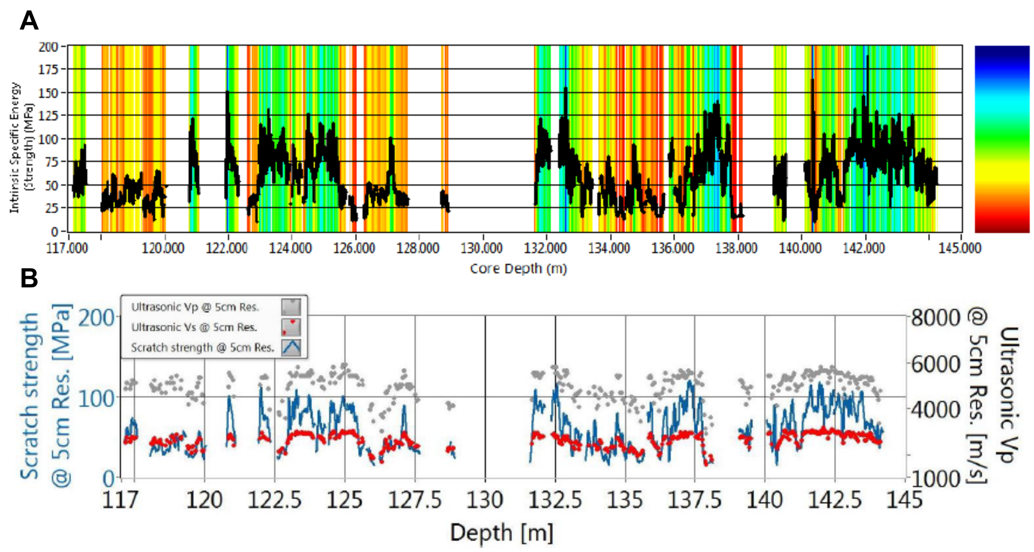

Figure F120. Processed imaging spectroscopy from Hole CM2B. **A.** Lightened MSCL-I image of a zone altered to serpentine, talc, and carbonate. **B.** False-color infrared composite image from the SWIR sensor. Wavelengths displayed are as follows: red = 2.310 µm, green = 1.577 µm, blue = 1.085 µm. Colors depend on the Fe content and mineralogy. **C.** Mineral classification derived using combinations of band depths (Clark and Roush, 1984) and by comparison with spectra of pure minerals from the USGS spectral library (Kokaly et al., 2017) to assess the presence and absence of diagnostic mineral features indicative of minerals of interest. Other minerals and additional mixing are likely present but are not shown in this view for simplicity.

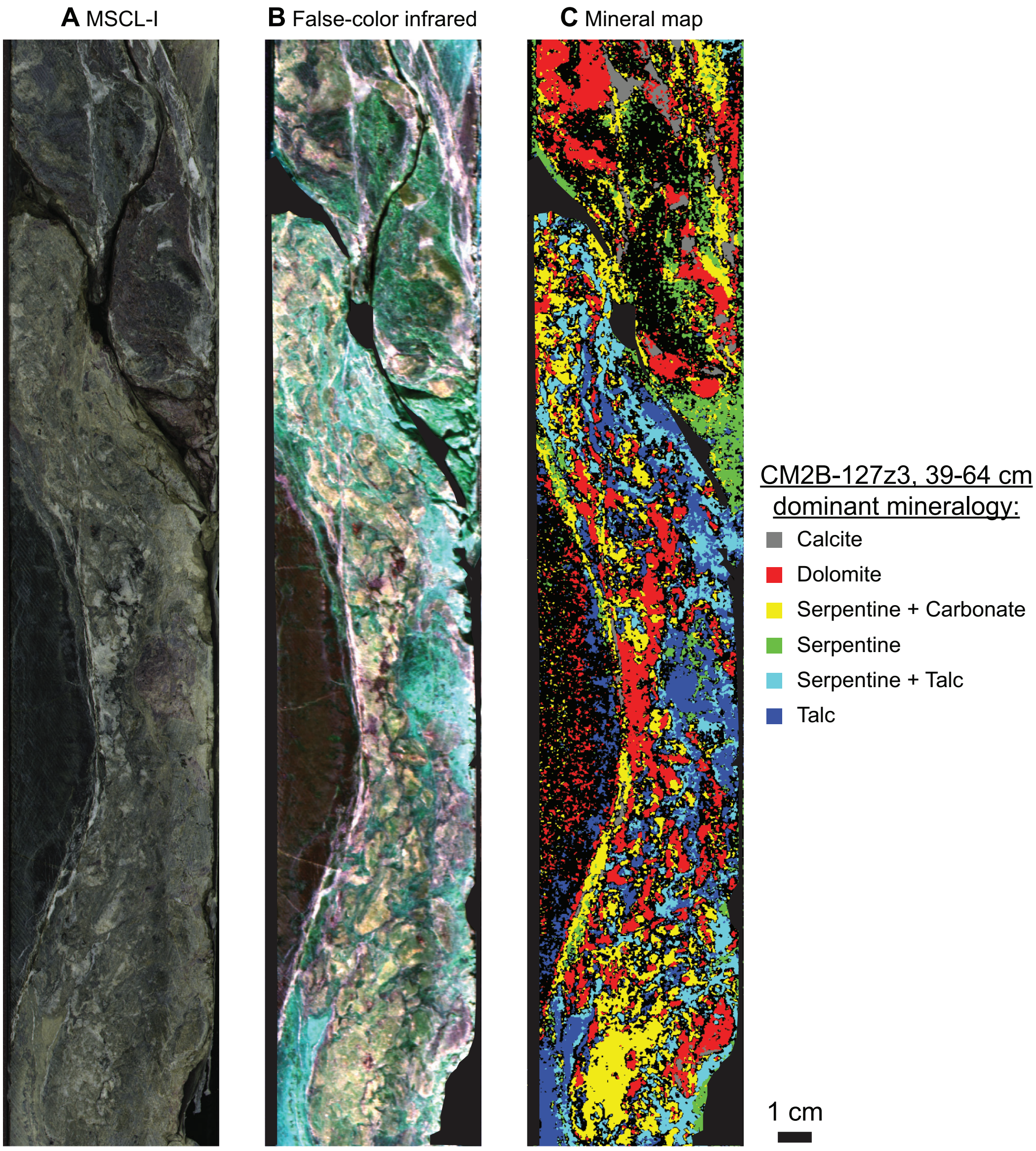

Tables

Table T1. Drilling operations, Site CM2. **This table is available in Microsoft Excel format.**

Table T2. Cuttings lithology log, Hole CM2A. **This table is available in Microsoft Excel format.**

Table T3. Number and thickness of units/subunits in each principal lithologic sequence, Hole CM2B. **This table is available in Microsoft Excel format.**

Table T4. Details of the principal lithologic sequences, Hole CM2B. **This table is available in Microsoft Excel format.**

Table T5. Assumed peridotite mineral compositions for mode regression, Hole CM2B. **This table is available in Microsoft Excel format.**

Table T6. DTS-2B dunite standard replicate analyses, USGS preferred composition, and correction factor applied to bulk rock data, Hole CM2B. **This table is available in Microsoft Excel format.**

Table T7. Compilation of secondary minerals identified by XRD aboard *Chikyu*, Hole CM2B. **This table is available in Microsoft Excel format.**

Table T8. XRD analysis of on-site bulk rock powders, Hole CM2B. **This table is available in Microsoft Excel format.**

Table T9. Characteristics of vein generations, Hole CM2B. **This table is available in Microsoft Excel format.**

Table T10. Sense of shear indicators, Hole CM2B. **This table is available in Microsoft Excel format.**

Table T11. Alteration vein dips, Hole CM2B. **This table is available in Microsoft Excel format.**

Table T12. Types of fault zones, Hole CM2B. **This table is available in Microsoft Excel format.**

Table T13. Vein generations, Hole CM2B. **This table is available in Microsoft Excel format.**

Table T14. Whole-rock LOI, major and trace elements, total and inorganic carbon, and H_2O, Hole CM2B. **This table is available in Microsoft Excel format.**

Table T15. Whole-rock trace element compositions of selected samples, Hole CM2B. **This table is available in Microsoft Excel format.**

Table T16. Clinopyroxene trace element compositions of selected samples, Hole CM2B. **This table is available in Microsoft Excel format.**

Table T17. Orthopyroxene trace element compositions of selected samples, Hole CM2B. **This table is available in Microsoft Excel format.**

Table T18. Natural remanent magnetization and principal component analysis results, Hole CM2B. **This table is available in Microsoft Excel format.**

Table T19. Bulk magnetic susceptibility and anisotropy of MS results, Hole CM2B. **This table is available in Microsoft Excel format.**

Table T20. Summary of whole-round and section-half physical property measurements, Hole CM2B. **This table is available in Microsoft Excel format.**

Table T21. Summary of discrete physical property measurements, Hole CM2B. **This table is available in Microsoft Excel format.**

Table T22. Velocity, density, porosity, and electrical resistivity measurements, Hole CM2B. **This table is available in Microsoft Excel format.**

Table T23. Thermal conductivity measurements, Hole CM2B. **This table is available in Microsoft Excel format.**

Supplemental tables

Table ST1. Detailed descriptions of all described intervals/units/subunits, Hole CM2B. **This table is available in Microsoft Excel format.**

Table ST2. Summary of all described units and subunits, Hole CM2B. **This table is available in Microsoft Excel format.**

Table ST3. Summary of igneous thin section descriptions, Hole CM2B. **This table is available in Microsoft Excel format.**

Table ST4. Mineral modes, mode residuals, and corrected bulk rock major element compositions and trace element concentrations, Hole CM2B. **This table is available in Microsoft Excel format.**

Table ST5. Alteration log, Hole CM2B. **This table is available in Microsoft Excel format.**

Table ST6. Vein log, Hole CM2B. **This table is available in Microsoft Excel format.**

Table ST7. Spreadsheet calculations for plots, Hole CM2B. **This table is available in Microsoft Excel format.**

Table ST8. MSCL-W (GRA density, NGR, *P*-wave velocity, MS and NCR), Hole CM2B. **This table is available in Microsoft Excel format.**

Table ST9. MSCL-C (Color spectrum and MS), Hole CM2B. **This table is available in Microsoft Excel format.**

Supplemental figures

Figure SF1. XRD compilation of Cores CM2B-1Z through 50Z. **This figure is available in PDF format.**

Figure SF2. XRD compilation Cores CM2B-51Z through 100Z. **This figure is available in PDF format.**

Figure SF3. XRD compilation Cores CM2B-101Z through 125Z. **This figure is available in PDF format.**

Figure SF4. XRD compilation Cores CM2B-126Z through 129Z. **This figure is available in PDF format.**